Artificial Kagome Spin Networks - From Short-Range Degeneracy towards Long-Range Dipolar Order

Ioan-Augustin Chioar

UNIVERSITÉ GRENOBLE ALPES

THÈSE

Pour obtenir le grade de

DOCTEUR DE L'UNIVERSITÉ GRENOBLE ALPES

Spécialité : **Physique/Nanophysique**

Arrêté ministériel : 7 août 2006

Présentée par

Ioan-Augustin CHIOAR

Thèse dirigée par **Benjamin CANALS** et
co-encadrée par **Nicolas ROUGEMAILLE**

préparée au sein de **l'Institut Néel**
dans **l'École Doctorale de Physique de Grenoble**

Glaces kagomé de spin artificiels
De la dégénérescence à courte portée vers l'ordre dipolaire

Thèse soutenue publiquement le **16/10/2015**,
devant le jury composé de :

M. Peter HOLDSWORTH
Rapporteur
M. Sylvain PETIT
Rapporteur
Mme Virginie SIMONET
Président
M. Daniel LACOUR
Membre
M. Benjamin CANALS
Directeur de thèse
M. Nicolas ROUGEMAILLE
Co-encadrant de thèse

I would like to dedicate this thesis to my loving parents, Maria-Mihaela and Dumitru.
Mulţumesc!

Declaration

I hereby declare that, except where specific reference is made to the work of others, the contents of this dissertation are original. This dissertation is my own work and contains nothing which is the outcome of work done in collaboration with others, except as specified in the text and in the Acknowledgements.

Some parts of the contents of chapters 2 and 3 of this thesis have been published in the following jointly authored manuscripts respectively:

1) **I. A. Chioar**, B. Canals, D. Lacour, M. Hehn, B. Santos Burgos, T. O. Menteş, A. Locatelli, F. Montaigne, and N. Rougemaille - *Kinetic pathways to the magnetic charge crystal in artificial dipolar spin ice*, Phys. Rev. B **90**, 220407 (2014).

2) **I. A. Chioar**, N. Rougemaille, A. Grimm, O. Fruchart, E. Wagner, M. Hehn, D. Lacour, F. Montaigne, and B. Canals - *Nonuniversality of artificial frustrated spin systems*, Phys. Rev. B **90**, 064411 (2014).

Ioan-Augustin CHIOAR
November 2015

Acknowledgements

I would like to begin by thanking my supervisors, Benjamin Canals and Nicolas Rougemaille. The rich knowledge that they have shared with me, along with their patience, relentless support and careful guidance, have immensely contributed to this work and to my professional and personal development over the past years. Working with them has been a privilege and a pleasure and they have never ceased to share their ideas, thoughts and passion for research. I am also very grateful for the opportunity to perform both experimental and theoretical work, a mix that I've very much enjoyed and that they have constantly supported. This has continuously supplied us with new ideas and a rich spectrum of fascinating research avenues, thus making my work ever more motivating. As I've said many times and probably way too much, I've been their little Padawan learner and, thanks to them, I've not fallen to the dark side.

I would also like to thank all the people associated to this project. In particular, I would like to thank Michel Hehn, Daniel Lacour and François Montaigne, our partners from the Jean Lamour Institute in Nancy, for supplying the samples, thus allowing me to experimentally explore artificial spin ice behavior. I am also grateful for many fruitful discussions and for the time spent in Nancy, both for working in the lab and for visiting the lovely town. I would further like to thank Edouard Wagner for designing the experimental protocol used for demagnetizing the artificial nano-scaled arrays. A big thanks goes to Olivier Fruchart, who not only trained me for using the Magnetic Force Microscope (MFM) but has also offered many useful insights that have helped me further develop my research project. Zahid Ishaque has always been there when something went wrong during my early MFM measurements and I am grateful for his patience. Simon Le Demnat has also been very supportive when it comes to Magnetic Force Microscopy and I am particularly grateful for all the hard work he has done to retrofit the microscope for allowing measurements under applied field. I would also like to thank Andrea Locatelli, Telfik Onur Menteş and Benito de Santos Burgos from the ELLETRA Synchrotron in Trieste, who, along with my supervisors and partners from Nancy, have performed the measurements on thermally-active artificial kagome spin ices. This has brought additional experimental input to my thesis and has proven to be a very rich set of data that has helped me further understand the fascinating behavior of kagome spin ice.

I would like to further thank Peter Holdsworth, Daniel Lacour, Sylvain Petit and Virginie Simonet for accepting to form the doctoral committee.

This thesis has been supported by the Laboratoire d'Excellence LANEF in Grenoble and I am grateful to them for the financial support given over the past three years.

I have also been very eager to teach during my PhD and I would like to thank Julien Delahaye for entrusting me with a group of students for the seminar and lab training sessions of his course on Electrostatics. It has been a very enriching experience which I have very much enjoyed.

I would further like to thank all members of the Condensed Matter Theory group and those of the Micro and Nanomagnetism team for their warm welcome, their support and the numerous and helpful discussions. Special thanks go here to Arnaud Ralko and Rafik Ballou for helping me understand many puzzling aspects related to spin models and frustrated magnetism.

Further thanks go to all my office-mates, both past and present. Marc Ganzhorn and Eva Dupont-Ferrier have kindly welcomed me to the Phd-life in the lab. Emilie Lefrançois has been a constant source of catchy tunes and Evan Constable was always there when I had a LaTeX issue. A special thanks goes to Karim Ferhat for the numerous scientific discussions and particularly for his inspirational presentation on the 1/3 filling of the kagome lattice, which has ultimately lead me to the geometrical construction that unraveled the ordering patterns in the low-temperature regime of the dipolar kagome Ising antiferromagnet. I've been working on that for a long time and it just popped-up after that seminar!

Life at the laboratory would not have been so cheerful without Yann Perrin and I would like to thank him for the many discussions on artificial spin ices and for his unique and refined humor. Sorry again for not letting you take that souvenir from the conference in Nancy and thanks for all the French-slang lessons. Thanks to Van Dai Nguyen for helping me with the calibration of the demagnetizing coil and to Clement Février for numerous discussions, particularly on how to optimize the structure factor analysis code. Unfortunately, I didn't manage to get it done in time so I couldn't include the data in this manuscript, but it works quite well now.

I would also like to thank my friends, who have been by my side over the past years. A heartily thank you to Alexandru Trifu and Alexandru Todoran for a true and treasured friendship. Thanks to Jose Luiz Ferreira for being my tennis partner and to André Suchet for his good advice and all the unique sport activities. Further thanks to Daniel Langley, Cristina Stanciu, Ovidiu Florea, Andrei Bechet, Rodica Munteanu and Mugur Fratila for their friendship and support.

Last but not least, I would like to thank my entire family for their unconditional love and support, particularly my parents, Maria-Mihaela and Dumitru. Mulţumesc!

Abstract

Artificial spin networks have been initially proposed as toy-spin models destined for the investigation of magnetic frustration effects in two-dimensional spin lattices[1], a complementary approach to the study of the magnetic frustration encountered in condensed matter spin ice pyrochlores[2]. Generally fabricated by employing lithography techniques, these arrays of nano-scale magnetic islands can be designed at-will. Furthermore, given the size and shape of the magnetic elements, the magnetization is almost uniform throughout their volume, thus making these islands act like giant classical Ising spins. Combined with the possibility of individually imaging the magnetic degrees of freedom in real space, these systems offer an almost infinite playground for the investigation of competing interactions in magnetostatic frameworks and potential for the experimental discovery of novel and exotic magnetic phases. However, unlike their condensed matter counterparts, the first-generation artificial spin networks are insensitive to thermal fluctuations, requiring other driving mechanisms for accessing their complex low-energy manifolds. A field-protocol has thus been employed[3] for driving such networks towards their ground-state configurations. Although the lowest-energy states have not been accessed so far by these means, this procedure nevertheless manages to partially accommodate inter-island interactions. More recently, thermally-active artificial spin networks have been introduced[4–6], managing to go beyond the limits of demagnetized arrays in the quest for exotic low-energy spin textures.

This thesis presents experimental and numerical studies performed on artificial kagome spin arrays, one of the most frustrated two-dimensional lattices. The kagome spin ice geometry has received most of the community's attention during the past years as it presents highly degenerate manifolds and unconventional spin arrangements. Furthermore, within a dipolar long-range framework, it displays a low-temperature regime characterized by the coexistence of a crystalline phase, associated to the magnetic charge, and a disordered spin lattice[7–9]. While demagnetizing such artificial kagome arrays cannot access this exotic state, thermally-active networks can locally retrieve such a phase, creating crystallites of antiferromagnetically-ordered magnetic charges[6, 10–12]. The first part of this work presents the experimental protocol employed for this purpose. Curiously, although such artificial networks are subject to thermal fluctuations, they present clear signs of an out-of-

equilibrium physics. A kinetic model is also proposed that successfully captures the observed experimental features and explains the efficiency of this approach.

The second and main part of the current thesis presents a study of a novel artificial spin ice system, the artificial kagome Ising network. This network primarily differs from the intensively-investigated kagome spin ice array by having its magnetic moments pointing along the vertical axis instead of lying in the network's plane. A recent study[13] of this system has concluded that, after demagnetization, these two artificial kagome networks display similar pairwise spin correlation development. In addition, their final frozen states can be well characterized by employing a short-range interaction picture, despite the long-range dipolar coupling between the nanoislands. Through the use of demagnetization protocols, magnetic force microscopy measurements and Monte Carlo simulations, it is demonstrated that long-range dipolar interactions between the constituting magnetic elements cannot be neglected when describing the remanent states of the demagnetized artificial kagome networks[14]. These results assess the limits of the reported universal behavior of the artificial kagome lattices and enrich the spectrum of magnetic phases that can be potentially achieved with such nanostructured systems. Indeed, Monte Carlo simulations indicate that this kagome Ising network presents a different low-energy behavior than kagome spin ice, the incipient stages of which have been accessed experimentally, but its dipolar ground-state configuration remains, so far, unknown. Nevertheless, by inspecting the low-temperature thermodynamic features of this array and through the use of a geometrical construction, a ground-state candidate is provided, which is in good agreement with all results reported so far.

Résumé

Les réseaux artificiels de nano-aimants ont été récenment utilisés pour étudier les effets de frustration géométrique dans des réseaux bidimensionnels de spin[1], une approche complémentaire à l'étude de la frustration rencontrée dans les glaces de spin pyrochlores[2]. Généralement fabriqués en utilisant des techniques de lithographie, ces réseaux de nanoaimants peuvent être élaborés avec un grand degré de liberté. Etant donné la taille et la forme de ces plots magnétiques, l'aimantation est essentiellement uniforme dans tout leur volume, un aspect qui fait que ces aimants peuvent être considérés comme des spins Ising classiques. En ajoutant la possibilité d'imager chacun de ces degrés de liberté magnétiques dans l'espace direct, ces systèmes offrent un large spectre d'opportunités pour l'étude de la frustration et la mise en evidence de phases magnétiques exotiques. Toutefois, contrairement à leurs homologues de la matière condensée, la première génération de glaces de spin artificielles est pratiquement insensible aux fluctuations thermiques. Par conséquent, d'autres dynamiques sont nécessaires pour amener ces systèmes vers leurs variétés de basse énergie et un protocole de désaimantation a été généralement utilisé dans ce sens[3]. Malgré le fait que les variétés fondamentales n'ont pas été obtenues expérimentalement par cette méthode, ces processus arrivent à accommoder partiellement les interactions entre les nano-aimants. Plus récemment, des réseaux artificiels de spin thermiquement actifs ont été introduits[4–6] et permettent de dépasser les limitations des réseaux désaimantés pour la recherche de textures de spin exotiques.

Cette thèse présente des études expérimentales et numériques réalisées sur des réseaux de spin kagomé. La glace artificielle kagomé planaire a été un point central d'intérêt ces dernières années, grâce à ses variétés énergétiques hautement dégénérées et aux textures de spin non-conventionnelles. Ainsi, dans un cadre magnétostatique, elle présente une phase exotique caractérisée par la coexistence d'un état cristallin, associée à la charge magnétique, et un réseau de spin désordonné[7–9]. Bien que la désaimantation ne permette pas d'accéder à cet état remarquable, les réseaux thermiquement activés ont réussi à créer des cristallites de cette phase[6, 10–12]. La première partie de ce travail présente le protocole expérimental utilisé pour réaliser cet état. De plus, un modèle cinétique est proposé qui reproduit avec succès les caractéristiques observées et explique l'efficacité de cette approche.

Dans un deuxième temps, une étude sur un nouveau système de glace de spin artificielle est présentée: le réseau kagomé Ising artificiel. Ce système présente des moments magnétiques qui pointent hors du plan, contrairement au réseau kagomé planaire. Une étude récente[13] sur ce système a conclu que, après la désaimantation, ces deux réseaux kagomé artificiels présentent des corrélations de spin similaires et leurs états magnétiques à rémanence peuvent être bien caractérisés par des modèles de spin basés sur des interactions à courte portée, malgré la nature du couplage dipolaire à longue portée entre les nano)discs magnétiques. Grâce à l'utilisation des protocoles de désaimantation, aux mesures de microscopie à force magnétique et aux simulations Monte Carlo, il est montré que les interactions dipolaires à longue portée entre les éléments magnétiques ne peuvent pas être négligées lors de la description des états à rémanence des réseaux kagome artificiels désaimantés[14]. Ces résultats limitent la validité du comportement universel entre les deux réseaux kagomé artificiels et enrichissent la palette de phases magnétiques qui peuvent être réalisées avec de tels systèmes nanostructurés. En effet, des simulations Monte Carlo indiquent que ce réseau kagomé Ising présente un comportement à basse énergie différente de la glace kagomé planaire, mais la variété fondamentale dans ce cadre dipolaire reste inconnue. Néanmoins, en inspectant ses caractéristiques thermodynamiques à basse température et grâce une construction géométrique, un candidat pour l'état fondamental est fourni, en bon accord avec les résultats rapportés jusqu'à présent.

Abstract

Frustration is a ubiquitous concept and can be defined as a competition between interactions that cannot be all satisfied simultaneously. For example, two bar-magnets can be easily attached to one another by sticking the south pole of one to the north pole of the other, thus satisfying the magnetic interaction. Now take a third magnet and try to attach it to the others so that a 120° angle is formed between every pair. There is no way of doing this so that all pair interactions are satisfied and you either have two neighboring south or north poles at the crossing point. This is a typical example of magnetic frustration, which can be found in condensed matter compounds. If one continues this procedure and builds a network with such configurations, the result is a lattice of magnetic moments with exotic thermodynamic properties.

The current thesis studies such geometrical frustration effects in networks of nano-scale magnetic islands that generally serve as toy-models for condensed matter magnetic compounds that exhibit such features. The kagome network is intensively studied both experimentally and numerically, showing how long-range dipolar interactions between the constituting nanoelements can lead to the formation of exotic magnetic textures.

La frustration est un concept omniprésent et peut être définie comme une compétition entre des interactions qui ne peuvent pas être toutes satisfaites simultanément. Par exemple, deux aimants peuvent être facilement attachés l'un à l'autre en collant le pôle sud de l'un sur le pôle nord de l'autre, satisfaisant l'interaction magnétique. Prenez maintenant un troisième aimant et essayez de le joindre aux autres de telle sorte qu'un angle de 120° se forme entre chaque paire. Il n'y a aucune façon de satisfaire toutes les interactions dans ce cas et vous devez soit coller deux pôles nord ou deux pôles sud ensemble au point de croissement. Ceci est un exemple typique de frustration magnétique, qui peut être trouvé dans des composés de la matière condensée. Si l'on continue cette procédure en construisant un réseau avec ce type de configurations, le résultat est un réseau de moments magnétiques ayant des propriétés thermodynamiques exotiques.

Cette thèse a été focalisée sur les effets de frustration géométrique dans des réseaux de plot magnétiques à l'échelle nanométrique qui servent généralement de modèles pour les composés magnétiques de la matière condensée. Le réseau kagomé est intensivement étudié expérimentalement et numériquement, montrant comment les interactions dipolaires à longue portée entre les nano-éléments peuvent conduire à la formation de textures magnétiques exotiques.

Contents

List of Figures

List of Tables

Chapter 1

Introduction

> *"...in the great chess-board of human society, every single piece has a principle of motion of its own, altogether different from that which the legislature might choose to impress upon it. If those two principles coincide and act in the same direction, the game of human society will go on easily and harmoniously, and is very likely to be happy and successful. If they are opposite or different, the game will go on miserably, and the society must be at all times in the highest degree of disorder."*
>
> Adam Smith - Selected Philosophical Writings - Part VI - Of the Character of Virtue[15]

1.1 Geometrical Frustration

The notion of frustration is generically used to describe a situation in which there is a prevention, an inability or even the impossibility to achieve a goal[16]. In physical systems, frustration is generally defined as a competition between interactions such that not all of them can be simultaneously satisfied and generally arises when there is an underlying contradiction developing within the system[17, 18].

One of the most common examples is the triangle with antiferromagnetically-coupled Ising spins[19], as represented in Figure 1.1.a. Due to the contradictory information that is transmitted through the links, there is no way of arranging the three spins such that all pairwise interactions are satisfied and the best that can be done is to have just one unsatisfied coupling. This means that, out of the 8 possible configurations, 6 of them form the ground state manifold, while the remaining two correspond to excited, higher energy states (see Figure 1.2.b). This type of frustration effect is referred to as geometrical frustration, as it

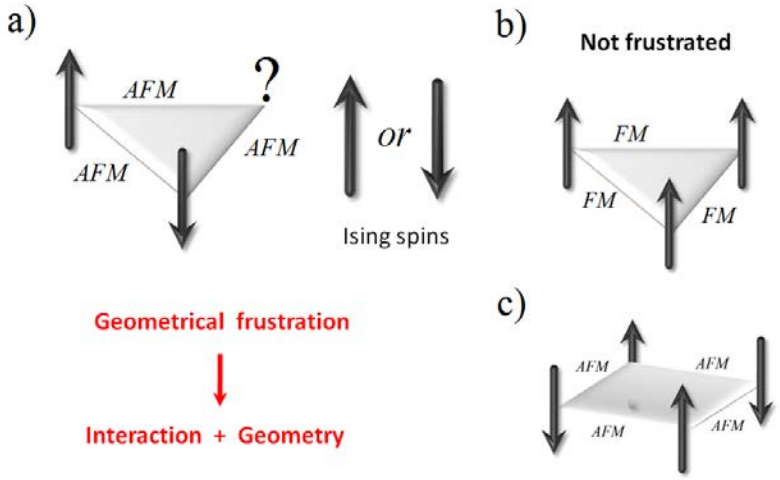

Figure 1.1 - (a) A common example of geometrical frustration: the triangle with Ising spins at its corners that are all coupled antiferromagnetically (AFM). Simply put, given two orientations for the spin arrows (up and down), the goal is to find a way to arrange them such that every spin is surrounded by nearest neighbors with then opposite orientation. Placing the first two spins can be done without encountering any difficulties, but when it comes to placing the last, there is a contradiction, and one interaction would end up not being satisfied, hence the term frustration. This particular case is called geometrical frustration as it is an interplay between a certain type of interaction, generally the same for all components, and a certain network geometry. (b) Changing the interaction type to a ferromagnetic (FM) parallel alignment while keeping the triangular symmetry does not result in any contradiction and no frustration is present. (c) Also, keeping the same interaction type and changing the lattice can also result in non-frustrated cases, particularly for bipartite lattices like the square network.

is a result of the interplay between a certain type of interaction that develops on a periodic lattice. For instance, if we take the same triangle and now couple the same vertically-aligned Ising spins ferromagnetically, they can all point either up or down, satisfying all pairings (see Figure 1.1.b.). Also, for a square with just nearest-neighbor interactions, an antiferromagnetic coupling does not yield any contradictory situations and hence does not result in any geometrical frustration (Figure 1.1.c.).

An intriguing aspect of geometrical frustration arises when looking at its effects on a network scale. For example, let's take the triangle with antiferromagnetically-coupled Ising spins and try to pave the 2D space with its ground-state configurations, thus creating a tessellation of triangles. In view of what was mentioned previously, this means that every such triangle must have one frustrated interaction. Starting from one of the 6 possible ground-states, we continue by adding the neighboring three triangles and then proceed with the definition of the spin orientations (see Figure 1.2). One of the spins can be exactly defined, but the other two can freely choose their state (see Figure 1.2.b). Therefore, for a cluster of 4 triangles, there are 4 configurations that have just one frustrated interaction per triangle. The

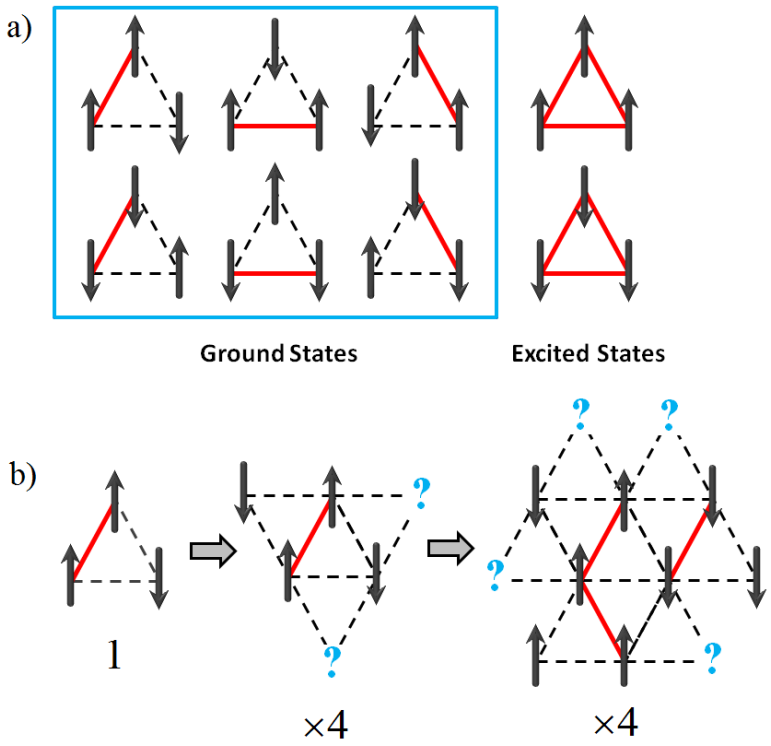

Figure 1.2 - (a) Since the triangle has 3 sites and the spins are Ising type, with two possible configurations, this gives a total of $2^3 = 8$ states. In an antiferromagnetic-coupling case, 6 of them share the ground-state energy while the other two correspond to higher energy states. Given the geometry and the interaction type, the best that can be done is to have just one unsatisfied coupling/triangle, represented here by a red line. (b) Building up a triangular network with the ground states of the triangle as elementary bricks can be done in may different ways. Starting from one configuration (step 1), one neighboring triangle can already be exactly defined as they both share the same frustrated bond. However, the the neighboring triangles cannot be chosen precisely, and there are 4 different ways to continue (step 2). For one of these configurations, there are 4 additional paths that can be taken at the next stage (step 3), making a total of 16 possibilites for 10 triangles so far. In fact, the number of possible configurations that respect the "one frustrated bond/triangle" rule increases exponentially. If only nearest-neighbor interactions are taken into account, this manifold becomes the ground-state and is characterized by a residual entropy.

procedure can be continued, and, at the next step, one can easily realize that, for each of the 4 configurations of the 4-triangle cluster, there are 4 extra possible ways to continue paving, yielding a number of 16 configurations for a 10-triangle cluster. In fact, the total number of configurations (Ω) increases exponentially with the size of the network, $\Omega \sim q^N$, where N stands for the number of triangles, while q is a real number greater than unity. If only nearest-neighbor interactions are assumed, all these states share the same energy and would form the ground-state manifold of a triangular lattice with antiferromagnetically-coupled Ising spins. This manifold is said to be massively degenerated and its entropy would be given by Boltzmann's relation, $S = k_B \cdot ln(\Omega) \cong N \cdot k_B \cdot ln(q)$. Taking the entropy/site, this would yield $s = S/(3N) \cong k_B \cdot ln(q)/3$ and, given that $q > 1$, this would ultimately be a non-vanishing finite value. In fact, this value was exactly calculated by Wannier[20] to be $S = 0.3383R$, where R is related to the ideal gas constant[1]. This would appear to violate the third principle of thermodynamics, at least in Planck's formulation, which states that: "The entropy of all systems in internal equilibrium is the same at absolute zero, and may be taken to be zero."[21]. In fact, a reformulation that would include the above-given example would be: as the temperature approaches absolute zero, the entropy of a system tends towards a constant, which can be taken equal to zero if possible[2]. Such systems do not generally present a unique ground-state ordering and, for the triangular network presented here, there are no critical phenomena down to absolute zero. Theoretically, this system can explore the vastness of its ground-state manifold without or with very little energy costs, which would make it fluctuate intensively, even at low temperatures. Such features are quite exotic and have attracted the interest of the scientific community since their discovery[17]. While this is a pure and classical example of a geometrically-frustrated spin model, such effects can be found in condensed matter, with both magnetic and non-magnetic examples.

1.2 Water Ice and Spin Ice

The first and perhaps most famous example of condensed matter frustration can be found in Pauling's description of the low-temperature proton disorder in the common state of water ice (I_h)[22], although he never used the term "frustration" in his paper explicitly[3]. During the 1930s, several experiments performed by Giauque *et al.*[24, 25] revealed a rather surprising

[1]The ideal gas constant, R, is defined as $R = N_A \cdot k_B$, where N_A is Avogadro's number and k_B is the Boltzmann constant. The entropy given above would therefore correspond to a mol of spins. However, one can always define an entropy/spin, and, in the above case, this would yield $s = 0.3383$.

[2]Obviously, one has to take the entropy/component in this case, as it would otherwise continue to increase with the system size.

[3]This term was introduced much later by G. Toulouse in the context of spin glasses[23], though he also states that he was inspired by the famous phrase of P.W. Anderson, "The name of the game is frustration",

feature: water ice appears to present a residual zero-point entropy, showing no signs of long-range order at very low temperatures. In fact, the oxygen atoms in the hexagonal phase of water ice form an open tetragonal structure, while the hydrogen atoms are situated along the lines linking two neighboring oxygens[26]. Therefore, each oxygen atom has a tetrahedral proton environment and, if we consider only the electrostatic repulsion, then we might conclude that the protons should sit half-way between the neighboring oxygens. However, if the H_2O water molecules are to form a solid phase of ice, two of these protons need to be closer to the oxygen atoms while the others should be situated further away. Indeed, this tetrahedral proton environment is distorted in this ice phase and, if one draws the displacement vectors of these hydrogen atoms with respect to the mid-point of a O-O bond, then two of the vectors would be pointing towards the central oxygen atom while others would be pointing away (see Figure 1.3.a). This "two-in/two-out" configuration is one of the so-called Bernal-Fowler *ice rules*[26] and it is the cornerstone of Pauling's description of water ice that successfully accounts for the reported residual entropy.

Pauling emphasized that there are many different configurations that respect these ice rules, which ultimately explains the massively degenerated low-temperature manifold of water ice. He proposed two equivalent methods for estimating the residual entropy of this phase. One of the arguments he put forward is that, for each central oxygen atom, there are 16 possible configurations for its surrounding four protons, given that each proton has two positions available along a O-O link. However, out of all these configurations, only 6 respect the ice rules. Furthermore, if one considers N water molecules in the structure of water ice, there is a total of 2^{2N} proton configurations. However, the ice-rule obeying configurations need to be selected from this ensemble, and for large N, this would require a filtering for each tetrahedron, ultimately yielding $\Omega_{ice-rule} = 2^{2N} \cdot (6/16)^N = (3/2)^N$. It can thus be easily seen that the number of ice-rule obeying states increases exponentially with the number of molecules, and the entropy/molecule for this phase is given by: $s_{ice-rule} = \frac{1}{N} \cdot k_B \cdot ln(\Omega_{ice-rule}) = k_B \cdot ln(3/2) \cong 0.81 cal \cdot deg^{-1} \cdot mol^{-1}$. This result is in very good agreement with the experimental value found by Giauque and Stout[25], $s = 0.82 \pm 0.05 cal \cdot deg^{-1} \cdot mol^{-1}$.

Many other systems have been found to present similar behavior to the one of water ice[4] and a magnetic equivalent was identified in the pyrochlore magnetic structures of $Ho_2Ti_2O_7$[2] and $Dy_2Ti_2O_7$[28]. These compounds are part of a larger class of oxides, with the general formula $A_2B_2O_7$, where A is a rare-earth element and B stands for a non-magnetic

while attending his lecture at the Aspen Center of Physics in 1976. Therefore, the paternity of the concept is sometimes attributed to P.W. Anderson.

[4] One famous example is the study performed by P.W. Anderson[30] on the cation ordering in the inverse spinel structure.

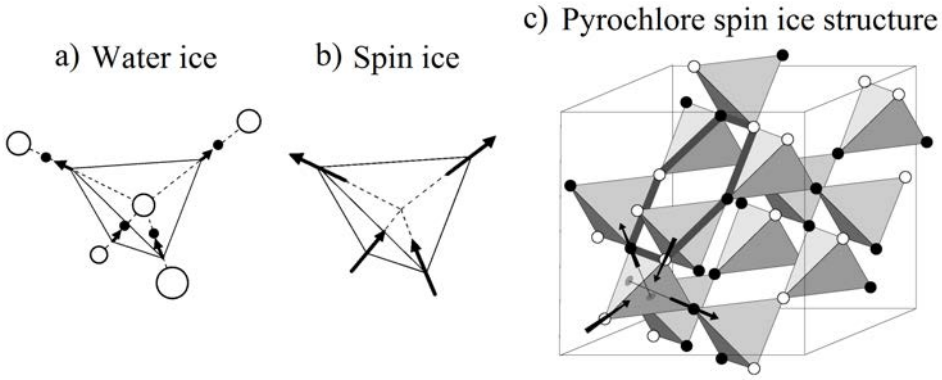

Figure 1.3 - (a) An example of a local proton configuration (black points) in the I_h phase of water ice that respects the "two-in/two-out" ice rules, as suggested by the displacement vectors for a tetrahedron centered around and oxygen atom (white circles). The various ways in which these ice rules can be obeyed ultimately result in a massively degenerated ground-state manifold, as suggested by Pauling[22]. After Bramwell and Harris[27]. (b) An ice-like physics has also been reported in magnetic oxides such as $Ho_2Ti_2O_7$[2] and $Dy_2Ti_2O_7$[28] in which the rare earth ions mimic the proton displacement vectors of water ice, thus earning them the name of spin ices. After Harris *et al.*[2]. (c) The pyrochlore structure of these compounds consists in a face-centered cubic lattice with a four-site tetrahedron unit cell. The white and black dots correspond to in and out spin configurations respectively if viewed from a "downward" tetrahedron. The given configuration respect the ice rules unanimously. After Melko *et al.*[29].

transition metal. Both metallic species form two inter-penetrating pyrochlore sublattices, which are corner-sharing tetrahedral structures as can be seen in Figure 1.3.c. In the relatively low-temperature regime, the magnetic rare-earth ions are effectively Ising-like due to crystal field effects and their easy-axis is defined by the [111] directions, i.e. the lines linking the centers of adjacent tetrahedra. Furthermore, Harris *et al.*[2] reported that the magnetization data for $Ho_2Ti_2O_7$ signals the presence of an effective ferromagnetic interaction between these Ising spins, but neutron scattering measurements show no clear evidence of long-range magnetic order in zero field down to 0.05K[2]. Indeed, if we just take one tetrahedron, we notice that there is no way of arranging the Ho^{3+} Ising spins to satisfy all ferromagnetic couplings simultaneously, which tend to form head-to-tail configurations. In fact, the best that can be done is to have two spins pointing towards the center of the tetrahedron while the others are pointing outwards (see Figure 1.3.b). As an analogy, these spin vectors can be perfectly mapped onto the displacement vectors of protons in water ice. This inspired the introduction of the term *spin ice* for such compounds and, within a nearest-neighbor interaction model (which became known as the short-range spin ice model), such geometrically frustrated ferromagnetic oxides are expected to display a residual entropy in accordance with Pauling's estimation for water ice[2]. Indeed, using a similar method to the one employed by Giauque

et al.[25], Ramirez *et al.*[28] have performed heat capacity measurements on $Dy_2Ti_2O_7$ and found good agreement with water ice behavior. However, in the former case, the massive degeneracy arises from magnetic disorder, contrary to water ice where it has a chemical origin. This encouraged the study of the effects of applied magnetic fields, as they can easily modify the energetic landscape of such magnetic compounds. Indeed, several studies have reported a partial[28] or total lift[2] of the reported degeneracy, thus recovering the Ising magnetic degrees of freedom. This field-dependent tailoring is a property that water ice does not necessarily possess and enables the exploration of a broader range of potentially exotic magnetic textures.

There is however a puzzling aspect that spin ice pyrochlores present. The nearest-neighbor interaction exchange between the Ho^{3+} or the Dy^{3+} ions is, in fact, antiferromagnetic [31, 32]. If this is the only ingredient for a short-range model description, then a long-range ordered ground-state exists where all tetrahedra would have "all-in/all-out" spin configurations[5]. However, both these pyrochlore oxides have shown effective ferromagnetic couplings between nearest-neighbors[2]. In fact, the rare-earth magnetic ions posses relatively high magnetic moments, making them subject to a dipolar coupling. As it turns out, the dipolar interaction is of the same order of magnitude as the exchange interaction[28, 32], requiring the consideration of both terms in an effective short-range spin ice Hamiltonian. However, the dipolar interaction is long-range by nature, decaying in strength by a $1/r^3$ factor. The question that immediately arises is how does this affect the reported degeneracy? Normally, interactions beyond first neighbors are expected to gradually lift this degeneracy and ultimately yield a long-range spin ordered state. Monte Carlo simulations have unveiled that, indeed, the dipolar contribution ultimately leads to a well defined spin ordered state[29, 33], but this phase has not been experimentally accessed so far[6], and a short-range description still manages to capture many of the observed features, although the very existence of a spin ice physics seems to be driven by these dipolar interactions[17].

Another interesting description of the low-temperature behavior of spin ice pyrochlores has been proposed by Castelnovo *et al.*[35] involving the emergence of magnetic monopole quasi-particles(see Figure 1.4). Since each spin behaves like a magnetic dipole, it can be effectively replaced by a dumbbell of magnetic charges with opposite signs. This corresponds to the so-called *dumbbell picture*. Furthermore, the individual charge contributions can be added up for each tetrahedra, resulting in an effective charge/tetrahedron. For an ice-like

[5]Contrary to the ferromagnetic case, this type of interaction develops "head-to-head" or "tail-to-tail" spin configurations for this pyrochlore symmetry. This is indeed possible for all lattice tetrahedra, without encountering any contradictions.

[6]A recent paper[34] has nevertheless reported experimental evidence of an incipient long range order development for $Dy_2Ti_2O_7$.

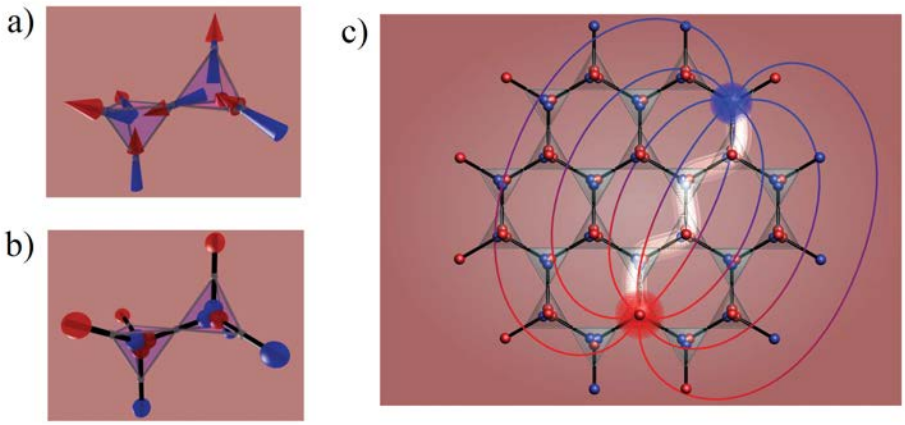

Figure 1.4 - Castelnovo *et al.*[35] proposed an effective description for the low-temperature behavior of spin ice pyrochlores through the use of the dumbbell picture, unveiling the emergence of magnetic monopole quasi-particles. (a) A spin ice configuration can be transformed into a 4 magnetic charge dumbbell formation (b) by considering each spin as a magnetic dipole having two opposite classical magnetic charges at its edges. This yields a zero magnetic charge for ice-rule obeying tetrahedra and a non-zero magnetic charge otherwise. (c) Flipping a chain of spins results in the formation of a Dirac string, having two magnetic monopole quasi-particles at its edges, while no additional ice-rule breaking occurs. The dipolar Hamiltonian can be translated, to a good approximation, into an effective Coulomb interaction Hamiltonian between these magnetic charges, similarly to an electrostatic field. After Castelnovo *et al.*[35].

configuration, these effective charges are zero, but a local ice-rule violation results in a neighboring pair of monopole-antimonopole particles. The interesting property of spin ices is that these two monopoles can be further separated from each other, forming a so-called "Dirac-string", but this process can be done without creating any additional violation of ice rules, thus there is no domain wall cost associated to their separation. Furthermore, these monopoles are effectively deconfined and they also interact via an effective Coulomb interaction that decays with $1/r$. This effective description with interacting magnetic monopole quasi-particles manages to capture many of the observed experimental features of the low-temperature spin ice physics. Nevertheless, it is important to note that these particles are not Dirac monopoles[36], but are instead classical magnetic charges acting as sources/sinks for the magnetic field $\vec{H}$ and do not violate Maxwell's equations[7].

[7]The magnetic field is related to the magnetic induction by $\vec{B} = \mu_0(\vec{H} + \vec{M})$, where $\vec{M}$ is the magnetization. Since $div\vec{B} = 0$ this implies that $div\vec{H} = -div\vec{M} = q$, where q is the associated magnetic charge. This last expression highlights the role of classical magnetic charges as sources/sinks of stray fields, similarly to an electrostatic picture. This is also the situation encountered in these pyrochlore spin ices.

1.3 Artificial Spin Ice

Pyrochlore spin ices have proven to be a beautiful condensed matter example of geometrical frustration driven by effective ferromagnetic interactions, which in turn have a deep dipolar root. The magnetic properties, the energetic landscape and the underlying spin arrangements for these magnetic oxides are generally determined through measurements of thermodynamic quantities, like the susceptibility or the specific heat, and via scattering techniques, such as neutron scattering. However, there is no direct visualization of how the magnetic degrees of freedom locally accommodate frustration effects and how the competing interactions drive the intrinsic fluctuations that make the system explore its vast and exotic degenerated manifolds. Local probing of the spins would indeed be a challenge in such condensed matter systems and a measurement may very likely alter the state that one intends to capture. Also, the spins are located on the lattice sites of a synthesized crystal structure, thus limiting the variety of geometrically-induced effects to networks that nature spontaneously constructs. Controlling and tuning the topology of the lattice at will would be a great advantage, enabling the exploration and engineering of a wide range of geometrically frustrated systems. It would be also interesting to have the capability to individually observe and control the magnetic degrees of freedom, thus facilitating the mapping and tailoring of the complex phase space at will, and the possibility to visualize both in and out-of-equilibrium spin dynamics. If all these could be combined in an experimental framework, then we would end up with an almost infinite playground for a detailed study of frustration effects.

This already seems like an utopia, but, at least to some extend, such a framework can be constructed by designing artificial-equivalents of such systems rather than synthesizing them. In fact, at about the same time as the spin ice story was unfolding, many different groups reported artificial two-dimensional realizations of magnetic systems that can exhibit frustration-induced effects. Examples include macroscopic arrays of micron-sized superconducting loops[37], compass needles[38], Josephson junctions[39] and self-assembled colloids[40], with the possibility of capturing the latter in optical traps[41]. In addition, motivated by recent advancements in lithographic design and nano-scale characterization, both Tanaka *et al.*[42, 43] and Wang *et al.*[1] independently pursued a different approach and created artificial spin systems by patterning magnetic thin films via e-beam lithography, finally yielding two-dimensional networks of tightly-packed magnetic nano-islands.

There are several major advantages to this latter approach. Firstly, there is almost total freedom in design as the e-beam lithography mask can be drawn at-will and then imprinted on the magnetic layer, thus creating networks with the desired topology, shape and size. The size of the islands is also a key factor, and, combined with the magnetic properties of the thin magnetic layer, can yield macroscopic, bulky versions of classical spins, such as Ising

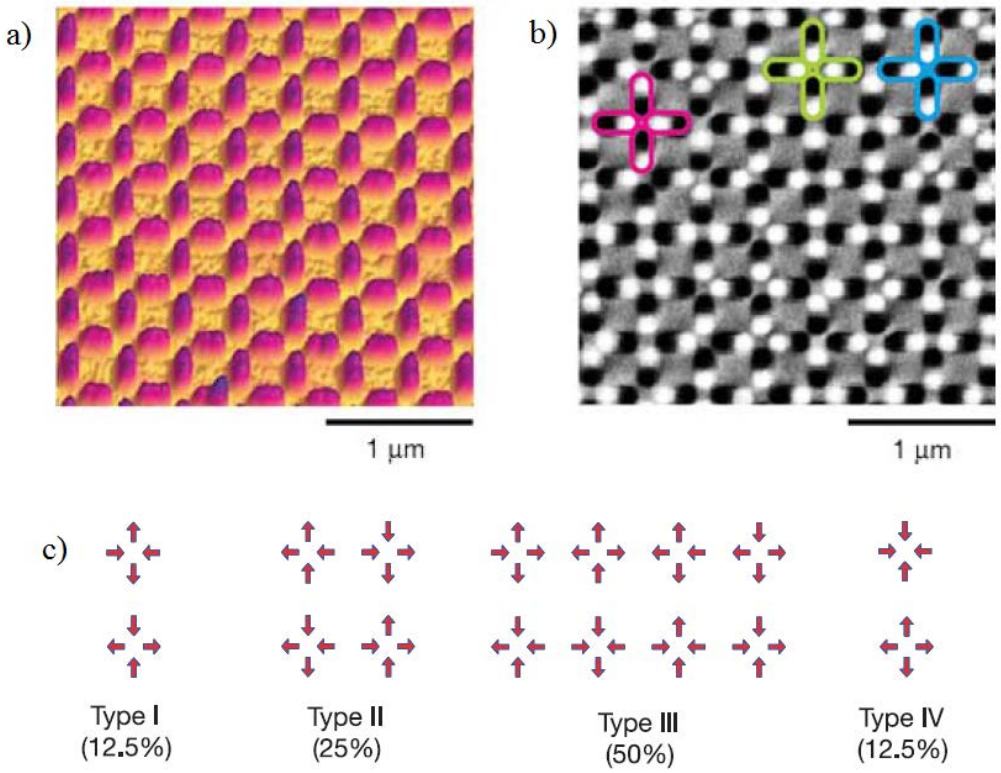

Figure 1.5 - (a) An atomic force microscopy image revealing the topography of a square network of nano-sized magnetic islands, as reported by Wang*et al.*[1]. Typical island dimensions are $220nm \times 80nm \times 25$ ($L \times l \times h$). (b) A magnetic force microscopy scan reveals that each island has a white and a dark contrast, signatures of an outgoing and incoming stray field. This reveals the local orientation of the magnetization for each island while also indicating their effective magnetic monodomain behavior. Since these islands can behave as Ising spins, there are 16 possible configurations for a square vertex and they can all be classified into 4 degeneracy classes according to their magnetostatic energy (c). Type I and type II are ice-like configurations and can be seen in the MFM image highlighted in magenta and blue respectively. Nevertheless, some defects are also present, like the type III vertex highlighted in green. The relatively high number of ice-rule obeying vertices indicates that these artificial systems appear to mimic the ice-like physics of their 3D counterparts, the pyrochlore spin ices. After Wang *et al.*[1].

spins. Indeed, both groups report that, due to their size and shape, the patterned nano-islands effectively behave as Ising spins, having an almost uniform magnetization throughout their entire volume[8] and presenting two preferential orientations for the magnetization along the island's long axis[9]. They were both able to determine these features by employing a Magnetic Force Microscopy (MFM) scan (see Appendix B for a basic description of the principle of Magnetic Force Miscroscopy).

Figure 1.5 gives the AFM/MFM reconstructions of the surface topography and the magnetic contrast for a square network of magnetic permalloy nano-islands as reported by Wang *et al.*.[1][10]. The magnetic map reveals that each island has two contrast spots, a white and a dark one, given by the interaction of the magnetic tip with the island's stray field lines[11]. Given the soft nature of the magnetic material, this confirms that the island possesses an effectively uniform magnetization. Notice that the scanning reveals the magnetic orientation of each island within the network, thus offering a direct visualization of the network's magnetic configuration in real space. This is another major advantage of this approach: by using standard nano-characterisation techniques, an almost exhaustive knowledge of the magnetic configuration can be achieved. Furthermore, individual probing is possible without altering the magnetization states of the components[12] and the magnetic texture of the network is stable over time. It would therefore seem that, so far, lithographically-patterned artificial

[8]This is actually the reason behind the manufacturing of nano-size elements. A ferromagnetic material normally contains several uniformly magnetized regions/grains, separated from each other by domain walls. This mosaic-aspect is the result of the competition between the exchange interaction, that wants to align all the elements parallel to each other, and the dipolar interaction, which heavily depends on the relative positioning of the spins and can promote an anti-alignment of the spins. These magnetic grains also arrange themselves as to diminish the so-called demagnetization field, yielding an overall magnetization that is close to zero. However, the domain walls come with a certain energy cost, related to the exchange and the anisotropy terms, the latter promoting an alignment of the spins along a certain direction called the easy-axis or within an easy-plane. If the size of the magnetic object is small enough, the cost of creating a domain wall is higher than that of the demagnetizing field and the island becomes a magnetic monodomain with a magnetization that is approximately uniform throughout its entire volume. Though this often requires very small sizes in the order of a few nanometers, an effective uniform behavior can also be obtained for larger islands as well.

[9]Both studies have used permalloy (Ni_xFe_{1-x}) thin films, which is a soft magnetic material. The anisotropy axis is therefore dictated by the demagnetization field, which is minimized if the magnetization points along the longest lateral size of the island.

[10]I shall focus here on the work of Wang *et al.*[1] and I shall further return to the results of Tanaka *et al.*[42, 43] in the next chapter, where the artificial kagome network is discussed.

[11]The magnetic moment of the island can be though of as a dumbbell of classical magnetic charges, similar to the description of Castelnovo *et al.*[35]. The white and black spots would thus correspond to a positive and negative magnetic charge, or otherwise sources and sinks of the magnetic stray field.

[12]Although Magnetic Force Microscopy is an intrusive technique that can potentially change the magnetic properties of the scanned sample, but by carefully choosing the tip moment and its coercivity one can avoid such situations. Nevertheless, in some cases, this feature is desirable for local manipulation. Other probing techniques have been used for such artificial spin systems, including X-ray Magnetic Circular Dicroism - PhotoEmission Electron Micrscopy[44, 45] and Lorentz-mode Transmission Electron Microscopy[46, 47].

spin ice arrays are in good accord with some of the demands listed at the beginning of this section: a high degree of liberty, flexibility and control in design and the possibility of direct and individual probing of the network's magnetic components without altering their state. However, this last advantage initially came with a certain price: such networks were insensitive to thermal fluctuations at room temperature.

As mentioned previously, one of the main goals of these lithographically-patterned spin systems is to explore the effects of frustration and observe how it is locally accommodated. To this end, an artificial system should be able to explore its phase space and preferably reproduce at-equilibrium thermodynamic behavior. The square lattice fabricated by Wang *et al.*[1] can exhibit frustration effects. In fact, the vertices of the square lattice (the meeting point between four neighboring elements) can potentially manifest an ice-like physics since the islands can be regarded as Ising spins and they can point either in or out of the vertex center. Therefore, this artificial square ice system seems to be a two-dimensional equivalent of pyrochlore spin ices. However, first of all, in order to talk about frustration, the patterned islands must interact with each other. In fact, these islands have relatively large magnetic moments (typically in the order of $10^7 - 10^8\ \mu_B$) and their tightly-packed formation should enable a magnetostatic coupling between them. Otherwise said, each island is normally found in a magnetostatic environment created by its neighbors, sensing a local magnetic field[13]. In this case, the island would like to align its magnetic moment with this local field, but in order to do so, it must overcome the intrinsic energetic barrier that separates the two preferential states situated along its easy-axis. Even if this energy barrier is higher than the thermal energy, a magnetic nano-particle still presents spontaneous flips of its magnetization due to thermal effects at finite temperatures that are below the Curie point of the constituting magnetic material. This is called the superparamagnetic regime[48], and the frequency of the flips depends on the relative strength of the anisotropy barrier of the particle with respect to the thermal input. Nevertheless, for the nano-islands reported by Wang *et al.*[1], the estimated time elapsed between two flips is colossal[14], rendering these networks practically insensitive to thermal fluctuations. Therefore, some other ways had to be found to allow the system to accomodate pairwise interactions and explore its phase space, particularly the low-energy regime where the exotic physics of frustration manifests itself. To this end, Wang *et al.*[1] suggested the application of a demagnetization protocol for driving these system towards their ground-states.

The idea behind the demagnetization procedure is to put the sample in an oscillating slowly-decaying external magnetic field that has an initial amplitude which is sufficiently

[13]The signatures of these interactions can be indeed seen in the network configurations mapped by MFM. This will be discussed shortly.

[14]These aspects will be described more quantitatively in the first chapter of this thesis.

high to fully saturate the artificial network[15]. As the field amplitude decays, there is a certain field window for which the external field is comparable to the island switching field, i.e. the field corresponding to the intrinsic energy barrier that needs to be overcome. At this stage, flipping the islands is possible, but these flips are mediated by the inter-island couplings which translate into a local effective field for each island. Therefore, the islands are expected to accomodate their mutual interactions at this stage. For fields lower than the intrinsic switching ones, no flips can occur anymore, and the magnetic configuration remains frozen and can be easily mapped by MFM at the end. Also, it is important to mention that, since the magnetic moments of the islands are sitting in the network plane, it is important to rotate the sample during the demagnetization cycle while the field is applied in the networks plane to avoid any favoring of a certain in-plane direction. More aspects on the demagnetization protocols will be presented later on.

After demagnetization, the magnetic configuration of the entire network can be extracted via MFM (in fact, Figure 1.5.b corresponds to a demagnetized state). To ascertain the efficiency of this protocol, the first step is to evaluate the remanent magnetization of the network. Indeed, Wang *et al.*[1] report that this procedure manages to significantly reduce the magnetization of the network, bringing it close to zero. This is already an indicator that the system has managed to minimize its energy to a certain extent. A more in-depth analysis and quantification of pairwise coupling accommodation can be made by studying the statistic ratios of the vertex populations. There are 16 possible configurations for a square vertex, given that each island has two possible orientations, and they are all represented in Figure 1.5.c. By calculating the energy of the vertices within a magnetostatic framework, they can be further classified into degeneracy classes. The first two classes correspond to ice-like configurations as they present two spins pointing in and two pointing out. Types III and IV correspond to higher energy states and are increasingly higher frustrated sites. By looking at the vertex populations, Wang *et al.*[1] noticed that a big majority (more than 70%) of the vertices respect the ice rules for the most tightly-packed square networks. While some defects are still present, this is nevertheless an encouraging result. The demagnetization protocol employed seems to be rather efficient in accommodating the frustration effects at the vertex sites, and this artificial spin system does seem to mimic the behavior of its three

[15] In a paper that was published right after their initial work, Wang *et al.*[3] explored the efficiency of different magnetization protocols and found that an alternating, rotating and slowly-decaying protocol gives the best results in terms of network energy minimization. A more recent study[49] suggests that this is not necessarily true, and that linearly-decaying the field while the sample rotates approaches the ground-state configuration slightly better. However, neither protocol manages to access it.

dimensional condensed matter counterpart. Another way of characterizing the efficiency of the demagnetization mechanism is to compute the pairwise spin correlations[16].

A pairwise spin correlation[17] is defined as the scalar product between the states of the considered pair of spins, $\vec{S}_i$ and $\vec{S}_j$:

$$C_{ij} = \vec{S}_i \cdot \vec{S}_j \tag{1.1}$$

Given that the islands are Ising-like, each spin can be written down as the product between a scalar value ($\sigma = \pm 1$) and a unitary vector defining its easy-axis: $\vec{S}_i = \sigma_i \cdot \vec{e}_i$ (for the square lattice, the Cartesian unit vectors can play this role). The vectorial form of the spin correlator can therefore be brought to a scalar form:

$$C_{ij} = (\sigma_i \cdot \sigma_j) \cdot (\vec{e}_i \cdot \vec{e}_j) \tag{1.2}$$

The second parenthesis is a geometrical factor which depends on the relative angle between the spins[18]. These correlators have to be defined in accordance with the lattice symmetry and the interaction coupling constants (see Figure 1.6). They are a very fine measure of the order established within a system, thus being a valuable tool for characterizing the position of the system in its phase space. Since the magnetic degrees of freedom can be mapped in direct space, these correlators can be computed in direct space too[19]. Network averages can be calculated for the same correlation type as follows:

[16] I shall frequently refer to the magnetic islands as spins from now one. However, one should recall that these are not elementary spins and not even macrospins, but they are the components of a system that replicates the exotic physics seen in frustrated spin models.

[17] For simplicity, I shall frequently use the term spin correlations or spin correlator instead of pairwise spin correlation or spin-spin correlations. Although the term might be misleading, one should however bare in mind that a pair is needed to define such a physical quantity. Unless specifically stated, I refer to spatial correlation and not time-dependent correlators.

[18] Notice that for the square array, this angle is either 0° or 90°. In the latter case, the geometrical factor will be zero which can erase any knowledge of correlation development. The scalar form is less sensitive to this aspect, but the definition of the correlations need to be carefully chosen and applied for each geometry in particular. Benchmarking it can be done by considering a perfectly ordered ferromagnetic/antiferromagnetic state for which their values must be +1/-1, depending on the convention.

[19] This is contrary to condensed matter systems where neutron scattering techniques reveal the spin correlation development in the Fourier space through the magnetic structure factor. This is also a very powerful characterization tool, capable of unraveling complex and subtle ordering patterns, and is starting to be employed for artificial systems as well[6, 50] as these systems can support both descriptions

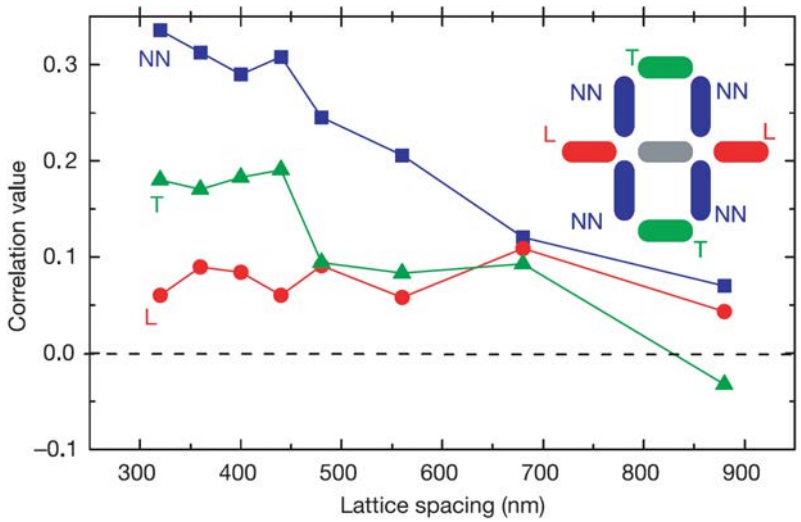

Figure 1.6 - Wang *et al.*[1] fabricated artificial square arrays with different lattice constants, thus tuning the strength of the magnetostatic coupling between neighboring islands. While for large lattice spacings the configuration seems to be totally random, the most tightly-packed ones display stronger nearest-neighbor correlations and a decay of the correlation strength with the distance between the pairs. The correlation classes have to be defined according to the lattice symmetry and the coupling strength (see inset). After Wang *et al.*[1].

$$C_{\alpha j} = \frac{1}{N_{\alpha j}} \sum_{\alpha} \vec{S}_{\alpha} \cdot \sum_{j|(\alpha j)} \vec{S}_{j} \tag{1.3}$$

where α stands for a network spin and j denotes a network spin that forms the desired spin pair with the α spin. The first sum is perforemd over all spin within the network, while the second one is performed only over the corresponding pairs. The value is normalized at the end according to the number of correlation pairs, $N_{\alpha j}$. This will give a unique value that can be afterwards compared to theoretical ones given by different interaction models.

By computing network averages of spin correlators for increasingly higher pair orders, Wang *et al.*[1] noticed a decay of the correlation strength with the increasing distance between the chosen spin pairs (see Figure 1.7). They concluded that the remanent states of these artificial square spin ices after ac demagnetization present only short-range order and, given the ice-like correlations, they highlighted the analogy with the behavior of condensed matter spin ice materials in which long-range order has not been observed experimentally, although the interactions of the magnetic elements are of dipolar long-range nature, just like in these artificial two-dimensional spin ices.

In the end, these lithographically-patterned arrays of magnetic nano-islands do seem to present many of the qualities and features that we were looking for at the beginning and

stand as a root for the local exploration of magnetic frustration effects. The fabrication via lithography offers almost limitless opportunities for the lattice topology, and by engineering the magnetic material, the nature of the spin can also be changed[51]. These magnetic elements interact with one-another in a dipolar framework, an interaction that seems to be of particular interest in the case of frustrated or ice-like systems. Furthermore, individual probing is possible without altering the state of the elements. The only inconvenience so far seems to be the athermal nature of the components, which ultimately requires the use of other mechanisms for the exploration of the network's phase space. Nevertheless, thermally-active artificial spin ices have recently entered the arena and the accommodation over time of dipolar pairwise interactions within heat-bath conditions has been observed *in situ*[5, 52, 53]. Even so, the demagnetization protocol may yet offer insights into out-of-equilibrium dynamics and the application of this semi-deterministic approach sometimes yields configurations that seem to present an effective thermodynamics[54, 55]. The relative ease in design and characterization has made this approach very popular, although there are many different types of artificial networks that fall under the label of artificial spin ices[37–41, 56]. Despite the fact that other groups such as Tanaka *et al.*[42, 43] have noticed the potential of lithographically-patterned arrays as toy-spin models before Wang *et al.*'s work[1], the latter contribution is largely considered as pioneering since they established a methodology for the investigation of frustration effects in such artificial systems and underlined their resemblance to spin ice behavior, thus making this a complementary approach for the study of ice-like physics. In fact, no long after this pioneering publication, magnetic monopoles in artificial spin ices started to become an interest[57–59], motivated by their discovery in pyrochlore spin ices[35]. This has quickly evolved into a self-standing branch of research in the artificial spin ice playground, as they promise to show some exotic transport features that can be tailored via the micromagnetic properties of the islands. For instace, these magnetic monopoles appear to have an overall non-random walk in some artificial structures[59, 60], and this has been attributed to the chirality of the associated domain wall[61]. Nevertheless, this avenue has not been pursued within this work, which has instead exploited the previously-mentioned goal of these artificial structures: the real-space exploration of geometrically-induced effects within a dipolar framework.

1.4 A Brief Look at the Kagome Network

In the first part of this introduction I have presented the notion of geometrical frustration and illustrated it with the triangular network containing antiferromagnetically-coupled Ising spins[20]. This system has largely become known as the first reported case of a frustrated

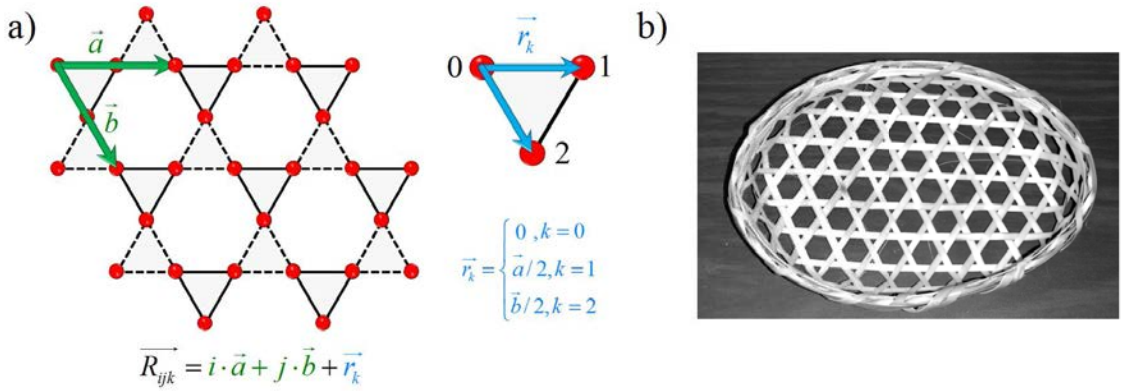

Figure 1.7 - (a) The kagome network is a non-Bravais lattice which can be defined as a triangular lattice with an equilateral triangular basis such that neighboring triangles share their corners. Three defining vectors are therefore necessary for determining the positions of the lattice sites. (b) The network earns its name to the Japanese word "kagome", which means bamboo basket woven pattern. After Mekata[66].

antiferromagnet[62]. In fact, at the end of the 1940s and the beginning of the 1950s, the study of phase transitions for different types of lattices became a central point of interest, motivated by the success of Onsager method for exactly solving the problem of the Ising model[19] on the two-dimensional square lattice[63]. The honeycomb and triangular lattices immediately followed[20, 64], and shortly after these successes, Syozi studied the statistical properties of a new type of triangle-based network by performing a star-triangle transformation on the decorated hexagonal lattice[65]. This network became commonly known as the kagome network, as initially suggested by Husimi and Syozi[65, 66].

Also referred to as the trihexagonal tiling, the kagome lattice is a triangular array of equilateral triangles that share their corners (see Figure 1.7.a). Etymologically, the word means "bamboo basket (kago) woven pattern (me)"[66], and this geometry can indeed be found on Japanese baskets (see Figure 1.7.b). Since this network is a non-Bravais lattice, an internal unit cell positioning vector is required in addition to the base vectors of the underlying triangular lattice to properly define each lattice site (see Figure 1.7.a). Every site has 4 nearest-neighbors, sharing the same coordination number z with the square lattice. However, while the latter is bipartite, the kagome tiling is not and can experience some intriguing frustration effects.

If classical Ising spins are now placed on the lattice sites of the kagome network, a new type of spin model is obtained, with promising frustrated features[20]. Indeed, Syozi proved that, while the ferromagnetic case exhibits a phase transition, the antiferromagnetic kagome array has no critical behavior at finite temperatures and remains disordered down

[20]Here and throughout this thesis, only classical spin models are discussed.

to absolute zero[65]. Shortly after this work, KanÔ and Naya[67] exactly calculated the residual entropy/spin of the ground-state of the kagome Ising antiferromagnet and found that $s = 0.50183$. This value is higher than the one reported for the triangular antiferromagnet[20] and the kagome antiferromagnet remains the most frustrated two-dimensional lattice known.

The above-mentioned results are valid for a nearest-neighbor interaction picture only and it would be interesting to see how higher order interactions affect this highly degenerated ground-state manifold. Indeed, several groups have undertaken this task both analytically and numerically[7, 8, 68–71] and found that this degeneracy can be completely lifted by second-order ferromagnetic interactions. Even so, the pure antiferromagnetic case can still presents a highly-degenerated ground-state manifold in a $J_1 - J_2$ framework[70] (both the nearest-neighbors(J_1) and the next-nearest-neighbors(J_2) are interacting), with spins that sit on zero-local field sites and can freely choose their orientations[70, 71]. Dipolar interactions might further order the system, possibly yielding exotic spin textures, but, so far, the ground state of a dipolar kagome spin network with only antiferromagnetic couplings remains unknown. With the artificial spin ice framework at hand, such features can be investigated experimentally and then directly compared to simulations for a better understanding of the complex frustrated behavior found in classical kagome spin models.

1.5 Motivation and Overview of the Thesis

The exotic frustration-driven physics of classical kagome spin models along with the possibility for experimentally observing and exploring it in the artificial spin ice framework has been the driving motivation of this thesis. In particular, the dipolar kagome antiferromagnet, which I shall call the dipolar kagome Ising network, has initially been the core of this work. The square and kagome networks with in-plane magnetized spins (kagome spin ice) have received a great deal of attention from the artificial spin ice community over the past years, and though the design via lithography facilitates the fabrication of a wide range of frustrated spin models on different types of lattices, few other geometries have been investigated so far. Given the exotic thermodynamic properties predicted for the kagome antiferromagnet[65, 67, 68, 70, 71] and the knowledge within our research group for engineering magnetic thin films to obtain artificial networks with perpendicularly-magnetized islands, the study of the kagome antiferromagnet has been undertaken both experimentally, by employing field-demagnetization protocols on artificial kagome Ising networks, and numerically, mainly via at-equilibrium Monte Carlo simulations. The low-temperature behavior of the dipolar kagome antiferromagnet remains, so far, unknown, and could unravel potentially exotic spin arrangements, which we hoped to observe with its artificial realization. However, the dipolar kagome spin

ice network presents an intriguing energetic landscape and undergoes two phase transitions until it reaches its spin ordered state[7, 8]. The intermediate phase is an exotic regime in which a partially spin disordered phase coexists with a crystalline phase[7–9]. This has motivated the community for experimentally accessing this regime and the current thesis includes work perform within this context as well. The thesis has therefore been structured into two chapters, which could very well be considered as two parts or two stories.

The first chapter focuses on the kagome spin ice network and its artificial realization. The thermodynamic properties of this spin system within the short-range and the dipolar long-range framework are investigated by at-equilibrium Monte Carlo simulations and compared to literature results[7, 8, 71]. Both models have been invoked for the description of the remanent states of demagnetized artificial kagome spin ice networks[46, 72, 73], so it is only fair to present them both. At the same time, the chapter also gives a literature overview of the main results obtained so far for the artificial realization of this geometry. The recent emergence of thermally-active artificial spin ices has motivated the exploration of the effects of a thermal annealing procedure on artificial kagome spin ices[6]. We have also found that the exotic phase that presents both a spin ordered and a spin disordered state can be locally accessed with such an experimental approach, but we interpret the efficiency of the procedure in terms of kinetic pathways that the system undertakes in the quest for energy minimization. These results have been the subject of a recent publication[11].

The second chapter is dedicated to the results obtained for a novel artificial spin system, the kagome Ising network, for which very few studies have been reported to date. In fact, only one other study has been performed so far, which concludes that this artificial kagome system with perpendicularly-magnetized moments presents similar correlation development to that of its in-plane counterpart, and the remanent states after demagnetization are well described by models based solely on nearest-neighbor interactions[13]. This would render the study of the artificial kagome Ising system rather redundant. However, the current work reveals that this is not necessarily true and that the experimental data extracted from demagnetized kagome Ising samples can be better described within a dipolar framework rather than a short-range one. While in some cases both nearest-neigbor and dipolar interaction models can account for the observed experimental features, the short-rage model fails after one point while the dipolar description continues to capture the observed correlation values. These results highlight the importance of dipolar interactions within the artificial spin ice framework and show how their long-range part can manifest itself experimentally, thus enriching the palette of spin textures that can be potentially accessed. These results have also been reported in a rather recent publication[14]. Similarly to chapter 2, the thermodynamic features of the kagome Ising network are described for both the short and the long-range interaction models,

simulated via the Monte Carlo method. Descriptions of the sample, the demagnetization protocol, the set of experimental values and the analysis method are also provided. The dumbbell picture that was formally presented in the case of pyrochlore spin ices has proven very useful in this case, and distinguishes our analysis and interpretation from other works. Since these results suggest that this dipolar artificial kagome Ising network is characterized by different low-energy magnetic textures than kagome spin ice, they have further motivated the exploration of these low-energy manifolds in the quest for an unknown and possibly exotic spin ordered ground-state. Through the use of an original geometrical construction and Monte Carlo simulations, this scenario is also explored.

Lastly, although each chapter contains a summary, highlighting the main results and conclusions, a general summary is also provided at the end along with avenues for future work. A short review is provided on the Monte Carlo method in Appendix A along with the description of how it has been implemented and how the relevant thermodynamic quantities are computed during a simulation run. Appendix B gives some basics on Magnetic Force Microscopy, the main characterization technique used for this work, while Appendices E and F report the set of MFM images from which the experimental data was acquired. Appendices C and D contain proofs and discussions that are not mandatory for the main storyline, but can be useful for a more in-depth understanding.

Chapter 2

Kagome Spin Ice - Spin Models, Artificial Realizations and Charge Crystallization

2.1 Introduction to Artificial Kagome Spin Ice

The pioneering work of Wang *et al.*[1] established an exciting framework for the investigation of magnetic frustration effects and they highlighted the advantages of this lab-on-a-chip approach by studying a square lattice of magnetic nano-islands. Interestingly, although the nano-islands are interacting through their dipolar fields, which are long-range by nature, the system appears to present only short-range order, and given the predominance of ice-like configurations, it could be considered as a 2D equivalent of spin ice pyrochlores. In fact, the proposed system seems to present itself as an experimental realization of the square ice model, a 2D equivalent of water ice, which was exactly solved by Lieb in 1967 [74, 75].

The square ice model is a vertex model that admits only ice-like vertices. Practically, the energy of the type I and type II vertex configurations are taken as 0 while the energies of types III and IV are set to infinity. However, as both type I and type II share the lowest vertex energy possible, there is no specific preference between the six ice-rule configurations and they will all be equally probable. Assuming a random distribution of the accepted configurations, the expected population ratios are 33% for type I and 66% for type II[1]. The ground-state of

[1]There is a slight deviation from these values due to the fact that each vertex has to comply with the configuration of its neighboring vertices. The vertex allocation isn't therefore fully random, but subject to these constrains, which ultimately yields a ratio of approximately 37% for type I and 62% for type II. For more details on square ice models and artificial realizations, see [76].

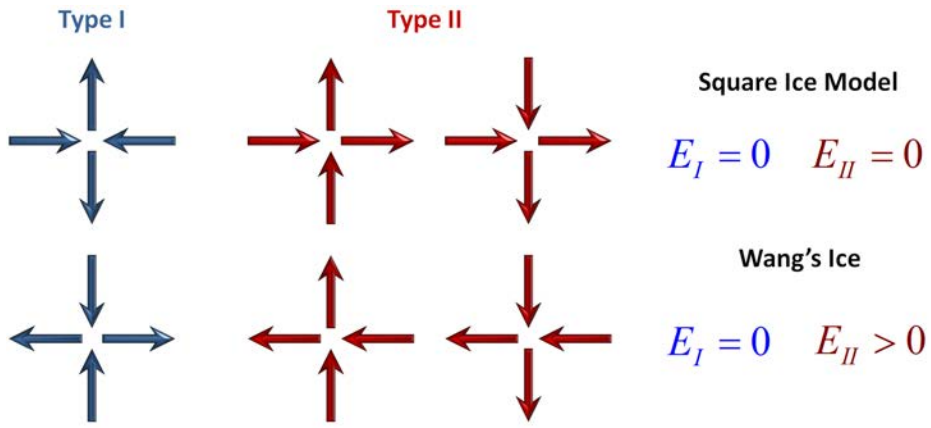

Figure 2.1 - Within the square ice model, all ice-like configuration share the same vertex energy and would ultimately lead to a macroscopically degenerate ground-state manifold for a square network. Wang's ice, however, presents a small energy difference between the two configurations, making it an artificial realization of the F model [77], lacking ground-state degeneracy, rather than the square ice one.

this model is macroscopically degenerated, with a residual entropy of $(4/3)^{3/2} \cong 1.5396$ as reported by Lieb [74].

The prospect of experimentally realizing a spin model with a macroscopically degenerate ground-state manifold is quite exciting. However, Wang's ice doesn't meet the requirement for the square ice model since the energy of the type I configuration is lower than the type II one (see Figure 2.1). This would imply the lifting of the degeneracy between ice-like vertices and the system would ultimately present a unique ground-state made out of type I configurations only. Furthermore, even for the smallest lattice spacing, type III vertices are still present, indicating that the system is still far from this final ground-state order.

While investigating the results of Wang *et al.*, Möller and Moessner [78] emphasize that the inter-island interactions at the vertex sites are not all equivalent. The islands that are perpendicular to each other are more strongly coupled than the parallel ones and this ultimately leads to the energy differences between the vertex types (see Figure 2.2.a). They nevertheless offer two solutions for achieving macroscopic degeneracy. The first one is to vertically displace the horizontal rows from the transverse lines of the square lattice. As the perpendicular islands are now further away from each other, this would soften their magnetostatic coupling, and, for a precise displacement value, the vertex energies of all ice-like configurations would be the same. However, realizing such a 3D system implies additional fabrication challenges and the creation of 3D artificial spin ices is an ongoing struggle today. The second option is rather an alternative: they propose the study of a honeycomb structure which corresponds to the kagome lattice. In this geometry, each vertex

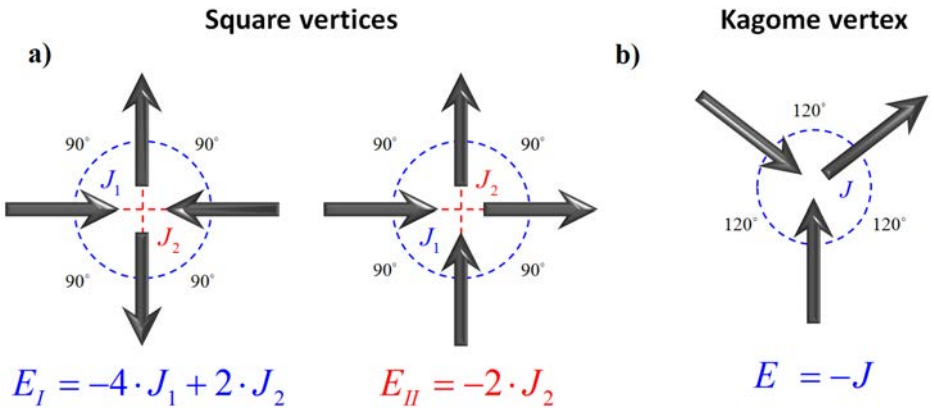

Figure 2.2 - Example of square (a) and kagome (b) vertices along with their corresponding vertex energies resulting from the inter-island couplings. As long as J_1 is larger than J_2, the type I vertex is more energetically favorable than type II, as appears to be the case in Wang's ice. As suggested by Möller and Moessner[78], a kagome vertex would however present the same nearest-neighboring coupling (J) between all islands, which could finally yield a macroscopically degenerate manifold.

is made up of three spins, each one located at 120° from the others, and the inter-island couplings are all equivalent (see Figure 2.2.b). If long-range interactions could be somehow suppressed, an artificial realization of the kagome array could present a macroscopically degenerated ground-state.

In fact, independently from Wang *et al.*[1], Tanaka *et al.*[42, 43] explored magnetic interactions in a lithographically-patterned permalloy honeycomb network. Apart from the different choice of geometry, the islands in this honeycomb tilling were connected at the vertex points. By mapping the stray field of the network through the use of a small-moment Magnetic Force Microscopy tip, they observed black and white contrast only at the vertex sites (see Figure 2.3). This lead them to conclude that the magnetization inside each island is uniform and that the interactions at the vertex sites are the ones which govern the orientation of each island and ultimately defines the network's magnetic configuration. Furthermore, the bright and dark spots seem to have the same intensity throughout the entire network, implying that the magnetic configuration of every vertex is subject to the kagome ice rules (a three-in or three-out configuration would yield a brighter/darker contrast). Therefore, they proposed an effective way of writing down the energy of the system:

$$E\{\vec{M}_i\} = -2 \cdot J \sum_{<i,j>} \vec{M}_i \cdot \vec{M}_j + \sum_i \vec{H} \cdot \vec{M}_i. \tag{2.1}$$

where $\vec{M}_i$ corresponds to the magnetization vectors of the nano-islands, J is the coupling constant between neighboring islands (J > 0 for this ferromagnetic case) and the summation

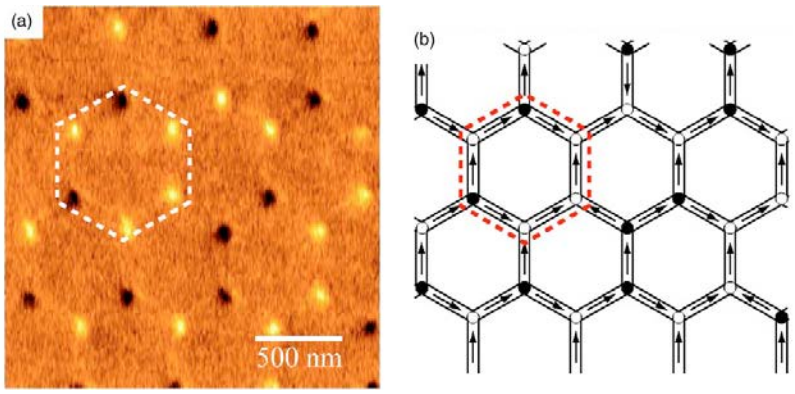

Figure 2.3 - (a) Magnetic contrast from a honeycomb lattice of magnetic nano-islands probed by Magnetic Force Microscopy. The presence of a stray-field only at the connection points suggests that the islands are effectively behaving as a single Ising-like spin and that all vertices respect the kagome ice rule. However, several magnetic configurations can yield the same contrast map. One possible arrangement is presented in figure (b). After Tanaka *et al.*[43]

is performed over all nearest-neighboring pairs. The second term accounts for the Zeeman interaction in case an external magnetic field ($\vec{H}$) is applied. They further remark that the first term bears a striking resemblance to a Heisenberg-exchange Hamiltonian and they emphasize the analogy between this artificial system and a short-range model of Ising spins distributed on the lattice sites of a kagome network.

The experimental realization of a kagome lattice that respects the kagome ice rules is therefore a promising result that could lead to macroscopic degeneracy induced by magnetic frustration effects, as the short-range model for a kagome network predicts. In the following section I will present the thermodynamic properties of the kagome network within the assumptions of this model and I will afterwards return to other reported artificial realizations of the kagome geometry that follow the protocol proposed by Wang *et al.*[1] and also relate to the short-range model.

2.2 A Short-Range Model for Kagome Spin Ice

2.2.1 The Short-Range Hamiltonian

As the name suggests, the short-range model assumes that only nearest-neighboring spins are interacting. If this interaction is isotropic and does not depend on the chosen pair of spins, it can be described by an exchange-type Hamiltonian:

$$H_{SR} = -J \sum_{<i<j>} \vec{S}_i \cdot \vec{S}_j. \tag{2.2}$$

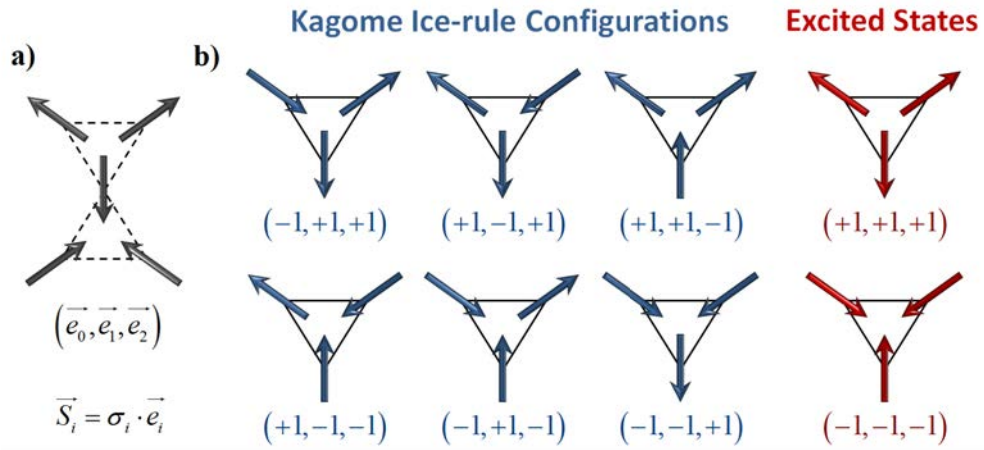

Figure 2.4 - (a) The convention for the unit vectors defining the orientation axes of the spin network. Each spin can be pointing along ($\sigma = +1$) or opposite ($\sigma = -1$) to its corresponding unit vector. (b) There are 3 spins/triangle and, since the spins are Ising-like, i.e. two possible states for each spin, the total number of triangle configurations is $2^3 = 8$. Out of these 8 configurations, 6 of them obey the kagome ice rules, while the remaining 2 correspond to excited states, which will also be referred to as 'forbidden states'. The values in the brackets are, in order, the scalar values of each spin.

where $\vec{S}_i$ and $\vec{S}_j$ denote the spins located at lattice-sites i and j, J represents the coupling constant and the summation is performed over all nearest-neighboring spin pairs[2].

Given the Ising nature of the spins, each spin vector can be written as the product between a ± 1 scalar value (to which I shall refer as the spin scalar value) and the corresponding unit vector associated to its orientation axis:

$$\vec{S}_i = \sigma_i \cdot \vec{e}_i. \tag{2.3}$$

Since the unit cell of the kagome lattice is a triangle, three such unit vectors are required, each pointing along the three bisectors. The orientation of these unit vectors is a matter of convention and I will consider them pointing outwards from a ∇-type triangle (see Figure 2.4.a). The Hamiltonian can then be rewritten as:

$$H_{SR} = -J \sum_{<i<j>} (\sigma_i \cdot \sigma_j) \cdot (\vec{e}_i \cdot \vec{e}_j). \tag{2.4}$$

The scalar product between the two unit vectors is a geometrical factor that depends on the relative orientation of the chosen spin axes. As the spin pairs are limited to first neighbors

[2]I will further use the notation $< i < j >$ to express the fact that each pair has to be taken into account only once in the summation. If the $< i, j >$ notation is employed, a $1/2$ factor is required to retrieve the system energy.

only and the bisectors form 120° with each other, this geometrical factor is always equal to $-1/2$. The vectorial Hamiltonian of equation 2.2 can thus been simplified to a scalar form:

$$H_{SR} = \frac{J}{2} \sum_{<i<j>} \sigma_i \cdot \sigma_j. \tag{2.5}$$

The sign of the coupling constant J determines the nature of the interaction and both the ferromagnetic ($J > 0$) and anti-ferromagnetic ($J < 0$) couplings can be studied[3]. Since the interest here is the behavior of artificial kagome spin ice arrays, the sign of this constant is determined by the sign of the dipolar coupling between nearest neighbors. By applying the point-dipole approximation[4] one can find:

$$J = D/(r_{nn})^3 \cdot [3 \cdot \frac{(\vec{e}_i \cdot \vec{e}_r) \cdot (\vec{e}_j \cdot \vec{e}_r)}{(\vec{e}_i \cdot \vec{e}_j)} - 1] = 7/2 \cdot D/(r_{nn})^3. \tag{2.6}$$

where $D = \frac{\mu_0 \cdot \mu^2}{4\pi}$ is the dipolar constant, r_{nn} is the distance between nearest-neighboring spins and $\vec{e}_r$ is the unit vector of the relative positioning vector $\vec{r_{ij}}$ between spins $\vec{S}_i$ and $\vec{S}_j$. The positive sign indicates that the coupling between the spin vectors is ferromagnetic and given the negative sign of the geometrical factor, the effective coupling between the spin scalar values is antiferromagnetic. It is worth mentioning again that, although this expression takes the form of a Heisenberg-exchange Hamiltonian, it does not stand for exchange interaction but for a dipolar coupling which is brought to this exchange-like form.

The scalar form of the Hamiltonian can facilitate a brief exploration of the thermodynamic behavior of the ferromagnetic kagome spin ice network[5]. By using the identity $(\sum_i \sigma_i)^2 = \sum_i \sigma_i^2 + 2 \cdot \sum_{i<j} \sigma_i \cdot \sigma_j$, we can sum up the spins scalar values for a given triangle[6]:

[3] It is important to note here that the coupling is considered ferromagnetic or antiferromagnetic with respect to the spin vectors, $\vec{S}_i$. Due to the negative sign of the geometrical factor, the scalar values would present the opposite effective coupling.

[4] As we shall later see, the dipolar approximation holds quite well only for second or higher order neighbors. Depending on the array spacing, the first neighbors can present a significant deviation from this approximation, which can be determined by micromagnetic simulations. However, the nature of the coupling is not affected by this deviation (rather enhanced).

[5] Although the nature of the interaction should always be specified, the focus here is on the ferromagnetic kagome spin ice. I will therefore drop the term 'ferromagnetic' to avoid repetition, but I will use it when ferromagnetic and antiferromagnetic cases are compared.

[6] This approach can be perform without reducing the Hamiltonian to a scalar form, as presented in [18]. This scalar form approach has also been reported in previous studies [79, 80].

$$(\sum_{i\in\triangle}\sigma_i)^2=\sum_{i\in\triangle}\sigma_i^2+2\sum_{i,j\in\triangle,i<j}\sigma_i\cdot\sigma_j. \tag{2.7}$$

Then, by summing over all the triangles, both ∇-type and Δ-type, we obtain:

$$\sum_{<i<j>}\sigma_i\cdot\sigma_j=\frac{1}{2}[\sum_{\nabla,\Delta}(\sum_{i\in\nabla,\Delta}\sigma_i)^2-\sum_{\nabla,\Delta}\sum_{i\in\nabla,\Delta}\sigma_i^2]. \tag{2.8}$$

Since $\sigma_i=\pm1,\forall i$, the last term is a constant, equal to three times the number of triangles, both ∇-type and Δ-type: $-3\cdot(N_\nabla+N_\Delta)$. Multiplying the relation by $J/2$, the left term becomes the system's energy and the ground-state can be determined by minimizing the first term on the right. This would require all triangles to have a sum of the spin scalar values equal to ±1, which is, in fact, another way of formulating the kagome ice rules. The ice-rule configurations and the highly-frustrated "all-in"/"all-out" states are represented in Figure 2.4.b. Finally, the energy of the ground-state can thus be written down as:

$$E_{GS}=-\frac{J}{2}\cdot(N_\nabla+N_\Delta). \tag{2.9}$$

Therefore, as long as the ice rules are unanimously obeyed, the system is in its ground-state manifold, regardless of the particular choice for each triangle. This would imply a massively degenerated ground-state which can be reached at lower temperatures once the highly-frustrated configurations are ruled-out. For a more detailed look at the thermodynamic properties of kagome spin ice, we shall now turn to the results given by Metropolis Monte Carlo simulations.

2.2.2 Single Spin Flips and Loop Flips

The Monte Carlo simulations presented here have been performed using a single spin-flip Metropolis algorithm with selective sampling and insuring decoherence between successive Monte Carlo measurement snapshots, as was presented in Appendix A. The simulation temperature is initially set to $T_{init}=10^2\cdot J_{NN}$, corresponding to a high-temperature paramagnetic regime, and is then gradually reduced by dividing it to a predefined temperature step (T_{step}). For each temperature value, a thermalization stage including 10^4 MMCS (modified Monte Carlo steps) is firstly applied, followed by 10^4 MMCS used for sampling (please refer to Appendix A for more details on modified Monte Carlo steps). The relevant thermodynamic

quantities are afterwards computed using the sampled data. Simulations have been performed for different system sizes and boundary conditions. However, all data presented in this section correspond to a network containing 432 spins ($12 \times 12 \times 3$) under periodic boundary conditions (PBC).

Since we've already got an idea about the behavior of the system's energy, I shall start by discussing its temperature-dependence, which is reproduced in Figure 2.5.a. At high temperatures, the average energy is approximately 0, reflecting the paramagnetic regime, in which the spins are decorrelated from each other, thus making all vertex configurations equally probable. We therefore expect a 25% presence ratio for the forbidden states ("all-in"/"all-out") and a 75% ratio for configurations respecting the kagome ice rules. The population ratio of forbidden states is plotted in Figure 2.5.b and confirms these expectations at high temperatures. As the temperature is lowered, the forbidden states ratio slowly declines until these configurations are completely removed and the system enters the spin ice manifold. This is achieved for a temperature value of about $0.3J$[7]. The energy of this ground-state manifold is given by equation 2.9. Since the system has periodic boundary conditions, the total number of spins is equal to three times the number of ∇-type (or Δ-type) triangles. Therefore, using equation 2.9, the energy/spin of the ground-state is equal to:

$$e_{GS} = -\frac{J}{3}. \tag{2.10}$$

and the simulations are in perfect agreement with this result (see Figure 2.5.a). We expect this energetic manifold to be macroscopically degenerated. To ascertain and quantify this degeneracy, we will further turn our attention to the temperature dependencies of the specific heat and the entropy.

However, before moving on to other relevant thermodynamic quantities computed during the simulations, a discussion on the efficiency and ergodicity of the spin dynamics is required. At high temperatures, the thermal energy dominates the inter-island coupling and spin-flips are almost always accepted, even if the system energy is increased. This can be seen in the spin acceptance ratio temperature-dependence plotted in Figure 2.6. As expected, the single spin-flip dynamics is very efficient in mapping the system's phase space in this regime. As the temperature decreases and the spin ice manifold is accessed, the spin acceptance ratio drops to an average value of 0.456. This is due to the rejection of a spin-flip that might momentarily create a forbidden state. Therefore, to ensure decoherence, a minimum of three decorelation Monte Carlo steps are performed between successive measurements.

[7] Since the passage from the paramagnetic state to the spin ice regime is a cross-over, a precise transition temperature cannot be defined. Nevertheless, the beginning of the pure spin ice regime is marked by the highest temperature value for which no forbidden states are observed anymore and their ratio is strictly 0 at all times.

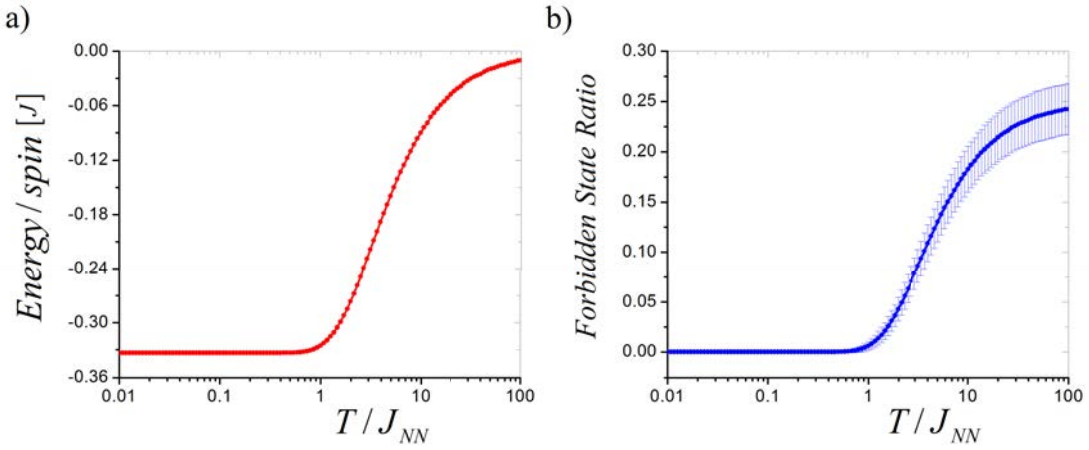

Figure 2.5 - (a) The energy/spin and (b) the forbidden state ratio as a function of temperature for a kagome spin ice system with only nearest-neighbor coupling. At high-temperatures, one out of four vertices is a defect. As the system cools, these excited states become less and less present and this has a direct consequence on the system energy. As soon as the spin ice manifold is reached, forbidden states are supressed and the energy remains constant down to the lowest temperature. The error bars correspond to the standard deviation of the distribution of network averages computed over the 10^4 Monte Carlo snapshots for each temperature.

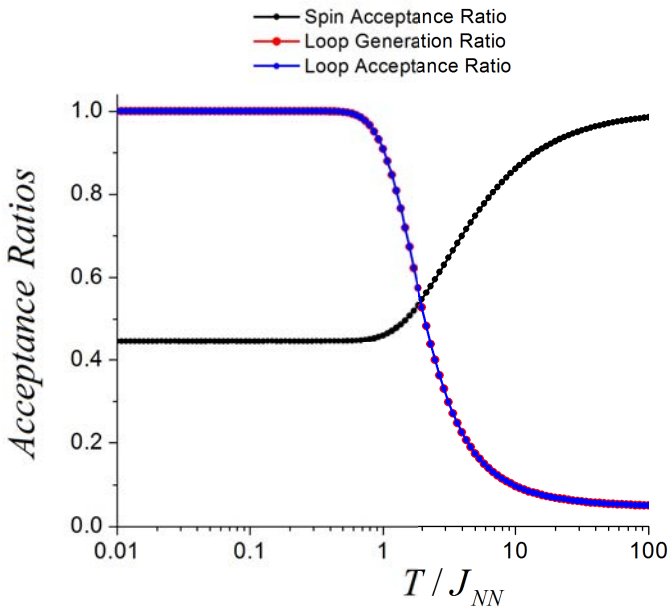

Figure 2.6 - The acceptance ratios of the single spin-flip (black) and the loop-flip dynamics (blue). The slowing down of the spin dynamics is due to the possibility of creating a defect during the Monte Carlo steps, which is immediately rejected in the spin ice phase. A loop in the spin configuration can always be found in this regime, regardless of the starting point. Furthermore, its flip is instantly accepted as it comes with no energy costs, thus making this dynamics an ideal method for exploring the spin ice manifold.

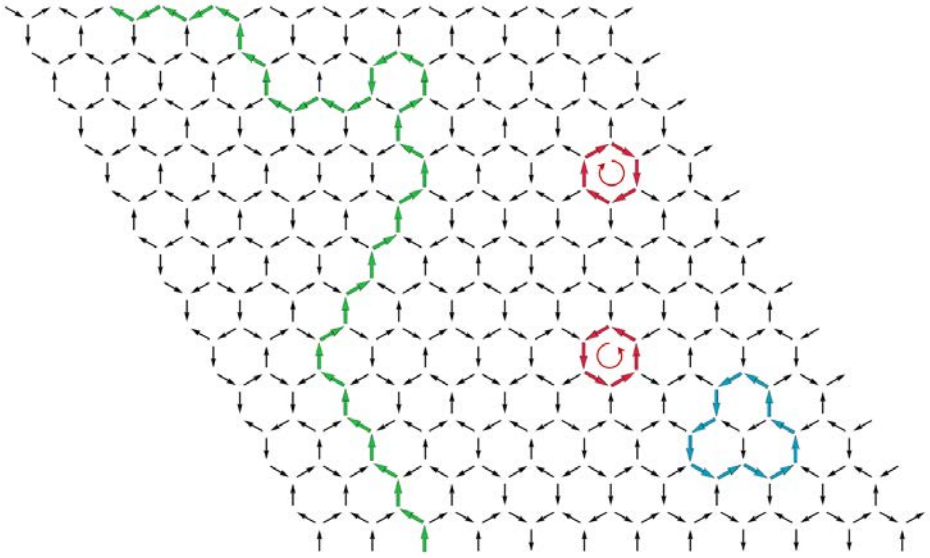

Figure 2.7 - A typical spin ice manifold configuration for a lattice of 432 spins (12×12). The smallest loop configuration possible contains 6 spins that define a hexagon of the lattice (red loops) and can turn either clockwise or anti-clockwise. Larger loops can wind around several spins (blue loop). In case of a system with periodic boundary conditions, there is also the possibility of finding loops that stretch through the entire lattice length (green loop), marking a contour on the surface of the torus on which the network is wrapped upon. Note that, for free boundary conditions, loops that stretch from one end to another are still eligible and flipping them will not break the ice rules.

There is, however, a remarkable way of exploring the spin ice manifold. A close inspection of the spin configuration reveals that the spins tend to form closed-loops. These loops can circle around a hexagon of spins, define the perimeter of a cluster of network hexagons or even stretch around the whole network given the wrapping of the system on the surface of a torus (see Figure 2.7). In fact, a loop is a chain of spins with alternating spin scalar values (σ_i) and this is actually the way a loop can be generated: 1) randomly choose a spin of the network (σ_i); 2) choose one of its neighboring spins (σ_j) so that $\sigma_i \cdot \sigma_j = -1$; if multiple choices can be made, choose one at random or abort the loop generation sequence if unable to choose; 3) move to the selected spin (σ_j); 4) go back to step 2) and keep repeating steps 2) to 4) insuring that the loop does not go backwards. This repeat sequence is halted when a spin that has already been chosen is again selected ("the snake has bitten it's tail"). At this point, the remaining part of the tail needs to be dropped, yielding a closed-loop of spins[8]. The reason for cutting-off the tail resides in the possibility of creating a defect at loop's initial or ending points. This is the reason why only closed-loops are considered.

[8]I shall frequently refer to loop dynamics and loop-flips without mentioning the fact that I am dealing with closed-loops. Unless specifically states, one should assume that I am implicitly referring to closed-loops or winding loops.

Since a loop is a chain of neighboring spins, each network triangle that a loop crosses contains two of the loop's spins. Take one such triangle and assume that all spins of the loop are now flipped. The third spin of the triangle (the one not contained in the loop) has seen its neighboring spins switch orientations (or effectively switched places). However, its local interaction environment and its contribution to the total system energy has not changed. Therefore, flipping such a closed-loop of spins will not change the system energy, but it will modify the spin configuration. Furthermore, such a loop-flip cannot break the kagome ice rules. These facts make these loop updates an ideal dynamics for mapping the phase space of the spin ice manifold and is not affected, in this short-range model, by a critical slowing down effect.

Figure 2.6 gives the temperature-dependencies of the loop generation ratio and the loop acceptance ratio. The two plots are superposed on one-another, expressing the fact that, if a loop is found, its flip is immediately accepted. Due to the presence of defects (forbidden states) at high temperatures, the loop generation algorithm presented earlier gets stuck in such a defect vertex, the process being then aborted. In fact, at very high temperatures, 1 out of 19 tryouts manages to generate a loop. However, in the spin ice manifold, both ratios are constant and equal to 1, highlighting the efficiency this dynamics.

In these simulations, loop flip dynamics are always accompanied by single spin-flips. Permitting only loop-dynamics while the system is not yet in the spin ice manifold will pin down the already-present defects and the system will no longer be able to explore its phase space in an ergodic manner. Therefore, to ensure ergodicity throughout the simulation, a hybrid-flip has been implemented, involving one single spin-flip attempt and followed by one loop-flip attempt. While this approach is interesting, it usually comes with an increase in simulation runtime due loop generation procedures. Furthermore, the results obtained using a hybrid-flip and a single spin-flip dynamics are essentially the same for the short-range model. Therefore, the simple single spin-flip approach is practically prefered. Nevertheless, this hybrid-flip implementation will become very useful once long-range dipolar interactions are introduced.

2.2.3 The Specific Heat and the Entropy

The temperature dependencies of the specific heat (C) and the magnetic susceptibility (χ) are usually the standard thermodynamic quantities that are computed in the Monte Carlo simulation of a spin model, since they offer insights into the system's critical behavior. As we are dealing with an at-equilibrium scenario, the two quantities can be computed using the fluctuation-dissipation theorem. To this end, the variances of the energy and the

magnetization for each sampling cycle were calculated. The entropy at a given temperature is then determined by integration:

$$S(T) = S(T \to \infty) + \int_{\infty}^{T} \frac{C}{T} dT. \tag{2.11}$$

The temperature-dependencies of the specific heat and the entropy in this short-range picture are given in Figure 2.8, both being normalized to the number of spins. The results are in accordance with the ones reported by Wills *et al.*[71] [9]. The specific heat exhibits a broad peak ranging over a large temperature window[10], with a maximum of $0.112 k_B/site$ corresponding to a temperature value of $T/J \sim 2$. As the temperature further drops, fluctuations decrease and the specific heat is reduced to 0 once the spin ice manifold is reached. To determine the entropy's temperature-dependence, a convention/reference must first be established. In the paramagnetic regime, the system can be approximated with a network of non-interacting spins. Therefore, each spin has two possible orientations, reflecting its Ising nature. In this case, the entropy/spin would be: $s(T \to \infty) = ln(2)$. This convention has been largely used [7, 8, 10] and I will also employ it throughout this work.

The system passes from a state in which all vertex configurations are possible to a spin ice regime where only ice-rule configurations are allowed. A peak in the specific heat and a drop in the entropy were therefore expected. The residual entropy/spin of the spin ice manifold given by these Monte Carlo simulations is $0.501687 k_B$, which is in very good agreement with the exact value, $s_{spin-ice} = 0.50183 k_B$, calculated by KanÔ and Naya [67][11].

Wills *et al.*[71] also present a way of estimating this residual entropy following the method that Pauling used to determine the residual entropy of water ice [22]. However, they do point-out that this method actually calculates the entropy of a Bethe lattice, which is not actually the same as in the kagome case (see Figure 2.9). Remarkably, the result is very close to the precise value, with a relative error of $9.38 \cdot 10^{-4}$.

[9] Note that temperature in the specific heat and entropy plots reported by Wills *et al.* is normalized to $J(S^2)$ and not to $J(\vec{S}_i \cdot \vec{S}_j)$ like in this case. This give rise to an apparent shift of the temperature axis between this plot and the one they report. Nevertheless, the results are compatible.

[10] Simulations performed on different system sizes show that this peak does not change its shape as the system size increases and remains broadly distributed over a large temperature window. This behavior is, in fact, a signature of a cross-over phenomenon rather than a phase transition.

[11] The numerical residual entropy value depends on the integration method employed and on the temperature sampling. In all cases, an integration by trapezoids has been used and a certain numerical error is expected. The result presented here corresponds to a $T_{step} = 10/9$. For $T_{step} = 10^{\frac{1}{30}}$, the final value is $0.502518 k_B$, while for $T_{step} = 10^{\frac{1}{50}}$ it is $0.501894 k_B$.

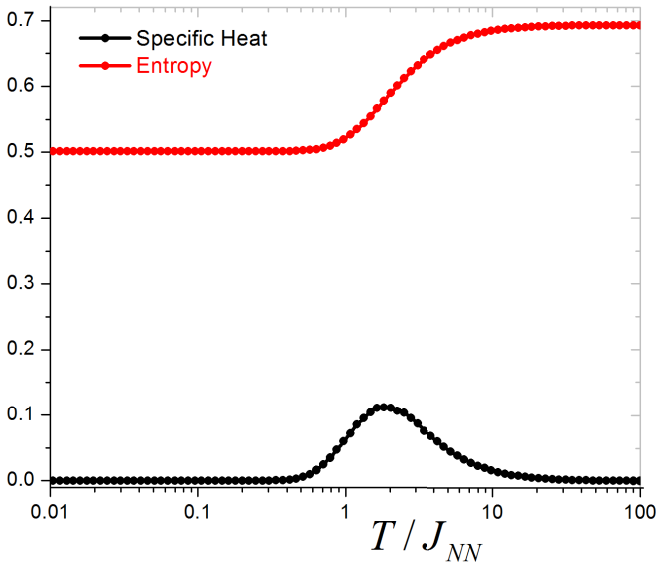

Figure 2.8 - The specific heat and entropy plots for a kagome spin ice system presenting only nearest-neighboring coupling. Both quantities are reported in $k_B/site$ units. The specific heat presents a broad peak, invariant with the lattice-size and maximum value for $T/J_{NN} \cong 2$. The entropy drops from the $ln2$ paramagnetic value to the spin ice entropy, which is approximately 0.501, without presenting any other changes as the system further cools down. This is one of the most highest residual entropy/spin values known for a 2D lattice.

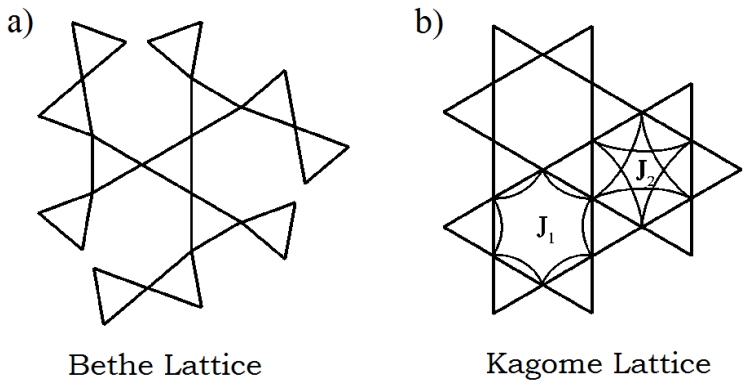

Figure 2.9 - The (a) Bethe and (b) the kagome lattices. The Bethe lattice presented here can be generated by considering a rooted-tree with a coordination number of 3 (similar to a Husimi cactus). Placing triangles at each vertex so that they share their corners yields this Bethe lattice. The absence of connection points between the outgoing branches facilitates the direct determination of the spin ice entropy. Remarkably, this is very close to the exact value of the kagome spin ice residual entropy. After Wills *et al.*[71]

Lets start by selecting a triangle of the network that is in an ice-rule configuration. All it's neighboring triangles will have one of its spins already fixed. Therefore, out of the 8 possible configurations, only 4 are left for them, and out of this 4, only 3 respect the ice-rules. The total number of spin configurations of the lattice is $2^{N_{spins}}$, but we must filter out the ones that do not obey the kagome ice rules, which implies multiplying by a factor of $(3/4)^{N_{triangles}}$. This would yield a number of spin ice configurations equal to $\Omega_{spinice} = 2^{N_{spins}} \cdot (3/4)^{N_{triangles}}$. Assuming a PBC case, we have $N_{spins} = 3/2 \cdot N_{triangles}$ and the entropy/spin is therefore:

$$s_{spin-ice} = \frac{1}{N_{spins}} ln(\Omega_{spin-ice}) = 1/3 \cdot ln(9/2) \cong 0.50136. \tag{2.12}$$

The same result can be obtained by handling the PBC case differently. First set all the ∇-type triangles into ice-rule configuration. There are 6^{N_∇} ways to do this. The question now is what is the chance of having the Δ-type triangles in ice-rule configurations as well? Each of them is surrounded by three ∇-type triangles and since the spins of these triangles have been chosen independently, any of the eight configurations is possible for a Δ-type triangle, but only six of them respect the ice-rules. The chances of having an ice-rule obeying Δ triangle are therefore $6/8$ and having all of them is $(6/8)^{N_\Delta}$.[12] Since $N_\nabla = N_\Delta = N_{spins}/3$, the total number of configurations for the spin ice manifold is therefore $\Omega_{spin-ice} = (6 \cdot (6/8))^{N_{spins}/3}$, the same as before.

The residual entropy/spin of the spin ice manifold is quite high. In fact, Wills *et al.*[71] conclude their paper by stating that "It is [therefore] the most highly geometrically frustrated "ferromagnetic" ground-state yet to be studied".

2.2.4 The Magnetic Susceptibility

The magnetic susceptibility behavior of kagome spin ice within the short-range model is given in Figure 2.10.a. Interestingly, once the system has reached the spin ice manifold, the susceptibility continues to increase as the temperature drops, appearing to present a singularity at a very low temperature. This behavior is strikingly similar to that of a paramagnet. In fact, in terms of susceptibility, the system presents two distinctive paramagnetic regimes,

[12] Although this seems like a rigorous approach, this is actually where the approximation is hidden. The argument holds for one Δ-type triangle being surrounded by three ∇-type ones whose configurations were chosen independently. The number of states respecting the ice rule for this cluster is $6^3 \cdot 6/8$. However, when treating another Δ-type triangle the same way, one may need to assume again completely independent configurations for a ∇-type triangle that has already been considered before, which is an inconsistency. In other words, the same triangle of the kagome lattice is treated differently in two different cases. If the network does not connect around its hexagons, then we would not face such a contradiction. This is actually the case of the Bethe lattice (see Figure 2.9). Obtaining the same result is therefore not surprising.

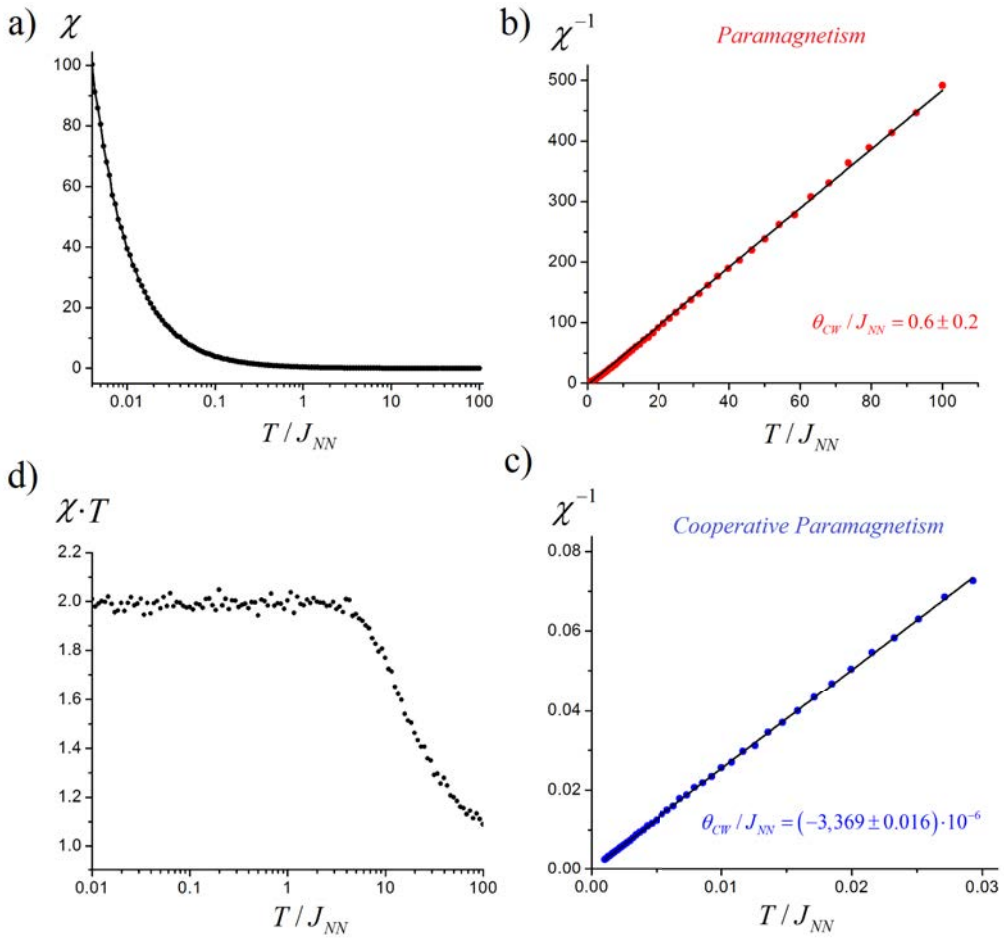

Figure 2.10 - (a) The magnetic susceptibility as a function of temperature. As in the case of the specific heat and the entropy, all susceptibilities presented here are normalized to the number of spins. The Curie-Weiss plots for the (b) pure-paramagnetic regime and (c) the cooperative-paramagnetic regime. The linear fits can help determine the values of the Curie-Weiss temperatures (θ_{CW}), which are numerically found to be approximately 0.6 for the paramagnetic case and approximately 0 for the coorperative paramagnet. (d) The two different paramagnetic regimes can be distinguished by plotting $\chi(T) \cdot T$ and can also help determine the Curie constants for each of them. The non-zero value in the low-temperature regime is another indicator that, for the cooperative-paramagnetic case, $\theta_{CW} = 0$. This plot is compatible with the results reported by Macdonald *et al.*[81].

both subject to the Curie-Weiss law: a pure paramagnetic phase and a cooperative paramagnetic phase[82]. Unlike the pure paramagnetic phase in which the spins are uncorrelated, this cooperative paramagnetic regime presents non-vanishing, short-range spin-spin correlations (see Figure 2.11.a), and the system still fluctuates intensively. Figure 2.10 gives the dependence of $\chi^{-1}(T)$ for the paramagnetic phase (b) and the spin ice phase (c). The Curie-Weiss temperature for the paramagnetic phase obtained by a numerical fit is approximately $T/J = 0.6$, while the one for the cooperative paramagnetic regime is approximately 0. This fact reinforces what has already been suggested by the entropy's temperature-dependence: once the spin ice manifold is reached, the system continues to fluctuate down to absolute zero, without recovering any other degrees of freedom. Otherwise said, the short-range kagome spin ice displays no critical behavior, just as Syozi initially reported[65].

Another way of looking at the susceptibility behavior is to plot the temperature-dependence of $T \cdot \chi(T)$. If the two paramagnetic regimes are indeed governed by the Curie-Weiss law, then this function should exhibit two clear plateaus. This is indeed the case, as presented in Figure 2.10.d. Interestingly, this function can also serve as a subtle measure of the topological constrains that are imposed on a short-ranged kagome spin ice system [81], be it constrained (kagome plane of a spin ice pyrochlore with a magnetic field along the [111] axis) or unconstrained (the present kagome spin ice model).

2.2.5 The Spin Correlations

As presented in the introduction, pairwise spin correlations can be a very sensitive way of measuring the order that is established within a system. It is therefore interesting to compute these quantities during the simulations. Furthermore, they are a very useful tool for bridging experimental results obtained for artificial realizations of spin models with the theoretical predictions[1, 6, 11, 13, 14, 73, 83]. Throughout this work, the definition and the nomenclature proposed by Wills *et al.*[71] for the first seven pairwise spin correlations of the kagome topology will be employed (see Figure 2.11.b).

Figure 2.11.a gives the temperature-dependencies of the ensemble averages for the first seven pairwise spin correlations as established by the nomenclature of Wills *et al.*[71], each point corresponding to an average computed over the 10^4 Monte Carlo snapshot averages. At high temperatures, all correlations are effectively zero, as there is no order that is established in the paramagnetic regime. As the temperature drops, the system starts to correlate. Once the spin ice manifold is reached, the correlation values cease to evolve, but they do fluctuate

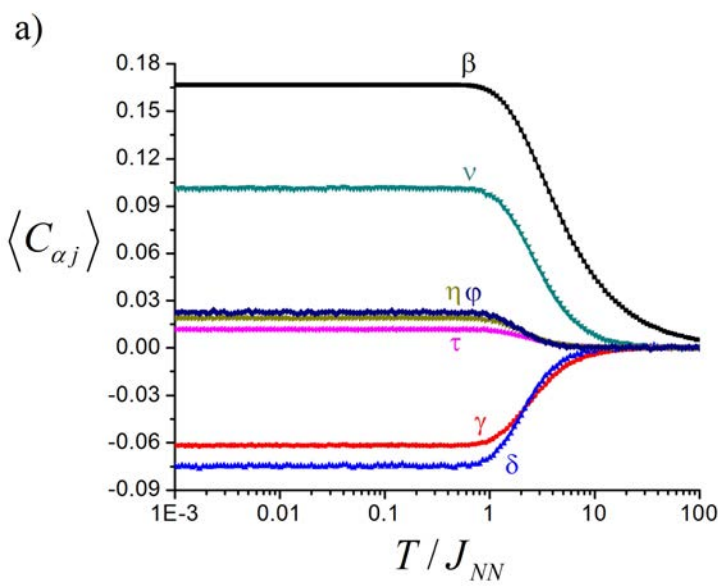

c)

	Will's Ice	Current Simulations
$C_{\alpha\beta}$	0.166	0.166
$C_{\alpha\gamma}$	-0.059	-0.061
$C_{\alpha\nu}$	0.101	0.101
$C_{\alpha\delta}$	-0.072	-0.074
$C_{\alpha\tau}$	0.012	0.011
$C_{\alpha\eta}$	0.017	0.018
$C_{\alpha\varphi}$	0.007	0.022

Figure 2.11 - (a) The first seven pairwise spin correlations as a function of temperature for a short-range kagome lattice. These plots are obtained from a simulation performed on a (12×12) network. (b) The definition of the correlation pairs, as established by Wills *et al.*[71]. (c) The correlations do not depend on the system temperature once the spin ice regime is reached and their final ground-state values are reported here. A very good matching is found with the data provided by Wills *et al.*[71].

around the ensemble average values due to the lattice finite size. These values are given in Figure 2.11(c) and are in good agreement with those reported in the literature[71][13].

2.2.6 The Magnetic Charge and the Charge Correlations

The spins of the kagome network have an associated magnetic, which can be regarded as a magnetic dipole with two opposite classical magnetic charges located at its edges (see Figure 2.12.a). Assuming that these dipoles stretch between two neighboring vertex points[14], we can actually sum up the individual charge contribution at each vertex site and define an effective charge/vertex. As presented in the introduction, this dumbbell picture was proposed by Castelnovo *et al.*[35] to describe the exotic magnetic monopole excitations above the ground state of pyrochlore spin ice. However, unlike its 3D counterpart, the vertices of the 2D kagome spin ice cannot present charge neutrality as the contributions from the three spins

[13] I do note however that there is a slight difference between the spin ice values of $C_{\alpha\varphi}$ obtained by Wills *et al.*[71] and these simulations. Nevertheless, the value reported here is in agreement with what has been reported by Rougemaille *et al.* [73].

[14] This assumption appears to be in sharp contrast with the basic requirement of the point-dipole approximation. This is, in fact, another approximation on its own, which will be further discussed when introducing the dipolar spin ice model.

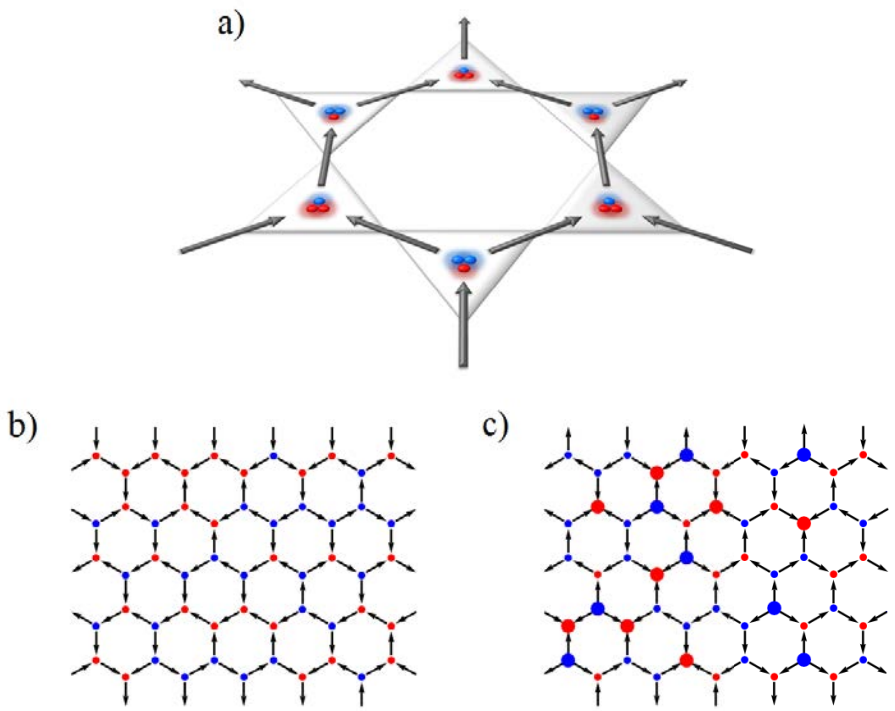

Figure 2.12 - (a) A spin can be regarded as a dumbbell with two opposite magnetic charges located at its edges. The spin network can then be transformed to give rise to a hexagonal network of charges if the individual contributions are summed up at each vertex. After Chioar *et al.*[14]. The spin and the magnetic charge networks for (b) a spin ice manifold configuration and for (c) a high-temperature paramagnetic one. Since the ice rules are obeyed, there are only ± 1 charges in the spin ice phase. The paramagnetic case, however, present several defects, with equal probabilities for the $+3$ and -3 configurations.

that form up a kagome vertex cannot cancel out. Nevertheless, the charge neutrality of the network is still preserved as each spin contributes with two opposite unitary charges.

The vertex charges can be defined by using the spin scalar values (σ_i) associated to the spin vectors. For each Δ-type triangle, the vertex charge is given by $Q_\Delta = \sum_{i\in\Delta} \sigma_i$, while for a ∇-type triangle, the vertex charge is equal to $Q_\nabla = -\sum_{i\in\nabla} \sigma_i$. Hence, there are four possible values for a vertex charge, ± 3 and ± 1, corresponding to the forbidden states and the ice-rule configurations, respectively (see Figures 2.12.b and 2.12.c). The spin ice ground state of the short-range kagome spin ice is therefore a hexagonal network of ± 1 magnetic charges (Figure 2.12.a.). However, there appears to be no particular charge order within this manifold. To further investigate this, a nearest-neighbor charge correlator can be defined and a network average ($Q_i Q_{i+1}$) can also be computed.

The temperature-dependence of the nearest-neighbor charge correlator is given in Figure 2.13. This behavior has previously been reported by Rougemaille *et al.*[73] and the current

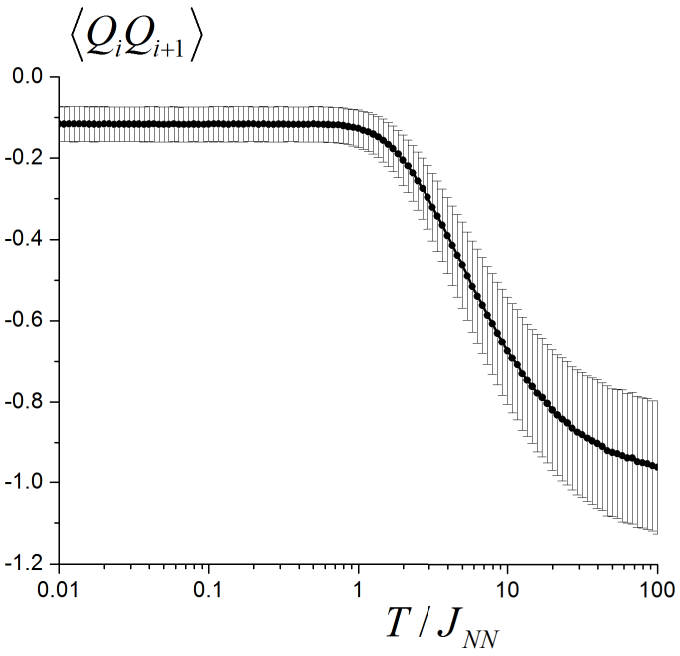

Figure 2.13 - The nearest-neighbor charge correlator plot for a short-range kagome spin ice. The error bars correspond to the standard deviation of the distribution of network averages computed over the 10^4 Monte Carlo snapshots for each temperature. The network size is (12×12). The $-1/9$ plateau of the spin ice manifold highlights the existence of a very weak charge-charge correlation.

plot accurately reproduces their results. Interestingly, in the paramagnetic regime where all spin correlations are suppressed, the charge correlator appears to be close to -1, which would signal the presence of a charge order. However, this is not the case, as this -1 value is a residue of the definition of the vertex charges within the dumbbell approximation. By writing the charges as sums of spin scalar values, one can develop the expression of the nearest-neighbor charge correlator in terms of pairwise spin correlations. After summing up on the network scale, a relation between the nearest neighbor charge correlator and three pairwise spin correlations can be found (the demonstration is provided in Appendix C):

$$Q_i Q_{i+1} = -1 + 8 \cdot C_{\alpha\beta} + 4 \cdot C_{\alpha\gamma} - 2 \cdot C_{\alpha\nu}. \tag{2.13}$$

Given that, on average, all spin correlations cancel out at high temperatures, the charge correlator is therefore -1. The reason for this pending -1 term in expression (2.12) is related to the fact that each spin is the connection point between two vertices and hence between two neighboring charges. The spin forcibly contributes with a $+1$ magnetic charge in one vertex and with -1 magnetic charge in a neighboring one and, when computing the charge

correlator, these two values will add up and yield the -1 factor. Otherwise said, this -1 value is the testimony of the underlying dependence between two neighboring charges, given that they both share a network spin.

As the temperature drops, the forbidden states slowly disappear, and so do the $+3$ and -3 charges. The charge correlator increases until the system enters the spin ice manifold where it reaches its maximum value of about $-1/9$. Therefore, the system is far from presenting any clear charge order.

This concludes the survey of the thermodynamic properties of kagome spin ice within the short-range model. I shall come back to experimental realizations of this geometry and particularly discuss the results of Qi *et al.*[46] who explored the matching between artificial kagome spin ice correlators and those given by the present model.

2.3 Is Artificial Kagome Spin Ice Truly Short-Range?

Although the approach of Tanaka *et al.*[42, 43] didn't involve any spin or charge correlation analysis to ascertain the validity of the short-range model for their artificial kagome spin ice system, they do note that all vertices respect the ice rule. In fact, their MFM image (see Figure 2.3) is a map of the associated magnetic charge network, and since the ice rule is obeyed throughout the entire array, all the charges have either a $+1$ or -1 value. However, this result was rather expected, as the islands are connected at the vertex points and the occurrence of a forbidden state would be too costly in terms of magnetostatic energy. Furthermore, although it is exciting to have realized a spin ice manifold configuration by connecting the islands, this option comes with a certain price: their MFM image cannot give any specific detail about the magnetization of each lattice element. This makes it impossible to exactly reproduce the spin configuration and further study this system as a spin model rather than an effective charge model. Also, the system hasn't been subjected to any particular dynamics that might help it explore the different configurations and gradually accommodate frustration effects, as proposed by Wang *et al.*[1][3].

Approximately two years later, Qi *et al.*[46] make the next step and report a study on a very similar permalloy-based kagome spin ice by following the protocol established by Wang *et al.*[1]. However, instead of using a Magnetic Force Microscope for determining the magnetic configuration, they choose to employ a Transmission Electron Microscope operating in Lorentz mode. Since the islands are magnetized, the incident electron beam will find itself in a magnetic field when crossing the islands and will therefore be subjected to a Lorentz force. This will give rise to a deviation to either the left or right side of the island, depending on the orientation of its magnetization. By looking at the contrast at the

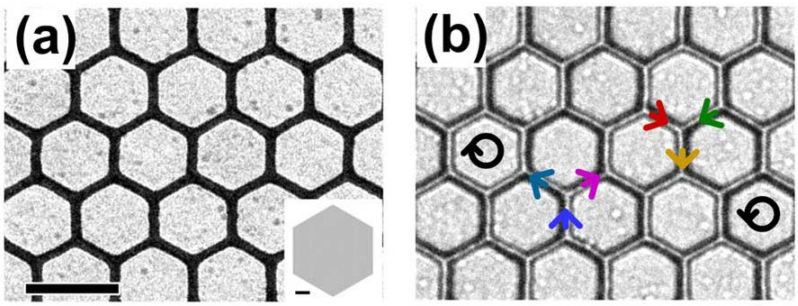

Figure 2.14 - An artificial realization of the kagome spin ice system by Qi *et al.* (a). Like in the case of Tanaka *et al.*, the islands are interconnected and the scale bar corresponds to 1μm. Using a Transmission Electron Microscope in Lorentz-mode, the magnetization of each island of the artificial array can be determined by analyzing the bright and dark contrasts forming up at the sides of each element (b). Note that this scan area contains two short-loop configurations, with opposite chiralities. After Qi *et al.*[46].

edges, one can determine the orientation of each of the artificial kagome spin ice's islands (see Figure 2.14). Also, since there is no change in contrast along an island's edges, this confirms that they act as magnetic monodomains.

This approach offers an exhaustive knowledge of the spin orientations on the lattice scale, which enabled Qi *et al.*[46] to performed a correlation analysis by using the nomenclature provided by Wills *et al.*[71]. They computed the first ($C_{\alpha\beta}$), second ($C_{\alpha\gamma}$), third ($C_{\alpha\delta}, C_{\alpha\nu}$) and sixth ($C_{\alpha\varphi}$) order spin correlators by averaging throughout their experimental network containing 12846 elements. They further compare their results to the ones reported by Wills *et al.*[71] for the spin ice manifold within the short-range model (see Table (2.1)). However, the data provided by Wills does not contain any standard deviations. To offer a more accurate analysis, Monte Carlo simulation data for a kagome lattice with 13068 spins ($66 \times 66 \times 3$), the typical size of the experimental network, is also given[15]. As this standard deviation is size-dependent, matching the size of the simulated network with the experimental one is important for a more precise comparison. Note that, when defining the spin correlations, Qi *et al.*[46] do not take into account the geometrical factor arising from the relative angle between the considered pair of spins. Therefore, to compare with the spin ice manifold correlations, the theoretical values have been adjusted to this convention.

Since the ice rule is unanimously obeyed by all vertices, the nearest-neighbor spin correlator is 0.333. This is in perfect agreement with both sets of Monte Carlo simulations. Furthermore, the short-range model would appear to work rather well, as all correlations agree in terms of sign and roughly in terms of magnitude with the simulation data, a fact also reported by Qi *et al.*[46]. However, if we now turn our attention to higher order correlations,

[15]Except for the network size, the simulation parameters are the same as described in the previous section.

Table 2.1 - The experimental data after Qi *et al.*[46] along with Monte Carlo averages for the spin ice phase reported by Wills *et al.*[71]. The last two columns contain results given by a short-range model Monte Carlo simulation for a network of comparable size with the experimental one. All theoretical values are computed for the spin ice manifold.

Correlation type	Experimental Data		Will's Ice	Spin Ice Data	
	mean	stdev	mean	mean	stdev
$C_{\alpha\beta}$	0.333	0	0.333	0.333	0
$C_{\alpha\gamma}$	-0.158	$\pm$0.008	-0.118	-0.123	$\pm$0.003
$C_{\alpha\nu}$	0.165	$\pm$0.013	0.101	0.101	$\pm$0.006
$C_{\alpha\delta}$	-0.130	$\pm$0.015	-0.072	-0.074	$\pm$0.009
$C_{\alpha\phi}$	0.057	$\pm$0.007	0.007	0.022	$\pm$0.009

we notice that the matching becomes less and less accurate as the correlation order increases. The relative deviation for $C_{\alpha\gamma}$ is about 28%, for $C_{\alpha\delta}$ is about 75% and for $C_{\alpha\varphi}$ is about 160%. This increasing mismatch raises several questions.

Firstly, it should be noted that the nature of the dynamics is not the same in the experimental procedure and in the simulated spin model. The sample is demagnetized in a slowly-decaying rotating ac field, which is a semi-deterministic process that gives the system the opportunity to accommodate the inter-island interactions within a narrow field window[3, 83] and allows only energy-reduction updates to occur. On the other hand, the simulations explore the at-equilibrium thermodynamic properties of the system in a ergodic manner, which differs significantly from the one-shot experimental protocol. Nevertheless, this approach sometimes yields results that are miraculously close to the ones predicted by at-equilibrium Monte Carlo simulations of spin models[13, 14, 73] and the deviations could be the residue of the out-of-equilibrium physics characteristic to the demagnetization protocol used for exploring the configuration space.

Secondly, the experimental lattice is subject to many design imperfections. The lithographic process does not guarantee identical islands throughout the network, and a certain distribution of island moments, reversal fields and inter-island couplings should be considered. The misalignment with the network axes and the island roughness can also play a significant role in selecting the series of magnetic configurations the system explores during demagnetization. The latter case was indeed confirmed by Kohli *et al.*[84] through a magneto-optical Kerr effect study of the magnetization reversal of an artificial square ice and similar lattice anisotropies have also been reported for the kagome geometry [73]. Extensive simulations have also been performed by Budrikis *et al.* and they confirmed that

the disorder strength, more than its particular origin, plays a decisive role in determining the demagnetization pathways and thus the final state of the network[85–87][16].

Lastly, it should be again emphasized that these networks are, in fact, in a magnetostatic framework. The islands are coupled through their stray fields, which are long-range by nature. It is quite remarkable that an effective short-range model seems to capture the essential physics and correlation development in such artificial arrays, as Wang *et al.*[1] reported for artificial square ices. It is as if, somehow, the long-range part was washed away. However, the deviations from the short-range case reported by Qi *et al.*[46] for the artificial kagome network might be signatures of an incipient long-range dipolar order. They indeed emphasize in their paper that the magnitude of higher order correlations are larger than predicted by the short-range model (see Table (2.1)). These biased deviations actually motivate a full dipolar treatement of such arrays and a comparison between experimental data and the predictions of the dipolar spin ice model.

The following section is therefore dedicated to the exploration of the thermodynamic properties of the kagome spin ice system assuming long-range dipolar interactions between the islands. I shall afterwards return to artificial kagome spin ice realizations which compare the ac demagnetized networks to this model.

2.4 The Dipolar Spin Ice Model

2.4.1 Adding Dipolar Long-Range Interactions

The cornerstone of the dipolar spin ice model is the point-dipole approximation, which assumes that the interactions between the magnetic moments can be described only by the dipolar term, the first term of the multipolar expansion of the magnetic vector potential[88]. This starts to be accurate if the size of the magnetic moments is much smaller than the distance between them. In this case the moments can be considered as point-like and the total energy of a system of interacting magnetic moments is given by:

$$E_{dip} = -\frac{\mu_0}{4\pi} \sum_{(i<j)} [\frac{3 \cdot (\vec{\mu}_i \cdot \vec{r}_{ij}) \cdot (\vec{\mu}_j \cdot \vec{r}_{ij})}{r_{ij}^5} - \frac{\vec{\mu}_i \cdot \vec{\mu}_j}{r_{ij}^3}], \tag{2.14}$$

where $\vec{\mu}_i$ and $\vec{\mu}_j$ are the magnetic moments, $\vec{r_{ij}}$ represents the relative positioning vector between them and μ_0 is the vacuum magnetic permeability. However, this is hardly the

[16] It should be noted that Budrikis *et al.* have simulated a rotating constant-magnitude field protocol instead of an ac demagnetization protocol.

case in artificial spin ices since the nano-scale islands are tightly packed in networks with lattice constants that are comparable in size with the lengths of the components. Directly implementing this approximation would be a rather rough approach, particularly for nearest-neighboring islands, but it might hold for higher order neighbors.

In the case of periodic lattices, the spin pairs can be sorted into spin correlation classes. As these pairwise spin correlation classes are defined in accordance with the lattice symmetries and the relative distances between the spin pairs, the coupling constant is the same between any pair within a class. We can thus rewrite the total system energy as a linear combination of pairwise spin correlators ($C_{\alpha\lambda}$) and their associated coupling constants ($J_{\alpha\lambda}$):

$$E_{dip} = \frac{1}{2}\sum_{\alpha}\sum_{j} J_{\alpha j}(\vec{S_\alpha}\cdot\vec{S_j}) = \sum_{\alpha}\sum_{\lambda} J_{\alpha\lambda}\cdot N_{\alpha\lambda}\cdot C_{\alpha\lambda}. \tag{2.15}$$

where λ designates the correlation order and the α-indexed sum is made over all the network spins ($\vec{S_\alpha}$) and the j-indexed sum is performed over all its neighboring spins ($\vec{S_j}$). In the first term, each pair is counted twice and a $1/2$ factor is required to retrieve the system's energy. In the final expression, the spin pairs have been regrouped into their correlation classes and since $C_{\alpha\lambda}$ is the network average for the λ-type correlation, its value needs to be multiplied by the number of correlation pairs ($N_{\alpha\lambda}$) to get the total contribution of this correlation type to the system's energy. Therefore, if the correlations and the coupling constants are known up to a certain order, one can estimate the energy using this method (see Appendix D for more details).

This form also helps us to reshape the point-dipole approximation to the case of tightly-packed magnetic moments with finite sizes. Using micro-magnetic simulations, Rougemaille *et al.*[73] have calculated the coupling constants of the first seven spin correlation types for their particular artificial kagome spin ice realization. They found that, while the micro-magnetic nearest-neighboring coupling ($J^{micro}_{\alpha\beta}$) is significantly higher than the value given by the point-dipole approximation ($J^{dip}_{\alpha\beta}$), this approximation holds well for second order pairs and beyond. Furthermore, the actual coupling between the first-order neighbors can be conveniently written as $J^{micro}_{\alpha\beta} = J_1 + J^{dip}_{\alpha\beta}$, where J_1 is a coupling constant accounting for the deviation. The dipolar part $J^{dip}_{\alpha\beta}$ can be regrouped with the higher order terms, thus retrieving the full expression of the point-dipole approximation Hamiltonian, and by adding the J_1 contributions for all $\alpha\beta$ pairs one can obtain the dipolar spin ice Hamiltonian which describes the interactions between the nano-islands within an artificial spin ice array:

$$H_{DSI} = -J_1 \sum_{<i<j>} \vec{S}_i \cdot \vec{S}_j + D \cdot \sum_{(i<j)} [\frac{\vec{S}_i \cdot \vec{S}_j}{r_{ij}^3} - \frac{3 \cdot (\vec{S}_i \cdot \vec{r}_{ij}) \cdot (\vec{S}_j \cdot \vec{r}_{ij})}{r_{ij}^5}]. \tag{2.16}$$

where the first sum is performed only on the nearest-neighboring pairs, while the second is performed over all pairs, including first-order neighbors. The J_1 correction depends on the shape of the islands, their relative displacement and the spontaneous magnetization of the constituent alloy. In their case, Rougemaille *et al.*[73] found $J_{\alpha\beta}^{micro} \cong 5 \cdot J_{\alpha\beta}^{dip}$, which would yield $J_1 \cong 4 \cdot J_{\alpha\beta}^{dip}$. However, this ratio varies form one artificial network to another and it is generally important to determine its value if experimental data are confronted with the model.

The dipolar spin ice model Hamiltonian can also be brought to a scalar form in the same way as the short-range model Hamiltonian. Using the predefined unit vectors ($\vec{e}_i$) and the spin scalar values (σ_i), we find:

$$H_{DSI} = \frac{J_1}{2} \sum_{<i<j>} \sigma_i \cdot \sigma_j + \frac{D}{r_{nn}^3} \cdot \sum_{(i<j)} \frac{r_{nn}^3}{r_{ij}^3} [(\vec{e}_i \cdot \vec{e}_j) - 3 \cdot (\vec{e}_i \cdot \vec{e}_r) \cdot (\vec{e}_j \cdot \vec{e}_r)] \cdot (\sigma_i \cdot \sigma_j). \tag{2.17}$$

where $D = \frac{\mu_0 \cdot \mu^2}{4\pi}$ is the dipolar constant, r_{nn} is the distance between nearest-neighboring spins and $\vec{e}_r$ is the unit vector of the relative position vector $\vec{r}_{ij}$. This scalar form proves to be very useful for the model's implementation in the Monte Carlo simulation code. Before moving on to the thermodynamic properties of kagome spin ice within this dipolar spin ice model, a few remarks regarding the implementation used throughout this work should be made.

In section 2.2 the thermodynamic behavior of kagome spin ice has been simulated using periodic boundary conditions, which is usually the procedure followed to avoid boundary effects and yield isotropic environment for all spins, like in an infinite lattice scenario. Real lattices though have finite sizes and the spins located at the edges do not have the same coupling environment as the bulk spins. However, if there is only a short-range order, these effects are quickly washed away and a sufficiently large finite lattice can be considered as quasi-infinite. This is actually the case of kagome spin ice with only nearest-neighbor coupling, its ground state presenting a spin liquid behavior. However, introducing long-range interactions is expected to change this, as the system would further correlate and the correlation length is presumed to increase, eventually augmenting the impact of border effects. This can be circumvented by taking periodic boundary conditions, but how far are the interactions now summed up if the network is wrapped around a torus? One way to avoid

making a spin interact with itself redundantly is to take a certain interaction cut-off. In other words, each spin interacts according to the Hamiltonian with all the spins situated in a disk of a predefined cut-off radius. This radius should be taken a large as possible, usually as half the network's size. If the interactions fall off quickly with the relative distance between the spin pairs, very high order pairs are expected to bring minor contributions to the total energy and this approach proves to be a good approximation[17]. This is actually the case here, as the dipolar spin ice Hamiltonian scales with $1/r^3$ and the long-range sum converges rather quickly. This technique will be used through this work when dealing with periodic boundary conditions and dipolar long-range interactions.

It should also be noted that there is a way of simulating a pseudo-infinite lattice. The idea is to make copies of the original lattice and place them around it thus paving the 2D space. The more copies are made, the more the system approaches an infinite lattice case, but the dynamics are performed solely in the original one. Any modification occurring to it is immediately reported to its clones. However, if many images are made, directly summing up the interactions throughout all the copies would be a colossal task. However, this is where the advantage of this technique lies. Although copying the original lattice leads to a fake infinite network, the periodicity can be exploited by summing up the energy contribution in Fourier space. The Ewald summation technique[89] employs this procedure, summing up short-range contributions in direct space and the ones between the original lattice and its copies in the reciprocal space. Also, the Ewald scheme proposes a way of speeding up the convergence of the summations, proving to be a more accurate and very useful tool for the simulation of systems with distance-decaying interactions like the Coulomb one.

The thermodynamic properties of kagome spin ice network within the dipolar model have been studied theoretically and numerically by Möller and Moessner[7] and Chern *et al.*[8] using summation of copies. Although this work doesn't employ Ewald sums, the results which will be further presented here are in very good agreement with these references and particularly with the results reported by Chern *et al.*[8][18].

2.4.2 Critical Slowing Down and Loop Updates

Monte Carlo simulations have been performed using the dipolar spin ice Hamiltonian on a kagome spin ice network with $(12 \times 12 \times 3)$ spins and periodic boundary conditions. The deviations from the point-dipole approximation are accounted for by taking $J_1/J_{\alpha\beta}^{dip} = 4$ and

[17] In fact, the cut-off procedure can be considered as a new model itself, with its own approximation for the Hamiltonian that has been cut out of the infinite summation.

[18] Möller and Moessner use a bar model, taking into account the length of the magnetic moments, while Chern *et al.* rely on the dipolar approximation, just like in this work.

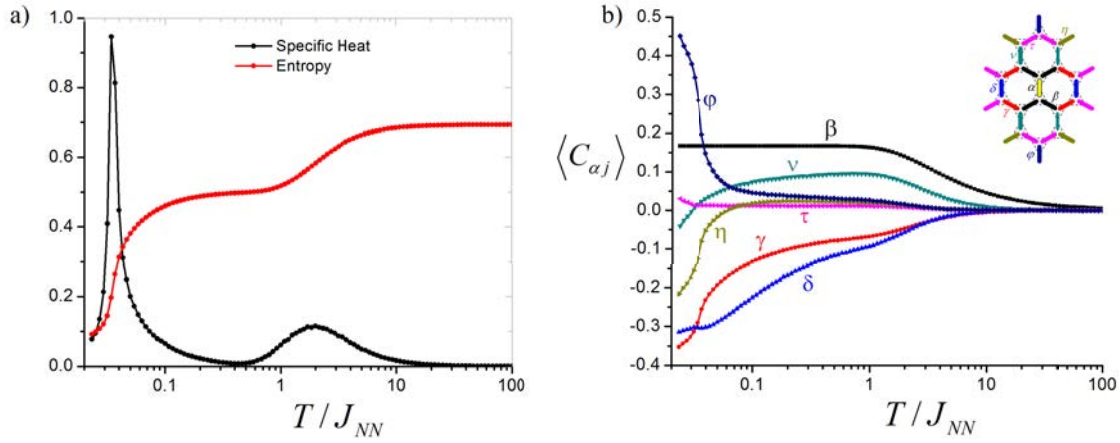

Figure 2.15 - (a) The specific heat and the entropy of kagome spin ice with long-range interaction spins. The presence of the a second peak of the specific heat signals a phase transitio, but single spin-flip dynamics are incapable of exploring the low-energy manifold efficiently. The possibility for further evolution is underlined by both the entropy's non-zero value (which doesn't present a plateau) and (b) the first seven kagome spin correlators. The inset of (b) gives their definition (after Chioar *et al.*[11]).

the cut-off radius is set to five times the lattice parameter. A single spin-flip dynamics is initially implemented following the Metropolis algorithm.

The temperature-dependencies of the specific heat and the entropy are given in Figure 2.15.a, both being normalized to the number of spins. As expected, the behavior is very similar to that of a short-range kagome spin ice (see Figure 2.8) for temperatures that are higher or of the same order with the nearest-neighboring coupling constant ($J_{NN} = J_{\alpha\beta}$). The system thus passes from a paramagnetic regime into the spin ice manifold characterized by a entropy value of about $0.501 k_B$. However, as the temperature further decreases, higher order interactions start to play their part and all spin correlations beyond first order continue to evolve, most of them increasing in absolute value (see Figure 2.15.b).

The specific heat presents a sharp peak at $T/J_{\alpha\beta} \cong 0.034$, which could signal the presence of a phase transition. As a consequence, the entropy also drops rather quickly to a value of about $0.092 k_B$. However, the simulations stop at this point and the absence of an entropy plateau suggests that the system hasn't actually reached a new degenerated ground state manifold. This is also emphasized by the spin correlations. With the exception of $C_{\alpha\beta}$, all correlations present a strict monotonic behavior at this stage, indicating the tendency of the spin network to further order itself, whereas a macroscopically degenerated manifold would present plateaus for the network averages of the spin correlations, just like in the short-range case. However, an inspection of the spin acceptance ratio (see Figure 2.16) reveals the reason for this sudden stop: spin-flips are almost always rejected in this low-temperature regime and

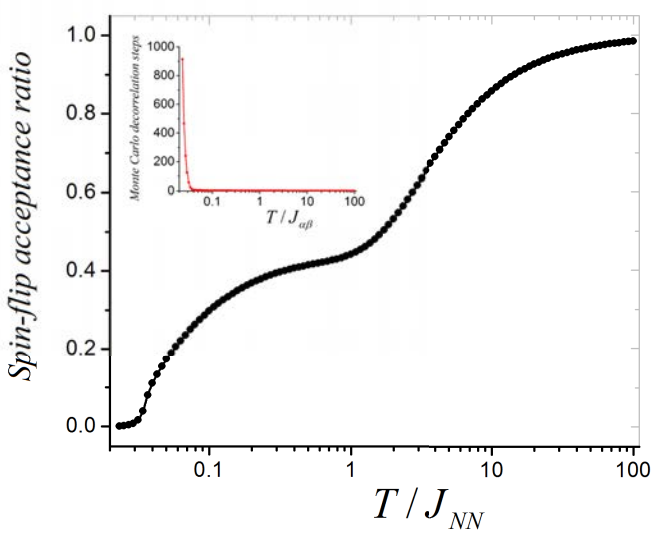

Figure 2.16 - The standard single spin-flip approach has proven to work well for short-range kagome spin ice, but it eventually slows down if dipolar interactions are included. At low temperatures, almost 1 out of 1000 tryouts are accepted, requiring an increase in the Monte Carlo decorrelation steps (inset).

the simulation is aborted if the inverse spin acceptance ratio passes over a established limit, which is set to 1000 Monte Carlo decorelation steps. The single spin-flip dynamics suffers from a *critical slowing down* effect, usually occurring near a phase transition point. The non-vanishing value of the entropy suggests that the system has not ordered yet and further evolution is to be expected. However, exploring further these low-temperature manifolds using this dynamics would result in a drastic increase of the simulation runtime and a growing difficulty for insuring proper thermalization and ergodicity. Finding a new spin-dynamics that can enhance the exploration of these manifolds while preserving ergodicity is thus necessary for further investigation.

There is however a remarkable feature that can be found in the behavior of the nearest-neighbor charge correlator (see Figure 2.17.a). As expected, the plot follows the short-range one (see Figure 2.13) all the way to the spin ice manifold. However, it does not present a plateau at $-1/9$, but it gradually drops back to -1. This indicates that nearest-neighboring charges get more and more correlated as the system cools down, preferring an antiferromagnetic alignment. The lowest network average is very close to -1, suggesting that the charges are forming up into a crystal of alternating ± 1 values. Indeed, a snapshot of the system reveals a perfect charge order (see Figure 2.17.b). This is an exciting feature, particularly because the magnetic charge does not explicitly appear in the system Hamiltonian[73]. In fact, the formation of a charge crystal during the accommodation of dipolar long range interactions between spins at low temperatures is an exotic and emerging order and the

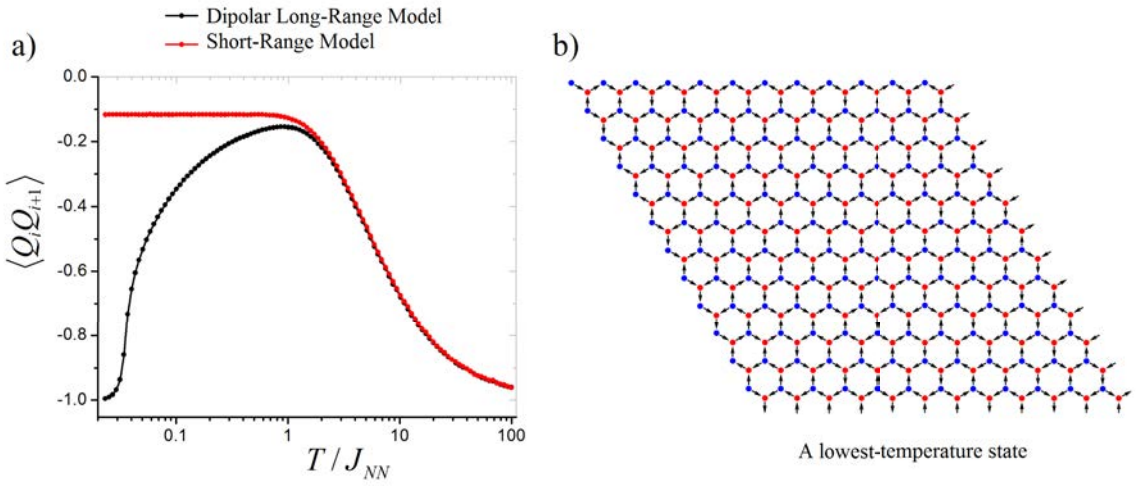

Figure 2.17 - (a) The -1 value of the charge correlator at the lowest temperatures signals the presence of an underlying charge order. Indeed, a snapshot of the spin and charge configurations reveals a perfect charge crystal embedded in a partially disordered spin lattice displaying many short closed-loop configurations (b). Spin flips that might destroy this emerging charge order will be filtered out by the detailed balance condition, leading to the critical slowing down of this dynamics.

staggered magnetic charge proves to be the order parameter of the phase transition signaled by the peak of the specific heat[7, 8].

The presence of this charge order reveals why the single spin-flip dynamics suffers form a critical slowing down effect. Once the spin ice manifold is reached, any spin-flip that would result in the creation of a forbidden state (± 3 charge value) is immediately rejected by the detailed balance condition. While this preserves the ice rules everywhere, it can easily change the state of a vertex charge from $+1$ to -1 or vice-versa. Since the system clearly manifests a desire for charge ordering at low temperatures, spin-flips that would change an already-established local antiferromagnetic charge arrangement become less and less accepted and finally results in a critical slowing down of the single spin-flip dynamics. Clearly, the spin configuration needs to be modified using a spin-cluster dynamics that does not alter this emerging order.

Notice that a vertex charge remains unchanged if an in-pointing spin and an out-pointing spin are flipped simultaneously. This is actually straightforward if we recall the definition of the vertex charge as a sum of the spin scalar values: $Q_i = \pm \sum_{j=1}^{3} \sigma_j$. A pair of spins pointing head-to-tail corresponds to a pair of $+1$ and -1 σ-scalar values. Flipping the spins will therefore not change the value of the charge. However, such a flip changes the state of the neighboring charges, which could have already been in a favorable configuration (opposite values with respected to the initial one). Nevertheless, the same procedure can be applied for them too. In other words, for each neighboring charge, one of the not-yet-flipped spins

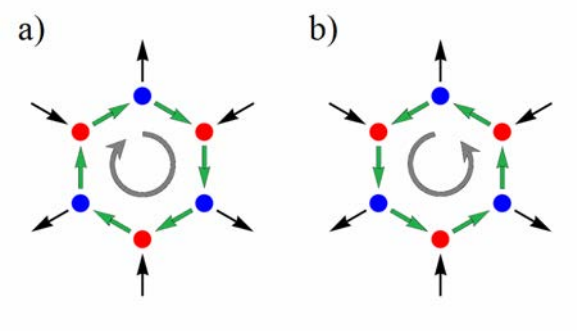

Figure 2.18 - The magnetic charge crystal cannot be altered if a closed-loop of head-to-tail pointing spins is flipped. In this example, the right-hand chirality loop (a) can turn into a left-hand chirality one (b) without changing the charge values.

that is either head-to-head or tail-to-tail with the already-flipped one needs to be flipped to preserve the initial charge value. The changes are further propagated throughout the lattice, but they can be mutually canceled out if the two outgoing spin chains rejoin at another vertex. By tracing back the flipped spins, we realize that they form a closed spin-loop, similar to the ones that have been previously presented (see Figure 2.7). Therefore, flipping a closed spin-loop defined by the algorithm presented in section 2.2.2 will not change the value of the vertex charges that it crosses (see Figure 2.18). Also, we have seen that this dynamics is an ideal way of exploring the spin ice manifold and a loop can always be generated from any chosen spin. These features suggest that this dynamics might be the key to further explore the low-temperature manifolds for which the single spin-flip dynamics critically slows down[19].

2.4.3 Spin Order in Two Steps

Additional Monte Carlo simulations have been performed using the same parameter values as presented in the previous section, but loop updates have also been included through a hybrid-flip procedure as described at the end of section 2.2.2. Since a loop-flip cannot change the vertex charges, using only this dynamics would restrict each vertex to its existing charge value throughout the entire simulation. Therefore, single spin-flips have to be included as well to ensure full ergodicity.

The specific heat and entropy plots are reproduced in Figure 2.19.a). The specific heat presents three distinctive peaks, each one marking the passage from one regime to another.

[19] As mentioned in Appendix A, such loop dynamics have been priorly used to investigate the low-temperature regime of Ising pyrochlore spin ices like the $Ho_2Ti_2O_7$ and $Dy_2Ti_2O_7$. Monte Carlo simulations with such loop updates completely recover the residual entropy of spin ice[29, 33]. However, experimentally accessing this predicted ordered phase has proven to be a very challenging task and the short-range model still appears to capture the low-temperature physics of these pyrochlores[28]. A recent paper[34] has nevertheless reported experimental data that signals the first stages for the development of long range order for $Dy_2Ti_2O_7$.

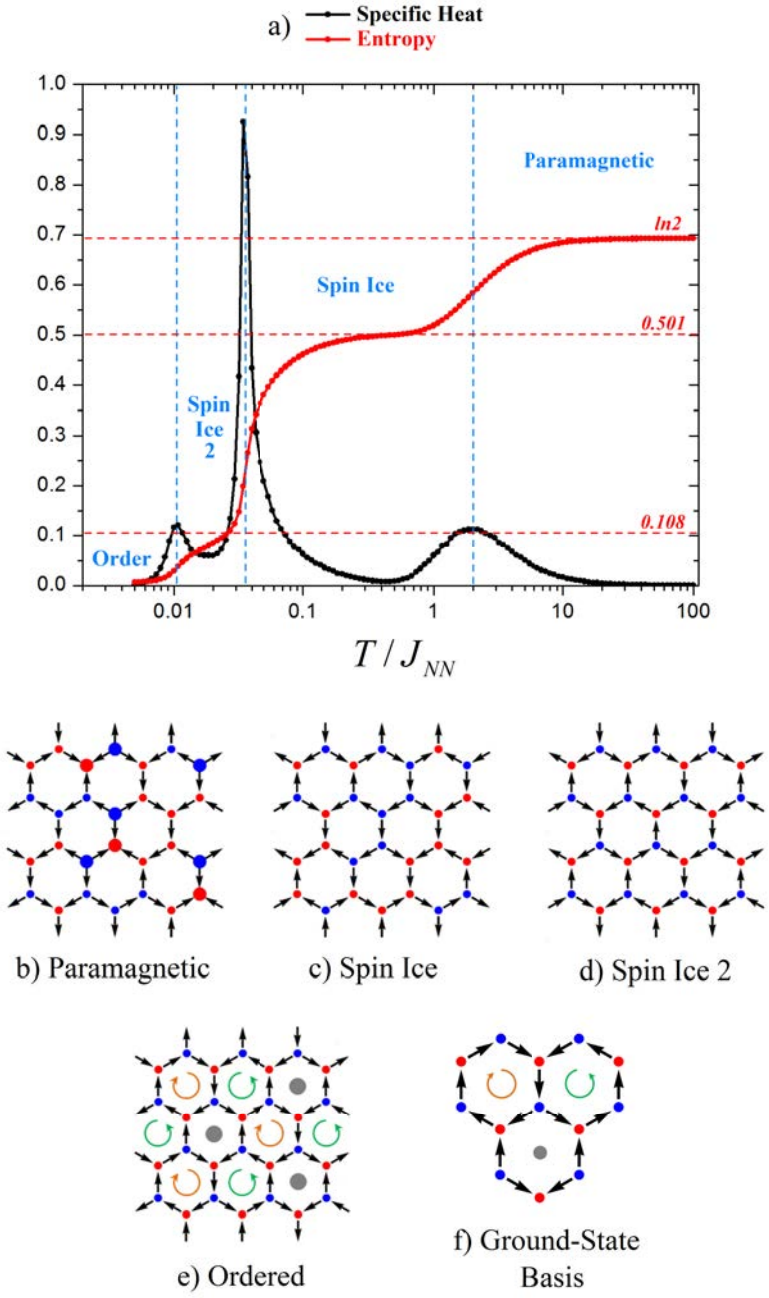

Figure 2.19 - (a) The temperature-dependencies of the specific heat and the entropy for kagome spin ice assuming a dipolar spin ice model. The introduction of long-range interactions eventually leads to a total recovery of the residual entropy of short-range kagome spin ice, but this recovery is done in two steps, passing by a charge order state first and then reaching the fully ordered one. These numerical results are in very good agreement with what has already been reported in the literature. [7, 8].

The first peak distinguishes the paramagnetic state form the spin ice manifold. The second peak is situated[20] at $T/J_{\alpha\beta} \approx 0.034$ and separates the spin ice state with disordered charges from the so-called spin ice 2 state in which the charges have crystallized, but the spin network still remains partially disordered. The last peak marks the passage from a spin ice 2 regime to the final ground state in which both the spins and magnetic charges are fully ordered. Typical snapshots for each regime are given in Figure 2.19.b-.e along with one of the possible 6 basis of the ground state configuration. Furthermore, the entropy gradually drops towards zero, passing through the $0.501k_B$ plateau of the spin ice phase and the $0.108k_B$ value specific to the spin ice 2 regime. This entropy value of $0.108k_B$ has also been explained by Möller and Moessner[7] through an analogy with the triangular lattice of antiferromagnetically-coupled Ising spins, the residual entropy of which was exactly calculated by Wannier[20] and is equal to $s_{\Delta}^{AFM} = 0.338314$. The entropy of the spin ice II phase is thus $s_{SI2} = s_{\Delta}^{AFM}/3 \cong 0.108$.

Reaching the final ground is possible thanks to the efficiency of the loop dynamics. The acceptance ratios of both single spin-flips and the loop-flips are plotted in Figure 2.20. As expected, single spin-flips present the same behavior as in Figure 2.16.a, but once the system is deep within the spin ice 2 manifold, for $T/J_{\alpha\beta} \cong 0.012$, they completely freeze and the entire exploration of the energetic landscape is undertaken solely by the loop-flips. Notice that, as long as the ice rules are unanimously obeyed, the loop generation ratio is always equal to 1, but the acceptance slows down and only 1 out of 3 loop-flips are accepted in the spin ice 2 phase[21]. In fact, within the dipolar spin ice model, loop-flips no longer preserve the system energy as they did in the case of the short-range model, but can increase and decrease it depending on their dipolar environment. They are thus subjected to the detailed balance condition and sensitive to the thermal input. It is therefore expected to have an increasing filtering of loop movements as the temperature decreases. Although this dynamics suffers from a critical slowing down effect too, it manages to help the system recover all its spin degrees of freedom and drive it into its non-degenerate ground state manifold.

The magnetic susceptibility is also severely affected by the introduction of dipolar long-range interactions (see Figure 2.20.b). The short-range behavior persists all the way to the

[20] It should be noted that this is a rough estimate taken directly from the simulated data, without any finite size scaling. Chern *et al.* have characterized this phase transition and found that $T_C/D \approx 0.267$, where D is the dipolar constant. By renormalizing it to the coupling between nearest neighbors $J_{\alpha\beta}$ we obtain $T_c \approx 0.03 J_{\alpha\beta}$, in relatively good agreement with the previous rough estimation. Furthermore, since the dipolar spin ice Hamiltonian is implemented here by using a cut-off radius, small variations from the pseudo-infinite case of the transition temperatures are to be expected.

[21] Interestingly, Möller and Moessner[7] report that the loop acceptance ratio stays close to unity while the system is in the spin ice 2 regime, thus describing it as a loop gas. This appears to be in sharp contrast with these results. However, it should be noted that their approach essentially differs from the one presented here, since they are performing multipole expansions for magnetic needles with lengths almost equal to the lattice parameter while the current results assume point-like magnetic moments.

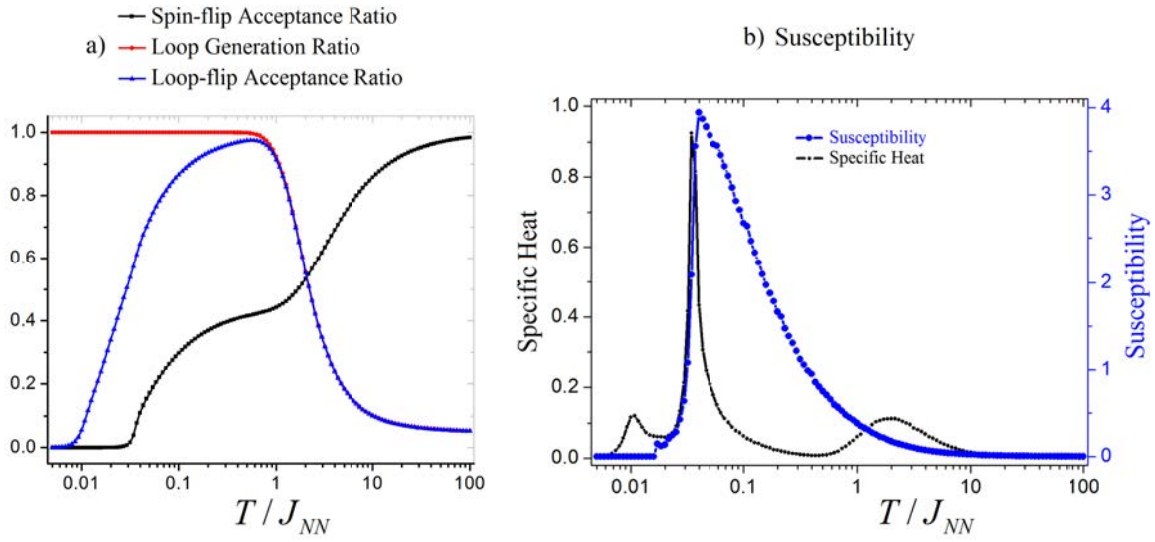

Figure 2.20 - (a) As previously seen, the spin-flip acceptance ratio drops to zero as the system enters the spin ice 2 manifold (black line). The task of exploring the phase space is then undertaken by the loop-flips (blue line). However, they too are gradually filtered out as the system searches for the final spin-ordered state. As before, their generation ratio (red line) always remains at 1 as long as the ice rules are unanimously obeyed. (b) The magnetic susceptibility plot (blue line) resembles the short-range one down to the transition towards the spin ice 2 state, where the system is brought out of the cooperative paramagnetic regime due to the constrains imposed by the charge order and the magnetization fluctuations are finally suppressed, yielding a 0 susceptibility value. To ease the identification of the corresponding temperature regime, the specific heat plot (black line) is reported as well.

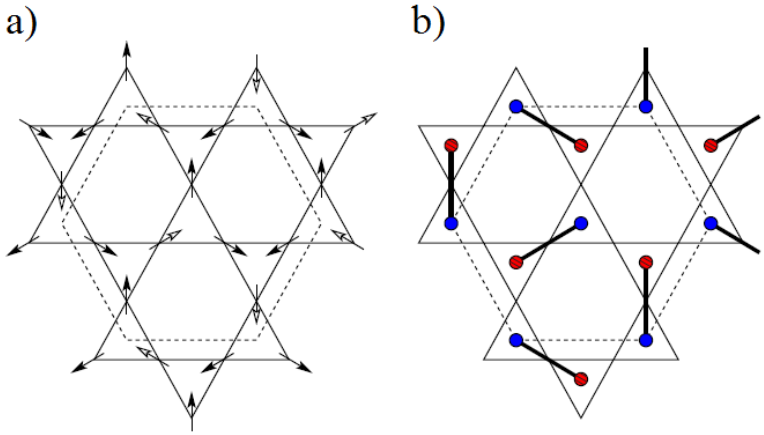

Figure 2.21 - (a) The minority spin picture and (b) the dimer covering of the ground state configuration of dipolar kagome spin ice. Any spin ice 2 state can be depicted by a dimer covering, and the maximization of dimer pairs separated by a $\sqrt{3} \times l$ distance eventually leads to the ground state. After Chern *et al.*[8].

spin ice-spin ice 2 transition, and both pure-paramagnetic and cooperative-paramagnetic regimes can still be found. However, single spin-flips are ruled out at the first critical point and magnetization fluctuations can then be realized only through loop-flips. A non-stretching loop (see Figure 2.7) does not present a net magnetic moment, hence it cannot change the total magnetization. On the other hand, winding loops that stretch around the entire network do carry a net magnetic moment, but they eventually disappear while the system evolves towards its spin ordered state. The magnetization fluctuations are therefore suppressed and the susceptibility vanishes when the system passes towards the final ordered state.

The existence of a intermediate spin ice 2 state is quite remarkable and the tendency towards charge order can be understood by using the dumbbell picture proposed by Castelnovo *et al.*[35] for Ising pyrochlore spin ices. By replacing all spins with their corresponding charges and then summing them up at the vertex points, we obtain a hexagonal network of interacting magnetic charges (Q_i). This magnetic Coulombian interaction can be described by the following Hamiltonian[35]:

$$H_Q = \frac{K}{2}\sum_i Q_i^2 + \frac{\mu_0}{4\pi}\sum_{(i<j)} \frac{Q_i \cdot Q_j}{r_{ij}}. \tag{2.18}$$

where the first sum is introduced to accurately account for the nearest-neighboring interaction between the original spins and plays the role of a capacitive term. It also emphasizes the need for unitary charges in case of energy minimization, as a ± 3 charge value would significantly increase the system energy. Minimizing the first term therefore yields the spin ice manifold. The second term contribution is minimized if nearest-neighboring charges have opposite values and since the hexagonal network is bipartite, this is possible without any additional frustration effects, leading to the spin ice 2 phase. However, further evolution is no longer possible within this dumbbell approximation and the underlying spin network described by such an approach would remain macroscopically degenerated in the spin ice 2 phase. The passage towards the final ordered phase is thus assured by higher order spin correlations. Nevertheless, this charge description directly suggests the tendency towards charge ordering, with the staggered magnetic charge playing the role of the order parameter. Given its $\mathbb{Z}_2$ symmetry, the phase transition is expected to be of the Ising class and this was indeed confirmed by Chern *et al.*[8].

The long-range spin ordered ground state is a triangular lattice with a basis made up of three kagome triangles (see Figure 2.19.f). There are six possible ground state configurations, each one related to the other by lattice translations and time-reversal symmetry. The presence of the two loop chiralities within the ground state basis highlights the system's preference for

closed-loop configurations and the importance of loop updates. Chern *et al.*[8] present an interesting dimer covering for this ground state. As soon as the spin ice manifold is reached, there is a minority spin per triangle, given the "two-in/one-out" or "one-in/two-out" kagome ice rules. However, if the charges crystallize, the minority spin plays this role in two adjacent triangles (see Figure 2.21.a). In addition, it can be regarded as a superposition between a $+2\vec{\mu}$ magnetic moment pointing its way and a opposite $-\vec{\mu}$ magnetic moment. The $-\vec{\mu}$ moment rejoins the majority spins to create an "all-in"-"all-out" spin covering of the entire lattice, but on top of this configuration lie the $+2\vec{\mu}$ moments, which can be seen as a dimer covering of a spin ice 2 state. The energy of the system can thus be written as the sum of a constant energy related to the frozen "all-in/all-out" state and the energy arising from the interaction between these dimers. As it turns out, the energy is minimized if the dimers are separated by $\sqrt{3} \times l$, where l is the lattice constant (see Figure 2.21.b)[22]. Finally, they used this dimer covering to explain the nature of the final transition and they report that, if the system size is relatively small, the transition is a Kosterlitz-Thouless one, while for large sizes the transition is found to be compatible with the three-state Potts model class.

2.4.4 The Spin and Charge Correlations

The evolution of the pairwise spin correlators is given in Figure 2.22. These results are in good agreement with the literature [11, 73]. Interestingly, two correlators, $C_{\alpha\nu}$ and $C_{\alpha\eta}$, do not present a unique monotonous behavior and even pass from positive values, specific to the spin ice manifold, to negative ones at lower temperatures.

The charge correlator is plotted in Figure 2.23.a along with its evolution in the short-range model. As soon as the spin ice 2 manifold is reached, the charge correlation is locked at -1, but the spin correlators still continue to evolve, with the exception of $C_{\alpha\beta}$, which has already been fixed at $1/6$ since the spin ice phase was reached. If we now return to the relation between the charge correlator and the first three pairwise spin correlators (2.13), these two conditions further constrain the evolution of the $C_{\alpha\gamma}$ and $C_{\alpha\nu}$ correlations (see Figure 2.23.b). In fact, they mutually compensate each other so that $3C_{\alpha\nu} - 6C_{\alpha\gamma} = 2$. Although constrained, their evolutions along with those of higher order correlators will determine the system energy and finally select the spin-ordered ground state.

In fact, the dipolar spin ice Hamiltonian can be refashioned to express these three passages by conveniently arranging the spin correlators and their coupling constants. Relation 2.13

[22]This picture bears a striking resemblance to the one describing the spin fragmentation procedure proposed by Brooks-Bartlett *et al.*[9]. However, the current description was introduced to explain the nature of the last phase transition and does not assume a fragmentation of each spin. The latter may be invoked to the same ends, but it is in fact richer as it quantitatively accounts for the underlying charge crystal and the spin structure factor map.

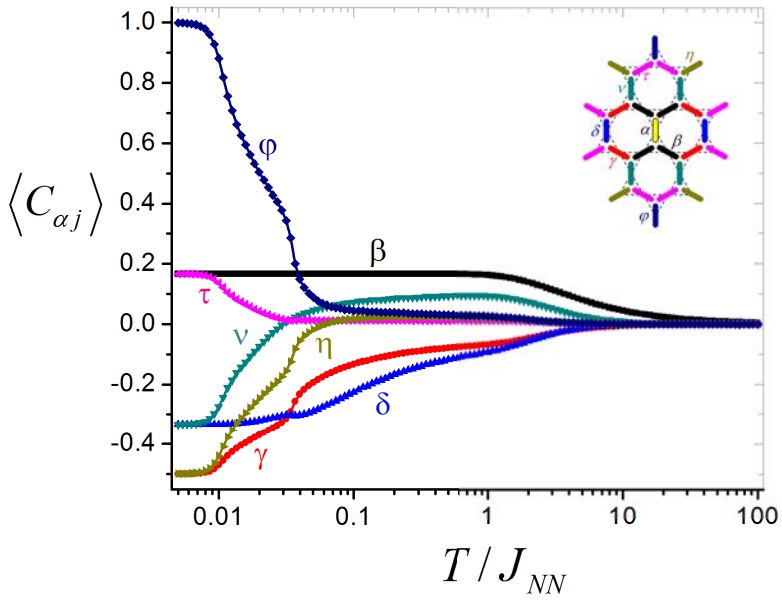

Figure 2.22 - The evolution of the first seven spin correlators averaged on the network scale for a dipolar kagome spin ice. Some of the correlators change drastically their behavior compared to the short-range case, a fact that can be exploited to differentiate between a short-range and a dipolar regime for artificial spin ices. The inset gives their definitions, after Chioar *et al.*[11].

can be also exploited to make the charges appear too and the Hamiltonian can be brought to the following form:

$$H_{DSI} = \frac{\overline{J_{\alpha\beta}}}{2} \sum_{<i,j>} \sigma_i \cdot \sigma_j + \frac{\overline{J_{QQ}}}{2} \sum_{<u,v>} Q_u \cdot Q_v + O(1/r^3)_{r \geq 2r_{nn}}. \tag{2.19}$$

For details on the deduction and the values of these constants, see Appendix D. The first term is like a short-range model Hamiltonian and is minimized if the system is brought into the spin ice regime. The second term is a short-range Hamiltonian for the magnetic charges and it is minimized if the charges arrange themselves into an antiferromagnetic crystal. So far, this looks very similar to the Hamiltonian of the dumbbell approximation 2.18. The remaining contributions however will eventually select the final ground state spin order and come from spin pairs that are separated by a distance equal or greater than the kagome lattice parameter. The short-range nature of the two sums is motivating for simulations and could quickly capture some features of the system's overall behavior. This approach has been made by Zhang *et al.*[6] to describe the formation of charge crystallites. However, cutting off the last terms severely modifies the system behavior, no longer accessing the ground state (see Appendix D for more details on the matter).

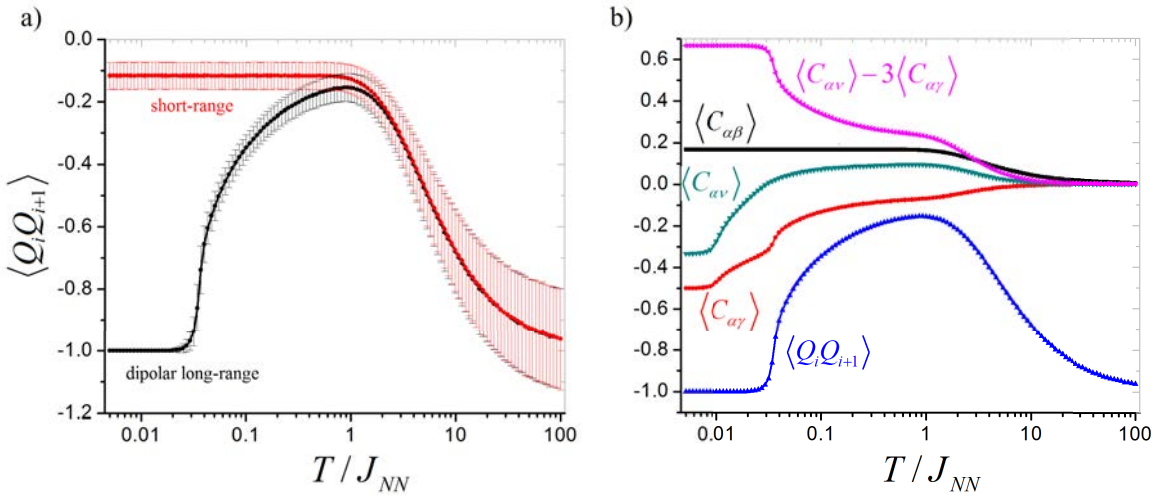

Figure 2.23 - (a) The temperature plot of the network average of the nearest-neighbor charge correlator for the kagome spin ice with long-range spin interactions. The bars correspond to the standard deviations of the set of network averages for a lattice of $(12 \times 12 \times 3)$ spins and is related to the intrinsic thermal fluctuations due to the system's finite size. Notice the mapping between the short (red line) and long-range (black line) plots down to the spin ice manifold. (b) Once this correlator reaches the -1 value of the charge ordered states, the evolutions of the $C_{\alpha\gamma}$ and $C_{\alpha v}$ spin correlators are constrained, as emphasized by the magenta-coloured plot which present a plateau at $2/3$. They nevertheless contribute to the selection of the ground state.

There is an important aspect to be emphasized here. Although the spin ice 2 state is characterized by a magnetic charge crystal, such a charge order can also be obtained if the spin network is saturated by the application of an external magnetic field. Is this state also part of the spin ice 2 manifold? The charge picture alone cannot discriminate between these two, and one needs to turn towards the spin correlations. For instance, a saturated state would have $C_{\alpha v} = 1$, whereas its spin ice 2 manifold values are negative. This sharp difference clearly points out that a saturated state is not representative of the thermodynamic low-energy spin ice 2 state. Furthermore, the spin correlators can also be used to discriminate between the spin ice 2 state and the ordered state since both require a charge crystal.

Finally, it should be mentioned that a rather different picture has been recently proposed[9] that describes the spin ice 2 phase as a fragmented spin network with a superposition between a ordered spin lattice, related to the magnetic charge crystal, and a disordered one that bears the signatures of a Coulomb phase[90], characterized by a divergence-free field that does not display any long-range order. This picture already encompasses the charge crystal description, but also highlights the nature of the fluctuating spin component which turns out to be an algebric spin liquid. This spin fragmentation has also been proposed for spin ice pyrochlores as well, but it requires the existence of a charged background, i.e. the presence of a magnetic charge at each vertex site. Since kagome spin ice presents only charged vertices by definition,

the signatures of this spin fragmentation description might be more easily highlighted in such a system rather than in the condensed matter spin ice compounds.

2.5 Mapping Demagnetized Artificial Kagome Spin Ice on the Dipolar Spin Ice Model

Until recently, artificial spin ice systems were insensitive to thermal fluctuations. Althought their athermal nature has its advantages, the price to pay for it seems to be quite high as the potential of exploiting such devices as toy-spin models in a heat bath seems to be fading away. The solution proposed by Wang *et al.*[1] was to apply a slowly-decaying ac demagnetization protocol in the hope of retrieving relevant thermodynamic states. The output configurations are then compared to snapshots of at-equilibrium Monte Carlo simulations[1, 46, 73]. However, the comparison requires that similar quantities be confronted and this usually implies assuming a certain interaction model. In fact, there are generally two main choices to be made, both for the experiment and for the simulations: the dynamics and the interaction model (see Figure 2.24).

Experimentally, the output of the demagnetization protocol depends on the field step size (ΔH), but cannot access the ground state manifold, even for $\Delta H \to 0$, as reported by Ke *et al.*[83] for artificial square ice networks. Budrikis *et al.*[85, 86][92] have also confirmed the importance of the switching field distribution and that of disorder in the inter-island coupling for a rotating constant-magnitude field demagnetization protocol. Since spin-flips occur for applied fields comparable to the switching fields of the nano-islands, the distribution of the latter (generally characterized by its standard deviation, σ_{SF}) is expected to play a significant role in choosing the pathways during ac demagnetization. There are, of course, other quantities that characterize the demagnetization protocol, but these two parameters play a major role in determining the final magnetic configuration.

Numerically, the general choice inclines towards Monte Carlo simulations, possibly due to the initial desire to replicate the predicted thermodynamic behavior of spin models. Therefore, sequential dynamics results are confronted with at-equilibrium thermodynamic behavior[23]. To explore the thermodynamic properties, the system is placed in a heat bath at a fixed temperature T. To proceed further, one must first define an interaction model between the constituting spins. There are many possibilities here, but the option should be made in accordance with the nature of the interactions within the experimental system. Two main

[23]There have been several other approaches, the most notably being the numerical demagnetization procedures proposed by Budrikis *et al.*[92] and the entropy maximization techniques implemented by Nisoli *et al.*[54, 55] and Morgan *et al.*[91].

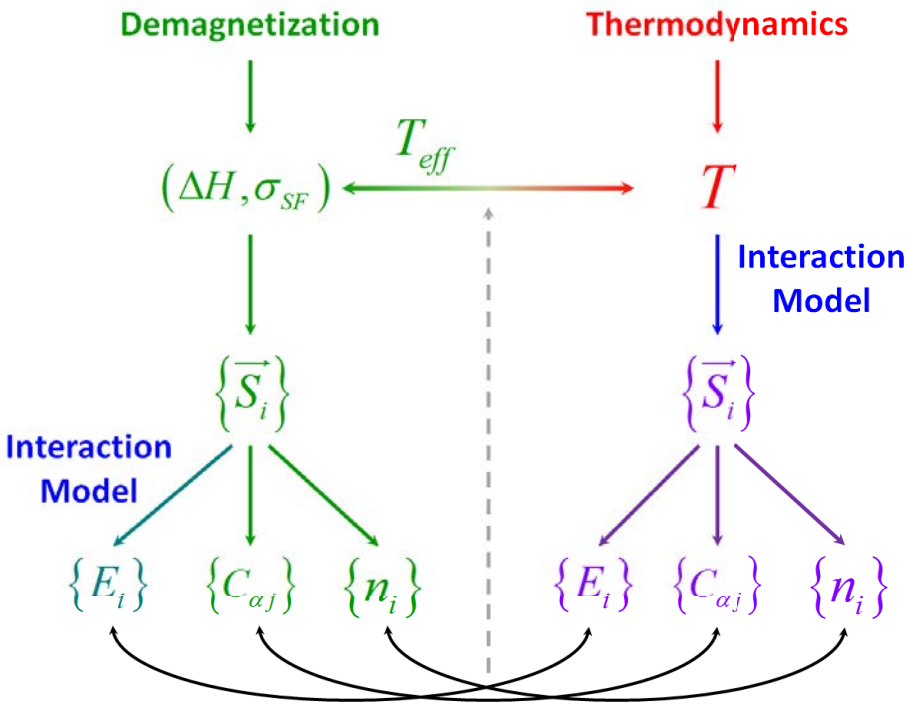

Figure 2.24 - Artificial spin ices that lack thermal fluctuations are generally subjected to a demagnetization protocol[3]. Within a narrow applied field window, spin-flips occur in order to accommodate the inter-island interactions. The final network configuration is frozen and can be characterized by different physical quantities such as the energy, the spin and charge correlations and the vertex population ratios. Note that some of them require the choice of a interaction model while others do not. These quantities can then be compared to their counterparts arising from the behavior of a system placed in a heat-bath at a fixed temperature T. The temperature dependence can depend heavily upon the chosen interaction model/spin model and there has been a certain debate surrounding the use of a short-range or a dipolar long-range Hamiltonian to better describe the output of a demagnetization process[1, 13, 14, 46, 72, 73]. Although the two dynamics are essentially very different, they sometimes yield similar results and the concept of an effective thermodynamics has been proposed and discussed mainly for the square ice network using the vertex population ratios[54, 55, 91]. However, the effective thermodynamics of artificial kagome networks remains mostly unexplored.

models have been used so far to describe artificial kagome spin ices: the short-range model and the dipolar long-range model. They are both based on the fact that the experimental nano-islands are coupled via their stray fields, but the short-range model assumes that only nearest-neighbor couplings are relevant. The temperature evolution of the different thermodynamic quantities is then driven by the strength of the inter-spin interactions relative to the thermal bath.

Typical quantities that can be used to bridge the two approaches are the energy [44, 45, 73], the spin or charge correlations [1, 13, 14, 46, 72, 73, 83] and the vertex-type ratios [1, 49, 54, 55, 86, 93]. Although the computation of the experimental spin and charge correlations does not require the choice of a certain interaction model, their Monte Carlo values generally depend upon the choice of the model. Since we are stuck with demagnetization for the moment when dealing with athermal artificial networks, the latter statement raises the question of which of the two basic models presented so far better describes the output of a demagnetization procedure applied to artificial kagome spin systems[24].

This is exactly the point addressed by Qi *et al.*[46] when confronting their experimental spin correlations with their ground-state counterparts of the short-range spin ice model (see Section 2.3). They notice that the matching is rather poor for higher order correlators (note the differences in Table 2.1 between the experimental values of $C_{\alpha\gamma}$, $C_{\alpha\nu}$ and $C_{\alpha\delta}$ and the Wills's ice values for the ground state). For example, the exprimental value of $C_{\alpha\nu}$ is located at almost $C_{\alpha\nu}^{GS} + 10 \cdot \sigma_{\nu}^{GS}$, making it a very unlikely event within this model. Similar features can also be seen in the data provided by Li *et al.*[72]. Note that, in this case, the islands are no longer connected at the vertex points. However, the network averages they provide are computed over about 3000 islands and the associated standard deviations are higher than in the case of Qi *et al.*[46], making the short-range model appear to be a good candidate for capturing the essential characteristics of these demagnetized artificial arrays due to finite-size effects.

The dipolar model presented in the previous section behaves similarly to the short-range one down to the spin ice manifold, but the two models part ways at this point. Can the dipolar model better characterize the frozen state of demagnetized artificial spin ices than the short-range one does?

To answer this question, Rougemaille *et al.*[73] have ac demagnetized several artificial kagome spin ice networks containing 342 disconnected islands and compared the resulting

[24]Starting from these two models, several other models can be developed that include randomness in inter-island couplings, network anisotropies that strengthen some interactions with respect to others etc. Here we are considering only the comparison of the experimental data with the ideal case of a perfect network without any anisotropies and randomness. However, including such effects in the simulations may prove to be more realistic.

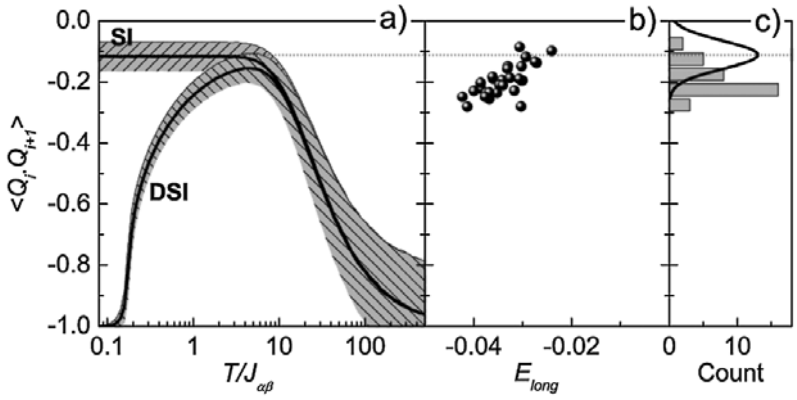

Figure 2.25 - (a) The temperature dependencies of the nearest-neighbor charge correlator within the short-range and the dipolar long-range models as reported by Rougemaille *et al.*[73]. Since the size of the experimental network is rather small, the standard deviations associated to the set of network averages are significantly higher. However, the experimental values (b) seem to better agree with the behavior predicted by the long-range model, clearly deviating from the short-range plateau. The histogram of their 34 experimental values (c) emphasizes this biased deviation and the long-range model appears to better support these experimental findings. After Rougemaille *et al.*[73].

network averages of the correlators to the ones given by Monte Carlo simulations assuming both a short-range and a long-range model. Their conclusion is that dipolar long-range interaction terms need to be included when describing the output of a demagnetization protocol.

They observe severe deviations of certain spin correlators from the short-range ground state manifold, particularly for $C_{\alpha\gamma}$ and $C_{\alpha\nu}$. Nevertheless, the matching appears to be overall improved when considering long-range terms, and this aspect is highlighted even better by the charge correlator (see Figure 2.25). The experimental charge correlation values seem to match those of a kagome system placed in a heat-bath with a temperature corresponding to the entrance into the spin ice manifold. Both short and long-range models could normally be invoked to describe such a regime. However, some experimental values are close to -0.3, which is way beyond the reach of the standard deviation of the short-range spin ice charge correlation distribution for this network size. Just as for the spin correlations, the charge correlators are better described by a long-range model, which accounts for such values if the simulated system starts down the path towards the magnetic charge crystal phase. A similar result has also been confirmed by Yi Qi in his PhD thesis[94]. He reports a charge correlation value of -0.3079 and explains the tendency towards charge ordering using the dumbbell picture Hamiltonian (see equation 2.18). These charge correlators along with the deviations of certain spin correlators seem to point out that long range interactions are indeed at play during the demagnetization protocol and, if the experimental data points are compared

to Monte Carlo averages, long-range dipolar interactions should not be ignored. This is, in fact, the conclusion of the study of Rougemaille *et al.*[73]: "As soon as the system enters the spin ice manifold, the kagome dipolar spin ice model captures the observed physics, while the short range kagome spin ice model fails".

The fact that Monte Carlo simulations based on the dipolar long-range model capture the essential features of demagnetized artificial kagome networks is quite remarkable, given the different natures of the two dynamics. However, although demagnetization manages to make the first steps towards the magnetic charge crystal phase, it seems to be limited to reaching the spin ice manifold. In fact, the best correlation values that one can achieve via demagnetization are characteristic to a simulated system with a temperature $T/J_{\alpha\beta} \sim 1$, which is still far from the exotic spin ice 2 phase and the spin ordered phase. Recall that even a system that explores ergodically its phase space through single spin-flips has difficulty in accessing the spin ice 2 phase. Since demagnetization is a selective sequence of single spin-flips that can only reduce the system energy, it is rather expected that such a protocol cannot yield a charge crystal. Therefore, to further explore the intriguing properties of artificial dipolar kagome arrays, a different experimental approach has to be employed. Recently, new techniques have been proposed[4–6, 52], in which artificial spin ices are rendered thermally-active. These can potentially surpass the experimental limits of ac demagnetization and hopefully reach lower energy manifolds, particularly the charge ordered state. These aspects will be the subject of the next section.

2.6 Artificial Kagome Spin Ice - The Quest for the Magnetic Charge Crystal

2.6.1 Thermally-Active Artificial Spin Ices

In a short retrospective, the playground of artificial spin ices, as established by Wang *et al.*[1], seems almost limitless, given that a wide range of two-dimensional spin models can be engineered via lithography techniques and can then be thoroughly characterized to achieve an almost exhaustive knowledge of the network's magnetic degrees of freedom in real space[95, 96]. However, all these advantages seem to come with a certain price: most artificial spin ice realizations are practically insensitive to thermal fluctuations at room temperature. This is mainly due to the fact that the constituting elements behave like Ising spins and their size and shape yield energy barriers separating the two preferential orientations of the magnetization which are several orders of magnitude higher than the room-temperature thermal input. Therefore, the exploration of the complex energetic manifolds of frustrated

systems has initially been made by employing demagnetization protocols[3], but the ground states of the corresponding spin models seem far out of the reach of such driving mechanisms. In fact, it has been intensively reported that this dynamics can only result in a short-range order[1, 46, 54, 72], despite the long-range nature of the magnetostatic coupling between the elements. Nevertheless, although long-range effects are more difficult to reveal for artificial square ices, the kagome spin ice network has shown incipient signs of magnetic charge ordering[73, 94], which is directly related to the presence of dipolar long-range interactions within the arrays. This is quite an exciting result as the kagome spin ice network presents a remarkable feature in the dipolar framework at low temperatures: a so-called spin-ice II phase, characterized by the coexistence of a crystalline phase, associated to the magnetic charge, and a disordered spin lattice which bears the signatures of a Coulomb phase[7–9, 90]. Nevertheless, ac demagnetization protocols have not been able to access this regime as they usually get stuck at the onset of the spin ice phase. Therefore, if lower energy manifolds are to be reached, new techniques may have to be employed.

One of the main disadvantages of ac demagnetization is its one-shot approach for energy minimization. In other words, during a field-ramping, each island normally has only one flip available, after which it cannot change its magnetization state anymore. This ultimately results in the system getting jammed in a local energy minimum and being unable to further accommodate inter-island pairings. Rendering the nano-islands sensitive to thermal fluctuations might overcome this drawback, as the system would gradually accommodate pairwise interactions over time, hopefully mimicking the heat-bath conditions of its corresponding spin models. This would require the islands to retain a relatively high magnetic moment, thus interacting strongly with their environment, while also being able to practically overcome their intrinsic anisotropy energy barriers thanks to the thermal input[25]. This can be achieved in the so-called superparamagnetic regime[48], which has generally been the cornerstone for thermally-active artificial spin ices, one of the main interests of the community during the last few years[4–6, 10–12, 52, 53, 97–100].

For finite temperatures lower than the Curie point and under the macrospin hypothesis, an isolated monodomain magnetic island can spontaneously change its magnetization orientation after a certain period of time, which is called the Néel relaxation time[48]. This duration increases exponentially with the energy barrier separating the preferred magnetic orientations according to the Néel-Brown law:

$$\tau = \tau_0 \cdot exp(\frac{\Delta E}{k_B T}) \tag{2.20}$$

[25]These two requirements are sometimes mutually exclusive, as a high magnetic moment implies a high shape anisotropy barrier. Therefore, a compromise between the two has to be found.

where τ is the Néel relaxation time, τ_0 is the attempt time which depends on the magnetic material and is typically in the order of 10^{-10}s to 10^{-9}s, $\Delta E = K \cdot V$ is the energy barrier, proportional to the magnetic volume V and the anisotropy constant K, and $k_B T$ stands for the thermal energy. Given the exponential increase of the relaxation time, even a relatively small $\Delta E/k_B T$ ratio can result in a very long period of time after which a spontaneous flip might occur. For example, a $\Delta E/k_B T \sim 42$ ratio would result in a Néel relaxation time of about 10 years, while for $\Delta E/k_B T \sim 25$ it would be reduced to the order of minutes. For most athermal artificial spin ices, the ratio is typically in the order of 10^5, yielding colossal relaxation times. To decrease it to the order of seconds or minutes one can (1) decrease the anisotropy constant, K, (2) reduce the volume of the nano-islands, V and (3) increase the environmental temperature. In practice, all three options can be combined to this end as there are advantages and inconveniences for each option and employing just one can render the process technologically or practically impossible[26].

If one performs measurements with a period τ_m higher than the Néel relaxation time of a monodomain magnetic particle, i.e. $\tau_m \gg \tau$, the sampled states are uncorrelated over time. This is the so-called superparamagnetic regime[48]. It is important to distinguish between a pure paramagnetic regime that occurs for temperatures higher than the Curie temperature of the constituting magnetic material and a superparamagnetic regime, which is delimited by a temperature window, $T \in [T_B, T_C]$, where T_C is the Curie temperature and T_B is the so-called blocking temperature, which is defined as the temperature for which $\tau_m = \tau$:

$$T_B = \frac{\Delta E}{k_B \cdot ln(\tau_m/\tau_0)} \tag{2.21}$$

One can immediately notice that the value of the blocking temperature depends on the measurement time and is not a constant that solely depends on the sample characteristics. Within the superparamagnetic regime, the magnetic material retains its ferromagnetic state at the microscopic level, but presents a paramagnetic-like behavior at the macroscopic scale.

The above discussion has focused on an isolated-island case. If external fields are applied, the intrinsic energetic barrier ΔE is no longer symmetric and can be tuned to favor one state over the other. In the case of arrays of tightly-packed magnetic monodomain nano-islands,

[26]For lithographically-patterned artificial spin networks, increasing only the temperature can result in sample destruction or contamination due to film/sublayer diffusion[6]. Reducing an island's lateral dimensions is limited by the current state-of-the-art lithographic techniques, but smaller islands present smaller magnetic moments and thus a reduced coupling between the elements[98]. Tuning the anisotropy constant K seems the most viable option, but for uniaxial shape anisotropy cases, this mainly requires the reduction of the demagnetization field, which implies a magnetization decrease, which again results in a lower coupling between the islands. Also, decreasing the island lateral dimensions usually implies an increasingly poor control over the roughness and the size of the magnetic elements. This would result in a large distribution in island sizes and moments, hence a pronounced deviation form the isotropic spin model case.

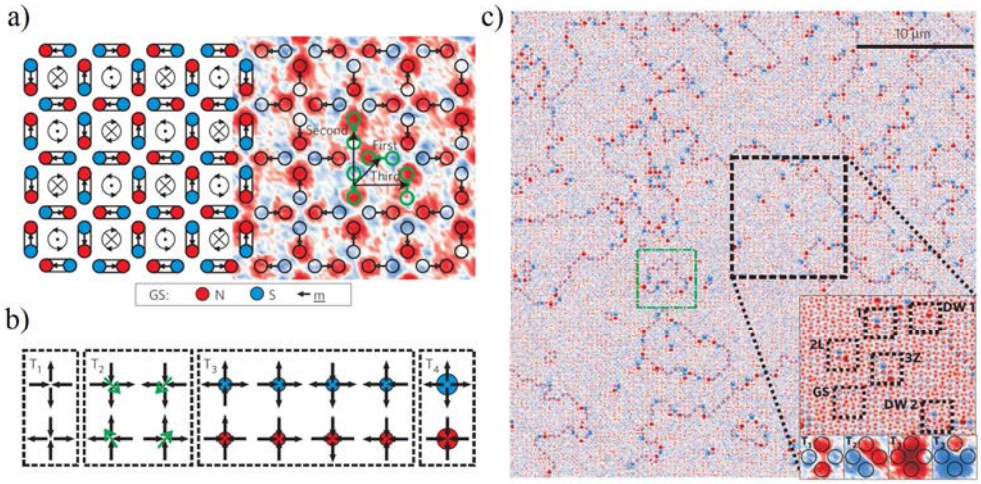

Figure 2.26 - Morgan *et al.*[4] have managed to create large domains of the ground-state of Wang's ice[1] by employing an approach that thermally accommodates the pairwise spin interactions in the early stages of magnetic island growth. (a) A square ice ground-state patch showing the short closed-loop spin formations with alternating chiralities. This corresponds to a paving with type I vertices only. The 16 vertices and their corresponding categories are given in (b). (c) A large network scan reveals ground state domains that stretch over extended areas, reaching more than $10\mu m$ in lateral size. The defects are type II and type III vertices that usually form chains that separate one domain form the others and correspond to elementary excitations above this ground state. After Morgan *et al.*[4].

each magnetic element is situated in a dipolar environment created by its neighbors and feels a certain effective local field that shifts its energetic barrier. If the island is in the superparamagnetic regime, it will thermally fluctuate between the two associated Ising states, but it will prefer one over the other depending on the direction of the local effective field. This way, the pairwise island interactions could be accommodated in heat-bath conditions and by tunning the temperature in the superparamagnetic temperature window the rate of the fluctuations can be controlled. This contrasts with ac demagnetization protocols and may ensure the at-equilibrium exploration of the energetic manifolds and also provide a route to low-temperature behavior.

One of the first cases of thermally-active magnetic artificial spin ices was reported by Morgan *et al.*[4], ushering these magnetic nanostructured arrays into a "thermally-active era"[27]. Instead of directly patterning a magnetic film, they deposited the $Ni_{80}Fe_{20}$ magnetic material in a square pattern that was previously carved in the resist via e-beam lithography.

[27]Thermally-active artificial spin ice systems have long been a goal for the community and alternative versions of artificial spin ices that can exhibit thermal effects have been reported prior to this work. Examples include artificial colloidal ice systems[40, 41] and arrays of magnetically-coupled superconductive rings or Josephson junctions[37, 39]. Another interesting case is a network of compass needles which, although it is subjected to a random magnetic field, it bears the signatures of a thermalized state[38]. Nevertheless, the work

Afterwards, they directly imaged their square spin ice arrays by MFM, without deliberately applying any external fields or demagnetization protocols. They observe domains of ground-state order that stretch over large areas of the sample surface, a feature that hasn't been observed before for demagnetized artificial spin ices (see Figure 2.26). They attribute this ground-state ordering to the thermal fluctuations occurring during the early stages of the deposition. As the islands grow, their magnetization increases and tends to form short loop-like configurations, specific to the ground-state ordering of square spin ice. However, in the meantime, the thermal effects slow down and the deposited material ultimately finds itself in a frozen state after a few nanometers have been deposited. At this stage, the magnetic configuration does not change anymore and the final network can be considered, as they describe in their paper, "a frozen-in residue of true thermodynamics that occurred during the fabrication of the sample"[4]. In addition, by analyzing the vertex populations resulting from such an approach, they conclude that such states can be properly described within a vertex-model canonical ensemble[91], showing improved agreement with thermalized states than the effective thermodynamics reported for demagnetized artificial spin arrays[55] and even accessing lower effective temperatures.

Another signature of thermal effects in artificial spin networks was reported by Kapaklis *et al.*[97] who performed a "melting" of an artificial square spin ice. Their samples were patterned out of δ-doped Pd(Fe) thin films, characterized by a low Curie temperature (230K), and were heated up to room temperature starting from 5K while a magnetic field was applied to saturate the square lattice either along the [10] or the [11] direction. Before reaching the Curie point of the constituting material, the array magnetization drops to zero, a fact that they associate to the presence of thermal fluctuations that produce type I and type III vertex states which are excitations for the type II ground-state under an applied field.

Several other studies on thermally-active artificial spin arrays have been performed by Farhan *et al.*[5, 52, 53]. Their approach involves the patterning of permalloy wedge thin films[28], ultimately yielding a set of artificial spin networks with different island sizes and lattice spacings. This way, thermal fluctuations can be tuned in the superparamagnetic window not only by adjusting the environmental temperature[29], but also by the different island thicknesses, thus achieving a rich spectrum of thermally-driven behavior for artificial spin networks. In addition, they image the time-evolution of an array's magnetic configuration by employing an X-ray Magnetic Circular Dichroism - Photo-Emission Electron Microscopy

of Morgan *et al.*[4] is one of the first examples of thermalization for artificial spin ices as established by Wang *et al.*[1].

[28]The wedge parameters changes from one study to another. The thickness generally increases from 0nm to 15-20nm, while the wedge spans over a distance in the order of 2-3mm. This gives enough space for fabricating many arrays with varying island thicknesses and different lattice parameters.

[29]The studies have mostly been performed at room temperature or slightly above.

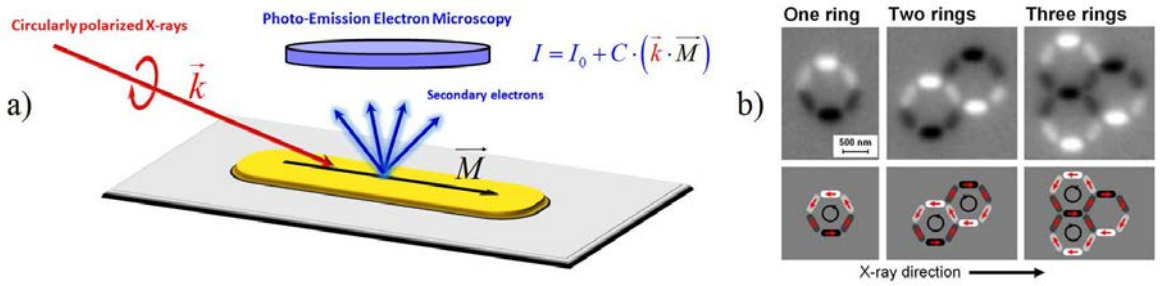

Figure 2.27 - (a) Schematics of the XMCD-PEEM measuring principle. An X-ray beam with either a clockwise or anticlockwise circular polarization is directed towards the sample with a grazing incidence. The X-ray-magnetic-sample interaction results in the emission of electrons which are then analyzed by a Photo-Emission Electron Microscope. Since the intensity of the electron beam is sensitive to the relative orientation between the X-ray wave vector and the sample's magnetization and also to the chirality of the circular polarization of the incoming beam, this results in a black and white contrast of the magnetic islands with respect to a background noise. (b) XMCD-PEEM contrast for kagome spin ice rings reported by Mengotti *et al.*[44]. The white regions correspond to magnetic elements that are aligned with the direction of the $\vec{k}$ vector, while the black regions correspond to anti-parallel alignment. The faded contrast is due to the relative angle between the two vectors directions. The magnetic configuration can thus be thoroughly reproduced. After Mengotti *et al.*[44].

technique (XMCD-PEEM), thus achieving an in-situ observation of heat-bath conditions for artificial spin ices.

XMCD-PEEM is a synchrotron-based technique that has been largely used for the study of artificial spin ice arrays[5, 10, 11, 44, 45, 52, 53, 73]. It involves the mapping of secondary electron emissions resulting from the exposure of a sample to circularly-polarized X-rays[30]. Somewhat similar to the Magneto-Optical Kerr effect, the interaction between the incident circularly-polarized X-ray beam and a magnetized material yields different absorption rates depending on the magnetization orientation relative to the incoming beam. This ultimately translates into a selective emitted electron intensity for different magnetic moment orientations. In fact, the electron intensity is proportional to the product between the X-ray wave vector, $\vec{k}$, and the magnetization vector of the scanned material, $\vec{M}$, and the

[30] In a quantum mechanical description, a circularly-polarized X-ray beam can be regarded as a flux of photons that are found in an eigenstate of the angular momentum operator, $\hat{J}_z$, where z stands for the direction of the propagation described by the wave vector, $\vec{k}$[101]. For a clockwise/anticlockwise polarization, the eigenvalue is $+\hbar/-\hbar$ and for a linearly polarized beam this value is 0. This reinforces the selection rules for the electronic transitions that can be triggered with an x-ray beam, requiring two conditions: $\Delta l = \pm 1$ and $\Delta m = \pm 1$, where l is the orbital quantum number and m is the magnetic quantum number. A $\Delta m = 1$ corresponds to a clockwise polarization transition, while $\Delta m = -1$ to an anticlockwise one. If a magnetic field is applied, the different energetic levels, $|l,m\rangle$, will split due to the Zeeman effect. For a 1s -> 2p transition, there will be a selectiveness regarding the Δm value. If a $|1,1\rangle$, level is fully occupied and a $|1,-1\rangle$ level is not, then the latter transition is possible, but it can be triggered only by one circular polarization chirality and not the other. For more details, please consult reference [101].

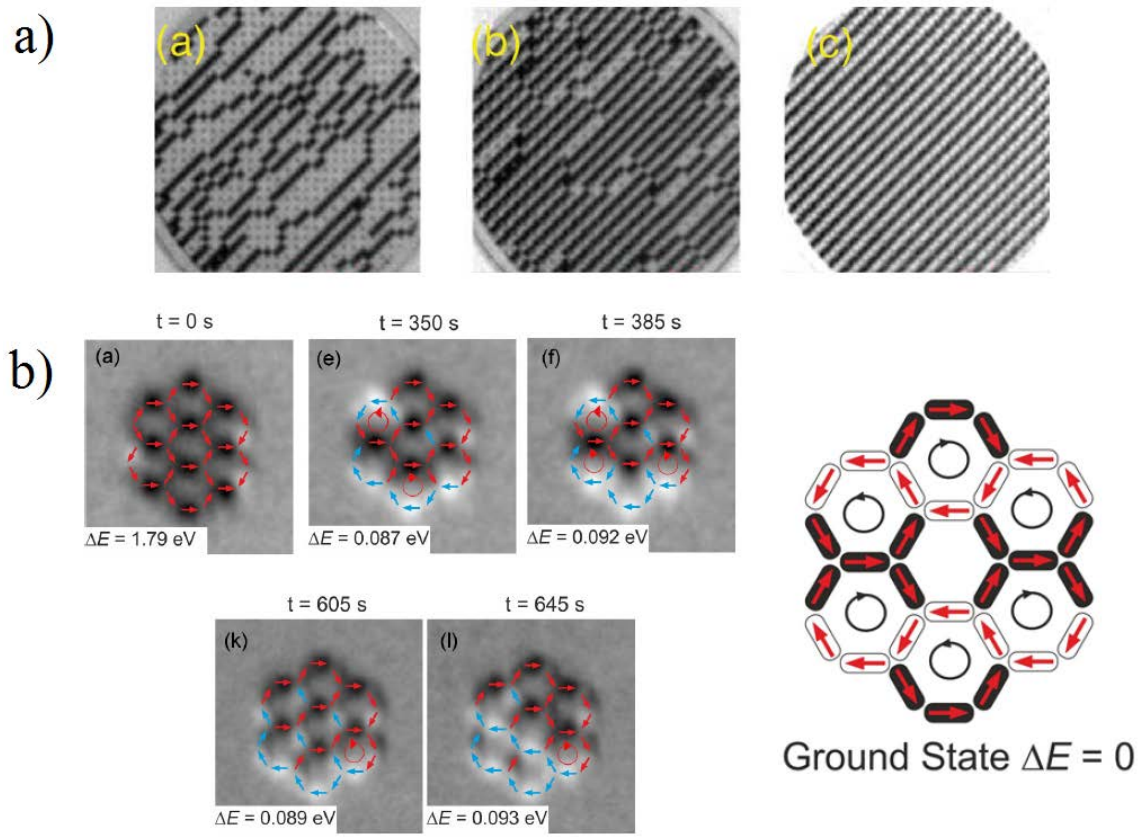

Figure 2.28 - (a) By working in the superparamagnetic temperature window, Farhan *et al.*[52] have observed how a saturated artificial square lattice slowly forms chains of type I vertices and then fully retrieves its ground-state configuration thanks to thermal effects and inter-island couplings. After Farhan *et al.*[52]. For clusters made up of seven kagome spin ice rings, this approach reveals how the magnetic configuration evolves from the initial state and the system explores the phase space while trying to satisfy the frustrated dipolar interactions. Although it manages to get the network close to its ground state, it can never access it fully. This raises questions to whether a spin ice II phase can be achieved for larger thermally-active artificial kagome spin ice networks. After Farhan *et al.*[53].

proportionality constant changes sign with respect to the employed circular polarization (see Figure 2.27). Therefore, by fixing the incident wave vector, the individual magnetic moments of an artificial spin array can be directly identified through the visual contrast of the photo-emission electron microscope[31]. The spin texture of the entire network can thus be imaged *in-situ* and the time evolution of the array can also be observed[32].

[31] To obtain the final contrast, the subtraction of an average image or of an initial frame is usually performed[5]. For the current work, the contrast was obtained by subtracting images obtained with clockwise (I_c) and anticlockwise (I_{ac}) X-ray beam polarizations and then normalizing the difference: $I_f = I_c - I_{ac}/I_c + I_{ac}$.

[32] Notice that this is a non-perturbative technique, unlike Magnetic Force Microscopy which can alter the magnetic state of the sample. However, it requires a good collimation of the incident X-ray beam, thus normally necessitating synchrotron radiation.

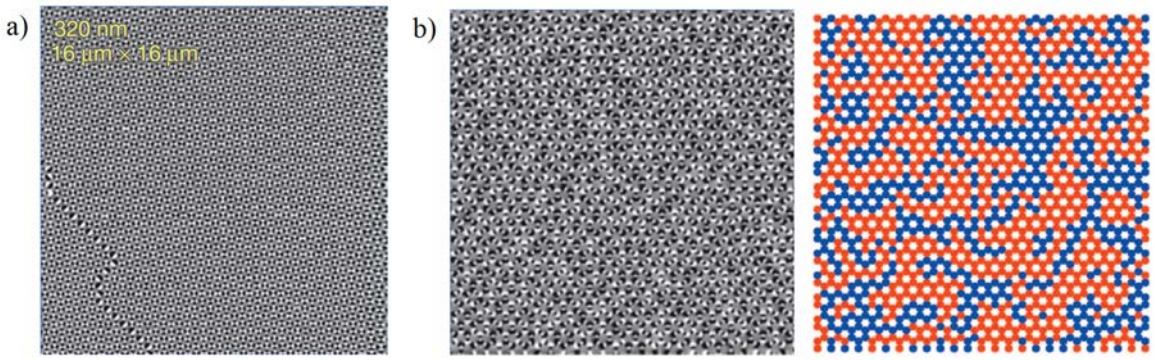

Figure 2.29 - The annealing procedure proposed by Zhang *et al.*[6] is another thermal approach for accessing lower energy manifolds for artificial spin networks. Cooling down to room temperature from above the Curie point yields an almost perfectly-ordered square ice crystal (a), while kagome spin ice shows incipient charge crystallization (b). Both MFM images reproduced correspond to the most tightly-packed networks that Zhang *et al.* reported. The reconstruction of the underlying hexagonal charge network for kagome spin ice samples reveals large charge-ordered domains. The red/blue coloring is not associated to the ± 1 charge value but is simply a color-code that distinguishes one charge domain form another. After Zhang *et al.*[6].

For a square spin ice array that was initially saturated into a type II crystal, Farhan *et al.*[52] observed how the network slowly creates chains of type I vertices, driven by the superparamagnetic thermal fluctuations and filtered by the inter-island dipolar couplings (see Figure 2.28.a). Ultimately, the entire network slips into a type I crystal, the long-sought ground state of Wang's ice[1] which corresponds to Lieb's F-model[77]. For artificial kagome spin ices, they investigated the pathways taken by small clusters of kagome spin ice rings through their phase space[5] (see 2.28.b). While these rings also show a selectiveness in their phase space exploration, governed by the inter-island interactions, the ground state configuration is increasingly difficult to achieve as the number of rings rises[53][33]. This is probably due to the inability of the single spin-flip dynamics to reach the kagome spin ice ground state, as it was discussed in the previous chapter. In fact, the single spin-flip dynamics has shown algorithmic difficulties in accessing the exotic spin ice II phase. Given the inability to reach the ground state for small clusters of kagome spin ice rings, the hope of achieving a charge crystal embedded in a disorder spin texture via a superparamagnetic regime approach seems to gradually fade away as the number of hexagonal elements increases.

While most approaches presented so far rely on the superparamagnetic regime for thermally-induced behavior in artificial spin ices, Zhang *et al.*[6] proposed a different thermal approach, involving an annealing procedure above the Curie temperature of the island magnetic material. After sample fabrication, square and kagome artificial arrays of

[33]They report that, for clusters made up of 7 rings, the ground state configuration was never observed.

different lattice spacings were heated slightly above the Curie point of the $Ni_{80}Fe_{20}$ material used (approx. 820K) and then cooled down to room temperature. The remanent states were imaged using Magnetic Force Microscopy and revealed an almost perfect spin order for square ice, with just a small domain boundary made up of type II vertices (see Figure 2.29). For the most tightly-packed kagome spin ice arrays, no more defects are observed, contrary to demagnetized samples, and all vertices respect the kagome ice rule, highlighting at-least a pure spin ice regime. In addition, by taking the dumbbell picture, they observe large domains of magnetic charge order, i.e antiferromagnetically-aligned crystallites of magnetic charges. Such charge textures are normally found deep within the spin ice manifold and haven't been reported before for kagome spin ice as ac demagnetization protocols jam the system at the onset of the spin ice regime. They further explain the formation of these charge domains by an effective charge-charge interaction[34] and find good agreement with Monte Carlo simulations, leading them to conclude that these states are truly thermalized ones[6]. These annealed artificial arrays have thus managed to surpass the limits of ac demagnetization, allowing for a better magnetic charge organization in the background of the kagome spin lattice[6, 10–12]. In addition, the large charge-ordered domains might be seeds of an exotic, but frozen, spin ice II regime.

Following the procedure proposed by Zhang *et al.*[6] and employing a lower-Curie temperature material, similar charge crystallites have been recently reported for artificial kagome spin ices[10, 11]. However, by mapping the experimental results on at-equilibrium Monte Carlo simulations based on the dipolar spin ice Hamiltonian (see expression 2.16), a contradiction between certain correlators is found, thus highlighting the presence of an out-of-equilibrium process. A kinetic model has been proposed that accounts for these inconsistencies with Monte Carlo simulations and also explains the efficiency of this annealing procedure in developing large crystallites of magnetic charges[11] by means of dipolar spin interactions instead of effective nearest-neighbor charge couplings. These results, as reported in reference [11], are detailed in this chapter.

2.6.2 Experimental Protocol and Data

Artificial kagome arrays comprising 342 connected nano-islands have been e-beam patterned out of a $Gd_{0.3}Co_{0.7}$ thin film, with typical island dimensions of $500 \times 100 \times 10\ nm^3$. The samples were fabricated by François Montaigne, Michel Hehn and Daniel Lacour at the Jean

[34]The Hamiltonian that they propose contains a nearest-neighboring coupling term for spins and a short-range interaction between nearest-neighboring magnetic charges[102]. This is, in fact, equivalent to expression 2.19, if all contributions coming from spin pairs separated by a distance equal or greater than the lattice parameter are cancel out.

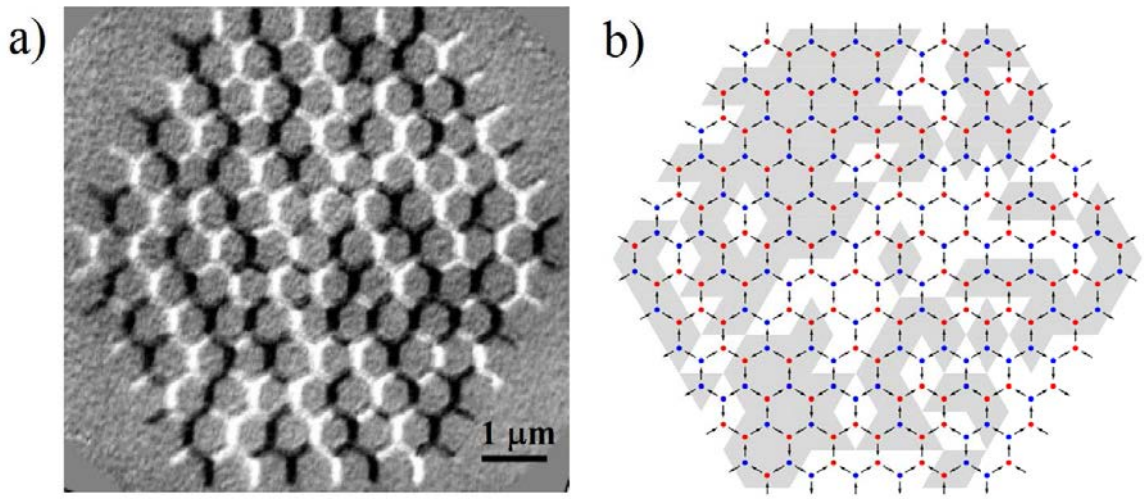

Figure 2.30 - (a) A typical PEEM image of an artificial kagome spin ice network made out of 342 GdCo nano-islands after being annealed above T_C and then cooled down to room temperature. After Montaigne et al.[105]. (b) A reconstruction of the network that reveals the antiferromagnetically-ordered charge crystallites.

Lamour Institute in Nancy. GdCo is part of a rare earth-transition metal ($RE_{1-x}TM_x$) alloy class in which the exchange interactions between the two 3d metallic species is strongly ferromagnetic, yielding a TM ferromagnetic sublattice, while the exchange coupling between the RE and TM spins is generally antiferromagnetic[103], especially for heavier RE elements like Tb[104]. We therefore have a ferromagnetic TM sublattice coupled antiferromagnetically with a RE sublattice, resulting in a ferrimagnetic-type alloy. While most of these alloys are amorphous, thus resulting in a sperimagnetic behavior[103][35], GdCo displays a mostly collinear spin texture over a wide range of compositions and remains ferrimagnetic[104]. For the current composition, it presents a spontaneous magnetization of about 355±50kA/m at room temperature[105] and a Curie temperature of about 475K[10, 11].

Given the possibility of annealing the samples beyond their Curie point without destroying the magnetic nano-islands, a thermal demagnetization procedure can be applied to these artificial kagome spin ice networks. The samples were therefore heated up to 500K and then cooled back to room temperature in the absence of any specifically-applied magnetic field. Afterwards, the remanent magnetic configuration was retrieved by XMCD-PEEM measurements performed at the nanospectroscopy beam line of the Elettra Synchrotron

[35] Sperimagnetism is briefly discussed in the following chapter, where the TbCo alloy is presented.

Radiation Facility[36]. A PEEM image is provided in Figure 2.30 along with the reconstruction of the magnetic moment orientations and the underlying magnetic charge network.

The first aspect that can be observed is the complete absence of forbidden states, i.e. vertices that do not respect the ice rule. This is, however, not a surprise as the magnetic islands are connected at the vertex points, thus making a ± 3 charge state energetically very unfavorable. In fact, this particular property has already been reported before for field-demagnetized artificial kagome lattices[46]. Nevertheless, the embedded charge network reveals a striking feature: this procedure has succeeded in producing large domains of antiferromagnetically-ordered charges, some of them comprising large parts of the network (almost 1/3 of the total number of spins in certain cases).

At first sight, this approach seems to perform better than field-demagnetized samples, a fact that raises several questions. Firstly, which effective temperature regime best describes the final magnetic states of these annealed artificial kagome spin ices? Clearly, the networks are at-least in a spin ice manifold, but could these spin configurations provide more convincing evidence for the signatures of dipolar long-range interactions by accessing even lower-energy manifolds than field-demagnetized ones? Secondly, to which regime do the magnetic charge crystallites belong to? Both the spin ice 2 and the ordered ground-state of kagome spin ice present perfect antiferromagnetic charge order, and it would be interesting to see which phase has been locally accessed this way. Thirdly, and more generally, what is the driving mechanism that could explain this local charge order?

Since we find ourselves again with a set of snapshots that have to be compared with simulated networks that can employ various interaction models (see Figure 2.24), the idea is to compute the spin and charge correlators, as has already been done for field-demagnetized artificial kagome spin networks[13, 14, 46, 72, 73], and then refer to the numerical results. These correlators can be computed on the network scale to ascertain the efficiency of this procedure for reaching low-energy manifolds. Furthermore, since we also want to identify the regime characterizing the charge crystallites, the spin correlators should also be calculated locally, within the ordered charge domains, since they can discriminate between one phase and the other. Table 3.1 gives the experimental ensemble averages for each spin correlator, $< C_{\alpha j} >$, and for the nearest-neighbor charge correlator, $< Q_i Q_{i+1} >$ computed at the newtork scale[37]. Also, averages for the spin correlators computed within the charge crystallites are provided. Since small domain sizes would contain only few spin correlation

[36] I have not personally participated at these measurements, but I have been involved in data analysis and modeling. This beam-time measurement session was performed by Nicolas Rougemaille, François Montaigne, Michel Hehn, Daniel Lacour, Andrea Locatelli, Telfik Onur Menteş and Benito Santos Burgos.

[37] These values are, in fact, averages of each network average computed over 18 imaged experimental kagome spin ice networks.

Table 2.2 Average values for each spin correlator computed on the full network scale and within domains that contain at least 20 magnetic charges. The values are averaged over the 18 PEEM images obtained. The value of $C_{\alpha\beta}$ computed within the charge crystallites might seem disturbing, given that the ice rules are respected overall and that for a pure spin ice state this value is strictly $1/6$. However, this is an effect of the random border shapes of the domains which often include $\alpha-\beta$ pairs at the border, but the third spin with which they create a vertex is situated in a neighboring domain (such examples can be seen in Figure 2.30.b.). This results in a deviation from the $1/6$ value. Data courtesy of François Montaigne, Michel Hehn and Daniel Lacour.

Correlation	Full Network	Domains
$C_{\alpha\beta}$	0.16667	0.1756
$C_{\alpha\gamma}$	−0.17983	−0.28077
$C_{\alpha\nu}$	−0.07534	−0.03183
$C_{\alpha\delta}$	−0.36964	−0.36827
$C_{\alpha\tau}$	−0.00106	−0.01459
$C_{\alpha\eta}$	−0.03877	−0.09447
$C_{\alpha\varphi}$	−0.00692	0.13211
Q_iQ_{i+1}	−0.22549	

pairs which are generally associated only to lower order correlators, only large domains are taken into account here. These domains provide data for higher order correlators as well, which generally present an abrupt evolution between the spin ice 2 state and the ordered ground-state (see Figure 2.22), thus facilitating the identification of the corresponding regime. Also, large domains display a wide range of sizes and shapes and they have all been grouped together in size classes. The data presented here corresponds to averages performed within domains that contain a number of charges equal or greater than twenty[38]. This ensures that higher order spin correlators are also represented.

These experimental values are firstly compared to their at-equilibrium Monte Carlo averages. Now that the artificial arrays are thermally-active, it would be interesting to see how this affects the mapping onto at-equilibrium thermodynamic averages. To bridge experiment with theory, a correlation scattering analysis protocol has been employed. Details for this procedure are provided in section 3.4.2. Basically, the question that we ask is to which extent can we actually compare the experimental snapshots with the model predictions and it turn out that we can identify an effective temperature that describes quite well the output of annealing by minimizing the overall deviations of the experimental correlators from the Monte Carlo ensemble averages. This can be done by defining a spread-out function:

[38]Taking the minimal size too large would result in a poor domain statistics as there are very few domains that contain more than 40 charges, for example. On the other hand, taking the limit too low would increase the statistics for lower order spin correlators, but values from small crystallites would be mixed up with those from larger one, the latter being more relevant for a comparison with a spin ice 2 or an ordered phase.

$$K(T) = \sqrt{\sum_j (C_{\alpha j}^{snapshot} - < C_{\alpha j}^{MC}(T) >)^2} = \sqrt{\sum_j [\Delta(C_{\alpha j})]^2} \tag{2.22}$$

where $C_{\alpha j}^{snapshot}$ is a snapshot network-averaged correlator, $< C_{\alpha j}^{MC}(T) >$ is the corresponding ensemble average for a certain temperature T and the summation is performed over all extracted correlators. By computing this function for each Monte Carlo sampling temperature, a minimal value can be found, the argument of which corresponds to an effective temperature that serves as an energetic label describing the spin order established within the experimental snapshot. Notice that this physical quantity is not a real temperature describing a thermodynamically equilibrated state. The results of the correlation scattering analysis are discussed in the following section.

2.6.3 Mapping onto Monte Carlo. Fingerprints of an Out-of-Equilibrium Physics

The experimental data were compared to Monte Carlo simulations performed on a kagome spin ice lattice with 342 spins having the same size and shape as the experimental network and under free boundary conditions[39]. Similarly to the simulations described in the previous chapter, a hybrid-flip procedure has been employed, including both single spin-flips and loop-flips and insuring that the sampled configurations are well decorrelated between eachother[40]. Both short-range and dipolar long-range models are reconsidered. However, given the absence of periodic boundaries, the summation for the dipolar couplings is made over all spin pairs, without cutting off the long-range dipolar Hamiltonian at a certain distance as it was done previously.

Figure 2.31 gives the two sets of experimental correlators, computed both globally (over the entire network) and locally (within the charge domains) up to the 7th neighbor. The ground state values for both models are also provided for comparison (see red and blue dots). The first aspect that can be immediately seen is that both sets cannot be well described within a nearest-neighbor interaction framework, presenting clear deviation from the short-range spin ice plateaus (red dots) that exceed the standard deviations of the correlation distributions

[39] Similar results are found if the comparison is made to a periodic boundary condition case with a lattice made of $12 \times 12 \times 3$ spins

[40] Since there are no free boundary conditions, winding loops no longer exist. Nevertheless, a loop that stretches from one border to another is still a viable option and it cannot yield any forbidden states if flipped. Therefore, such loops have also been considered in the spin dynamics, facilitating the exploration of the spin ice energetic manifolds and beyond.

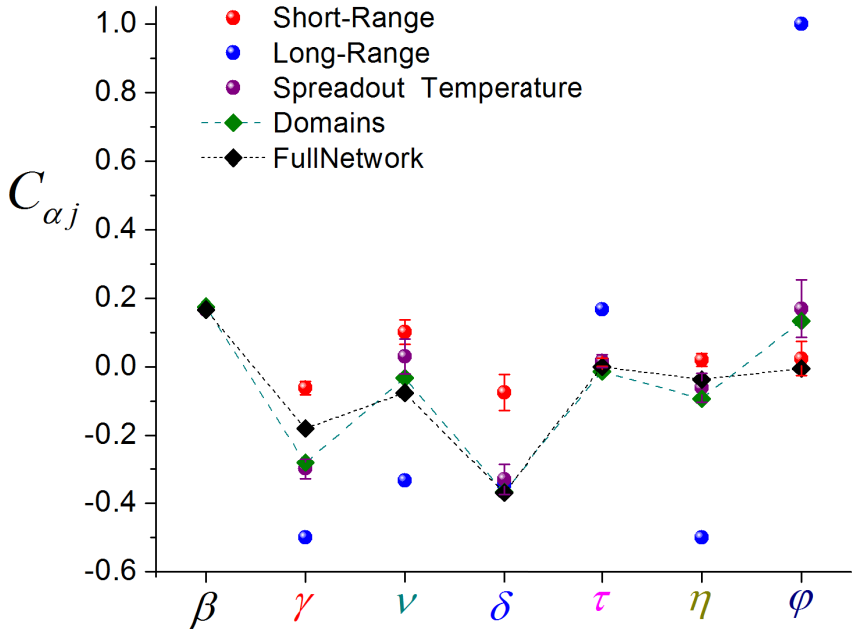

Figure 2.31 - Both sets of spin correlators, computed on the network scale (black diamonds) and within the charge crystallites (green diamonds), are compared to the Monte Carlo values. The red points correspond to averages for the short-range ground-state, i.e. the spin ice plateaus within a nearest-neighbor interaction picture, while the blue dots represent the values for the long-range dipolar ground-state. Since the short-range plateau values display intrinsic fluctuations due to finite-size effects, they are accompanied by error bars reflecting these variations from the ensemble average. Although both data sets are still far from the dipolar ground state, the short-range model clearly fails to reproduce the values of lower order correlators like $C_{\alpha\gamma}$, $C_{\alpha\nu}$ and especially $C_{\alpha\delta}$. Furthermore, an overall good match is found between the correlators calculated locally and the Monte Carlo averages for a temperature of $T/J_{NN} = 0.03687$, which corresponds to the spin ice 2 phase. The lines between the experimental points do not have any physical meaning and serve just as visual guides.

reflecting the intrinsic fluctuations due to finite size effects. In fact, all correlations deviate towards the long-range ground-state values (blue dots), and although they are still far from them, this feature clearly highlights the fingerprints of higher order dipolar couplings and the need for their consideration when describing the output configurations of artificial kagome spin ices after being thermally annealed. This result reinforces what has already been reported for ac demagnetized artificial kagome networks[73].

By employing a correlation scattering analysis, a minimum is found for the $K(T)$ function for each experimental correlation set, thus defining an effective temperature. The locally-computed set (within the chagre crystallites) presents a striking feature: overall, these experimental correlators are in very good agreement with the Monte Carlo averages for a temperature of $T/J_{NN} = 0.03687$, which corresponds to the onset of the spin ice 2 phase. This is an exciting result, as this phase hasn't been accessed before with ac demagnetization protocols. In fact, the best that ac demagnetization has managed to do so far is to reach states with a T/J_{NN} that is one order of magnitude higher than this value. Also, if we choose to normalize the temperature with the dipolar coupling constant D instead of the nearest-neighbor coupling J_{NN}, this would yield $T/D \cong 0.5$. Therefore, this procedure seems to be more sensitive to the dipolar strength D somewhat similar to how ac demagnetization is sensitive to the nearest-neighboring coupling strength, J_{NN}.

The matching of the experimental data with the effective temperature $T/J_{NN} - 0.03687$ can also been seen in Figure 2.32.a where the experimental points are related to their temperature evolution plots and more than half of them fall within the standard deviations of the intrinsic size-dependent fluctuations. Nevertheless, it should be emphasized again that, although the matching is very good, this does not necessarily imply that these crystallites are truly thermalized spin ice 2 states, in equilibrium with the heat bath conditions[41]. In fact, if one turns to the values computed globally, signatures of a possible out-of-equilibrium process emerge.

For the experimental network averages, the spread-out function yields an effective temperature of $T/J_{NN} = 0.05012$, which is a deep spin ice temperature regime. This is in contrast with the results found locally. Furthermore, although some data points agree with the Monte Carlo values, certain correlators show some problematic deviations (see Figure 2.32.b). For instance, $C_{\alpha\nu}$ and $C_{\alpha\varphi}$ both deviate severely from their expected at-equilibrium values of the effective temperature found. In addition, the experimental average value of Q_iQ_{i+1} is about -0.22, which is normally found either in a high-temperature paramagnetic regime or in the spin ice phase (see inset of Figure 2.32.b)[42]. This is therefore an extremely rare event

[41] This subject is discussed in more detail in section 3.4.2.

[42] Clearly, this would correspond to the spin ice regime as there are no forbidden states, which would drastically increase the system's energy.

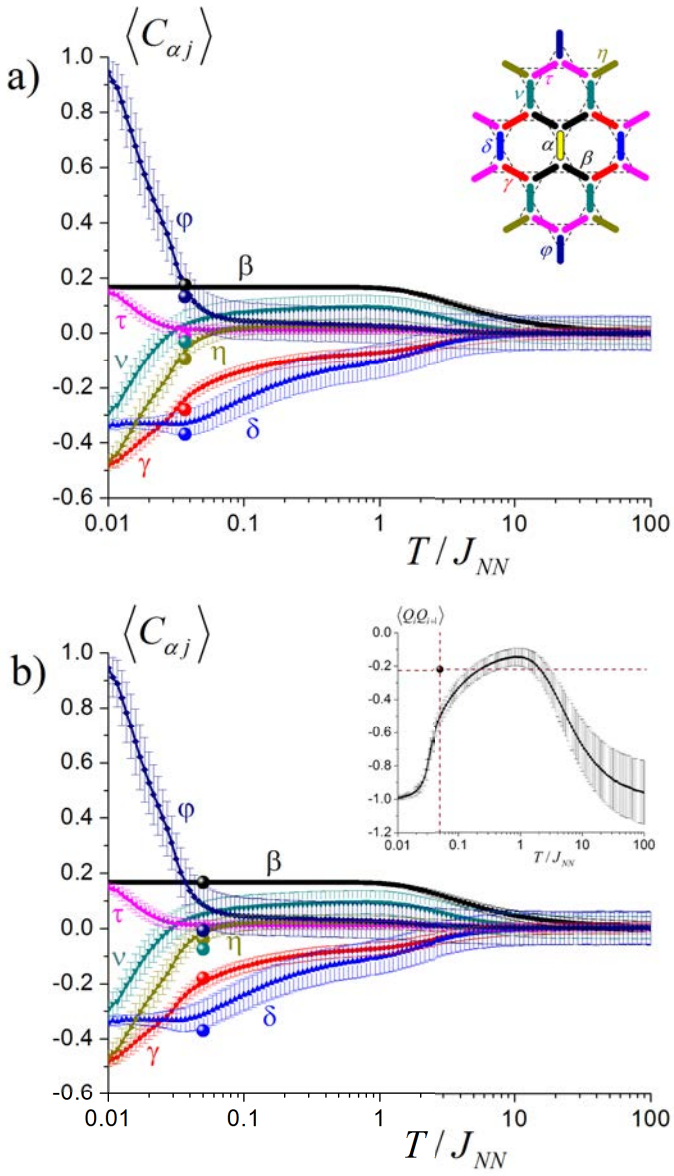

Figure 2.32 - (a) The experimental averages computed within the charge domains with respect to the Monte Carlo averages corresponding to the effective temperature, $T/J_{NN} = 0.03687$. The matching is quite good and the crystallites seem to correspond to the spin ice 2 regime. The inset gives the definition of first seven spin correlators, after Chioar *et al.*[11]. (b)By employing the same analysis procedure, an effective temperature is found for the global experimental averages. However, the matching is not as good as before, with certain correlators like $C_{\alpha\nu}$ and $C_{\alpha\varphi}$ displaying strongly biased deviations. More striking is the deviation of the nearest-neighbor charge correlator, Q_iQ_{i+1}, provided in the inset. This experimental value is situated at more than 5 times the standard deviation of the correlator distribution sampled at-equilibrium by Monte Carlo simulations for the effective temperature of $T/J_{NN} = 0.05012$ (see vertical line). In fact, the -0.22 average value for $Q_iQ_{i+1}^{exp}$ is generally found in the spin ice phase (see crossing of the horizontal line with the MC plot). This emphasizes the presence of a kinetic, out-of-equilibrium process as some of the correlation values belong to a deep spin ice regime while others are specific to a "warm" spin ice regime.

for a sampling performed in heat-bath conditions at $T/J_{NN} = 0.05012$, where the expected value is about -0.51053, and it is situated at more than 5 times the standard deviations of the correlator's distribution. In the end, this deviation is not surprising, as the charge correlator can be written as a linear combination of the first three spin correlators (see expression 2.13) and since $C_{\alpha\nu}$ already presents a deviation then it is expected to observe one for Q_iQ_{i+1} as well. However, it is quite remarkable that, although these networks are thermally-active, the overall matching of the global correlation set seems to be worse than in the case of ac demagnetized samples. These results contrasts with the conclusion of Zhang *et al.*[6], which states that this annealing procedure creates truly thermalized states. Also, a biased distribution of the parity of the charge crystallites has been observed[10], and all these features seem to highlight the fingerprints of an out-of-equilibrium process within this description that unfolds during the cooling stage.

In a brief retrospective, the spread-out function analysis has helped us identify the temperature regime on the network scale, a deep spin ice state, and establish that the charge crystallites are well described by spin ice 2 correlation developments. The question that still remains is what is the underlying mechanism that creates this out-of-equilibrium state?

2.6.4 A Kinetic Approach

The major difference between the approach proposed by Zhang *et al.*[6] and the superparamagnetic regime exploration widely employed by Farhan *et al.*[52] is that, in the former case, the networks are annealed by surpassing the Curie point of the thin film material. Therefore, the nanomagnets should loose their magnetization and the array would be made out of islands with no magnetic moment. However, when the Curie point is crossed again during cooling, the islands start to remagnetize. In an isolated environment, any of the two preferential easy-axis orientations would be equally probable, but if an island senses a local magnetic field, it would likely align with it. This local field can be ensured by a neighboring island that has already magnetized and creates a small stray field around it, influencing the remagnetization of its neighbors. Therefore, the remagnetization of the network might well be a sequential process in which already-magnetized elements selectively trigger the next ones that are to be magnetized.

This description is in fact, the basis of a kinetic model proposed for explaining the outcome of the thermal annealing procedure applied to artificial spin ices. Of course, the real process is far too complex and some assumptions have to be made. Firstly, it is assumed that, at the Curie point crossing, a few islands fully remagnetize simultaneously and independently from each other. These are the so-called nucleation sites and each one's magnetization state is chosen randomly between the two preferential orientations. Given the magnetostatic nature

of the couplings, J_{ij}^{dip}, all not-yet-remagnetized islands feel the local contributions coming from the stray fields of all "switched-on" elements: $\vec{H}_{eff}^{i} = \sum_j J_{ij}^{dip} \vec{S}_j$.

As previously mentioned, an island would remagnetize quickly in the presence of a local field, given the divergence of the magnetic susceptibility at the critical point. However, at the critical temperature, magnetic domains nucleate and then tend to expand and finally occupy the entire volume of the island. If a field exists, then the domains already aligned with it would be favored for expansion, but the influence of the local field must be related to the thermal energy, which acts as to randomize the domain distributions and can ultimately align the island's magnetization opposite to the field. The stronger the local field, the less likely it is that such an event would occur. Also, as the magnetic volume increases so does the demagnetizing field and implicitly the energy barrier separating the two preferential states. This would make an effective flip of the magnetization less and less likely. To simply model this complex transitory behavior, it is further assumed that an island fully magnetized in one step and its final magnetization state is selected through a Boltzmann-like probability, thus reflecting the intrinsic early-stage fluctuations by taking into account the relative strength of the local field contribution with respect to the thermal energy. For relatively high temperatures, the bias given by the local field is practically canceled out and both states are equally probable. On the other hand, for a relatively low thermal bath, the local field dictates the remagnetization of the islands. Practically, the island is firstly aligned with the field and then the Boltzmann-type probability is employing to determine if a flip is likely[43]. The expression of the probability reads:

$$p = \frac{1}{1 + e^{-\Delta E / k_B T}} \tag{2.23}$$

where T is the environmental temperature[44], and $\Delta E = 2 \cdot \vec{S}_i \cdot \vec{H}_i^{\,eff} > 0$. A random number is then uniformly generated between 0 and 1 and, if its value is higher than the probability, the island is set to point contrary to the local field direction. After the direction has been chosen, the island fully remagnetizes, regaining the magnetic moment it possessed previous to the annealing step, and does not change this state anymore due to its relatively high anisotropy barrier. Therefore, this algorithm is also a one-shot approach, similar to ac-demagnetization, but presenting a thermal stochastic component.

[43] This transition probability is, in fact, a Glauber transition probability[106].

[44] This is, in fact, related to another assumption of the model. Since the timescale of the remagnetization of an island is in the order of nanoseconds and the cooling rate is in the order of a few Kelvins/second, it can be assumed that all remagnetizations occur at a constant temperature, which is assumed to be equal to the critical one.

After the initial points have been set, all islands can start remagnetizing, but each remagnetization changes the stray field map. From an algorithmic point of view, this requires an immediate global update of the local fields. Therefore, the question now is which island is magnetized next? This brings us to another assumption of this kinetic model: after the initial step, the next island to be magnetized is the one that feels the highest local field value[45]. After the island in question has been magnetized and the local fields have been again updated for all non-magnetized spins, the process is repeated until the entire network is fully remagnetized. Figure 2.33 gives the logical schema of this algorithm[46].

Several simulation runs of this kinetic algorithm have been performed on kagome spin ice networks comprising 342 spins, reproducing the size and shape of the experimental networks, with free boundary conditions. The temperature has been gradually dropped in steps starting from a high-temperature paramagnetic regime, $T/J_{NN} = 100$, down to $T/J_{NN} = 0.0001$[47]. For each temperature value, a number of 10^4 tryouts are performed and, after each complete remagnetization of the network, the relevant physical quantities are computed and stored (usually the energy, the magnetization and the spin and charge correlators). For the chosen temperature, this yields a distribution of values for each quantity, which has its own average and standard deviations that are computed at the end of the sampling stage, just like in the Monte Carlo simulations. Although the experimental data highlights at-a-glance the fingerprints of long-range dipolar interactions through the values of the spin correlators, both short and dipolar long-range interaction models have been considered for this kinetic algorithm as well. Furthermore, the influence of the number of nucleation sites (n) on the overall spin organization has also been investigated for both models[48].

Figure 3.9 gives the temperature evolutions of the first seven pairwise spin correlators for both the short-range and the long-range models in the case where only one spin is randomly magnetized in the beginning. Overall, the behavior appears to be very similar to the one given by at-equilibrium Monte Carlo simulations (see Figures 2.11 and 2.22). This is probably due to the fact that the underlying interaction model is the same in both cases, making the energetic landscape identical. Nevertheless, the phase space is explored differently and the ergodic sampling provided by Monte Carlo simulations is replaced by a one-shot approach

[45] If several spins share the maximum local field value, then one of them is picked up randomly.

[46] The idea behind the algorithm was proposed by Benjamin Canals and the simulation plots that appear in the publication[11] are the result of his own simulation code. Nevertheless, the correlation data analysis has been performed entirely by myself for both the article and the current work and the correlation plots of the kinetic algorithm in this thesis are my own. My own implementation yields the same results as the one initially performed by Benjamin Canals.

[47] Contrary to at-equilibrium Monte Carlo simulations, this procedure does not suffer from a critical slowing down effect, which facilitates the sampling of a wider range of temperatures, particularly lower ones.

[48] Simulations have been performed for the following numbers of preset spins: 1, 5, 10, 20 and 50.

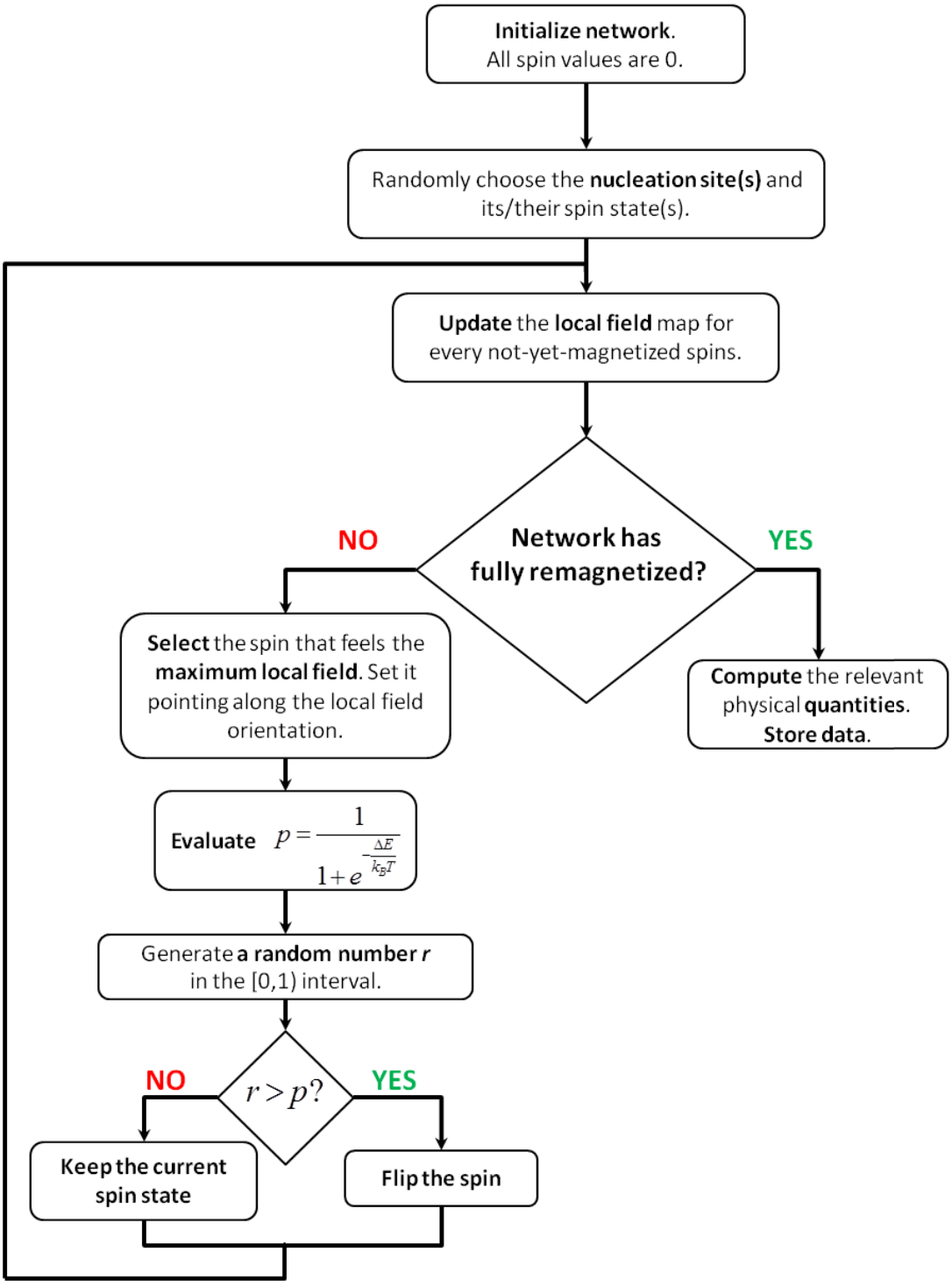

Figure 2.33 - The logical schema of the proposed algorithm that sequentially remagnetizes each of the network's spins at the Curie point crossing. Similarly to demagnetization, this is a "one-shot" approach, as each island has only one choice for determining its final magnetization state, but this choice is made through a stochastic component that depends on the temperature.

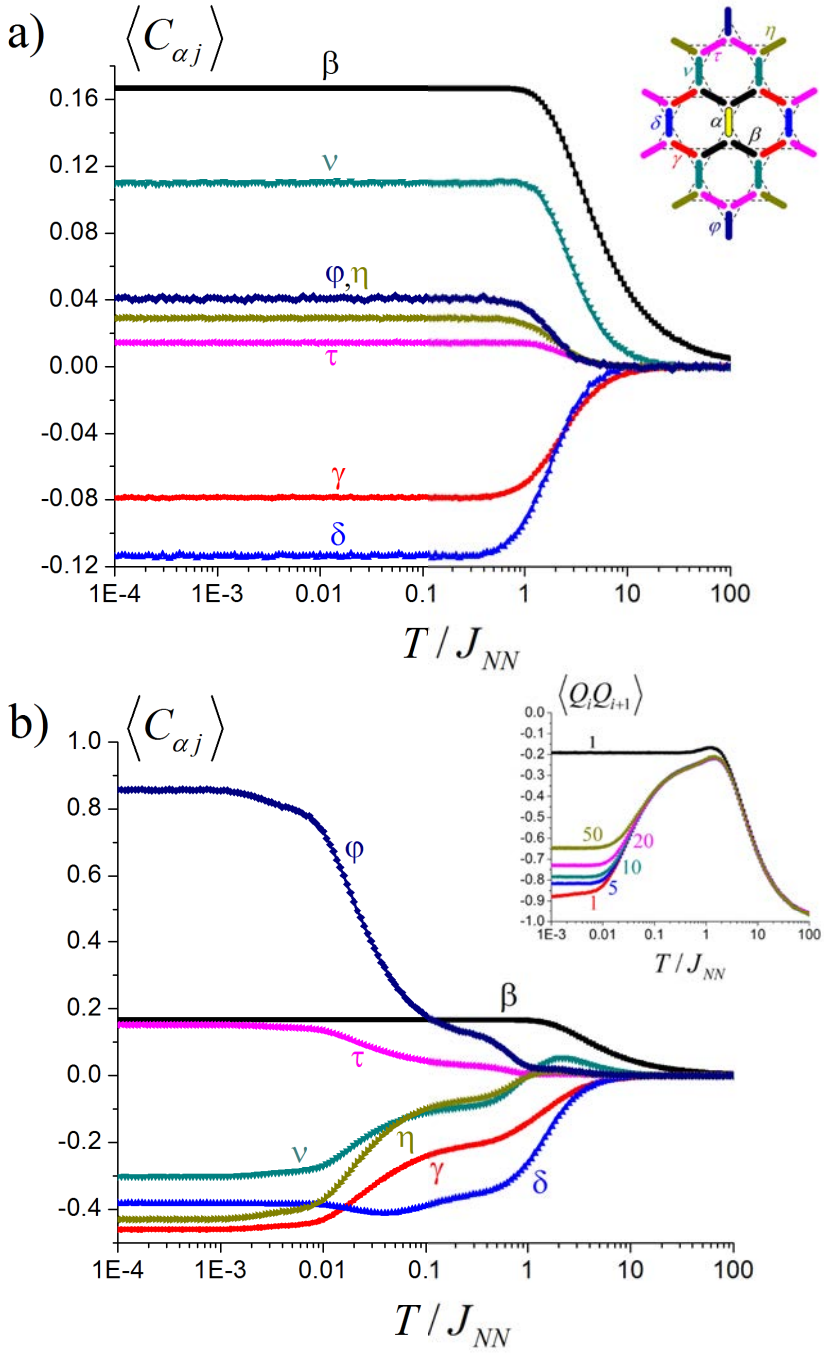

Figure 2.34 - The temperature evolutions of the first seven pairwise spin correlators for the (a) short-range model and (b) the dipolar long-range model. Notice the overall similarity between the Monte Carlo plots and these ones in the case of the short-range model. The dipolar long-range model displays more differences, particularly for $C_{\alpha\nu}$ and $C_{\alpha\delta}$. Remarkably, the low-temperature values of most correlators are very close to the dipolar ground-state ones. The inset of (b) gives the evolution of the nearest-neighbor charge correlator. Both short and long range plots (for one nucleation site) show similarities to at-equilibrium behavior and the long-range plot even manages to drop to -0.9. As the number of nucleation sites increase, the formation of large crystallites is hindered. This can be seen on the charge correlator plots, where the numbers indicate the number of preset spins. Inset of (a) is taken from Chioar *et al.* [11].

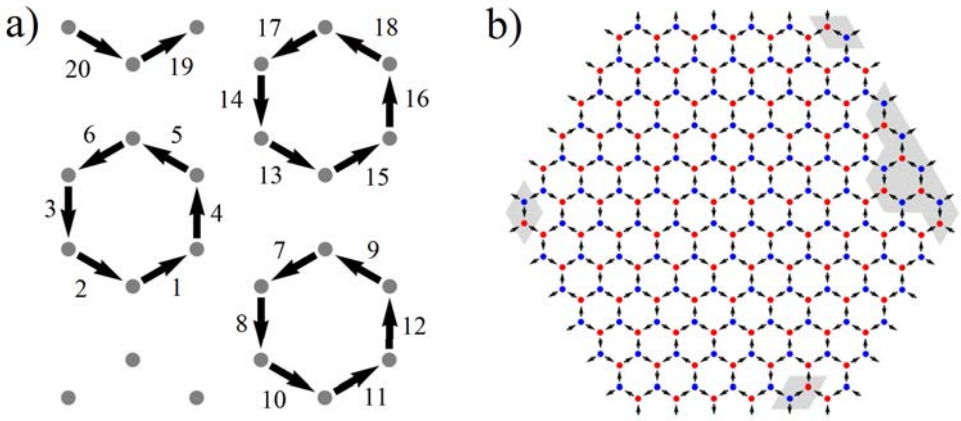

Figure 2.35 - (a) The sequential remagnetization of a kagome spin ice network given by the kinetic algorithm for a dipolar long-range scenario at very low temperatures and with just one nucleation site. The numbers indicate the order in which the spins are magnetized. Notice how loops are formed one at a time and how the algorithm jumps from one loop to another without connecting them. (b) Repeating this process until the whole network is magnetize can yield large charge crystallites, covering almost the entire network.

that "switches-on" the spins one-by-one, taking the model out of the canonical ensemble's framework. This difference in spin dynamics is expected to yield some differences. While the short-range picture displays the same features as the at-equilibrium case, except for the behavior of $C_{\alpha\delta}$ which has a higher absolute value than expected, the long-range model presents more differences, particularly for $C_{\alpha\nu}$ and $C_{\alpha\delta}$ once the spin ice manifold is reached. $C_{\alpha\nu}$ slightly passes to positive values at the onset of the spin ice phase, but then drops to its low temperature value of approximately $-1/3$, whereas in the at-equilibrium case it remains positive until the transition to the spin ice 2 phase begins. $C_{\alpha\delta}$ has an even more striking behavior, quickly dropping to negative values that are close to -0.5, values that the Monte Carlo simulations rarely samples. This indicates an early and pronounced preference for aligning the $\alpha\delta$ pairs antiferromagnetically, possibly in the detriment of other correlations. Furthermore, notice that all correlators target their corresponding dipolar long-range ground state values for very low temperature, though not all reach them. This gives reason to believe that a charge crystal could be achieved by this kinetic process for very low temperatures. Indeed, the charge correlator follows a similar behavior as the Monte Carlo one, a fact that can be seen in the inset of Figure 2.34.b. At very low temperatures, the average correlator is almost -0.9, and for some tryouts an almost perfect charge crystal can be achieved, with a spin texture that resembles strongly to the ground-state configuration. This is, indeed, an exciting feature, but what is the driving mechanism that allows for such a good charge crystallization in the low-temperature regime?

A closer inspection of the sequential remagnetization process reveals that this kinetic algorithm spontaneously favors the formation of short closed-loops of spins that curl around the lattice hexagons[49]. Figure 2.35.a gives an example for a very low temperature ($T/J_{NN} = 10^{-5}$) of how the kinetic algorithm proceeds with spin remagnetization after one initial spin was selected. Notice that, after a hexagonal loop is formed, there is a jump to a neighboring hexagon that is not immediately adjacent to it. This is rather expected, given the maximum local field tracking, as any adjacent spin to the already-formed closed loop would create a complete vertex which has at least one highly-frustrated interaction. Therefore, this algorithm seems to profit from the fact that the spins are initially switched off and then gradually forms closed spin loops that are spatially disconnected from each other, thus avoiding the formation of frustrated vertices and magnetic vertex charges in the early stages[50]. Ultimately, by forming closed loops and filling up the missing spins, large charge crystallites can be formed, as can be seen in Figure 2.35.b, where the final state is an almost perfect charge crystal. Usually, some defects appear near the borders, where the isotropic environment is broken, and an occasional vanishing local field can leave the spins to choose freely between the two possible Ising states. These results are promising, but does this kinetic algorithm reproduce the experimental data features and, if so, which temperature regime is accessed?

A correlation scattering analysis was performed for each simulation type by including the first seven spin correlators and the charge correlator in the spread-out function definition[51]. The experimental points where then placed on the kinetic algorithm plots taking as a temperature the argument for which the minimum value of K(T) is achieved. For the dipolar long-range model, this is usually an effective temperature of about $0.5J_{NN}$ (see Figure 2.36.a). As can be seen, the matching has greatly improved from the Monte Carlo case, and for number of 10 nucleation sites, all correlators fit within the standard deviations of the correlator distributions for the given effective temperature[52]. This also solves the apparent paradox that the Monte Carlo simulations were displaying: the charge correlator

[49]Since such closed loops are formed of antiferromagnetically aligned $\alpha\delta$ pairs, this explains the large absolute values that this spin correlator displays.

[50]This process actually stops when a border is reached. Since the borders spins form unclosed loops, this creates a strong local field on the spins connecting this incomplete border loop to a fully-closed neighboring one. Therefore, at this stage, the spins connecting the otherwise disconnected loops start to be magnetized. If the initial nucleation site is a border spin, then the algorithm will form connected closed-loops from the beginning.

[51]While the effective temperatures may vary slightly, the same results are found if only the spin correlators are included. This contrasts with the mapping on to the Monte Carlo plots, which yields a very poor match if the correlators are mixed.

[52]For n ranging from 1 to 10 initial nucleation sites, there are no significant changes in the matching or the effective temperature. This is because the differences given by the increased number of preset spins are only felt at lower temperatures (see inset of Figure 2.34.b). As the number of nucleation sites increases, the differences are felt for increasingly higher temperatures, but these simulated results do not fit the present data.

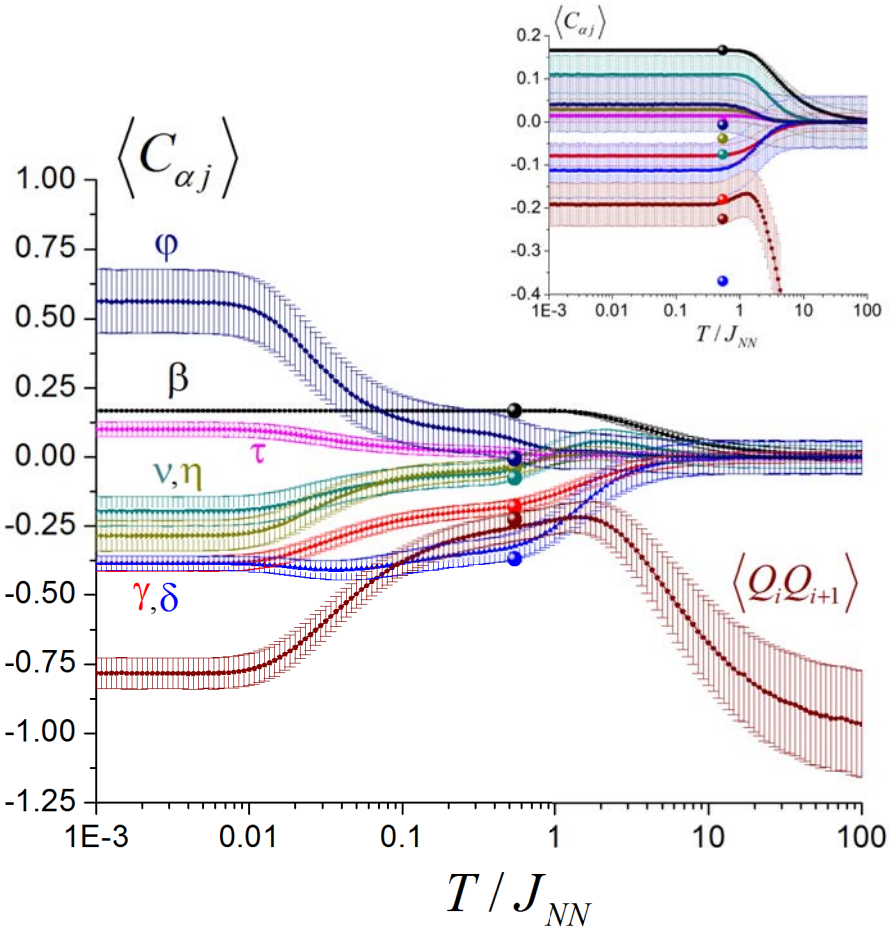

Figure 2.36 - By employing the correlation scattering analysis, a very good agreement is found between the experimental data and the average values of the spin correlators for $T/J_{NN} = 0.54117$. All data point fall within the standard deviations of the corresponding distributions, represented here by error bars. These plots correspond to a simulations performed with 10 preset spins. Notice that no mismatch is found anymore between the spin and charge correlators. This highlights a certain kinetic component of the complex remagnetization process that unfolds at the Curie point crossing. The inset gives the fitting for the short-range model, which, like in Monte Carlo, clearly fails to account for the observed values.

now agrees upon the same effective temperature with the spin correlators. On the other hand, the short range model fails drastically (see inset of Figure 2.36). Not only does it give a poor matching, displaying severe deviations for most correlators, just as in the Monte Carlo case, but it also has difficulty in finding an effective temperature as it slides along the spin ice plateaus while trying to find a spread-out function minimum. This again emphasizes the important role of dipolar long-range interactions in determining the outcome of the annealing procedure and unambiguously highlights how they express themselves in this scenario. The mapping onto the dipolar long-range plots is quite good, and although these artificial kagome spin ices are thermally active, they show some out-of-equilibrium features and the efficiency of the experimental procedure is interpreted in terms of kinetic pathways that the system takes during cooling and ultimately forms large charge crystallites, given the preference for closed-loop spin formations.

This good matching also gives hopes for future work that might take annealed artificial spin ices even further down the effective temperature scale, thus increasing more and more the size of the crystallites and hopefully achieving a perfect charge order. Such a work has been undertaken very recently by Drisko *et al.*[12], who have used a $FePd_3$ magnetic alloy to create thermally-active artificial spin ices. Following the same procedure, they find even larger charge crystallites in the remanent states. They interpret their results using kinetic Monte Carlo simulations and, for a certain degree of quench disorder, they find good agreement with their data. The current kinetic model does not include disorder effects, but does account for eventual pinning centers by setting up several spin directions from the beginning[53]. Therefore, although this kinetic model relies on many assumptions and can still undergo further improvements, it already reproduces very well the experimental data, solving the apparent paradox between the charge correlator and the spin correlators found with Monte Carlo simulations, proving the importance of long-range interactions and unveiling the fingerprints of an out-of-equilibrium process that governs the cooling of these thermally-active artificial spin arrays.

2.7 Summary

At about the same time as Wang *et al.*[1] published their work on lithographically-patterned square arrays of magnetic nano-islands, Tanaka *et al.*[43] reported the experimental realization of a honeycomb tilling of magnetic nano-bars. Since the magnetization inside each

[53]It is therefore no surprise that a simulation with more than just 1 nucleation site reproduces better the data, as the arrays still present disorder effects, island misalignments, which all translate into a distribution of interaction constants for the same coupling type.

nano-bar is uniform, this system can also be regarded as a kagome lattice of in-plane spins that point along the bisectors of each kagome triangle, also referred to as kagome spin ice[71]. Given that all the vertex sites of their experimental network respect the kagome ice rule, they propose a short-range model to describe the properties of such artificial kagome spin ice systems.

If only nearest-neighboring interactions are taken into account, the kagome spin ice network presents remarkable thermodynamic properties. At high temperatures, all 8 possible vertex configurations are equally probable, but as the temperature drops the system gradually enters its ground state manifold, where only ice-like configurations are accepted. This ground state manifold is characterized by a 0.50183 residual entropy/spin value[67], the highest value known for frustrated 2D Ising spin lattices. Also, short-range kagome spin ice presents no long-range spin order[65]. Furthermore, its ground state manifold is characterized by a cooperative-paramagnetic regime[82] which persists down to absolute zero and can be emphasized by the temperature dependence of the magnetic susceptibility. The spins form loop-like configurations that can even stretch from one network edge to the other if periodic boundary conditions are considered. Flipping such a loop can be done with no net energy cost, thus making it an ideal dynamics for exploring the spin ice manifold with Monte Carlo simulations. Furthermore, by taking the dumbbell picture[35], the spin network can be mapped onto a hexagonal network of unitary vertex magnetic charges which prove to be weakly correlated among nearest neighbors in the ground-state regime.

The absence of any "three-in/three-out" vertex configuration within the experimental network studied by Tanaka *et al.*[43] signals the realization of a spin ice configuration. However, due to the relatively high-energy barrier that an element has to overcome to flip its magnetization, the system is frozen at room temperature and cannot further explore its energetic landscape. Also, the reported MFM magnetic charge map does not give any detailed information about the exact orientation of the magnetization of each island, a requirement for assessing the validity of the proposed short-range spin model. Studying a similar artificial kagome spin ice system, Qi *et al.*[46] subjected the arrays to an ac demagnetization protocol[3] and then charted the entire spin configuration of their networks using Lorentz-mode TEM microscopy. By computing the pairwise spin correlators defined by Wills *et al.*[71], they note that, although some experimental values agree with the predictions of the short-range model, several higher-order correlations show significant deviations from the spin ice plateaus. The biased deviations point out that higher-order couplings might play a role during demagnetization and that long-range dipolar interaction should not be excluded. A full dipolar treatment is therefore necessary.

Within the long-range dipolar model, the kagome spin ice network fully recovers its spin ice residual entropy/spin, as proven by Monte Carlo simulations[7, 8]. However, it does this in two steps. Firstly, the system passes from a spin ice regime with disordered magnetic charges into a so-called spin ice 2 regime characterized by a magnetic charge crystal enclosed in a partially-disordered spin network which exhibits a clear preference for loop-like configurations. Single spin-flips prove to be very inefficient in mapping this emerging charge order manifold with Monte Carlo simulations, but this critical slowing down effect can be overcome by flipping the closed spin-loops and the system is finally driven into its ordered spin state. Although the macroscopic degeneracy of the short-range kagome spin ice is gradually lifted, the prospect of realizing a kagome spin network with a hidden $\mathbb{Z}_2$ emerging order is quite appealing. However, since the only method used so far for athermal artificial arrays is demagnetization, which model should be used to best describe its output?

Bridging the resulting magnetic configuration of a demagnetized artificial spin systems with the snapshots given by Monte Carlo simulations of corresponding spin models requires the assumption of a certain interaction model, particularly for the simulations. This model should be chosen in accordance with the nature of the interactions present in the real samples. In this case, the nano-islands are in a magnetostatic framework and coupled solely through their dipolar stray fields. The absence of long range couplings would therefore be quite remarkable, and it has been reported for artificial square lattices[1]. The short range model assumes that interactions beyond nearest-neighbors can be neglected and can reproduce some of the features of demagnetized artificial kagome spin ices[46]. However, a full dipolar model manages to better explain the spin correlations computed from the final magnetic state of artificial kagome spin ice arrays, as reported by Rougemaille *et al.*[73]. In particular, their nearest-neighbor charge correlation values obtained via demagnetization deviate quite drastically from the expected $-1/9$ plateau specific to the short-range model, but are in good agreement with the predictions of the dipolar long-range Monte Carlo simulations. Therefore, Rougemaille *et al.*[73] conclude that long-range dipolar interactions should be considered when describing the outcome of a demagnetized artificial kagome spin ice network. This is an exciting result that encourages the further exploration of the lower-energy manifolds of dipolar kagome spin ice in the quest for the magnetic charge crystal. The recently-introduced annealing techniques promise to be useful for this task.

Thermally-active artificial spin arrays have long been a goal for the community in the quest for ground-state order or exotic spin textures that cannot be accessed with ac demagnetization protocols. Two main directions have been proposed so-far: working in the superparamagnetic regime[5, 49, 53, 97, 99], usually requiring a tailoring of the size of the magnetic elements, and annealing the arrays above the critical temperature of the magnetic

film material and then cooling the sample back to room temperature[6, 10–12, 98], also requiring a certain engineering of the magnetic alloy employed. Both approaches manage to surpass the limits of ac demagnetization in the case of the square ice network, revealing large type I ground-state domains[6, 49] and even perfect spin order[52]. However, the highly frustrated kagome spin ice array still remains a challenge in this context, as even small clusters of hexagonal rings cannot access their corresponding ground-state configuration under the influence of thermal fluctuations[53]. Nevertheless, Zhang *et al.*[6] have reported the formation of large charge crystallites embedded in a disorder artificial spin lattice made of permalloy nano-islands by following the second procedure. Using an effective nearest-neighbor charge-charge interaction model and simulating the system's behavior through Monte Carlo simulations, they find good agreement with the experimental data, establishing that the ground-state of their effective Hamiltonian has been locally accessed and that these configurations correspond to truly thermalized states.

This chapter has presented results obtained following a similar procedure to that of Zhang *et al.*[6], but involving a GdCo ferrimagnetic alloy for which the Curie point can be tuned to lower temperature values, closer to the room temperature one. The experimental data presents similar features to that of Zhang *et al.*[6] and by computing the spin correlations within the charge crystallites, it has been shown that these are characteristic to spin ice 2 textures. However, mapping the experimental points onto the at-equilibrium thermodynamic predictions reveals a certain paradox: while the network-averaged spin correlators are characteristic to a deep spin ice phase, the charge correlator is specific to a high-temperature spin ice regime. This is a signature of a possible out-of-equilibrium process that most likely occurs while the network remagnetizes as the cooling crosses the critical temperature point. A kinetic model has thus been proposed that sequentially remagnetizes the network spins by tracking the maximum local field values and selecting the spin states according to a Boltzmann-type probability. The simulation captures very well the experimental data, solving the apparent contradiction between the correlators. In addition, this kinetic algorithm reveals how the annealing procedure profits from the absence of magnetized spins and conveniently remagnetizes them, creating closed spin loops and thus directly aiming for low energy spin configurations. This contrasts with the superparamagnetic approach which has to deal with all the spin interactions at the same time and the slightest thermally-induced modification can result in additional frustration being created, thus making the search for low energy textures very difficult and time-demanding. In fact, this mimicks the critical slowing down effect encountered by the simulated single-spin flip dynamics when the system start to transit to the spin ice 2 phase. This effect is somewhat avoided and the efficiency of this annealing

approach is interpreted in terms of kinetic remagnetization pathways which ultimately yield a frozen low-energy configuration with local charge order.

With the introduction of thermally-active artificial spin ices, it can be said that these nano-engineered arrays have entered in a second-generation era. However, while lower energy manifolds are yet to be accessed for some of the already-investigated networks, several other geometries are yet to be fabricated and explored, possibly revealing novel exotic spin textures. This is, in fact, the topic of the following chapter, which is dedicated to the study of a new artificial spin network: the kagome Ising array.

Chapter 3

Artificial Kagome Ising - A Novel Dipolar Kagome Array

3.1 Introduction to Artificial Arrays with Out-of-Plane Magnetic Moments

Artificial spin ice systems have proven to be an exciting playground for the exploration of frustration effects in two-dimensional lattices of magnetically coupled nanoislands[95, 96]. Over the past years, square and kagome lattices with in-plane magnetized elements have drawn most of the community's attention and their energetic landscapes have been intensively explored via demagnetization protocols[1, 3, 44, 46, 54, 55, 72, 73, 83, 85–87, 92, 107–110] and, more recently, with thermal annealing techniques[4–6, 10, 11, 52, 53]. The latter approach has proven to be an efficient way of driving square ice into its ground state configuration[6, 52] and it also manages to locally bring the kagome network into the spin ice II phase, as large crystallites of magnetic charges emerge from a partially-disordered spin background[6, 10–12].

The possibilities for exploring and engineering frustration effects in 2D lattices seem almost limitless within the framework initially proposed by Wang *et al.*[1], but other geometries remain rather unexplored, with just a few studies focusing on other types of networks such as the triangular geometry [111–113] and, the shakti network [100, 114]. Another avenue for the investigation of frustration effects and the potential discovery of exotic magnetic phases in two-dimensional lattices is to create artificial spin systems with out-of-plane magnetic moments [13, 14, 45].

Patterned arrays of nanoislands with perpendicular magnetic anisotropy are of particular interest for the magnetic recording industry. The passage from in-plane magnetized layers

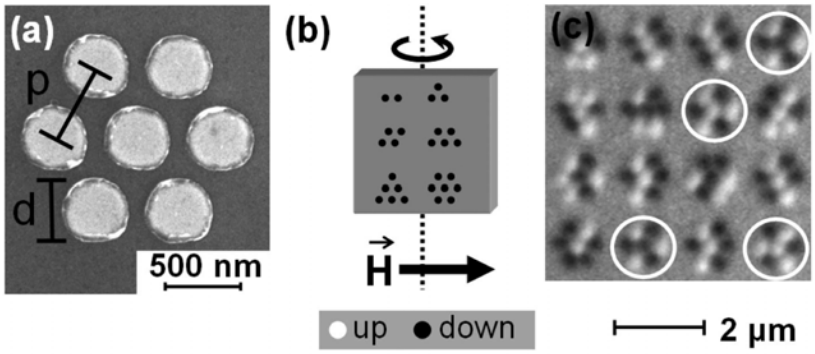

Figure 3.1 - (a) A Scannig Electron Microscopy image of a cluster of [Co/Pt] nanodots with perpendicular magnetic anisotropy. The diameter of an island is about 410nm while the center-to-center distance is set to 510nm. (b) Clusters of all sizes were demagnetized by linearly decreasing the amplitude of the external field while the sample rotated about an axis perpendicular to the field's direction. (c) An XMCD scan for several clusters of 7 nanodots reveals their remanent magnetic configuration. Each island has either a bright or dark contrast, corresponding to the two possible orientations along the vertical axis. This also highlights their effective monodomain nature of each nanodot. The encircled clusters correspond to ground state configurations. After Mengotti *et al.*[45].

to perpendicularly-magnetized thin films has already increased the storage capacity of hard drives[115, 116], but challenges such as the superparamagnetic limit and the signal-to-noise ratio (SNR) still remain[117]. The latter arises from the microstructure of thin-film based hard drives, as there is no clearly-defined limit between one bit and its neighbors within a track. Patterned perpendicularly-magnetized media stand as a possible route for addressing these issues, as each island can act as a localized, massive, single bit of information. However, if such a technology is to be successful it needs to guarantee both higher areal density and improved thermal stability than the current ones[117] and also be more cost-efficient[118]. Recent years have seen a growing interest in the fabrication and characterization of such devices, with promising results for improving the areal density[119, 120]. To maximize the areal density and the sensitivity of the read/write head, a tightly packed network of uniformly-magnetized, high-moment nanoislands with perpendicular magnetization is desired. However, this also implies strong interactions between these elements, which can potentially lead to the self-demagnetization of the track, hence losing stored information[117]. The study of the collective behavior and the response to external fields of such arrays of perpendicularly-magnetized nanoislands is therefore important. Such aspects have also been addressed by the artificial spin ice community, but the general goal here is the understanding of how competing interactions can eventually lead to new and exotic magnetic phases. For instance, Mengotti *et al.*[45] studied the response to ac demagnetization of clusters of [Co/Pt] multilayer nanodots with perpendicular magnetic anisotropy. Similarly to their study of the building blocks of kagome spin ice[44], they identified the lowest energy states for clusters of artificial triangular

networks of Ising spins and reported that, for cluster sizes ranging from 2 to 7 elements, they managed to reach the ground state configurations using ac demagnetization protocols (see Figure 3.1). However, such building blocks often exhibit a different behavior than the bulk of the networks and while ac demagnetization can sometimes retrieve ground state configurations for a few kagome spin ice rings[44], this protocol has proven to fail at the array-scale when used to reach low energy manifolds[73]. Can such a protocol then access the low energy phases for a network of perpendicularly-magnetized interacting nanodots?

To address this question, Zhang *et al.*[13] fabricated both frustrated (kagome) and unfrustrated (hexagonal) networks of islands with out-of-plane magnetic moments (see Figure 3.2). Their samples were patterned out of a multilayer film of $[Co(3Å)/Pt(8Å)]_8$, similarly to the procedure used by Mengotti *et al.*[45] to create the above-mentioned clusters. Due to the uniaxial anisotropy induced by the Co/Pt interface, the magnetization prefers to be aligned with the vertical axis. Furthermore, given the size, shape and materials chosen, the magnetization of an island is uniform and the magnetic moment is in the order of $10^7 \mu_B$. The islands are coupled via the magnetostatic interaction and since they are all pointing along the *Oz* axis, the coupling between any chosen pair is always antiferromagnetic. This contrasts with the in-plane magnetized networks seen before, the square and kagome spin ices, where the coupling can be either ferromagnetic or antiferromagnetic, depending on the relative position of the two chosen spins. Since there is a single quantification axis, these artificial networks can be referred to as artificial hexagonal/kagome Ising networks[14][1].

Like most of their in-plane counterparts, the hexagonal and kagome networks studied by Zhang *et al.*[13] have high energetic barriers separating the *up* and *down* states of an island's magnetization, thus rendering them practically insensitive to thermal fluctuations at room temperature. A demagnetization protocol was therefore employed to enable the islands to accommodate their pairwise couplings[3]. Similarly to the in-plane case, the protocol implies the application of a field along the vertical axis while slowly decaying its amplitude and reversing the polarity at each field step. The remanent states were extracted using Magnetic Force Microscopy (see Figure 3.2). For both geometries, Zhang *et al.*[13] studied networks with different lattice constants, thus tuning the inter-island coupling.

The hexagonal network is a bipartite network, exhibiting no short-range frustration, and is therefore expected to order itself antiferromagnetically. Indeed, Zhang *et al.*[13] observed large domains of antiferromagnetically ordered spins for tightly packed islands.

[1] This nomenclature can be misleading as even in square or kagome spin ice networks the spins are also of Ising type. However, Ising spins are usually associated with a vertical quantification axis and it is within this spirit that the term *kagome Ising* was introduced. I shall occasionally refer to the kagome Ising network as the *kagome uniaxial* network, in contrast with kagome spin ice which requires three axis of quantification, thus being called the *kagome multiaxial* network.

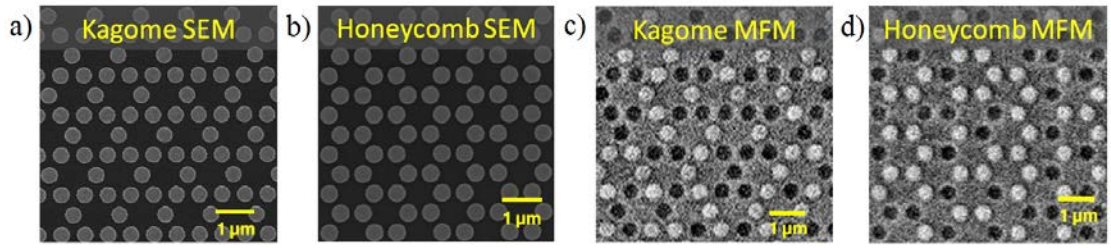

Figure 3.2 - (a,b) Scanning Electron Microscopy (SEM) and (c,d) Magnetic Force Microscopy (MFM) images of kagome and hexagonal/honeycomb lattices of [Co/Pt] nanodots with out-of-plane magnetic moments. (a-b) The radius of the islands is set to 200nm while the inter-island spacing is varied from 500nm to 1200nm, tuning the coupling strength. The presented arrays have a center-to-center distance of 600nm. (c-d) The uniform bright and dark contrasts of the islands emphasize that they are magnetic monodomains. (c) Note that, after demagnetization, most triangles of the kagome lattice respect the kagome ice rule, but there are nevertheless some exceptions. After Zhang *et al.*[13].

On the other hand, the kagome network is made up of triangles and since all interactions are antiferromagnetic there is no way of satisfying all pairwise couplings within a triangle. The minimum compromise that can be locally achieved is to have two islands pointing *up* and one down or two *down* and one *up*. This is, in fact, an adaptation for the kagome Ising network of the kagome ice rules seen before. The MFM images presented by Zhang *et al.*[13] indeed show that the kagome triangles tend to respect this nearest-neighbor constrain (see Figure3.2.c). However, is there any signature of a long-range spin order?

To characterize the order established in both hexagonal and kagome networks, Zhang *et al.*[13] computed the pairwise spin correlations up to the seventh order, similarly to what has been done for artificial kagome spin ices[46, 73, 107]. They argue that the extracted correlation values can be very well described by models involving only nearest-neighboring interactions, despite the long-range nature of the magnetostatic coupling between the islands[2]. Therefore, demagnetized artificial kagome Ising networks appear to be effectively short-ranged, just as it was initially reported for artificial kagome spin ices[46]. In addition, they also observe a very good matching between these kagome Ising spin correlations and those obtained for artificial kagome spin ice by ac demagnetization. This lead them to conclude that there is a universality in the development of pairwise spin correlations for a given network topology of a demagnetized artificial spin array[13]. In other words, the particular orientation of the Ising-like spins seems to be irrelevant and the network geometry appears to be the

[2]It is important to mention that a prior study performed on an alternative version of artificial kagome systems made up of magnetostatically-coupled superconducting rings points towards the same conclusion: the observed magnetic configurations show only short-range correlations and long-range order is very likely prevented by the high degree of disorder within the system[37].

only important factor that determines the order established at the output of a demagnetization process.

However, recent studies on the remanent states of a demagnetized artificial kagome Ising arrays point towards a different conclusion: the final frozen configurations of an ac demagnetized artificial kagome Ising network are better described by the dipolar spin ice model[14]. Similarly to what Rougemaille *et al.*[73] reported for kagome spin ice, these results highlight the fingerprints of long-range interactions between such perpendicularly-magnetized islands and emphasize that these couplings cannot be neglected when describing the demagnetization output. While the two kagome networks present similar behavior down to a certain point, they afterwards show clear distinctive features within this long-range framework. There are thus clear limits to the universality reported by Zhang *et al.*[13] and these results already offer such examples [14]. In other words, the artificial kagome Ising network has its own story to tell, thus enriching the spectrum of exotic low-energy manifolds that can potentially be explored with such artificial arrays.

This chapter gives a detailed description of these experimental results along with supporting numerical data, as reported in reference[14]. I shall firstly present the experimental approach by describing the sample, the demagnetization runs and the final output states characterized by Magnetic Force Microscopy. The thermodynamic behavior of kagome Ising networks governed by both short-range and long-range dipolar interactions will be afterwards presented and contrasted. A discussion section reflecting the differences between the two artificial realizations of the kagome geometry and the limits of the reported universality will follow. In addition to these published results[14], I shall afterwards focus on the thermodynamic behavior of the kagome Ising network and present a candidate for the long-range ordered ground state. To the best of my knowledge, the ground state configuration within this long-range dipolar picture for the kagome network with vertically-aligned Ising spins remains, so far, unknown.

3.2 Experimental Investigation of Artificial Kagome Ising Networks

3.2.1 The Sample

The artificial networks with perpendicular Ising moments presented in this work were fabricated by Michel Hehn, François Montaigne and Daniel Lacour at the Jean Lamour Institute in Nancy, France. The arrays were patterned out of $Si//Ta(5nm)/TbCo(40nm)/Ru(2nm)$ magnetic thin films grown on a *Si* substrate using a UHV sputtering machine in DC mode.

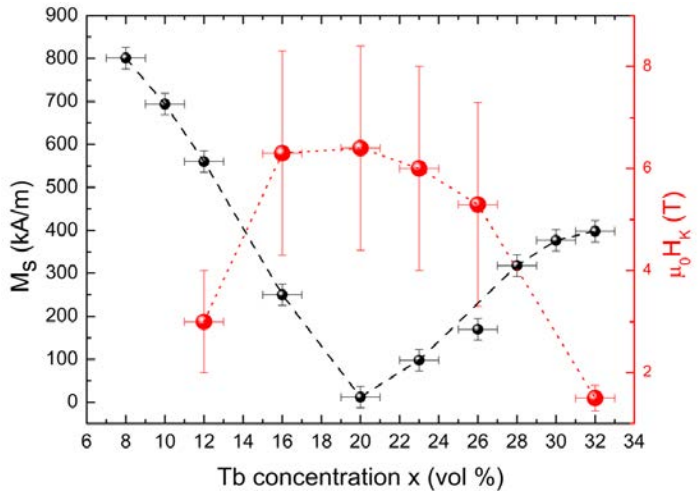

Figure 3.3 - The spontaneous magnetizations and the reversal fields at room temperature for different compositions of a Tb_xCo_{1-x} 20nm thin film. After Alebrand *et al.*[121].

The magnetic alloy's composition can be tuned by adjusting the relative sputtering power for the Co and Tb targets. The current films have a $Tb_{12}Co_{88}$ composition and have been deposited on a 5nm Tantalum sublayer, insuring a good adhesion to this substrate, and the magnetic film was capped with a 2nm layer of Ruthenium to prevent oxidation[3].

The $Tb_{1-x}Co_x$ alloy is part of the rare-earth transition-metal alloy class ($RE_{1-x}TM_x$), just like the GdCo alloy used to for the fabrication of the thermally-active artificial kagome spin ice arrays presented in section 3.2. The exchange interaction between the different metallic species leads to a ferrimagnetic type alloy[104]. However, these alloys are generally amorphous and the randomness arising from the noncrystalline structure translates into a randomness in the local orientation of the crystal field axes for the RE elements [103, 104], thus yielding an angular distribution of the RE moments orientation. However, these moments do not completely cancel out and these so-called sperimagnetic alloys still present a spontaneous magnetization, which varies with temperature and composition ratio (see Figure 3.3.). TbCo alloys fall into this sperimagnetic category and present a strong uniaxial anisotropy, the origins of which are not fully understood[104][4]. However, the bias voltage during sputtering and the stress induced by the substrate appear to play an important role in determining the magnitude and direction of the uniaxial anisotropy[104, 122–124]. The current $Tb_{12}Co_{88}$ films are in a Co-rich regime, presenting an anisotropic easy axis, perpendicular to the film's surface[125], and a spontaneous magnetization of about 560kA/m at room temperature[121].

[3]Ruthenium also has a good transmission for X-rays, which is ideal for XMCD-PEEM measurements.

[4]There is quite a vast bibliography on this matter, which surpasses the framework of this thesis. For more details, one should consult the work of Hansen *et al.*[104] and the references therein.

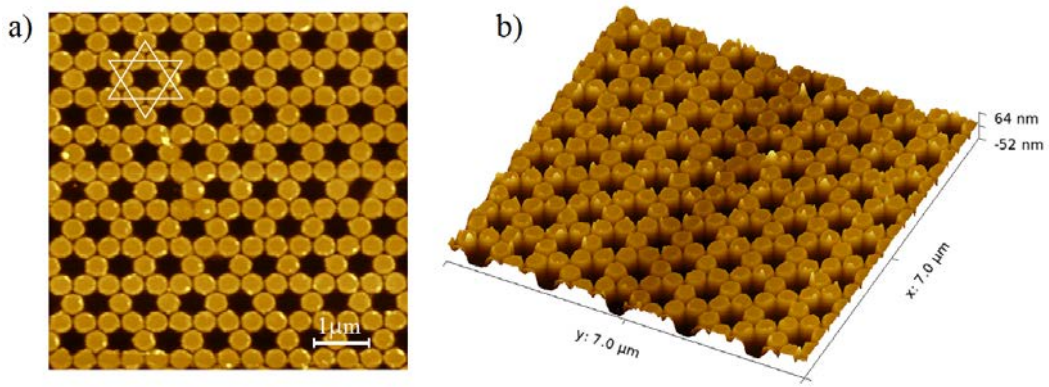

Figure 3.4 - (a) An AFM scan of the topography of a region of a kagome network of nanodots patterned out of a $Tb_{12}Co_{88}$ magnetic layer. Each island has an average radius of 150nm and the spacing between nearest neighbors is set to 400nm, yielding a tightly packed network. (b) A 3D reconstruction of the scanned surface using the Gwyddion software[126]. While the average height is about 65nm, higher values are sometimes measured due to the presence of contaminating agents or rough island edges.

The patterning of the films was performed using electron-beam lithography with a double-layer positive resist and an Aluminum mask. The masks were predefined to yield kagome, hexagonal and triangular arrays[5]. After mask lift-off, the exposed regions were ion-beam etched, yielding nanodots with an average diameter of 300nm and an average height of about 65nm. The center-to-center distance between neighboring islands is set to 400nm, insuring that they are physically separated by an average gap of 100nm. An atomic force microscopy (AFM) scan of a region of the kagome array is given in Figure 3.4.a along with a three dimensional reconstruction in Figure 3.4.b. The arrays are square shaped, with a side-length of about $28\mu m$, and normally contain 4869 nanodots[6].

Given the knowledge of the shape and the size of the islands as well as the sponatenous magnetization of the TbCo layer for the given composition, the individual island moments and the inter-island coupling can be estimated. It should be noted that these are estimations based on the data acquired form other works[121, 125] and that no experimental determination of these quantities has been performed during this work, except for the switching field distributions. Magnetic Force Microscopy scans confirmed that each island behaves as a single magnetic unit and, like in previous cases[13, 45], these nanodots act as an individual single massive spin, as if the magnetization inside it were uniform. For a 300nm diamater, a

[5] Although some triangular and hexagonal arrays were also studied, the focus has been on kagome arrays and results on the former array types are not presented in this work.

[6] Unfortunately, the sample has been contaminated over time and some areas can no longer be properly mapped with an AFM/MFM scan. Some islands are even missing, possibly being removed during the lift-off process.

40nm TbCo layer height and a spontaneous magnetization of 560kA/m[121], the magnetic moment of an islands is about $\mu \sim 1.7 \cdot 10^8 \mu_B$. This is almost three times higher than the magnetic moment reported by Zhang *et al.*[13]. Furthermore, the inter-island coupling can also be estimated using the point-dipole approximation[7] and the maximum value of the local effective field can be computed[8]. This corresponds to the situation in which all spins point in the same direction. For the given sample parameters, the nearest-neighbor dipolar coupling is $D_{eff} = \frac{\mu_0}{4\pi}\frac{\mu^2}{r_{nn}^3} \sim 23.44eV$ and the maximum value of the local field is about $\mu_0 H_{local}^{max} \sim 23mT$. Although this value is quite high, highlighting the strength of the inter-island coupling, it is not sufficient to self-demagnetize the array as the island switching fields are higher than this maximum local field. In fact, the switching field values are roughly distributed between $89mT$ and $278mT$, with an average switching field of about $\mu_0 H_{SF} \sim 167mT$ (see Appendix F for details). This implies that the energy barrier that has to be overcome to flip the magnetization of an island is four orders of magnitude higher than the thermal energy at room temperature.

Just like in the case of Zhang *et al.*[13], the high value of the energy barrier highlights the athermal nature of these networks. Therefore, thermal fluctuations at room temperature cannot be relied upon for the exploration of the complex energetic landscapes of these artificial frustrated topologies. Similarly to previous works[3, 13, 45], an ac demagnetization protocol has been used to drive these arrays into low-energy configurations. In the following section I shall describe the demagnetization protocol employed and the different demagnetization runs.

3.2.2 Demagnetization

In the case of artificial arrays with in-plane magnetized spins, demagnetization protocols usually involve the application of a magnetic field in the network's plane, sufficiently high-enough for achieving saturation, and then slowly decaying its amplitude with small field steps down to zero[3]. However, in-plane networks have two ore more axes along which the constituting elements are pointing and the sample plane needs to be rotated during the demagnetization process to avoid the favoring of one particular in-plane direction. For perpendicularly-magnetized samples, all moments are aligned with the vertical axis and demagnetization can be performed without necessarily rotating the sample. For the current

[7] As it will be shown in section 3.3.2, the point dipole approximation works quite well for out-of-plane geometries. The deviation for nearest neighbors estimated with micromagnetic simulations is about 150%, unlike in the in-plane networks where it can rise up to 500% for disconnected latices [73]. Higher order couplings match very well the dipolar approximation values.

[8] The energy can be rewritten as $E = -J_{ij} \cdot \sum_{(i,j)} \sigma_i \cdot \sigma_j = -\sigma_i \cdot H_{eff}^i$, where $H_{eff}^i = \sum_j J_{(i,j)} \cdot \sigma_j$ is an effective local field felt by spin i as a result of the interactions with all its neighbors.

work, a sinus-type field signal was applied parallel to the island moments and the field amplitude was slowly decayed down to zero over time (see Figure 3.5.a). Another equivalent technique is to linearly drop the field to zero while the sample is rotating about an axis perpendicular to the field direction[13, 45][9].

There are three distinctive regions in the time-line of a demagnetization run (see Figure 3.5). Firstly, the field is high enough to fully saturate the network and all islands follow the field direction. The second region is defined by the distribution of the islands' switching fields, with an additional broadening due to the inter-island coupling. It is within this region that all spin-flips occur and where the array gradually and selectively accommodates pair island interactions and frustration effects. Finally, the last region corresponds to applied fields for which reversals cannot be triggered any longer and the state selected at the exit of the second region is normally preserved until the end of the demagnetization session. Hence, the most important region is the window of the switching fields and the demagnetization protocol should be implemented so that the time spent within this region is as high as possible.

The flip of an island's moment can be realized if its total effective field (the sum of the external field and the local effective field given by interactions with neighboring islands) is higher than the island's own switching field. Of course, flips can only occur if the spins are not aligned with the applied field. These conditions can be summarized into the following mathematical form:

$$-\vec{S}_i \cdot \vec{H^i_{eff}} \geqslant H^i_{SF} \tag{3.1}$$

where $\vec{S}_i$ is a spin of the network, $\vec{H^i_{eff}} = \vec{H^i_{local}} + \vec{H}_0$ is the effective field felt by this spin and H^i_{SF} stands for its intrinsic switching field. Since all these vectors are pointing along the vertical direction, the relation can be reduced to a scalar form:

$$-\sigma_i \cdot (H_0 + H^i_{local}) \geqslant H^i_{SF} \tag{3.2}$$

where $\vec{S}_i = \sigma_i \cdot \vec{e}_z$, while H^i_0 and H^i_{local} are the projection of the applied and local effective fields along the vertical axis. In an ideal scenario, all interactions are isotropic and all islands share the same switching field. In this case, the first flips normally occur when $H_0 = H_{SF} - H^{max}_{local}$. However, if a flip is performed, the local effective field of every neighboring

[9]The two approaches are, indeed, equivalent. However, Zhang *et al.*[13] have chosen a combination between the two by rotating the sample and additionally switching the field's polarity at each step. During the abrupt field ramping, island switching can also occur and this slightly increases the total number of switching scenarios the network exhibits during the whole demagnetization run.

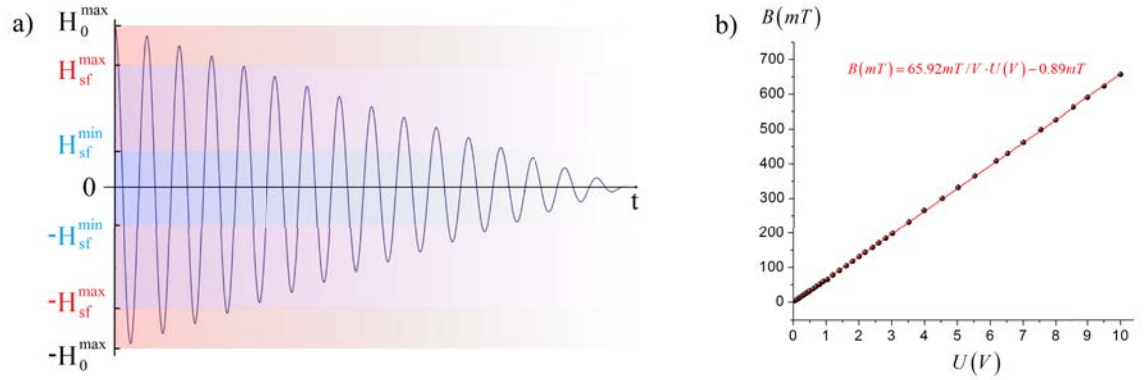

Figure 3.5 - (a) The linear time decay of the external field during an ac demagnetization run. There are three distinctive applied field regimes: the high-field regime (red) in which the network is fully saturated, the switching field window (purple) during which the inter-island couplings are accommodated by individual island reversals and the low-field regime (blue) where the driving field can no longer trigger any flips. The applied field window for which flips occur for the networks presented in this work ranges roughly between $66mT$ and $301mT$ (see Appendix F). (b) The field-voltage calibration for the coil used for sample demagnetization (data courtesy of Van-Dai Nguyen).

island changes and the above condition needs to be updated[10]. In addition, given the fact that the interactions are magnetostatically driven, this update should be made at the array scale, although the effect decays rapidly with increasing inter-island distance. Therefore, after a spin-flip, the corresponding island can no longer change its orientation while aligned with the field, but it can influence the switching of neighboring islands. Since all pairwise couplings are antiferromagnetic, the higher the number of oppositely-oriented neighbors an island has, the more difficult it is to reverse its magnetization. In fact, the inter-island couplings shift the hysteresis loop of an island in the direction for which a reversal is unfavorable. As the external field amplitude continues to drop within this window, the islands' magnetization will freeze as soon as the Zeeman energy supplied by the external field is no longer sufficient to overcome the intrinsic energy barriers separating the *up* and *down* states. In addition, these barriers are reinforced by the contributions from the neighboring interactions. This way, frustration effects are gradually accommodated.

Before moving on to the demagnetization runs, it is important to remind that this procedure is a one-shot energy-minimization approach, as each island has only one opportunity to flip during a field ramping. This is in sharp contrast with the ergodic mapping of the energetic manifolds during thermalization. In his PhD thesis, Jason P. Morgan suggestively describes

[10]This assumes that the time evolution of the external field is slow compared to the timescale for the reversal of an island's magnetization. The latter is usually in the order of nanoseconds and, given the demagnetization parameters used in this work, the highest ramping rate during experiments is in the order of hundreds of mT/s. It can therefore be assumed that the process is quasi-static and that all island flips that can occur for a given applied field value have the time to do so.

demagnetization as being more like "stirring a box of sand rather than shaking it"[127]. Still, it is expected to yield some energy minimization, although the ground state hasn't been reached so far by applying such a procedure to in-plane magnetized networks. Nevertheless, the field step should be taken as low as possible to ensure that no scenarios are overlooked within the switching field window. However, even in the limit $\Delta H \to 0$, demagnetized in-plane networks cannot access their ground state manifolds[83] and a plausible cause for the inability to reach lower energy states can be related to the intrinsic, quench disorder within the arrays. There are many different types of disorder that can arise from sample fabrication such as switching field disorder, inter-island coupling disorder, positioning disorder and island orientation disorder[85]. By simulating the response of artificial square spin ices to different external field protocols, Budrikis *et al.*[85] found that the above-mentioned disorder types yield similar results, regardless of their particular origin. Through a quantitative analysis of the square vertex types, they distinguish two disorder regimes: a weak disorder regime, in which the remanent states are very similar to those obtained for an ideal network, and a strong disorder regime where pinning centers severely alter the demagnetization pathways and prevent the local accommodation of competing interactions. Therefore, a relatively high disorder value could limit the access to low-energy manifolds, yielding only small ground state domains for artificial square ice[86] and an apparent short-range order for artificial kagome networks[13, 72]. Although disorder can enrich the ensemble of demagnetization scenarios for a rotating constant-magnitude field protocol, it still renders higher energy states than those found for perfect networks[92]. Therefore, reducing disorder is important and by working with connected islands rather than separated ones in the case of artificial kagome spin ices, disorder has been reduced by one order of magnitude[47]. However, this is not an option for perpendicularly magnetized artificial networks since this will, in fact, destroy the network of individual, separated islands.

The sample was placed between the poles of an electromagnet in a region where the generated field is expected to be uniform. The electromagnet was connected to a *KEPCO*® AC/DC power supply which amplifies a sinus-type signal received from a low-frequency signal generator (LFG). The amplitude decays are assured through a LabView application program previously developed by Edouard Wagner at the Néel Institute in Grenoble. The input parameters that can be independently adjusted are the initial amplitude of the signal (U_0), the amplitude step value (ΔU), the frequency of the signal (f) and the number of periods for a given amplitude (n). The total demagnetization time (τ) is therefore:

$$\tau = \frac{n}{f} \cdot \frac{U_0}{\Delta U} \tag{3.3}$$

Table 3.1 - The parameters of the three demagnetization runs performed on artificial kagome Ising arrays. The first two runs are identical while the third run has a 16 times higher runtime and is expected to be more efficient.

Demagnetization	$U_0(V)$	$B_0(mT)$	$\Delta U(mV)$	$\Delta B(mT)$	n	τ
Run 1	6	400	8	0.52	2	$4h10min$
Run 2	6	400	8	0.52	2	$4h10min$
Run 3	6	400	1	0.066	4	$66h40min$

The field calibration of the electromagnet is given in Figure 3.5.b. For an applied voltage of 6V, the field between the poles is about $400mT$, high enough to saturate the sample, since the island switching fields vary roughly between $89mT$ and $278mT$ (in view of what was said earlier, the applied field window is larger than this interval and spans between $66mT$ and $301mT$.). This allows us to minimize the time the system spends in the first part of the demagnetization cycle by taking an initial amplitude which is slightly higher than the maximum switching field. The signal frequency was set to $f = 100mHz$ for all demagnetization runs.

In total, three demagnetization sessions have been performed, the parameters of which are given in Table 3.1. Although the first two demagnetizations runs are identical, the third one has a significantly higher runtime. In fact, the goal here was to study the role of the field step and how it can affect the protocol's efficiency. Also, since the first two runs share the same setup parameters, it is interesting to see if the same magnetic configuration is found in both cases.

After each demagnetization session, the remanent magnetic configurations of the arrays were mapped using Magnetic Force Microscopy. Results for each demagnetization run are detailed in the next section.

3.2.3 Magnetic Force Microscopy - Demagnetization Outputs

The magnetic configurations of all demagnetized kagome networks were imaged using a NT-MDT® NTegra-Aura Microscope operating in MFM mode. The stray field from the perpendicularly magnetized nanodots is quite intense and medium coercivity tips need to be used to avoid the flipping of the tip's magnetization due to sample-tip interaction. To this end, Nanosensor® PPP-MFMR tips have mostly been used, yielding a good spatial resolution and a high-quality magnetic contrast (see Figure 3.6). For each scanning line, a semi-contact/tapping mode is firstly employed to retrieve the surface topography (see Figure 3.4), followed by a secondary scan to map the magnetic configuration. This second

Table 3.2 - The remanent magnetization/spin (m) along with the forbidden states ratio (FSR) extracted form the 10 MFM images. Each reconstructed image contains about 1000 spins, except for the last two which are bigger. The low magnetization/spin and the relatively small number of highly-frustrated sites suggest that the demagnetization procedure employed is rather efficient for accomodating inter-island interactions.

Index	Demag	N_{spins}	m	FSR
1	Run 1	1005	-0.0182167	3.5672%
2	Run 1	1046	-0.0305927	4.0456%
3	Run 1	1039	-0.0284143	7.8888%
4	Run 1	1087	-0.0413983	3.3881%
5	Run 2	1058	0.0240296	2.4070%
6	Run 2	1036	-0.030888	3.0884%
7	Run 2	982	-0.021611	5.9096%
8	Run 2	977	-0.0214505	5.5236%
9	Run 3	1401	0.00054288	2.7119%
10	Run 3	1269	-0.0179267	5.0788%

scan is performed at a predefined lift-off height and follows the topography profile. Some general aspects on Magnetic Force Microscopy are given in Appendix B.

To achieve high-quality images for both the topography and the magnetic configuration, a high number of scanning lines is required. However, this can significantly increase the probing time, particularly if the entire array is directly scanned ($28\mu m \times 28\mu m$) as a low scanning frequency is necessary in this case to avoid destroying the tip. Therefore, the arrays were scanned by regions/quadrants containing about 1000 spins each[11].

To determine the efficiency of the demagnetization protocol employed and also characterize the established order within the network, the remanent magnetization and the pairwise spin correlations need to be computed. To this end, the magnetic configuration of each MFM image needs to be reconstructed and this has been done automatically using a *MATHEMATICA* analysis program previously developed by Benjamin Canals[12]. The computed quantities for all 10 MFM images are given in Tables 3.2 and 3.3[13].

The average residual magnetization/spin is about -0.0186, indicating that the demagnetization procedure employed is quite efficient in reducing the overall self-demagnetizing field of the network. This is a mandatory, but not sufficient condition for achieving ground

[11] The last two images contain more than 1000 spins. This has been taken into account when a comparison to simulation data is performed, as it will be seen later on.

[12] Basically, the program detects the "up" and "down" state of each spin by a spatial average of the pixel intensity. This ultimately yields a kagome network in which the position and state of each component is known, which can then facilitate the computation of relevant physical and statistical quantities.

[13] All MFM images can be found in Appendix E.

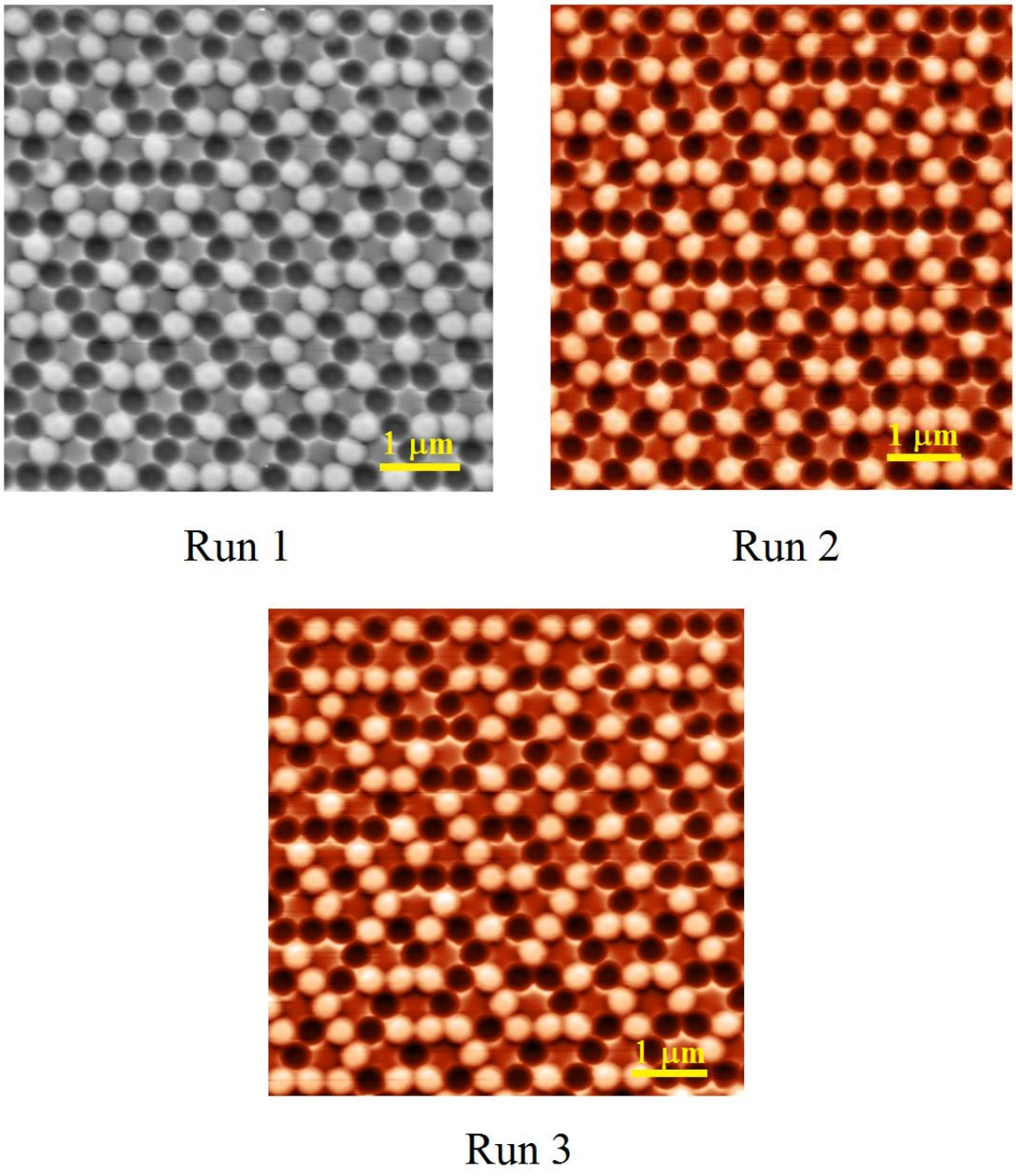

Figure 3.6 - MFM reconstructions of the magnetic configuration of the same region of the kagome sample for all three demagnetization runs. The white/black dots correspond to the two possible orientations of an island's magnetic moment. Notice that all islands have a uniform black or white contrast, indicating the uniform-magnetization state of each nanodot. Furthermore, white/black dots are usually encircled by black/white contours. Although this might seem to be just an artifact, these oppositely-coloured rings are, in fact, the fingerprints of the tip's sensitivity to the stray field lines which curl around the island edges. Also notice that, although the first two runs share the same parameters, the resulting configurations are overall different, even though it is the same sample region. This highlights the semi-deterministic nature of the ac demagnetization protocol. In all cases, an overwhelming majority of the triangles respect the "two up-one down"/"two down-one up" kagome ice rule, with just a few exceptions that can also be noticed here.

Table 3.3 - The first seven pairwise spin correlations extracted from the 10 MFM images. The definition follows the nomenclature established by Wills *et al.*[71] for kagome spin ice.

Index	$C_{\alpha\beta}$	$C_{\alpha\gamma}$	$C_{\alpha\delta}$	$C_{\alpha\nu}$	$C_{\alpha\tau}$	$C_{\alpha\eta}$	$C_{\alpha\varphi}$
1	−0.306694	0.047228	−0.060513	0.117556	0.007720	−0.051737	−0.004627
2	−0.30258	0.039197	0.033461	0.160134	−0.051625	−0.043021	0.040153
3	−0.285714	0.052813	0.004444	0.091357	−0.013570	−0.014392	0.004960
4	−0.317847	0.090616	−0.039558	0.069917	−0.006440	−0.050138	0.000920
5	−0.31814	0.047022	−0.001444	0.099686	−0.020024	−0.020989	0.012072
6	−0.307915	0.095560	−0.058880	0.074807	−0.035232	−0.026544	0.016409
7	−0.314948	0.060316	−0.040954	0.100466	−0.021288	−0.011722	0.008342
8	−0.303232	0.032556	−0.050205	0.107692	−0.006914	−0.029977	0.045571
9	−0.321422	0.070348	−0.022104	0.112422	−0.030502	−0.070903	0.003120
10	−0.290974	0.052736	−0.008323	0.095635	−0.046844	−0.051775	0.059423

state ordering. Furthermore, the forbidden states ratio (FSR), i.e. the number of triangles with either a 3-up or a 3-down configuration over the total number of vertices, is typically in the order of 3-5%, which also suggests that nearest-neighboring frustration effects have mostly been dealt with (see Figure 3.6). Interestingly, although the third demagnetization run has a field step that is one order of magnitude smaller than the one of the first two runs, there is only a slight difference in terms of forbidden state ratios (average values are 3.9% for the former case and 4.3% for the latter). Achieving a configuration that fully respects the kagome Ising ice rules seems to be an increasingly difficult task, possibly requiring long demagnetization runtimes.

Although the employed demagnetization protocol is, a priori, a deterministic process, different spin arrangements are found for identically-preset demagnetization runs (see Figure 3.6). Demagnetization therefore appears to be rather a semi-deterministic process, presenting some sort of stochasticity, which might very well have a thermal origin. As previously mentioned, the two energetically-favorable states for an island's magnetization are separated by a high energy barrier that cannot practically be overcome by room-temperature fluctuations. However, this is true if no external field is applied. Otherwise, the field will favor one state over the other by vertically shifting the energy levels (see Figure 3.7). This means that the energetic barrier that remains to be overcome is getting smaller as the switching field value is approached. In fact, in the vicinity of the switching field, the energy barrier is small enough to spontaneously trigger spin-flips at room-temperature, particularly if the field protocol can be considered quasi-static. Such a flip can significantly alter the demagnetization pathways that the system follows in a purely-deterministic scenario and might very well be the root of the semi-deterministic nature of the ac demagnetization protocol.

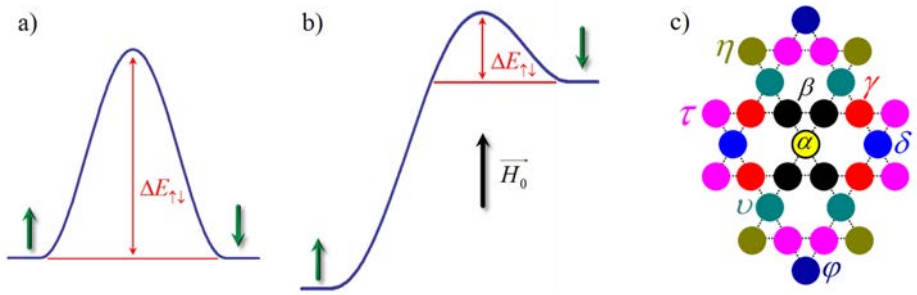

Figure 3.7 - (a) If no external field is applied, the *up* and *down* states of an island's moment are separated by a symmetric energy barrier related to the unaxial anisotropy. For the current samples and for an isolated island, this barrier is in the order of $10^5 k_B T$. (b) However, under an applied field, the two energy levels are shifted to favour the spin pointing along the field's direction and the barrier is gradually reduced. Close to the switching field, this barrier can be overcome by thermal fluctuations in a manner similar to superparamagnetic flipping. (c) The definitions of the first seven spin correlators for kagome Ising. After Chioar *et al.*[14].

To characterize the order established and further relate to statistical physics models, the first seven pairwise spin correlators were extracted from the MFM images. Their definition is the same as in the kagome spin ice case[71] (see Figure 3.7.c). However, since all moments are pointing along the Oz axis, these kagome Ising correlators are unaffected by geometrical factors arising from the relative orientation of the chosen spin pair. The sets of correlation values are given in Table 3.3.

Another interesting analysis can be made by defining vertex magnetic charges, in analogy with kagome spin ice. The dumbbell/charge picture has proven to be very useful in this case, as the magnetic charge turns out to be an emerging degree of freedom that crystallizes prior to achieving long-range spin order[7, 8]. Furthermore, the nearest-neighbor charge correlator, $Q_i Q_{i+1}$, has proven to be a useful tool for highlighting the fingerprints of long-range pairwise spin interactions for demagnetized artificial kagome spin ice arrays[73]. Defining an equivalent magnetic charge correlator for the kagome Ising geometry may help unravel patterns in the spin texture and also facilitate the comparison between the thermodynamic behavior of the two kagome lattices.

The definition of a vertex magnetic charge in the kagome spin ice geometry is quite straightforward (see Figure 2.12.a). By taking the dumbbell picture, one can easily notice that all charges are located in the network's plane and, given their proximity at the vertex sites, an effective charge/vertex can be defined by summing up the individual contributions from the spins. In fact, the charge values can be written as a sum of the contributing scalar spin values, with either a $+$ or a $-$ sign in front of the sum depending on the triangle type (see section 2.2.6):

$$Q_{\Delta} = \sum_{i \in \Delta} \sigma_i \quad Q_{\nabla} = -\sum_{i \in \nabla} \sigma_i \tag{3.4}$$

However, the situation for the kagome Ising case is more complex. Firstly, the charges are no longer located in the same plane, but instead form two kagome planes, above and below the network (see Figure 3.8.a). Secondly, the charges are no longer concentrate at the centers of the network triangles and do not collectively behave as a single effective charge. Nevertheless, the convention established for kagome spin ice (relations 3.4) can be implemented for the kagome Ising case too. The advantage of this definition is that it guarantees charge neutrality on the network scale as all charge contributions are taken into account. It will also be interesting to see if this so-defined magnetic charge plays the role of an order parameter for kagome Ising as it does for kagome spin ice. Furthermore, a nearest-neighbor charge correlator can be defined and, since the charge definition is analogous for the two lattices, the corresponding temperature dependencies for the two arrays can be compared and contrasted. In addition, the charge correlator can be written down as a linear combination of the first three pairwise spin correlators, just like in the kagome spin ice case (the full demonstration is given in Appendix C):

$$Q_i Q_{i+1} = -1 - 4 \cdot C_{\alpha\beta} - 2 \cdot C_{\alpha\gamma} - 2 \cdot C_{\alpha\nu}. \tag{3.5}$$

Although a certain geometric description can be found for this definition (see Figure 3.8.b), the vertex magnetic charge for the kagome Ising network does not have a direct physical meaning like in the in-plane multiaxial array. In this latter case, the vertex charge can be directly mapped with an MFM scan as it acts like a source or a drain of stray field lines. Nevertheless, in both cases, its associated correlator plays the role of a combination of spin correlations and will be useful for observing any constrains that may arise in the thermodynamic behavior.

The experimental values of the vertex charges can be determined by computing the sums in expressions 3.4 after the spin values were extracted from the MFM images. The network average of the nearest-neighbor charge correlator can then be directly calculated by summing up all the corresponding charge pair products. Another way to determine the experimental value of the charge correlator is by substituting the values found for $C_{\alpha\beta}$, $C_{\alpha\gamma}$ and $C_{\alpha\nu}$ into relation 3.5. Although the two methods are theoretically equivalent, it is important to note that they may not necessarily give the same result for the same MFM image. This is because a vertex charge is only defined if all the spins of a chosen triangle have been successfully

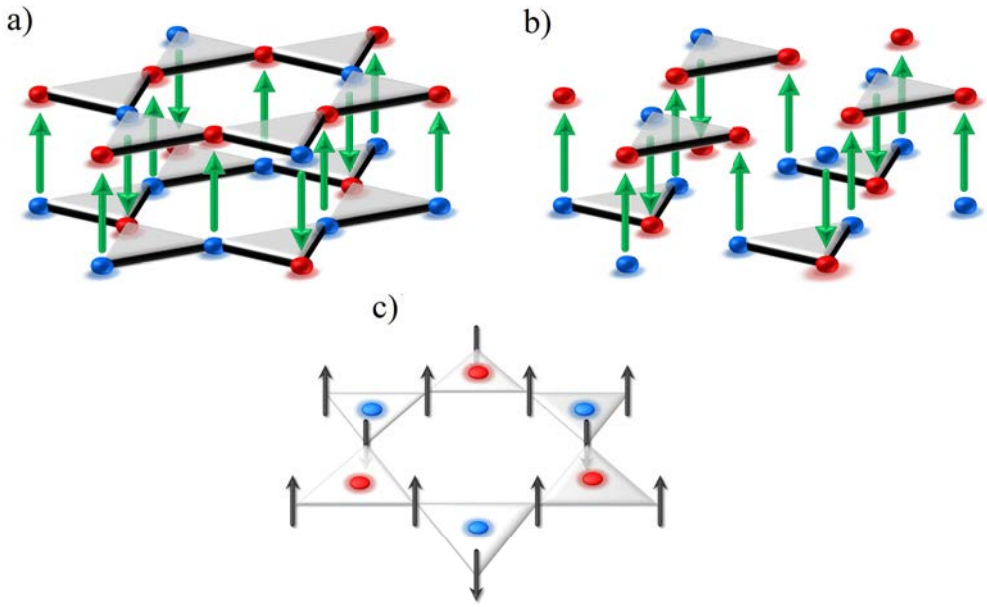

Figure 3.8 - (a) In the dumbbell description, the magnetic charges form two mirroring kagome planes, above and below the network's plane. (b) Convention 3.4 can be geometrically interpreted as grouping together all charges in the upper plane in Δ-type triangles and the charges below in ∇-type trinagles. This way, every contribution is taken into account and, by summing up the charges for each triangle, an effective hexagonal lattice of vertex charges can be defined (c).

Table 3.4 - The charge correlation values extracted form the 10 MFM images. $(Q_iQ_{i+1})_{corr}$ is computed using expression 3.5 while $(Q_iQ_{i+1})_{dir}$ is calculated after the hexagonal network of vertex charges has been constructed.

Index	Demag	$N_{vertices}$	$(Q_iQ_{i+1})_{corr}$	$(Q_iQ_{i+1})_{dir}$
1	Run 1	841	−0.102794	−0.134364
2	Run 1	964	−0.188337	−0.141361
3	Run 1	900	−0.145482	−0.18
4	Run 1	974	−0.049678	−0.106776
5	Run 2	914	−0.020863	−0.043763
6	Run 2	939	−0.109073	−0.12886
7	Run 2	863	−0.06177	−0.149479
8	Run 2	869	−0.067566	−0.081703
9	Run 3	1180	−0.079851	−0.113559
10	Run 3	1142	−0.132846	−0.1331

identified by the reconstruction software. For example, in the case where only two out of the three spins are reconstructed, no charge is assigned to that triangle, hence it does not contribute to any correlation pair. In fact, this corresponds to a vacancy in the hexagonal network defined by the vertex sites (see Figure 3.8.c). On the other hand, these two spins can form $C_{\alpha\beta}$, $C_{\alpha\gamma}$ and $C_{\alpha\nu}$ pairs with neighboring spins, thus affecting the average charge correlation value if the linear combination expression is employed. While the direct approach seems natural, it, in fact, replaces the real kagome spin network with an effective hexagonal magnetic charge network, and while doing so, some information on the underlying spin ordering patterns can be lost due to the impossibility to completely define a vertex charge. The other method does retain all information on the spin correlations, but the value found does not necessarily reflect the configuration of the hexagonal charge array. Therefore, both approaches are considered in this work and both sets of values will be compared to their corresponding Monte Carlo averages assuming both short and long-range interaction models. These values are given in Table 3.4. The following section thus focuses on the thermodynamic behavior of kagome Ising within the framework of these two models.

3.3 Monte Carlo Simulations of Kagome Ising

3.3.1 A Short-Range Model - Equivalence to Kagome Spin Ice

Similarly to the kagome spin ice case, the thermodynamic behavior of the kagome Ising network is firstly explored assuming only nearest-neighboring interactions. This can be seen as truncating the long-range dipolar Hamiltonian to the first term by cutting off all higher-order contributions. This leads to a Heisenberg-type Hamiltonian and, since all spins are pointing along the vertical axis, the scalar form can be implemented directly:

$$H_{SR} = -J \sum_{<i<j>} \sigma_i \cdot \sigma_j. \tag{3.6}$$

where σ_i and σ_j are two nearest-neighboring spins forming a $C_{\alpha\beta}$ correlation pair.

One can immediately notice the resemblance between this expression and the scalar form of the short-range Hamiltonian of kagome spin ice (see expression 2.5). In fact, both cases start from the vectorial form (see expression 2.2), but since the kagome spin ice $C_{\alpha\beta}$ pairs are affected by a $-1/2$ factor arising from the scalar product, the only difference between the two expressions is given by this geometrical factor. In other words, the coupling constants are the only ones that distinguish between the two cases. However, if the nature of the nearest-

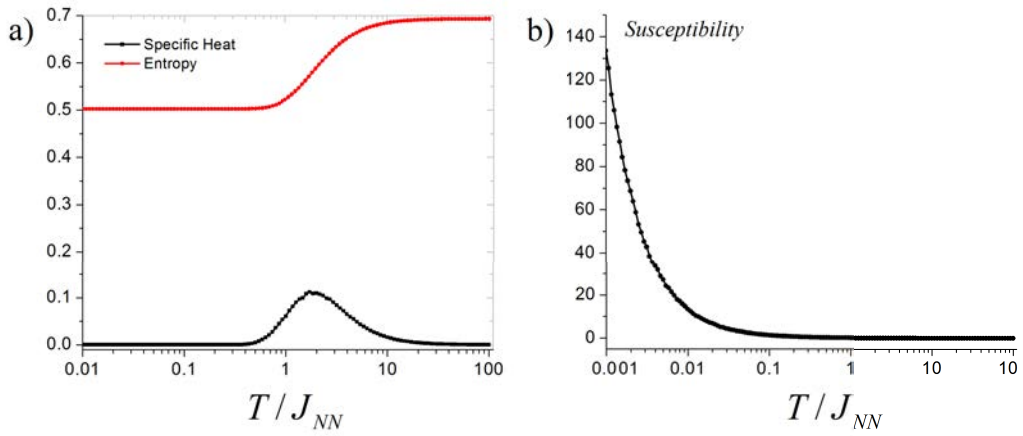

Figure 3.9 - The equivalence between ferromagnetic kagome spin ice and antiferromagnetic kagome Ising within the short-range model framework implies identical temperature dependencies for the (a) specific heat and the entropy and (b) the susceptibility.

neighboring interaction is ferromagnetic in one case and antiferromagnetic in the other, than the two Hamiltonians are equivalent, save for a overall energy shift. This is indeed the case. By taking the point-dipole approximation, one can prove that, the nearest-neighbor coupling is ferromagnetic for kagome spin ice, $J_{ksi} = 7/4 \cdot D/(r_{nn})^3 > 0$ (see 2.6), while for kagome Ising, $J_{kI} = -D/(r_{nn})^3 < 0$, making the coupling effectively antiferromagnetic[14]. Otherwise said, the scalar spin pairs tend to have opposite signs in both cases, which can be translated as an effective antiferromagnetic behavior. Nevertheless, it is important to emphasize here that the interaction between neighboring spin vectors in kagome spin ice remains ferromagnetic and the proof for this is the system's preference for spin-loop configurations in the spin ice phase and beyond. It is only in the framework of the spin scalar values that the two networks show equivalent antiferromagnetic coupling between first order neighbors.

This equivalence between the scalar-form Hamiltonians for the two cases within the short-range model has an immediate consequence: the thermodynamic behavior of the short-ranged kagome Ising network is equivalent to that of the short-ranged kagome spin ice. Therefore, if the temperature is scaled to the nearest-neighboring coupling in both cases, the temperature-plots for the specific heat, the entropy and the magnetic susceptibility are identical (see Figures 3.9 and 2.8). The kagome Ising system thus presents a cross over from a highly-disordered paramagnetic regime into a spin ice phase where every network triangle respects the kagome ice rule (adapted for the out-of-plane case): "two-up/one-down"

[14]The signs of each constant has to be in full agreement with expression 2.14. By writing the magnetic moments in terms of the spin scalar values, one can find the above expressions for the nearest-neighboring coupling constants. In the following section we shall see that the deviations caused by multipolar terms, which are reproduced with micromagnetic simulations, do not change the nature of the interaction.

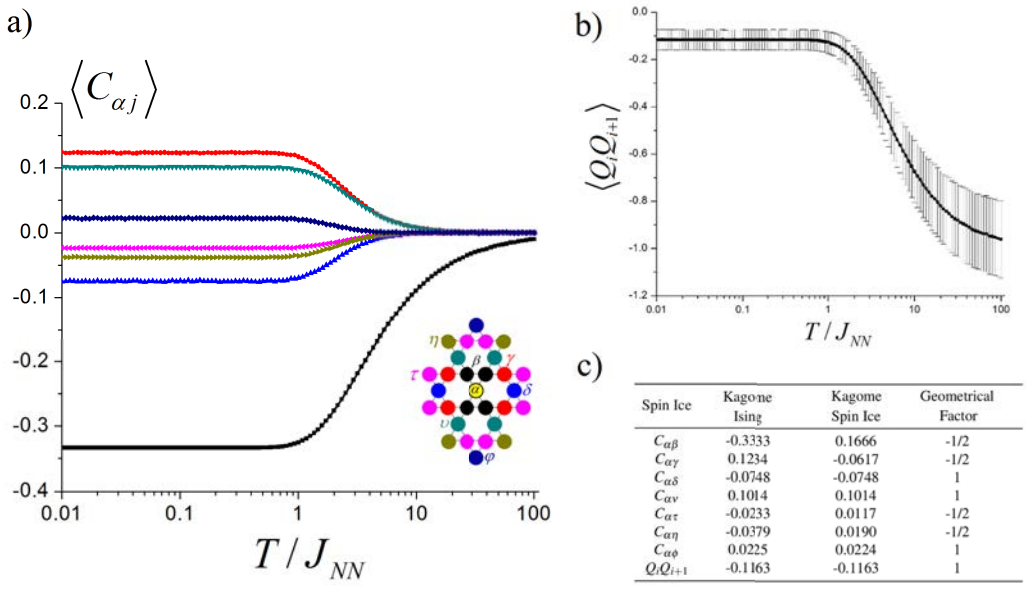

Spin Ice	Kagome Ising	Kagome Spin Ice	Geometrical Factor
$C_{\alpha\beta}$	-0.3333	0.1666	-1/2
$C_{\alpha\gamma}$	0.1234	-0.0617	-1/2
$C_{\alpha\delta}$	-0.0748	-0.0748	1
$C_{\alpha\nu}$	0.1014	0.1014	1
$C_{\alpha\tau}$	-0.0233	0.0117	-1/2
$C_{\alpha\eta}$	-0.0379	0.0190	-1/2
$C_{\alpha\phi}$	0.0225	0.0224	1
Q_iQ_{i+1}	-0.1163	-0.1163	1

Figure 3.10 - The (a) spin and (b) charge correlators also present an equivalent behavior, establishing an universality within the nearest-neighbor interaction model. The inset for the definitions of the spin corelators is taken from Chioar et al.[14]. (c) The ensemble averages for the spin ice plateaus for the correlators are given in this table. There are some deviations from the expected values ($< Q_iQ_{i+1} >= -1/9$) due to the system's finite size fluctuations.

or "two-down/one-up". This phase is characterized by the residual entropy/spin of spin ice, $s_{spin-ice} = 0.50183$[67], and by a cooperative paramagnetic regime[82] that persists down to the lowest temperature.

The temperature plots of the spin and charge correlators are also equivalent to kagome spin ice (see Figures 3.10.a and 3.10.b). Notice that some of the spin correlators of kagome spin ice, namely $C_{\alpha\beta}$, $C_{\alpha\gamma}$, $C_{\alpha\tau}$ and $C_{\alpha\eta}$, present a geometrical factor due to the relative orientation of the spin vectors and this has to be taken into account when comparing corresponding spin correlators. For example, in the spin ice phase, $C^{kI}_{\alpha\beta} =< \sigma_\alpha \cdot \sigma_\beta >= -1/3$, while $C^{ksi}_{\alpha\beta} =< \vec{S}_\alpha \cdot \vec{S}_\beta >= -1/2 < \sigma_\alpha \cdot \sigma_\beta >= 1/6$. Nevertheless, the correlation values are the same if one works with the spin scalar values only. Also, the $-1/3$ value of the nearest-neighbor spin correlator can be easily determined by recalling that the energy/spin in the spin ice phase is $e_{spin-ice} = J \cdot N_{\alpha\beta} \cdot C_{\alpha\beta}/(2 \cdot N_{spins}) = -J/3$ (see sections 2.2.1 and 2.2.2). Higher order correlations do not contribute to the system's energy, but have been deduced by Monte Carlo simulations and their values for the spin ice manifold are summarized in the table of Figure 3.10.c.

Although this mapping works perfectly in a short-range framework, magnetostatic interactions beyond nearest-neighbors are expected to break this equivalence in correlation

development, thus yielding distinctive thermodynamic behavior at low temperatures. These features are investigated in the following section.

3.3.2 The Dipolar Long-Range Model

The magnetostatic framework of artificial arrays of disconnected magnetic nano-islands normally requires long-range interactions to be taken into account when modeling their behavior. A thorough multipolar expansion is generally performed if the size of the magnetic elements is comparable to their relative displacements[7]. Furthermore, the finite size of the components might modify the uniform distribution of their magnetization, thus altering their Ising-like nature[60, 61]. However, Rougemaille et al.[73] have previously shown that multipolar contributions and shape effects are relevant only for nearest-neighboring pairs in the case of artificial kagome spin ice networks, the rest of the energetic contributions being quite well described by the point-dipole approximation. Furthermore, these effects can be captured by a Heisenberg-type Hamiltonian which effectively reinforces the coupling between first-order pairs. Therefore, the point-dipole approximation can still be used if these terms are properly taken into account. To this end, micromagnetic simulations have been performed using the OOMMF simulation package[128] to determine the deviation from the point-dipole approximation of the kagome Ising coupling pairs (see Figure 3.11). Similarly to Rougemaille et al.[73], results point out that only nearest-neighboring pairs are practically affected and that finite-size effects are relatively small for the given inter-island spacing ($J_{\alpha\beta}^{\mu mag} \cong 1.5 \cdot J_{\alpha\beta}^{dip}$). Hence, the point-dipole approximation can still be used to explore the thermodynamic properties of kagome Ising network with long-range magnetostatic interactions.

Similarly to kagome spin ice, the dipolar spin ice Hamiltonian presented in (2.16) can be further simplified for this specific case, leading to the following scalar form:

$$H_{DSI} = -J_1 \sum_{<i<j>} \sigma_i \cdot \sigma_j + D \cdot \sum_{(i<j)} \frac{\sigma_i \cdot \sigma_j}{r_{ij}^3}. \tag{3.7}$$

where $\sigma_i = \pm 1$ are the spin scalar values, r_{ij} represents the relative distance between a chosen spin pair, D stands for the dipolar constant and J_1 is the coupling constant that reinforces nearest-neighbor interactions to account for micromagnetic effects ($J_{\alpha\beta}^{\mu mag} = J_1 + J_{\alpha\beta}^{dip}, J_1 = 0.5 \cdot J_{\alpha\beta}^{dip}$). Furthermore, the energy of the system can be written as a linear combination of the pairwise spin correlations averaged on the network scale. Similarly to kagome spin ice (see 2.15), this yields:

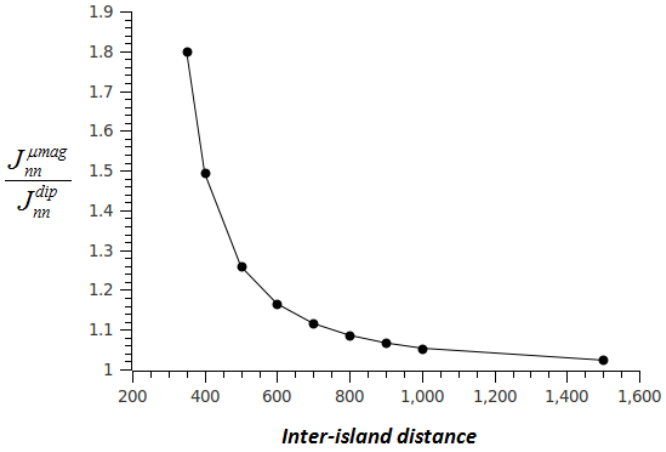

Figure 3.11 - Micromagnetic simulations performed using the OOMMF simulation package to determine the relative coupling between two nearest-neighboring magnetic elements that reproduce the features of the experimental patterned nanoislands. For the 400nm inter-island spacing, the ratio between the micromagnetic and the dipolar approximation couplings is 1.5, significantly smaller than the in-plane one [73]. By properly correcting the nearest-neighboring interactions, the long-range dipolar Hamiltonian can still be used to describe the energetic landscape of the kagome Ising network. Data courtesy of Nicolas Rougemaille.

$$E_{dip} = \frac{1}{2}\sum_{\alpha}\sum_{j} J_{\alpha j}(\sigma_{\alpha}\cdot\sigma_{j}) = \sum_{\alpha}\sum_{\lambda} J_{\alpha\lambda}\cdot N_{\alpha\lambda}\cdot C_{\alpha\lambda}. \tag{3.8}$$

and the coupling constant of each correlator can be written in terms of the nearest-neighboring dipolar coupling, J_{nn}^{dip}:

$$J_{\alpha\lambda} = J_{nn}^{dip}\cdot R_{\alpha\lambda}. \tag{3.9}$$

where $R_{\alpha\lambda} = (\frac{r_{nn}}{r_{ij}})^3$ is the relative coupling ratio driven by the relative distance between the considered pair. The values of this factor are given in Table D.1 in Appendix D for the first seven spin correlators. Since the scalar product between the spin vectors and the displacement vectors vanish in this case, the geometrical factors related to the relative positioning of the spin vectors ($G_{\alpha\lambda}$ - see Appendix D) do not play any part here. This completely changes the coupling ratios for the kagome Ising system with respect to kagome spin ice (see Table D.1) and a different development of pairwise spin correlations is expected once higher order contributions are comparable to the thermal bath.

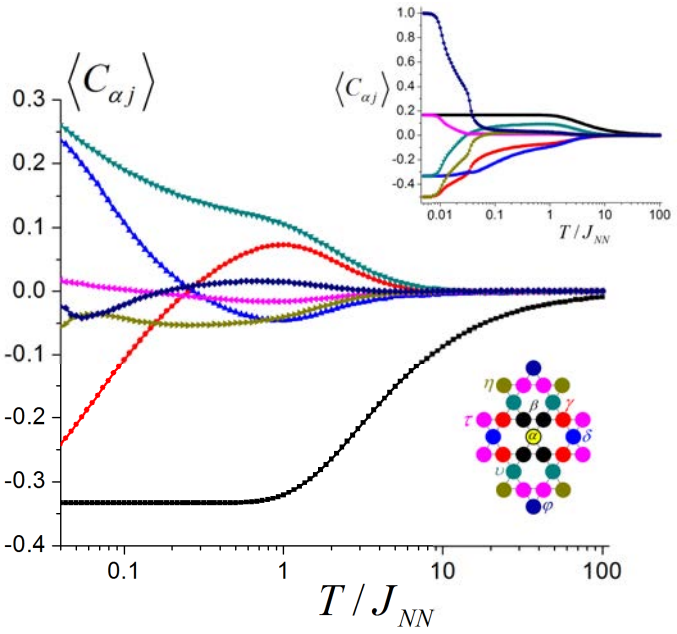

Figure 3.12 - The temperature evolution of the first seven spin correlators of the kagome Ising network within the dipolar long-range model. For comparison, the kagome spin ice long-range spin correlators are reported in the upper inset. The color code is the same for both plots and the definition of the correlation is given in the lower inset (after Chioar et al.[14]).

The thermodynamic properties of the kagome Ising network governed by the dipolar spin ice Hamiltonian was explored by single spin-flip Monte Carlos simulations. Different network sizes and parameters have been used, but the results presented in this section correspond to a simulation performed on a $12 \times 12 \times 3$ kagome network with periodic boundary conditions. The temperature was sequentially dropped, starting from a paramagnetic regime, then passing through the spin ice phase and continuing until the single spin-flip dynamics suffers from a critical slowing down behavior that compromises ergodicity and drastically increases simulation time[15]. For each temperature value, a number of 10^4 modified Monte Carlo steps are used for thermalization followed by 10^4 modified Monte Carlo steps for sampling.

The temperature-dependencies of the first seven spin correlators are reproduced in Figure 3.12. As long as higher order terms are negligible with respect to the thermal energy, the short and long-range plots are very similar (compare Figures 3.10 and 3.12). As expected, this resemblance changes once the system approaches the spin ice manifold. Even before every triangle fully respects the kagome ice constrains, second and third-order correlators

[15]The critical slowing down of the single spin-flip dynamics indicates the presence of a possible phase transition towards an ordered spin state at low temperatures. Nevertheless, for the temperature range presented here, the modified Monte Carlo steps ensure an ergodic mapping of the phase space and a proper sampling of the relevant thermodynamic quantities. The low-temperature regime along with the spin-flip acceptance ratio will be discussed later, in section 3.5.1.

already present a clearly distinctive behavior in the long-range picture than in the short-range one. Furthermore, all correlators continue to evolve within the spin ice manifold, some of them even changing their sign. For example, the average value of $C^{LR}_{\alpha\gamma}$ doesn't get higher than 0.1 and then drops to negative values, whereas $C^{SR}_{\alpha\gamma}$ monotonically increases until it reaches its spin ice plateau value of 0.123. A rather similar feature can be noticed in the evolution of the $C_{\alpha\delta}$ correlator.

There is also a sharp contrast between the evolutions of the same correlator in kagome spin ice and in kagome Ising within the dipolar long-range picture (see Figure 3.12 and its upper inset). For instance, the $C^{kI}_{\alpha\nu}$ correlator is monotonically increasing while $C^{ksi}_{\alpha\nu}$ mainly stays positive in the spin ice manifold and then drops to negative values once the transition towards the spin ice II occurs[16]. In fact, the kagome spin ice network prefers an antiferromagnetic alignment for its $\alpha\delta$ and $\alpha\nu$ spin pairs while the kagome Ising system favours an ferromagnetic alignment for them. This emphasizes the expected stark contrast between kagome spin ice and kagome Ising in the development of pairwise spin correlators within the long-range picture.

A very suggestive picture that captures both similarities and differences between kagome spin ice and kagome Ising is provided by the temperature dependence of the nearest-neighboring charge correlator, $< Q_i Q_{i+1} >$. This correlator has already proven very useful for unveiling the underlying preference for charge order in kagome spin ice and for highlighting the fingerprints of long-range interactions for demagnetized artificial kagome spin ice networks[73]. As mentioned in section 3.2.3, the convention established for defining vertex charges in kagome spin ice can be used to define effective magnetic charges for the kagome Ising network as well. A network average of nearest-neighbor correlations can then be computed on the underlying hexagonal lattice of magnetic charge for each temperature of the Monte Carlo simulation. The evolution of the this kagome Ising charge correlator, $< Q_i Q^{kI}_{i+1} >$ is reported in Figure 3.13 for both the short-range and long-range models. For comparison, the kagome spin ice charge correlators ($< Q_i Q^{ksi}_{i+1} >$) are also plotted.

Given the equivalence between the two kagome networks within the short-range model, a superposition between the two short-range plots of the charge correlator was expected (see black and green plots in Figure 3.13). However, as the system approaches the spin ice phase, the long-range correlators deviate from the short-range plot and its spin ice plateau. $< Q_i Q^{ksi}_{i+1} >$ drops to -1, indicating the presence of an emergent charge crystal, but the $< Q_i Q^{kI}_{i+1} >$ continues to increase, passing to positive values deep within the spin

[16]Notice that $C^{ksi}_{\alpha\nu}$ is not affected by the $-1/2$ geometrical factor and a direct mapping between the two geometries can be made. The same applies for $C^{ksi}_{\alpha\delta}$ which also presents a monotonic behavior in one case and a change of sign in the other.

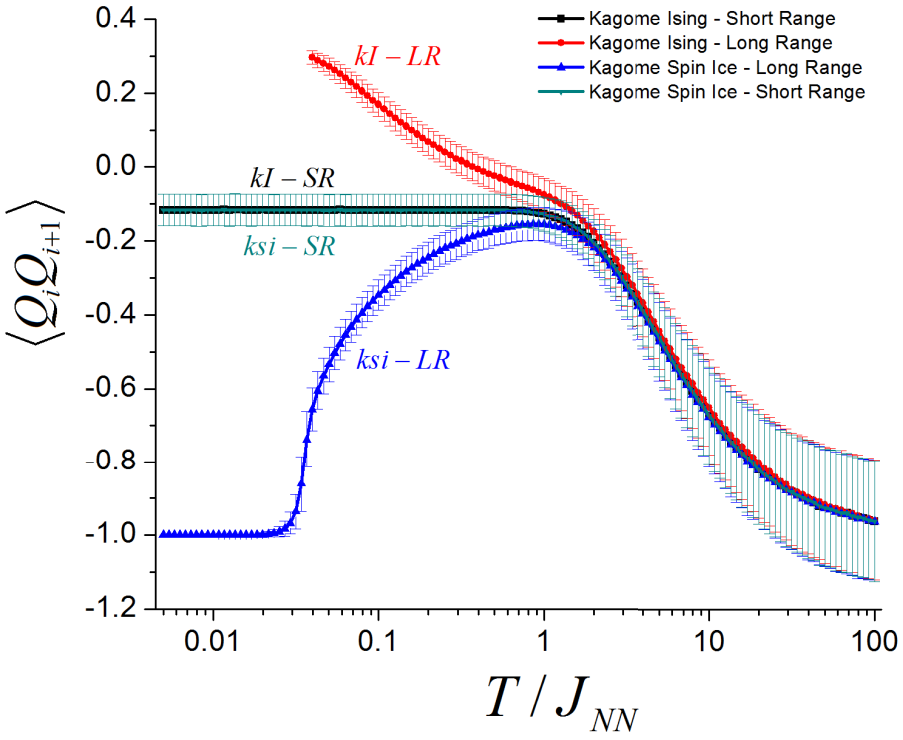

Figure 3.13 - The evolution of the network averages of the nearest-neighbor charge correlator for both the kagome Ising and the kagome spin ice systems within the short and long-range frameworks. The fluctuations around the ensemble average are given here as error bars. The short-range equivalence yields a superposition of the short-range plots (black and green lines) for all temperatures. The long-range plots follow the short-range ones in the high temperature window, but then present different behavior when entering the spin ice phase. While the kagome multiaxial network eventually forms a antiferromagnetic charge crystal, the kagome Ising system searches for a ferromagnetic alignment as its values become positive deep within the spin ice phase. The critical slowing down of the single spin-flip dynamics prevents the exploration of lower energy manifolds for the kagome Ising network, thus resulting in a abrupt halt to the temperature evolution of its long range charge correlator.

ice manifold and appearing to saturate at $+1/3$[17]. This behavior is in sharp contrast with its in-plane counterpart, as a positive correlation value would indicate a preference for a ferromagnetic alignment of neighboring charge pairs. In analogy with the analysis performed on kagome spin ice, this preference can be understood by artificially introducing the charge correlator into the dipolar long-range Hamiltonian to create an effective microscopic picture of the competing ordering between spins and magnetic charges.

Since the nearest neighbor charge correlator can be written as a linear combination of the first three spin correlators, $C_{\alpha\beta}$, $C_{\alpha\gamma}$ and $C_{\alpha\nu}$ (see expression 3.5), the linear combination form of the Hamiltonian (see expression 3.8) can be tailored to present a short-range pairwise spin interaction, a nearest-neighbor charge pair coupling and the remaining terms of the dipolar spin-spin interaction[18]. This microscopic Hamiltonian can therefore be written as:

$$H_{DSI} = \frac{\overline{J_{nn}}}{2} \sum_{<i,j>} \sigma_i \cdot \sigma_j + \frac{\overline{J_{QQ}}}{2} \sum_{<u,v>} Q_u \cdot Q_v + O(1/r^3)_{r \geq 2r_{nn}}. \tag{3.10}$$

where $\overline{J_{nn}} = D_{eff} \cdot \frac{27 - 4\sqrt{3}}{18}$ is the effective coupling constant for nearest neighboring spins and $\overline{J_{QQ}} = -D_{eff} \cdot \frac{1}{3\sqrt{(3)}}$ is the effective interaction strength between neighboring charges. The positive sign of $\overline{J_{nn}}$ reflects the antiferromagnetic nature of the first order spin pair coupling, while the negative sign of $\overline{J_{QQ}}$ indicates a clear preference for having neighboring charges of the same sign. Since $\overline{J_{nn}} > \overline{J_{QQ}}$, the first step towards energy minimization that the kagome Ising network takes is to make sure that every network triangle obeys the kagome ice rule. Once within the spin ice regime, the second step is to ensure a ferromagnetic alignment of the magnetic charges while still complying with the already-established kagome ice constrains. This explains the positive values of the nearest-neighbor charge correlator deep within the spin ice phase. However, while the kagome spin ice charge correlator drops to -1, thus perfectly minimizing the effective charge interaction, the kagome Ising correlator doesn't seem to reach the desired value of $+1$ for complete minimization. The remaining terms from the summation can also play a part here, preventing the charges from fully crystallizing, but their effective coupling constants is nevertheless lower than the pairwise charge one. Another reason for the impossibility to spontaneously obtain a ferromagnetic charge crystallization for kagome Ising could be simply due to the lattice topology which

[17] Since the single spin-flip dynamics critically slows down at the lowest temperatures sampled so far with this Monte Carlo algorithm, one cannot offer any guarantees about the ground state value of the charge correlator. Nevertheless, the monotonic increase of the charge correlator with decreasing temperature seems to slow down at this point.

[18] The deduction is very similar to the one performed for kagome spin ice, reported in Appendix C.

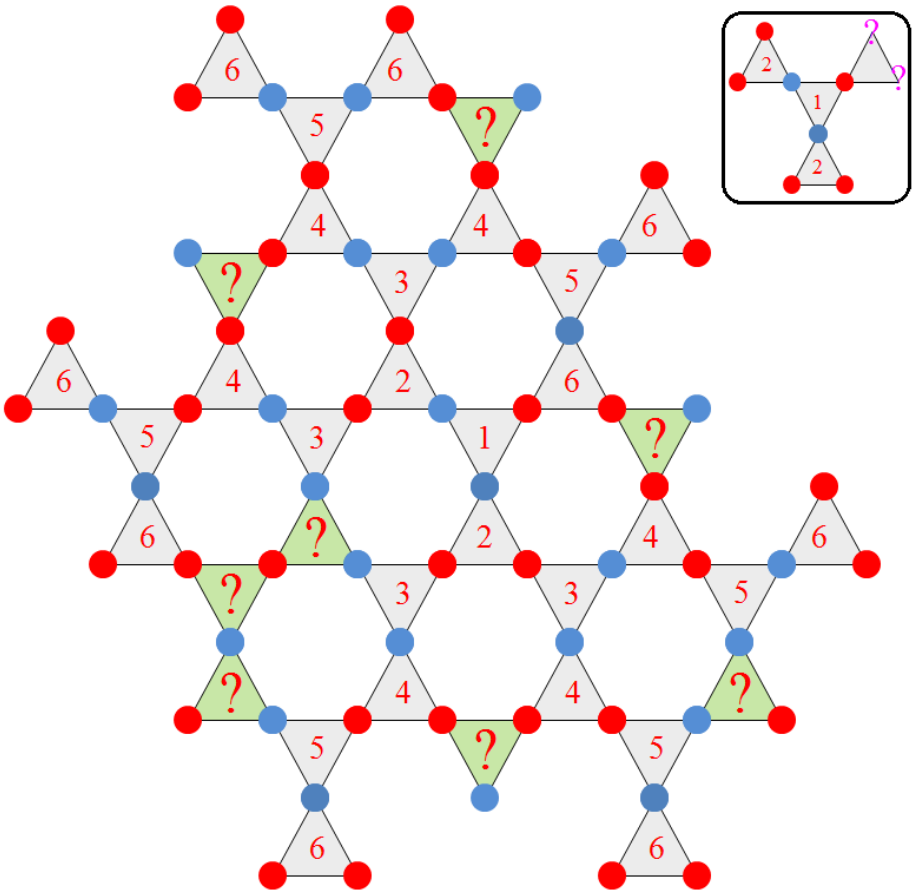

Figure 3.14 - Attempting to create a ferromagnetic charge crystal embedded in a kagome Ising network is bound to fail after a few steps, as illustrated in this picture. The kagome ice rules have to be obeyed by all triangles and, in addition, all vertices must share the same charge value with the one of the initially defined triangle. In this case, every triangle has a $+1$ magnetic charge, which means that each Δ-type triangle has two spins *up* and one *down* while every ∇-type triangle has two spins *down* and one spin *up*. The red and blue dots indicate the spin directions, corresponding to the *up* and *down* states, respectively. After selecting a spin configuration for the first triangle, two of its neighbors can be precisely defined at the next step, while the third one has two possibilities (see inset). If a triangles has more than one option for its spin orientations, the definition is skipped at that step and it will be deterministically defined later on. The numbers inside each triangle indicate the step at which their spins are exactly defined. One can notice that the definition proceeds by forming a Bethe lattice. However, when the procedure loops around a hexagon, encountering a previously defined triangle, there is no way of defining the triangle configuration while respecting the two imposed constrains (there is though one exception here). These situations are marked with a question mark within a green background triangle. The only remaining option here is to accept a spin configuration with a unitary vertex charge of opposite sign. Therefore, the construction of a ferromagnetic charge crystal is halted at this point.

doesn't comply with such a charge configuration. This is actually the case, as presented in Figure 3.14.

For the lowest temperatures sampled so far by Monte Carlo simulations, the charge correlator is about 0.297[19], which indicates that, on average, every vertex charge is approximately surrounded by two vertices with the same charge sign and one vertex of opposite sign[20]. Similarly to kagome spin ice, the higher order terms of the microscopic Hamiltonian are expected to play a key role in the low temperature regime by filtering the different spin textures and finally driving the system into a spin ordered state.

In retrospective, while the two kagome networks are effectively described by nearest neighboring correlations, their overall behavior is the same. However, if second and higher order contributions cannot be neglected, we expect signtures of distinctive behavior for the two cases, which could be suggestively highlighted with the help of the nearest-neighbor charge correlator, Q_iQ_{i+1}.

3.4 Artificial Kagome Ising - Another "Frozen" Dipolar Network

3.4.1 Artificial Kagome Ising - Back to Short-Range

The idea of using artificial spin ices as toy spin models for deepening our understanding of complex phenomena related to frustrated topologies is very exciting, particularly due to the high degree of control in design and the direct visualization of the magnetic degrees of freedom in real space[95]. However, the artificial networks with out-of-plane moments reported so far are thermally-insensitive at room temperature[13, 14, 45], thus requiring a demagnetization protocol for accessing lower energy manifolds[3]. This introduces an additional degree of complexity to the approach as this out-of-equilibrium, one-shot driving mechanism can be quite difficult to model in order to account for the final frozen states. As mentioned in section 2.5, there are generally two main ingredients to consider for the modeling: an interaction model and a dynamics. In the end, many different choices exist, among which we can mention at-equilibrium Monte Carlo simulations[13, 14, 46, 73], entropy maximization procedures assuming a vertex model[54, 55, 91] and numerical demagnetizations with different degrees of quench disorder[85, 86, 92].

[19]This value was obtained for a $12 \times 12 \times 3$ kagome lattice. For a larger network, $36 \times 36 \times 3$, the correlator is slightly higher, reaching the value of 0.3235.

[20]This would be exact if the network average of the charge correlator is $1/3$, without any standard deviations on the network scale.

In their study of artificial triangular clusters of perpendicularly-magnetized nanodots, Mengotti *et al.*[45] have quantified the occurrence of each configuration and, by computing the energy of all possible states in a point-dipole approximation framework, they evaluated the efficiency of the demagnetization protocol employed. For tightly packed clusters, they observe a clear preference for lower energy states and the ground state configuration is often realized. The choice for a magnetostatic description seems natural, but for such small clusters, dipolar long-range effects could be quite difficult to highlight as most inter-island couplings are $C_{\alpha\beta}$ pairs and energy minimization is dominated by nearest-neighboring pairs. In fact, the differences given by long-range interactions from a short-range picture are very small and could be easily screened by quench disorder effects during demagnetization. This would ultimately lead to an effective short-range description of the frozen states of such clusters, which could extend to the network scale.

Such an effective short-range picture that captures the features of demgnetized artificial kagome arrays with out-of-plane moments was reported by Zhang *et al.*[13]. Similar to previous works[46, 72, 73], they computed the first seven kagome pairwise spin correlators from their MFM images and confronted them with model predictions. Given the complexity and the out-of-equilibrium nature of the driving demagnetization dynamics, they focus on the description of the remanent states only and construct two different models that rely on the experimentally observed correlations: a quasiequilibrium Gibssian model (model G) and a kinetic quenched model (model Z)[13]. Taking advantage of the direct visualization of the microstates, they impose the experimental values of the nearest-neighbor spin correlator as the main constrain/target value for the two models. Model G assumes the probability of a configuration to be $P(s_i) = exp(K \cdot \sum_{NN} s_i \cdot s_j)$ and the effective constant K can be tuned to match the nearest-neighbor correlation constrain[21]. Model Z starts from a random configuration and flips spins only if, by doing so, the energy is lowered, and continues to do this until the experimental value of the nearest-neighbor spin correlator is achieved. They report that both models account rather well for the observed higher order correlations (see Figure 3.15) and they thus conclude that "the nearest-neighbor correlation constraint is a robust single physical measure that characterizes the outcome of the rotational demagnetization"[13].

There is however a curious feature that can be observed in Figures 3.15(a-b): model G performs better for kagome spin ice, while for kagome Ising it overestimates the correlation

[21] In the Supplementary Material of their paper[129], Zhang *et al.* report that this model better captures the values of higher order experimental correlations if a nearest-neighbor four spin term is added to the Hamiltonian. This can be translated into a majority-vote kinetic process that flips a spin only if its neighbors are of the same sign as the selected one[130]. However, this additional term takes the model out of the short-range framework, as it contains a mix of $C_{\alpha\beta}$, $C_{\alpha\gamma}$ and $C_{\alpha\nu}$ terms. It therefore appears that, by taking into account higher order correlations, model G performs better, which suggests that long-range interactions should be included when describing the frozen states of demagnetized arrays with perpendicularly magnetized elements.

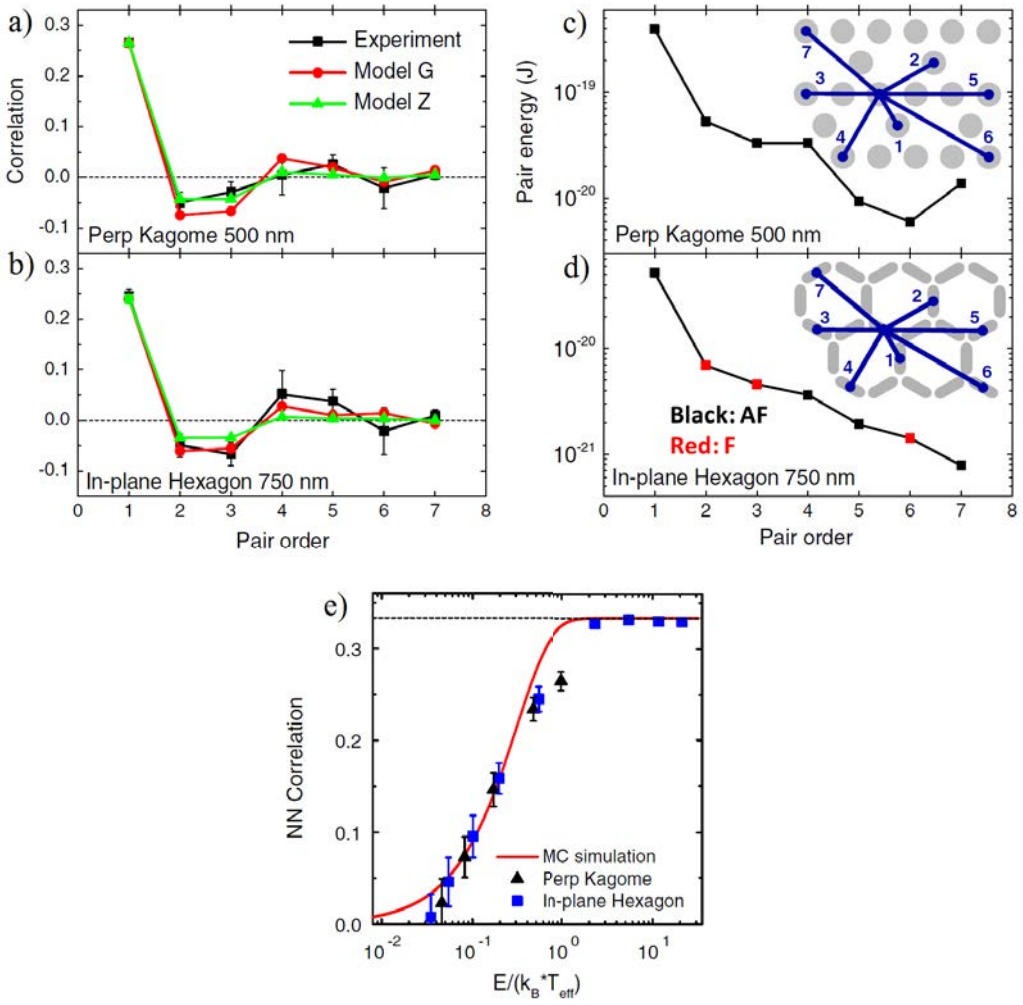

Figure 3.15 - (b-c) The experimental values for the first seven spin correlations along with the predictions of models G and Z as reported by Zhang *et al.*[13] for (a) artificial kagome Ising and (b) artificial kagome spin ice arrays. Note that the sign convention for the correlators is opposite to the one used in this work. Figures (c-d) give the definitions used by Zhang *et al.* for the spin correlations along with the strength of the corresponding inter-island couplings computed using the OOMMF micromagnetic simulation package[128] for the parameters of the experimental networks. Higher order correlations are rather well reproduced by the two models, but certain deviations can be noticed for second ($C_{\alpha\gamma}$), third ($C_{\alpha\nu}$) and forth ($C_{\alpha\delta}$) order correlations. (e) Monte Carlo simulations for thermalized kagome networks within a short-range model picture. In this case, the heat bath was fixed at a certain temperature and the nearest-neighbor coupling strength (E) was varied. This is, in fact, equivalent to fixing the nearest-neighboring interaction (J) and varying the temperature as presented throughout this work. The collapse of the experimental data for both networks on the $C_{\alpha\beta}$ plot is good, in spite of the out-of-equilibrium nature of the driving demagnetization protocol. This mapping lead them to conclude that there is an universality in the developement of correlations for demagnetized artificial kagome arrays, regardless of the particular orientation of the magnetic moment axes. However, notice that some deviations occur for higher values of the nearest neighboring correlations and for ones close to zero. After Zhang *et al.*[13].

values, particularly for second, third and forth orders[22]. On the other hand, model Z has quite the opposite behavior, performing better than model G for the perpendicular kagome array and underestimating the vales for the kagome spin ice case. As reported by Zhang *et al.*[13] for model Z, this effect can be attributed to the initial random state from which it starts. For strongly-coupled artificial kagome networks, experimental values of $C_{\alpha\beta}$ are closer to the spin ice value of $1/3$. However, model Z has difficulties in reaching this value as it relies on a majority-vote spin flip process that can easily get pinned if a spin has two predefined spin-up neighbors and two predefined spin-down neighbors[23]. Therefore, for strongly-coupled islands, model Z is bond to fail after a certain point, underestimating the correlation values, but it is expected to work rather well for networks presenting strong quench disorder. Also, the Z model can screen out long-range antiferromagnetic interactions as it acts to maximize the number of local antiferromagnetic couplings.

In addition to these two hybrid models, Zhang *et al.*[13] also compared their first order experimental kagome correlators to an at-equilibrium Monte Carlo simulation plot (see Figure 3.15.c). The simulated kagome networks were thermalized at a fixed effective temperature, T_{eff}, while the nearest-neighbor coupling constant was varied according to the computed micromagnetic values. Although the nature of the dynamics in this model is very different from the experimental one, the matching is remarkably good. Furthermore, since both sets of correlations belonging to the two kagome networks are well described by such short-range models, they repor a universality in the development of spin correlations for demagnetized artificial kagome arrays[13]. In fact, this is rather straightforward as it is a direct consequence of the equivalence between the two networks in the short-range framework. However, for weakly coupled islands, there are clear deviations form the simulation plot. As reported by Zhang *et al.*[13], in this weak interaction regime the demagnetization output is solely dictated by the distribution of the switching fields, thus yielding a nearest-neighbor correlator that does not present any signature of inter-island interactions. The high coupling regime also displays some deviations from the short-range model plot. While this regime may also be affected by quench disorder, couplings beyond nearest-neighbors start to play an increasingly important role in this regime. It is therefore important to consider a mapping on

[22]Interestingly, the $C_{\alpha\gamma}$, $C_{\alpha\nu}$ and $C_{\alpha\delta}$ correlators present higher values in the short-range model than in the long-range dipolar one for temperatures ranging roughly between $T/J_{\alpha\beta} = 1$ and $T/J_{\alpha\beta} = 7$. This is also the temperature interval for which the nearest-neighbor correlator would agree with the experimental one. Since the effective potential constant, K, is adjusted to fit the experimental nearest-neighbor correlator and the G model is implemented via Metropolis Monte Carlo simulations[129], this overestimation is very similar to the results given by short-range at-equilibrium Monte Carlo simulations previously presented in this work (see Figure 3.10).

[23]This may even result in forbidden states that cannot be overcome with these kinetics.

a full dipolar treatment for such artificial kagome Ising networks, which might better account for the observed deviations.

3.4.2 Correlation Scattering Analysis

As presented in Figure 2.24, comparing demagnetized artificial arrays to at-equilibrium Monte Carlo simulations requires a set of physical and statistical quantities that can be computed for both experimental and simulated networks. Since we find ourselves again in a certain debate over which interaction model best describes the frozen states of demagnetized artificial arrays, the experimentally extracted values should be free of any interaction model. In this case, the general choices are to compare vertex population ratios, particularly for square ices[1, 49, 55, 83, 93] or the spin and charge correlations[11, 14, 46, 73], a more common choice for kagome arrays.

If a system is placed in a heat-bath, it eventually reaches an equilibrium state in accordance with the imposed reservoir temperature. For an infinite system, its energy value is exactly defined, but the system can still explore its different microstates within this macrostate constrain. If the system is finite, the energy value will fluctuate around its expected value due to finite-size effects. In Monte Carlo simulations these features are reproduced in a canonical ensemble picture. After the thermalization steps have been performed, several different equilibrium configurations are sampled, thus yielding a distribution of the system's energy, with its own mean value and standard deviation, which characterizes the system's finite-size fluctuations. Notice that the ensemble average converges towards the expected energy value as the sampling number increases, but the intrinsic and finite-size fluctuations still persist. Since the energy can be written down as a linear combination of the spin correlators, the spin and charge correlations will also present fluctuations around their expected values as well. These fluctuations are strongly dependent on the system size and are generally represented throughout this work in the form of error bars.

Suppose we are given a certain at-equilibrium Monte Carlo snapshot sampled for an unknown temperature during a simulation run for a kagome Ising network in a dipolar long-range interaction model. The question that we then ask is to which regime it belongs, or, in other words, for which temperature do we have the highest chances of stumbling upon this particular configuration. Clearly, if we are dealing with a snapshot that contains forbidden states, such a configuration would have very little chances of occurring in a low-temperature regime. Since we only have a single snapshot available, the idea is to compute the network averages of the spin and charge correlators, $C_{\alpha j}^{snapshot}$, and then compare them to their corresponding Monte Carlo plots. However, as mentioned above, each Monte Carlo

plot consists in an ensemble average[24], $< C_{\alpha j}^{MC}(T) >$, and a standard deviation reflecting the fluctuations around this value. If the given snapshot is often realized for a certain temperature, then the deviations of its correlators from their corresponding ensemble averages should be rather small[25]. In other words, the correlators computed over the given snapshot would normally fall within the corresponding standard deviations for temperatures for which this configuration is more likely to occur. Therefore, one way to quantify the likelihood of occurrence for the given snapshot at a certain temperature is to compute the following function:

$$K(T) = \sqrt{\sum_j (C_{\alpha j}^{snapshot} - < C_{\alpha j}^{MC}(T) >)^2} = \sqrt{\sum_j [\Delta(C_{\alpha j})]^2} \tag{3.11}$$

where $C_{\alpha j}^{snapshot}$ is a snapshot network-averaged correlator, $< C_{\alpha j}^{MC}(T) >$ is the corresponding ensemble average for a certain temperature T and the summation is performed over all extracted correlators. I refer to the $K(T)$ function as the spread-out function as it quantifies the scattering of the snapshot network averages around their expected values. If its value is relatively high, the given configuration is very unlikely to be sampled for the considered temperature. On the other hand, if its value is relatively low, then there are increased chances for the snapshot to be selected at the given temperature.

Figure 3.16.a gives the evolution of K(T) for a snapshot sampled at $T/J_{NN} = 0.1$ in a dipolar long-range framework. The minimum is found for $T/J_{NN} = 0.0912$. However, notice that the function presents a rather smooth parabolic-like shape around this minimum, making the given snapshot likely to be sampled throughout a broader range of temperatures close to the minimum value one. Also, remark that $K_{min} > 0$, thus reflecting the fluctuations of the snapshot correlators around the ensemble averages due to the network's finite size. Obviously, if fewer correlators are taken into account in the definition of the spread-out function, the minimum value would be lower. However, this would also bring certain inconveniences and even inaccuracies to the analysis. Suppose we take a snapshot corresponding to $T/J_{NN} = 0.681292$, with $C_{\alpha\beta} = -1/3$ and $C_{\alpha\gamma} = 0.050926$. Firstly, we include only $C_{\alpha\beta}$ in the K(T) definition. In this case, the spread-out function would present a minimum plateau (see black

[24]The ensemble average is the average over the 10^4 network averages sampled throughout the 10^4 modified Monte Carlo steps after thermalization.

[25]In general, the distribution of a correlator's network-averages, sampled at a certain Monte Carlo temperature, has a Gaussian-like shape. If a snapshot correlator value is within the limits of its standard deviations then it has a high chance of appearing during an at-equilibrium exploration of the given energetic manifold. If the snapshot value is off by three standard deviations, for example, it has a roughly 0.27% chance of actually being sampled, thus making it very improbable.

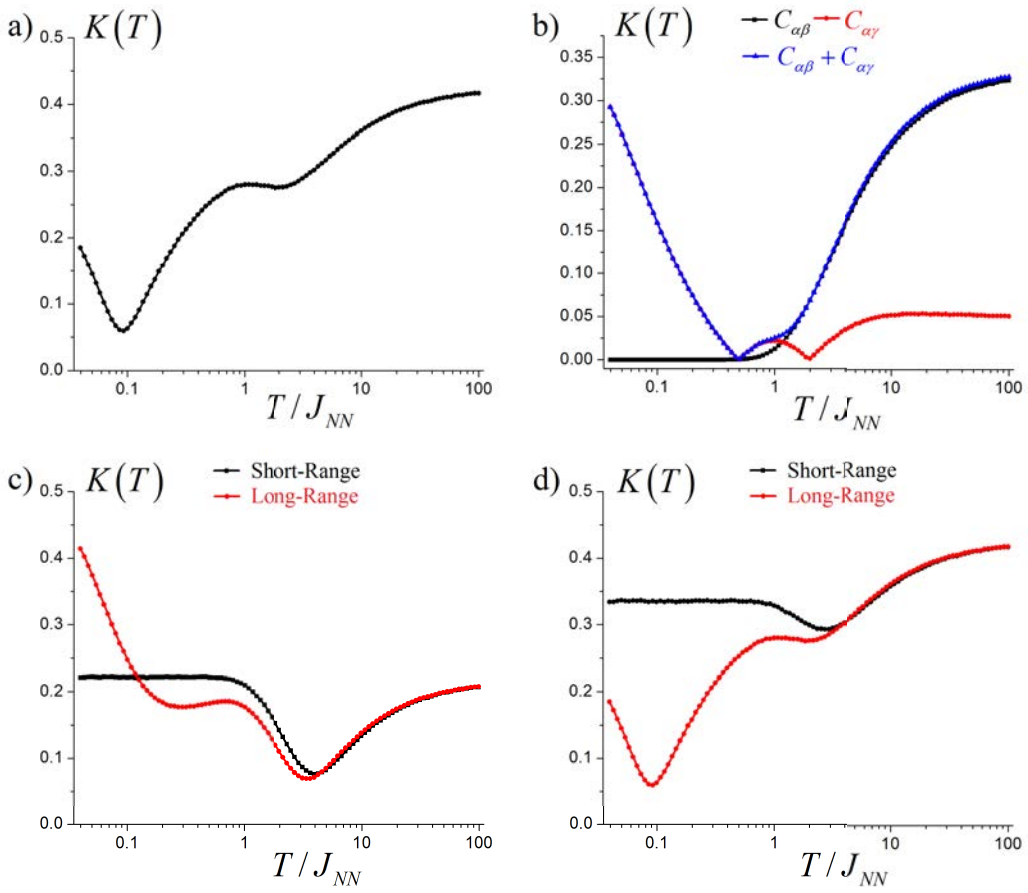

Figure 3.16 - The spread-out function, $K(T)$, quantifies the likelihood for a certain set of correlators to be sampled for a given simulation temperature, T. (a) The minimum of the function is found for $T/J_{NN} = 0.0912$, which is in the proximity of $T/J_{NN} = 0.1$ from which the snapshot was taken. The smooth shape of the minimum suggests that the selected configuration can be sampled for a broader range of temperatures in the vicinity of the minimum, but as the value of K(T) increases, the chances of stumbling upon it decrease. (b) One should be cautious when defining the spread-out function. Evaluating it solely through the use of nearest-neighboring correlators, the most strongly coupled pairs, can yield a broad range of compatible temperature, thus hiding the specific manifold from which the configuration was taken. Some correlators present non-monotonic behavior, which could result in multiple compatible regimes. In general, by taking as many correlators as possible improves the identification of the corresponding temperature regime. The spread-out function can also be employed to quantify the relative adequacy of one model over another for describing the given snapshot. (c) For a high temperature configuration, both short-range and dipolar long-range models agree upon the corresponding temperature with roughly the same minimum for K(T). In this case, both models can be invoked to describe the selected configuration. (d) However, for a deep spin ice configuration, the long-range model better accounts for the given set of correlators, presenting a clearly lower minimum and therefore a better match than the short-range model.

plot in Figure 3.16.b) since the $C_{\alpha\beta}$ correlator is always equal to $-1/3$ once the spin ice manifold has been reached. This would imply that the given snapshot has equal chances of being sampled for any spin ice temperature, a fact which is not true in a long-range dipolar framework. Now suppose we take only the $C_{\alpha\gamma}$ correlator for defining K(T). The spread-out function would present two minima in this case (see red plot in Figure 3.16.b) due to the non-monotonic temperature evolution of the $C_{\alpha\gamma}$ correlator (see Figure 3.12). The given value of $C_{\alpha\gamma} = 0.050926$ can be rather easily realized both for $T/J_{NN} \cong 0.7$, belonging to the spin ice phase, and for $T/J_{NN} \cong 2.0$, which is still in the paramagnetic regime. Therefore, the identification of the corresponding regime is ambiguous in this case. Nevertheless, by combining the two correlators in the definition of K(T), both the plateau and the twin minima behavior are avoided and a single minimum is found (see blue curve in Figure 3.16.b). Adding more correlators to the definition would increase the accuracy in the identification of the most representative temperature regime.

Suppose that we now give a certain Monte Carlo snapshot without specifying the interaction model that was employed for the simulation that sampled it. In this case, we can still proceed as before and compare the snapshot correlations to ensemble averages of simulations involving different interaction models. In our case, we consider the short-range interaction model (see expression 3.6) and the dipolar long-range interaction model (see expression 3.7). As was previously discussed, these two models present similar development for the spin and charge correlators in the paramagnetic phase, but differences start to be seen as the system enters the spin ice manifold. Therefore, if the given snapshot belongs to the high-temperature window, a spread-out function analysis should yield a compatible temperature regime for which both models agree rather well (see Figure 3.16.c). On the other hand, if the snapshot belongs to a manifold for which the two models present different ensemble averages, than one model should perform better than the other in determining the corresponding temperature (see Figure 3.16.d.). Both K(T) plots may well present a minimum, but the lower minimum suggests that several correlators included in the definitions are better accounted for. In other words, the lower the minimum of K(T) for a specific model, the more snapshot correlators can fall within the standard deviations of the MC plots reflecting the systems finite-size fluctuations, thus making the configuration more likely to occur for that temperature.

The situation presented above is similar to the one we are facing when confronting demagnetized artificial spin ice configurations to Monte Carlo plots: we have a few snapshots for which separate sets of correlators can be computed and then related to their corresponding thermodynamic evolutions. Since finite-size fluctuations are crucial here, the simulated network must match the size of the experimental one. However, one should be cautious when interpreting the results.

In previous cases, the snapshot was actually taken from a set of configurations that respect a Boltzmann energy distribution characterized by a certain temperature. Relating this configuration to a simulation plot described by the same at-equilibrium dynamics makes sense, and a match, a low minimum value for the spread-out function, can very well mean that the snapshot can indeed be selected by the system as it explores its energetic manifold at the given temperature. In the case of artificial spin ices, the driving dynamics is clearly out-of-equilibrium. Although the spread-out function can be used to find a temperature for which the Monte Carlo plot best fits the set of correlators, this temperature does not play the role of a Lagrange multiplier characterizing an equilibrium state. Proving that a system is in thermal equilibrium is rather hard, whereas proving that a state is out-of-equilibrium can be quite easy if some of its correlators show severe deviations from their corresponding at-equilibrium expected values. To make the difference between the Monte Carlo temperatures describing energy distributions governed by the Boltzmann law and the temperatures extracted from the minimum of the spread-out function, I shall call the latter effective temperatures, particularly for demagnetized snapshots[26]. I would like to emphasize again that this effective temperature is not describing an equilibrium state, but is rather an energetic label that plays the role of the argument for which the minimum of the spread-out function is achieved ($T_{eff} = argmin[K(T)]$).

The goal of employing the spread-out function analysis here is to ascertain which interaction model better describes the outcome of a demagnetization protocol when a comparison to Monte Carlo behavior is made. This is similar to the situations presented in Figures 3.16.c and 3.16.d. Although the natures of the underlying dynamics are different in the two cases, the dipolar long-range model offers a remarkable good description for the resulting correlation sets and performs overall better than the short-range model. In the following section, the relevance of the short and long range models will be discussed by employing this spread-out function correlation scattering analysis.

3.4.3 Long-Range Signatures and Non-Universality

For each set of spin and charge correlators reported in Table 3.3 a spread-out function analysis was performed to determine the best-suiting effective temperature regimes and also to quantify the adequacy of the two interaction models presented so far. To this end, single-spin flip Monte Carlo simulations have been performed on a kagome Ising network with $18 \times 18 \times 3 = 972$ spins under periodic boundary conditions, thus relatively matching

[26]Note that this type of effective temperature is different from the ones that have already been discussed for artificial spin ices[55, 91]. In this case, the effective temperature describes the observed distribution of the vertex populations of a demagnetized artificial square ice through a tailored Boltzmann-type law.

Table 3.5 - The effective temperatures, minimum spread-out function values and the compatibiliy ratios for the 10 experimental correlation sets presented in Table 3.3. The first seven spin correlators are used for the definition of the spread-out function.

Image index	T_{eff}/J_{NN}		K_{min}		Comp. Ratio	
	Short	Long	Short	Long	Short	Long
1	1.71133	0.68129	0.07308	0.04762	28.5714%	71.4286%
2	1.71133	0.27123	0.13562	0.07871	28.5714%	57.1429%
3	2.15443	1.71133	0.05789	0.04347	71.4286%	85.7143%
4	1.58489	1.25893	0.04054	0.04052	85.7143%	71.4286%
5	1.84785	1.4678	0.07318	0.04999	57.1429%	71.4286%
6	1.4678	1.25893	0.02154	0.04249	85.7143%	71.4286%
7	1.71133	1.25893	0.0477	0.02724	71.4286%	85.7143%
8	1.84785	1.25893	0.07446	0.0526	42.8571%	71.4286%
9	1.58489	0.58434	0.07222	0.03817	28.5714%	57.1429%
10	1.84785	1.35936	0.08362	0.07218	28.5714%	42.8571%

the average size and number of spins of the experimental networks[27]. As mentioned before, the definition of the spread-out function is a matter of choice and the first option is to take into account only the first seven pairwise spin correlators. The effective temperatures along with the spread-out function minima are reported in Table 3.5.

One of the first things that can be noticed is that almost all effective temperatures found are specific to the onset of the spin ice phase, i.e., $T_{eff}/J_{NN} \sim 1$. This is well in agreement with the forbidden state ratios reported in Table 3.2. For this temperature window, the Monte Carlo plots of all correlators discussed here start to show distinctive behavior between the short and the long-range models (see Figure 3.13). We might therefore expect one model to fit the experimental correlation sets better than the other. Indeed, the minimum values of the spread-out function show that, overall, the long-range model performs slightly better than the short-range one does[28]. This can also be seen in Figure 3.17.a. Remarkably, both models present rather low values for the spread-out function minima, of the same order of magnitude as the at-equilibrium Monte Carlo sampled snapshots (see Figures 3.17.b and 3.17.c). In addition to these quantities, it is also interesting to see how far off each experimental correlator is situated from the expected value of its effective temperature.

[27]The last two images present a higher number of spins (see Table 3.2). For these two cases, additional simulations were performed on a kagome lattice comprising $21 \times 21 \times 3 = 1323$ spins. The experimental data are confronted with these predictions for the last two indexes.

[28]In their Supplementary material[129], Zhang *et al.* report that they also see only a slight difference between Monte Carlo simulations performed on kagome Ising systems with nearest-neighbor couplings only and with dipolar interactions. However, the temperature range is not specified.

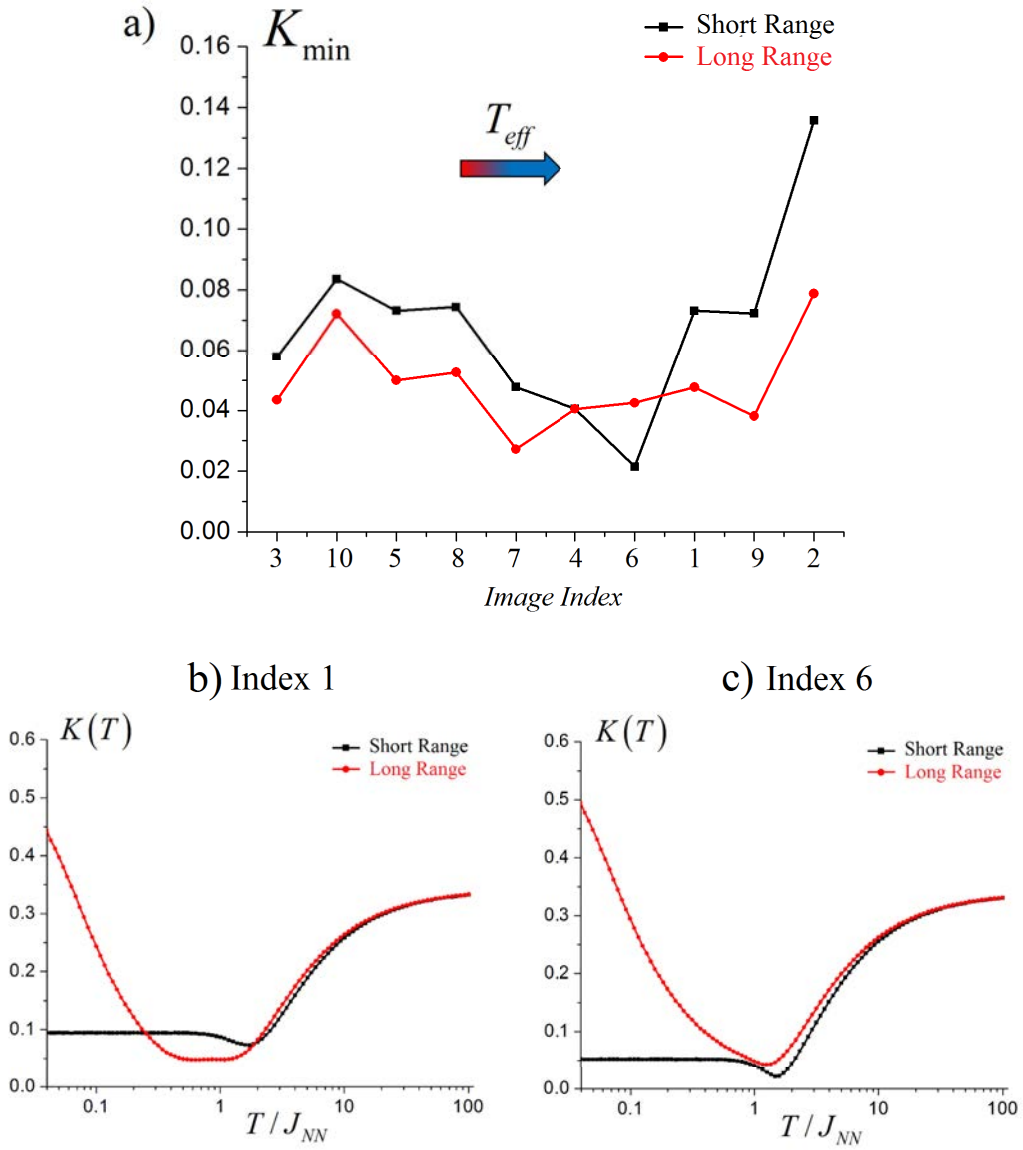

Figure 3.17 - (a) The minimum value for the spread-out function for all 10 MFM images. The indexes have been rearranged, ordering the images from the highest effective temperature given by the long-range model fit to the lowest. Notice that the minimum value for both models is very low, but the long-range models offers an overall slightly better fit than the short-range one. Note that the lines between the data points have no physical meaning and serve just as visual guides. (b-c) The spread-out function dependencies, K(T), for images indexed 1 and 6. The long-range model generally offers lower minima, with the exception of image index 6, and a plateau-like behavior can sometimes be observed for this particular definition of the spread-out function, making the models to disagree on the effective temperatures, even for relatively high-temperature regimes.

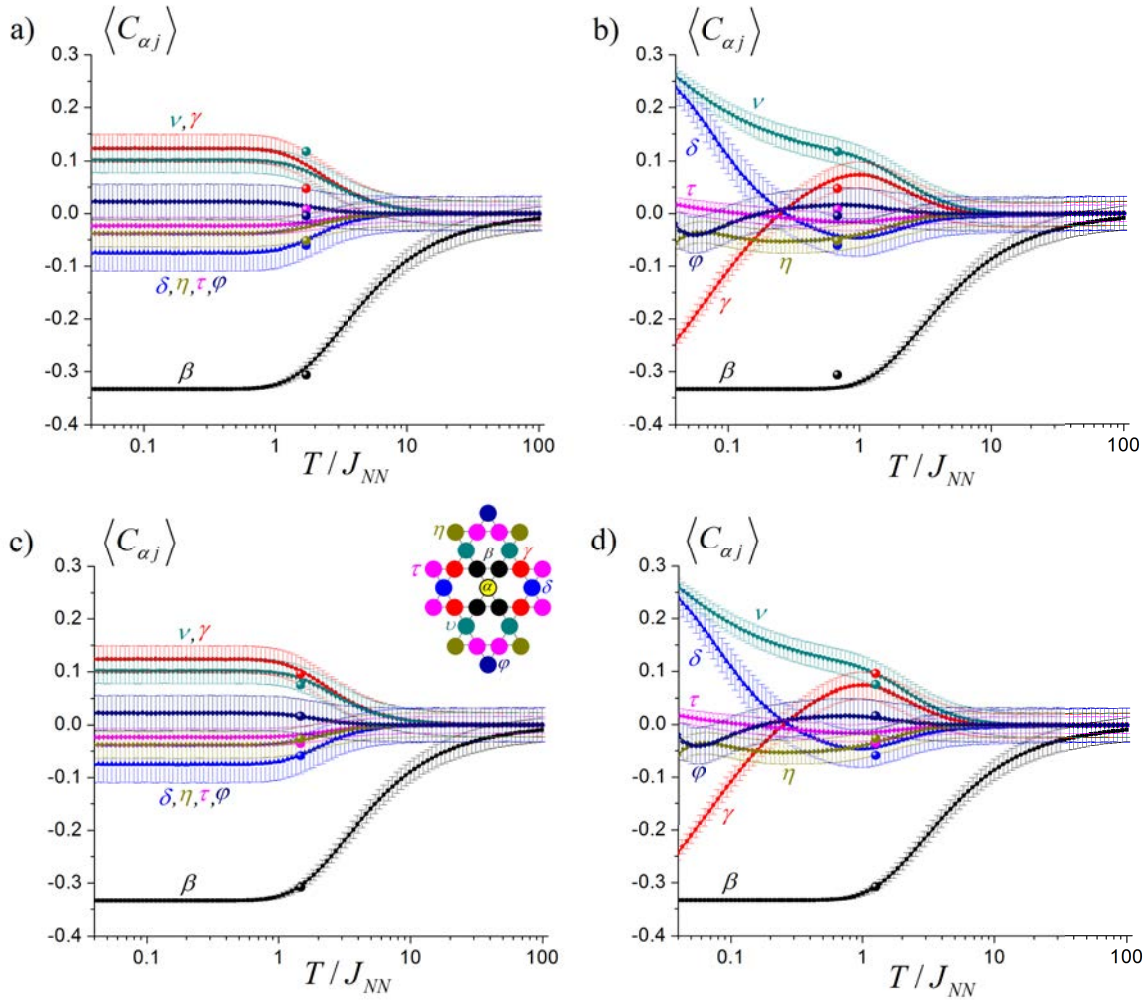

Figure 3.18 - Typical examples for the scattering of the experimental correlators around their Monte Carlo expected values. The two upper images correspond to image index 1, with a short-range model fit (a) and a long-range model fit (b). Similarly, the short (c) and long-range (d) model deviations are given for the correlators corresponding to image index 6. With the current definition for K(T), the long-range model fits slightly better the data. The inset of Figure (c) gives the correlators definitions, after Chioar *et al.*[14].

Therefore, a compatibility ratio has also been defined as the number of correlators fitting within the ensemble standard deviations over the total number of considered correlators. This quantity adds extra information to the spread-out function picture as it inspects more closely the deviations from the expected correlation values. For instance, for the 1^{st} indexed image, the spread-out function values are rather low for both models, but 5 out of 7 correlators fall within the long-range model's standard deviations, while the short-range model accounts only for 2 of the 7 this way (see Figures 3.17.c and 3.17.d). Also, if we look at the 6^{th} image, the short-range model better describes this state (the only exception seen so far). Yet, although the long-range model has a minimum spread-out function value twice as high as the short-range one, it still contains 5 out of 7 values within the corresponding standard deviations, making it still a good match (see Figures 3.18.a-d.). Therefore, overall, the long-range model performs slightly better in describing the remanent states of demagnetized artificial kagome Ising networks.

There is however a rather intriguing aspect here: the two models hardly agree upon the same effective temperature, even for relatively high temperature values where it is expected. A closer inspection reveals that the deviations of higher order correlators ($C_{\alpha\tau}$, $C_{\alpha\eta}$ or $C_{\alpha\varphi}$) are generally lower than those of lower order ones ($C_{\alpha\gamma}$, $C_{\alpha\delta}$ or $C_{\alpha\nu}$). In other words, the current definition of the spread-out function generally tends to achieve minimization by reducing $\Delta(C_{\alpha\beta})$, $\Delta(C_{\alpha\tau})$, $\Delta(C_{\alpha\eta})$ and $\Delta(C_{\alpha\varphi})$. This is rather curious since the $C_{\alpha\gamma}$, $C_{\alpha\delta}$ and $C_{\alpha\nu}$ correlations correspond to more strongly coupled spin pairs (with the exception of $C_{\alpha\beta}$, of course) and are expected to play a more significant role in determining the effective temperature in this situation, particularly for the long-range model plots. This is an effect of the definition used for K(T), which gives the same minimization priority to all correlations, regardless of their rank and corresponding coupling strength, and ultimately results in a mismatch between the effective temperatures found for the two models. This feature is nevertheless remedied by introducing the nearest-neighbor charge correlator in the spread-out function definition.

As mentioned at the end of section 3.2.3, two sets of nearest-neighbor charge correlators have been extracted from the MFM images: $Q_iQ_{i+1}^{dir}$, computed from the underlying hexagonal charge lattice defined using expressions 3.4, and $Q_iQ_{i+1}^{corr}$, evaluated using expression 3.5 and the experimental values of the spin correlators. The deviations of these experimental correlators from their expected values, $\Delta(QQ)$, are included in the spread-out function in addition to the first seven spin correlation terms, $\Delta(C_{\alpha j})$. The relevant correlation scattering analysis quantities are reported in Table 4.6 for $Q_iQ_{i+1}^{dir}$ and in Table 4.7 for $< Q_iQ_{i+1}^{corr}$.

The agreement between the two models on the effective temperature values for this spread-out function definition is significantly improved, particularly for relatively high effective

Table 3.6 - The effective temperatures, minimum spread-out function values and the compatibiliy ratios for the 10 experimental correlation sets presented in Table 3.3. The first seven spin correlators along with $Q_iQ_{i+1}^{dir}$ are used for the definition of the spread-out function.

Image index	T_{eff}/J_{NN}		K_{min}		Comp. Ratio	
	Short	Long	Short	Long	Short	Long
1	1.35936	1.4678	0.07772	0.0577	62.5%	62.5%
2	1.58489	1.4678	0.13905	0.11981	50%	50%
3	1.99526	1.99526	0.06408	0.04774	75%	75%
4	1.25893	1.25893	0.05827	0.04124	87.5%	75%
5	0.8577	0.54117	0.12974	0.05527	50%	62.5%
6	1.25893	1.4678	0.03098	0.04732	87.5%	62.5%
7	1.58489	1.58489	0.05133	0.04155	75%	87.5%
8	1.25893	1.16591	0.1042	0.05445	62.5%	75%
9	1.16591	1.16591	0.07874	0.05321	62.5%	62.5%
10	1.58489	1.58489	0.09359	0.07286	12.5%	62.5%

Table 3.7 - The effective temperatures, minimum spread-out function values and the compatibiliy ratios for the 10 experimental correlation sets presented in Table 3.3. The first seven spin correlators along with $Q_iQ_{i+1}^{corr}$ are used for the definition of the spread-out function.

Image index	T_{eff}/J_{NN}		K_{min}		Comp. Ratio	
	Short	Long	Short	Long	Short	Long
1	1.25893	1.25893	0.0879	0.04983	37.5%	87.5%
2	1.84785	1.84785	0.13581	0.13114	37.5%	37.5%
3	1.71133	1.71133	0.07733	0.0435	75%	87.5%
4	0.00136	0.92612	0.09338	0.0514	37.5%	75%
5	0.01711	0.46416	0.14375	0.05252	50%	62.5%
6	1.16591	1.35936	0.04241	0.04303	87.5%	75%
7	0.8577	1.000	0.09544	0.03635	62.5%	75%
8	1.000	1.000	0.11213	0.05618	62.5%	75%
9	0.92612	1.000	0.09201	0.04349	37.5%	75%
10	1.58489	1.58489	0.09368	0.07286	12.5%	62.5%

temperatures ($T_{eff}/J_{NN} > 1.0$), as it was expected. Furthermore, the minimum values of the spread-out function for both the short and long range models are following each-other (see Figures 3.19.a and 3.19.b) in this regime, but the long-range model still performs slightly better. However, in the low-temperature regime, the minima of K(T) for the short-range model starts to increase as the effective temperature decreases, while the long range fit is rather constant. Furthermore, the short-range model presents some intriguing effective temperature values (see indexes 4 and 5 in Table 3.7). This is a direct effect of the plateau behavior of all correlation plots in the short-range spin ice phase. In this regime, any spin ice temperature would do for the minimization of K(T) and the experimental correlators can be slided freely along the horizontal axis in the spin ice window and still find a satisfying minimum[29]. Overall, the experimental correlators deviate more and more from the spin ice plateaus as the effective temperature drops, but they do this by following the long-range Monte Carlo plots. This feature is beautifully reflected by the experimental points of the nearest-neighbor charge correlator (see Figures 3.19.c and Figure 3.19.d). For both charge correlator sets, the agreement with the Monte Carlo plots is remarkable and all Q_iQ_{i+1} experimental points fall within the standard deviations of the corresponding long-range effective temperatures. In fact, by taking only the charge correlators in the spread-out function definition, the resulting effective temperature picture is very similar to the ones that include both the spins and the charge correlators. This is also possible thanks to the strictly monotonic behavior of the $< Q_iQ_{i+1} > (T)$ plot, avoiding situations in which two effective temperatures can be equally favorable (see the $C_{\alpha\gamma}$ plot in Figure 3.16.b)[30]. It therefore seems that the nearest-neighbor charge correlator stands as a single estimator for the order established within demagnetized artificial kagome Ising networks. However, why does it play such a major role?

To understand the drastic change the charge correlator brings to the spread-out function analysis, recall that it can normally be written as a linear combination of the first three spin correlators (see expression 3.5). One of the experimental data sets was precisely defined this way, while the other set can still be written in a similar form, but the coefficients of the linear combination are not exactly the same and can vary from one image to another. In this case, the deviation of $Q_iQ_{i+1}^{corr}$ from the $< Q_iQ_{i+1} > (T)$ Monte Carlo plots, $\Delta(Q_iQ_{i+1})$, becomes:

$$\Delta(Q_iQ_{i+1}) = -4 \cdot \Delta(C_{\alpha\beta}) - 2 \cdot \Delta(C_{\alpha\gamma}) - 2 \cdot \Delta(C_{\alpha\nu}) \tag{3.12}$$

[29]Eventually, one minimal value is found due to the small variations in the ensemble averages.

[30]Notice that this feature does not apply for the kagome spin ice case, since its charge correlator behavior is non-monotonic. Higher spin correlators are required in this case to discriminate between a paramagnetic and a spin-ice regime, but even in this case the differences are rather small.

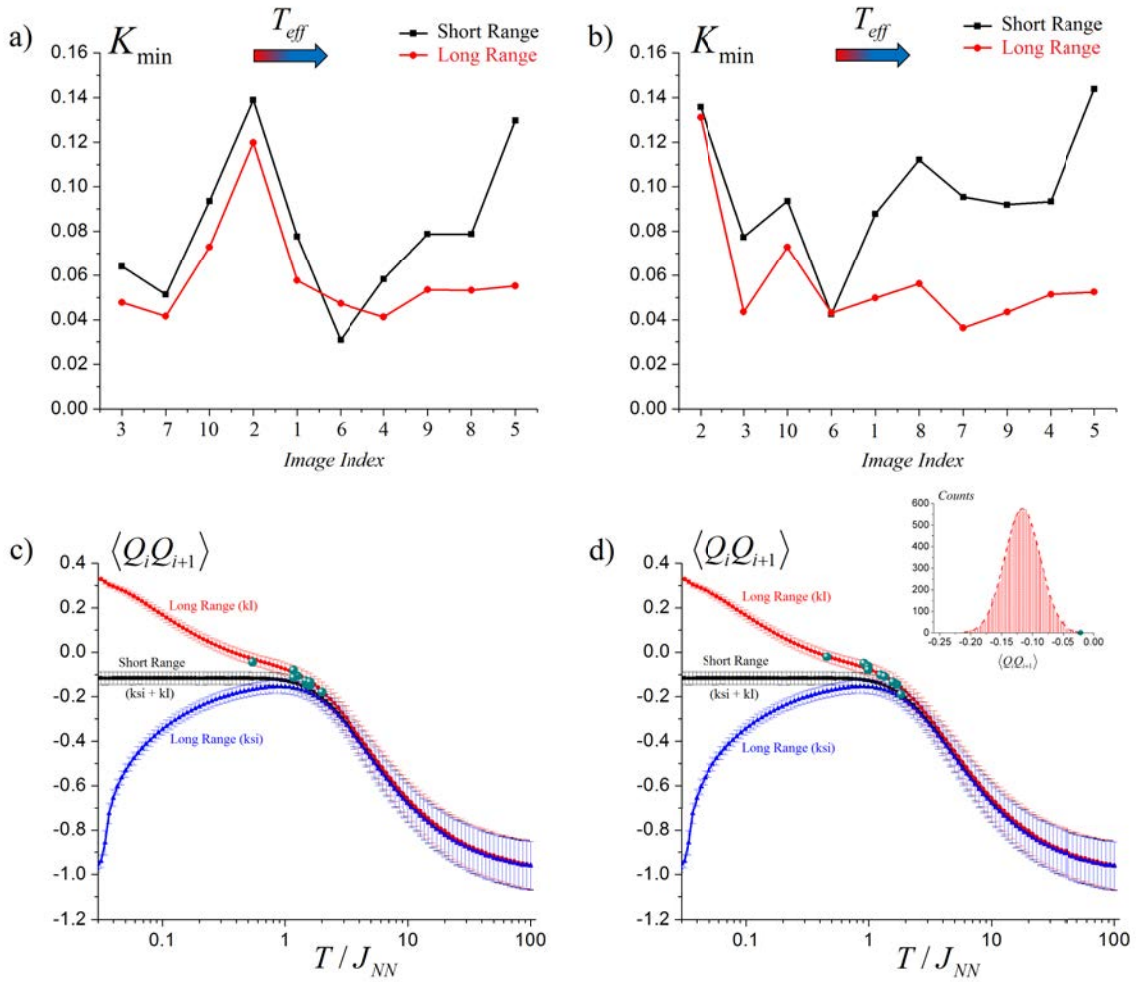

Figure 3.19 - The spread-out function minima for the 10 MFM images with (a) the $Q_i Q_{i+1}^{dir}$ values and (b) the $Q_i Q_{i+1}^{corr}$ values included in the K(T) definition. Overall the long-range model prevails, and the short-range model increasingly fails to reproduce the data in the low-temperature regime. The 10 values of (c) $Q_i Q_{i+1}^{dir}$ and (d) $Q_i Q_{i+1}^{corr}$ mapped on the Monte Carlo plots. The agreement with the long-range model is remarkable, and clear deviations can be seen from the spin ice ground state plateau. The inset of Figure 4.19.d, taken from Chioar *et al.*[14], shows how far off the experimental point is from the average of a $< Q_i Q_{i+1} >$ short-range spin-ice plateau distribution (more than three standard deviations). These results highlight the importance of long-range coupling terms and limit the apparent universality in correlation developement to relatively high effective-temperatures.

Therefore, the spread-out function definition can still be written as a linear combination of spin correlators:

$$K(T) = 17\cdot(\Delta(C_{\alpha\beta}))^2 + 5\cdot(\Delta(C_{\alpha\gamma}))^2 + 5\cdot(\Delta(C_{\alpha\nu}))^2 + \quad (3.13)$$
$$+16\cdot(\Delta(C_{\alpha\beta}))\cdot(\Delta(C_{\alpha\gamma})) + 16\cdot(\Delta(C_{\alpha\beta}))\cdot(\Delta(C_{\alpha\nu}) + 8\cdot(\Delta(C_{\alpha\gamma}))\cdot(\Delta(C_{\alpha\nu})) +$$
$$+(\Delta(C_{\alpha\delta}))^2 + (\Delta(C_{\alpha\tau}))^2 + (\Delta(C_{\alpha\eta}))^2 + (\Delta(C_{\alpha\phi}))^2$$

One can immediately notice that the role of the lower order spin correlators has been significantly enhanced in the minimization of the spread-out function, particularly for $C_{\alpha\beta}$[31]. These correlators correspond to the strongest-coupled pairs and they also display clear distinctive behavior between the two models at the onset of the spin ice phase, visually more pronounced than other higher order correlators like $C_{\alpha\tau}$, $C_{\alpha\eta}$ and $C_{\alpha\varphi}$ (see Figure 3.12). Focusing the analysis on these pairs thus seems natural. In addition, along with the squared deviations, there are also three terms of mixed products, which are also strongly reinforced by their coefficients. These terms play a crucial role since they can have positive and negative signs[32], thus making the analysis more sensitive to the collective correlation behavior. In the end, these reinforced terms account for the good matching between the two models in the relatively high effective temperature window, while the increased sensitivity to collective correlation development makes this spread-out function definition more sensitive to the small evolution of the Monte Carlo correlation plots.

Similarly to the case of artificial kagome spin ice reported by Rougemaille *et al.*[73], the nearest-neighbor charge correlator has proven to be a useful tool for highlighting long-range dipolar signatures in artificial kagome Ising systems. Figures 3.19 clearly show how some of the experimental data present significant deviations from the short-range ground state plateau. Almost half of the experimental charge correlators are outside the standard deviations of the short-range Monte Carlo correlator distributions at the corresponding temperature, making them increasingly unlikely to be accounted for by a nearest-neighbor framework. The inset of Figure 3.19.d presents such a case, where the experimental point falls off by more than three standard deviations, which, for a Gaussian distribution, would imply less than a 0.1% chance of occurring. However, the matching with the long-range model is very good. These results have a direct impact on the universality in correlation development previously reported by Zhang *et al.*[13].

[31] Indeed, the overall deviation of the $C_{\alpha\beta}$ correlator is reduced with this definition.

[32] Evidently, a negative value is desired for all of them, but they cannot be all negative at the same time.

The models proposed by Zhang *et al.* for their experimental data sets have been based on reproducing the experimental values of the nearest-neighbor spin correlator, $C_{\alpha\beta}$, which is roughly about -0.28 (see Figure 3.15.c)[33]. For a Monte Carlo sampling at $T/J_{NN} \sim 1.84785$, the ensemble average matches this value[34]. At this temperature, the differences between a nearest-neighbor description and a dipolar long-range one are very small, which makes such artificial spin systems appear as effectively short-range. Given the universality within the short-range framework, this automatically suggests that there is a common ground in artificial kagome networks, transcending the particular moment orientation as Zhang *et al.* reported [13]. Nevertheless, this universality stands only if the effective temperatures are rather high and since their best scenario for the $C_{\alpha\beta}$ value is -0.28, a regime with more pronounced differences was not accessed. Very likely, both their samples and the ones presented here present a strong quench disorder, which could prevent proper accommodation of inter-island interactions and hence the accessing of more correlated manifolds. However, the magnetic moment of the current TbCo nanodots is approximately three times larger than the one of the CoPt multi-layered dots used by Zhang *et al.* and the inter-island spacing is also smaller (400nm for the current samples and 500nm for the most tightly-packed array of Zhang *et al.*). This implies a stronger coupling between neighbors in this case, which has a better chance of overcoming quench disorder effects. Indeed, the average value of $C_{\alpha\beta}$ for the current experimental data sets is -0.30694, highlighting a more strongly-coupled spin network. In addition, $C_{\alpha\gamma}$, $C_{\alpha\nu}$ and $C_{\alpha\delta}$ values are overall better reproduced by long range interaction models, suggesting that this strong coupling very likely extends beyond the nearest-neighbors and influences the kinetic pathways during demagnetization. Such behavior is effectively reproduced by the experimental values of the charge correlator. In addition, given the effective microscopic Hamiltonian description (see expression 3.10) and the collapse of the data on the long range curve, slowly deviating from the short-range one, this suggests that the system starts to accomodate the effective charge couplings as well, going beyond the nearest neighbor term. Although the deviations are not very strong (no positive Q_iQ_{i+1} value has been obtained so far), they are sufficient for assessing the limits of the reported universality. In fact, some of the correlation sets presented here are roughly within its bounds, but almost half of them contradict it. Along with the results of Rougemaille *et al.*[73] (see Figure 2.25), these findings support the idea of a non-universal behavior in artificial kagome spin systems.

[33] I will use my sign convention for the correlators in this discussion, which is opposite to the one employed by Zhang *et al.*

[34] Notice that one of the correlation data sets reported here (image index 3) has such a $C_{\alpha\beta}$ value and all definitions of the spread-out function employed so far yield a relatively high effective temperature, close to the at-equilibrium case.

Since the dipolar kagome spin ice network has been intensively studied and has proven to display some exotic emergent phases and spin textures[7–9], which have been locally accessed experimentally[6, 10, 14], this result stimulates an effort for further investigation of the kagome Ising array, which might very well present some interesting features of its own. Such a study would have been rather pointless if the universality had hold in any situation, but this result offers the opportunity for discovering new exotic textures and behavior, both theoretically and experimentally. Numerically, such a task has already been undertaken in the context of this work and results are presented in the following sections.

3.5 In Search of the Dipolar Long-Range Ground State

3.5.1 Critical Slowing Down Effects

In previous sections we have seen some thermodynamic features of the kagome Ising network via Monte Carlo simulations governed by nearest-neighbor couplings and by dipolar long-range interactions. The statistics of the kagome lattice was firstly explored by Syozi[65], proving that a short-ranged 2D kagome antiferromagnetic lattice has no critical behavior down to absolute zero. Soon after, Kanô and Naya[67] calculated exactly the residual entropy/spin of its highly degenerated short-range ground state, finding a value of 0.50183 k_B, one of the highest yet found for a 2D frustrated lattice. If dipolar long-range interactions are taken into account, this degeneracy is expected to be gradually lifted as the systems further cools in the spin ice phase. However, the introduction of long-range dipolar interactions increases the complexity of the problem and exactly solvable solutions are often replaced by other techniques, such as mean-field approximations and Monte Carlo simulations. Such approaches have their own drawbacks and we have seen, in section 2.4.2, how the single spin-flip dynamics suffers from a critical slowing down effect and is unable to further explore ergodically the phase space of kagome spin ice. Nevertheless, the lowest temperature states sampled have unraveled some ordering tendencies in the spin textures, eventually leading not only to the discovery of the order parameter of the phase transition causing the critical slowing down effect, but also to the dynamics that can overcome it and ultimately drive the system into its ground state manifold.

Similarly to kagome spin ice, the single spin-flip dynamics encounters a critical slowing down effect deep in the spin ice phase of the dipolar kagome Ising system. Figure 4.20.a gives the temperature evolution of the spin-flip acceptance ratio. Given the universality between the two kagome networks in the paramagnetic regime, their acceptance ratios are the same for this temperature window. After entering the spin ice manifold, both long-range acceptance

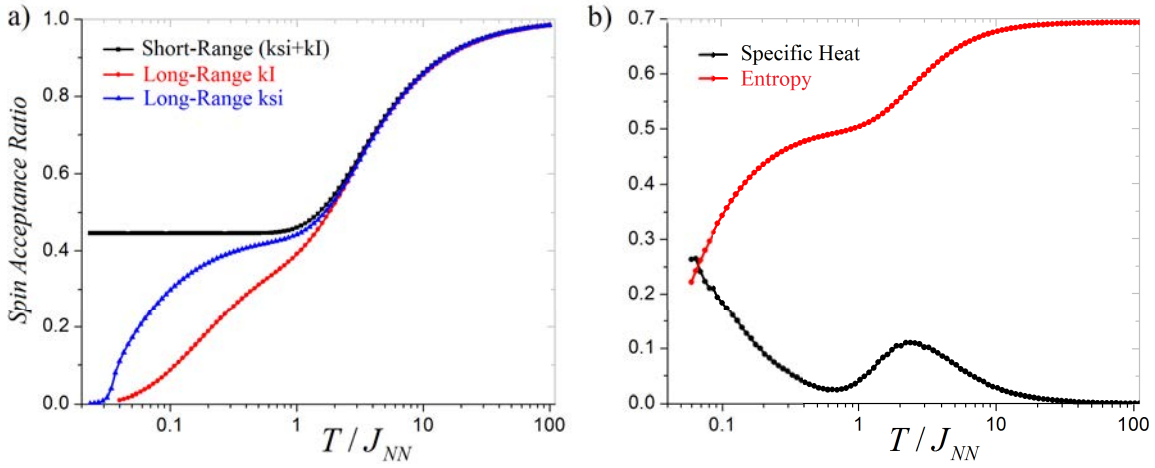

Figure 3.20 - (a) The single spin-flip acceptance ratio for a simulated kagome Ising system for both the short-range (black) and the long-range (red) models. The kagome spin ice long-range plot is also given for comparison (blue). These simulation data correspond to a $12 \times 12 \times 3$ kagome lattice with periodic boundary conditions. Notice the steep decrease of the acceptance ratio for dipolar kagome Ising compared to the other plots, eventually leading to a critical slowing down phenomenon. (b) The specific heat and entropy temperature plots given by the same Monte Carlo simulation for a kagome Ising network with long-range dipolar interactions. Just as the spin ice manifold is reached, the system proceeds quickly to further correlate and a phase transition appears to be present where the single spin-flip dynamics critically slows down. In contrast to kagome spin ice, the single spin-flip cannot sample the entire specific heat peak (see Figure 2.15).

ratios continue to decrease as the systems further correlate, with the kagome Ising plot falling faster to zero than the kagome spin ice one. For the last sampling temperature, $T/J_{NN} \approx 0.04$, an average of one spin-flip occurs in 100 tryouts and the number of required decorelation steps increases exponentially if the temperature slightly decreases further. Nevertheless, for the temperature window reported in previous cases, the modified Monte Carlo step algorithm employed ensures that the relevant thermodynamic quantities are properly sampled.

The steep decrease of the kagome Ising spin-flip acceptance ratio suggests that there might be a phase transition deep in the spin ice phase, which ultimately slows down this spin dynamics. Indeed, the specific heat and entropy (see Figure 4.20.b) indicate that the system is willing to recover more of its degrees of freedom in this low-temperature regime. In fact, the entropy value is still quite high at this stage and shows tendencies for further evolutions, as do the spin and charge correlators (see Figures 4.12 and 4.13). However, a new spin dynamics is necessary for continuing the exploration of lower energetic manifolds. This dynamics must comply with the already-established constrains of the spin ice phase, the kagome ice rules, and should have a relatively high acceptance ratio.

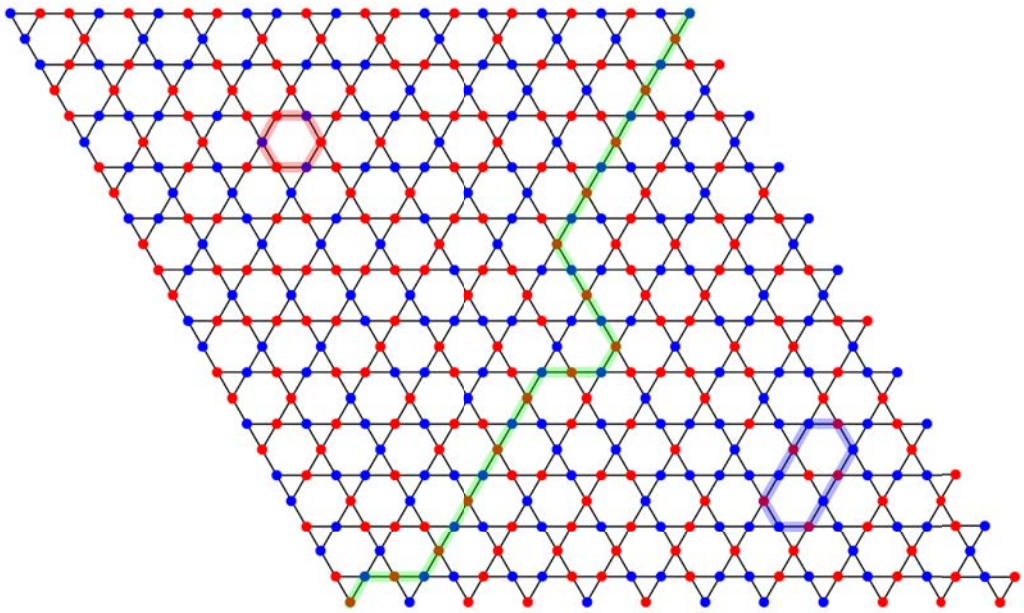

Figure 3.21 - A typical spin ice phase for the kagome Ising system ($T/J_{NN} \approx 0.7$). The red and blue circles correspond to up and down spin states, respectively. Similarly to kagome spin ice, three types of spin chains can be found: a short chain (red) curling around a hexagon, a long chain (blue) comprising more hexagons and stretching chains (green) that wrap around the torus on which the network is placed given the periodic boundary conditions.

In the case of kagome spin ice, the spins tend to form loop-like formations, curling around the lattice hexagons (see Figure 2.7). Furthermore, in a short-range framework, flipping these loops doesn't cost any energy and the ice rules are always preserved. Therefore, this loop dynamics is ideal for exploring the spin ice manifold and, in the case of kagome spin ice, it has proven to be the ingredient for overcoming the critical slowing down of the single-spin flip dynamics, ultimately accessing the ground state manifold. Since kagome Ising behaves equivalently to kagome spin ice within the nearest-neighbor coupling model, an equivalent loop dynamics would also efficiently map the spin ice energetic landscape.

In section 2.2.2 we have seen that the generation of a spin loop in kagome spin ice is done by passing from a spin to a neighboring one that has a scalar spin value opposite to the former. This process is repeated until a spin that is already in the loop is selected again. In the case of kagome Ising, all spins are aligned along the vertical axis and the loops become alternating ± 1 spin chains[35]. Figure 4.21 shows examples of the three possible cases. In addition to single spin-flip, a loop-flip dynamics has also been implemented in the modified Monte Carlo steps, as presented for kagome spin ice (see section 2.2.2). The temperature

[35] I will use both the "loop" and the "chain" terms for the kagome Ising case.

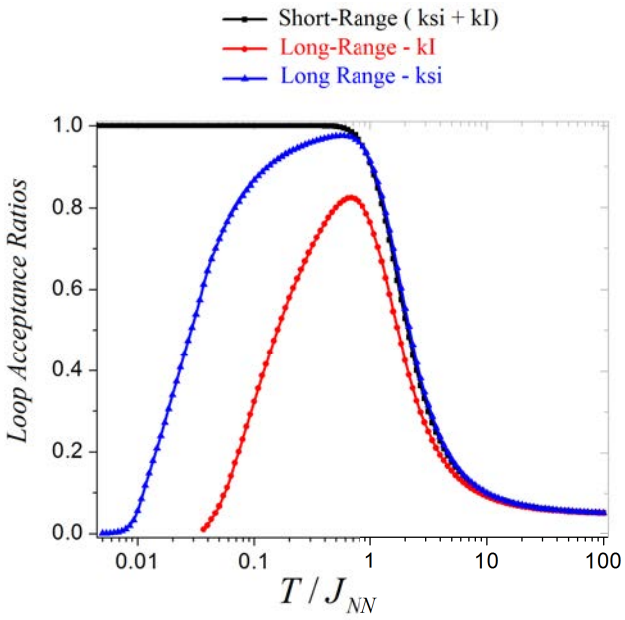

Figure 3.22 - The loop acceptance ratios for kagome Ising network with short-range coupling (black line) and dipolar long-range interactions (red). The long-range plot for kagome spin ice is also provided for comparison (blue line). The simulations were performed on a $12 \times 12 \times 3$ lattice with periodic boundary conditions. Clearly, the loop movements perform poorly for kagome Ising, and they freeze at about the same temperature as the single spin-flip dynamics.

dependence for the acceptance ratios for this supposedly efficient dynamics are reported in Figure 4.22.

As soon as the spin ice phase is reached, a closed-loop can eventually be found starting from any given spin. Therefore, the loop generation ratio is always equal to 1, regardless of the chosen interaction model. While the acceptance ratio remains equal to unity in the nearest-neighboring picture, the best scenario for the dipolar long-range framework is achieved at the onset of the spin ice phase, where the loop acceptance ratio reaches a maximum of about 0.83. This is less efficient than in the kagome spin ice case, where loop flips are almost unanimously accepted at this stage. Furthermore, the acceptance ratio drops rapidly back to zero, suggesting that loop movements present a critical slowing down effect similar to the single spin-flip dynamics. This is in sharp contrast with kagome spin ice, where loops completely take over the role of exploring the energetic manifolds once the spin ice 2 phase is reached. Ultimately, this is another example that reflects the distinctive configurational preferences that the two networks develop at low temperatures under the influence of dipolar long-range interactions.

The persistent rejection of loop-like movements in the low-temperature regime of dipolar kagome Ising can be due to the disruption of already-established preferential configurations.

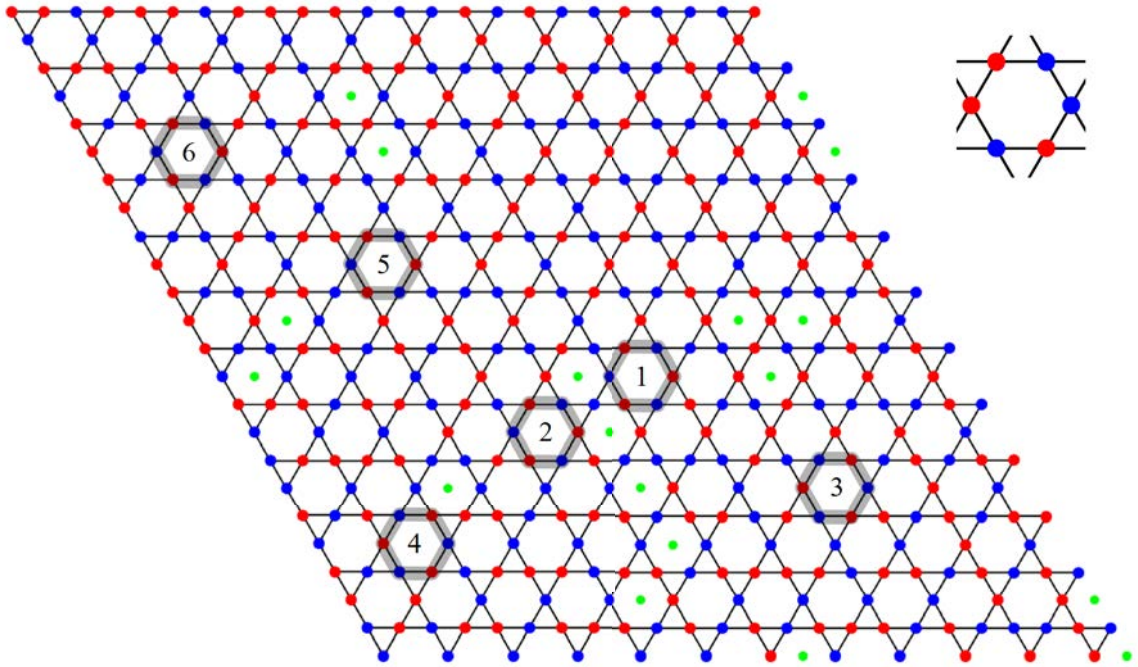

Figure 3.23 - A $(12 \times 12 \times 3)$ network snapshot taken at the lowest sampling temperature before the Monte Carlo simulation was halted due to the critical slowing down of the single spin-flip dynamics. The red and blue circles correspond to *up* and *down* spin states, respectively. The system shows a clear preference for hexagons with no net magnetization (the hexagons with net magnetization are marked by a green circle). Short loops can still be found, but flipping them will disrupt this apparent preference. This is the case of the highlighted loops numbered by 3, 5 and 6 as flipping any one of them will cause all its neighbors to have either a +2 or a -2 net magnetization. Flipping loop number 1 will actually benefit the neighboring magnetized hexagons as they will afterwards present no net magnetization, but it also creates 4 new defects by magnetizing the other neighboring hexagons. Similar situations can be found for loops number 2 and 4. Empirically, the loop dynamics seems to be refused because of these facts. Interestingly, out of the zero net-magnetization hexagon configurations, the system prefers the ones with two neighboring *up* spins and two neighboring *down* spins. One example is given in the inset.

Figure 4.23 gives a network snapshot sampled at the lowest temperature simulated so far. One can note that, apart from the kagome ice rule constrain, the system tends to have zero net magnetization for each of its network hexagons. In other words, the sum of the spins on any chosen hexagons is preferred to be 0. Equivalently to the vertex charge, one could define the sum over a hexagon's spins as a hexagonal charge. Therefore, the above observation can be also expressed by saying that the hexagonal charge tends to be 0. There are 20 possible spin configurations for a network's hexagon that respect this constrain, and the alternating chains would be the most energetically favorable for an isolated case. However, in this very low-temperature regime, the kagome Ising network does not seem to prefer such short loop hexagon configurations, but instead curiously tends to form hexagons that have two neighboring spins of the same sign (see inset of Figure 4.23). In addition, for such low temperatures, long loops are seldom found, and the loop generation algorithm mostly end up with either short hexagon loops or loops that extend from one edge of the network to the other, wrapping around the underlying torus. For the former case, flipping an alternating hexagon will change its equivalent kagome spin ice chirality[36], but this will modify the net magnetization for all its 6 neighboring hexagons and it mostly results in breaking the zero net magnetization of these neighbors (see Figure 4.23). For the latter, as the loop wiggles throughout the lattice, its flip can affect several hexagons, and some of them eventually loose their zero-magnetization configuration, thus making the loop-flip less likely. Given the preference for non-magnetized hexagons, this may very well be the reason why loop flips are often unaccepted in this low-temperature window. Naturally, these rejections have an energetic detailed balance root.

As the loop dynamics has proven to be inefficient for dipolar kagome Ising, other types of cluster algorithms must be constructed for further investigating the thermodynamic properties of this out-of-plane kagome network. Although some other trials have been made[37], the precise nature of the cluster dynamics needed for accessing the ground state manifold is yet to be found. Nevertheless, one can still get an idea about the ground state configuration by looking at the ordering patterns the system has already developed at the lowest simulated temperatures. This will be explored in the next section.

[36] In kagome spin ice, the two chiralities can be defined in a list-like form by using the spin scalar values of the vectors: (-1,+1,-1,+1,-1,+1) for clockwise and (+1,-1,+1,-1,+1,-1) for anticlockwise. Although there is no curl for the kagome Ising case, by equivalence to kagome spin ice, a chirality can also be defined.

[37] A loop-cluster dynamics has also been implemented. The idea behind it was that flipping the interior of a closed loop/chain would not alter the vanishing hexagonal charge constrain. However, while this holds for the interior, the exterior of the cluster can still break this constrain through a flip. In addition, it is increasingly complicated to find a long closed-loop in the low temperature regime.

3.5.2 The Arrow Picture. A Ground-State Candidate

So far, the low-temperature phase of the dipolar kagome Ising system appears to present two main constrains: 1) the kagome ice rules and 2) a vanishing hexagonal charge. In addition, we can also notice that the hexagons also tend to have two neighboring spins of the same sign, contrary to the expected alternating chain. Since one such configuration cannot simply be translated along the network's base vectors to form a crystal as it results in contradictory information, the system has to pave the 2D space with several of such configurations, all related to each other by rotation operations. Nevertheless, it is quite difficult to see a pattern emerging in the spin texture[38].

In the case of the kagome spin ice ground state, one can notice that the spins tend to align along their stray-field lines if a magnetostatic framework is considered. In fact, two neighboring clockwise and anti-clockwise spin loops reproduce the stray-field lines of their mutually-shared spin. Therefore, motivated by this kagome spin ice ground state feature, the nearest-neighbor stray-field lines have been drawn for the kagome Ising network as well. For the sake of simplicity, only the projection of these field lines in the network's plane are considered here and an arrow is therefore drawn from each spin *up*-state to all its neighboring spin *down*-states. The result is the so-called *arrow picture* for the kagome Ising network and, for low-temperature snapshots, it unveils a remarkable property, as presented in Figure 3.24.

The arrow picture reveals a tessellation of trapezoidal spin configurations (see Figures 3.24.b and 3.24.c). In other words, the entire 2D plane appears to be paved by this alternating trapezoidal spin chain, a possible elementary brick for the low-temperature regime of dipolar kagome Ising, which turns around to fit the gaps[39]. There are, of course, a few defects in these snapshots, particularly where the hexagonal charge is not 0. Also, an alternating hexagonal chain (short loop) does not yield a trapezoid (see defect no. 1 in Figure 3.24.b), and neither does a state in which spins of the same sign group on the same side of a hexagon, a so-called "onion-state" (see defect no. 2 in Figure 3.24.b). These states are seldom seen, but although the trapezoids dominate, there does not appear to be a clear organization pattern for these shapes. Very likely, the trapezoidal arrangement that minimizes the overall energy is the ground state of the dipolar kagome Ising system.

[38] At this stage, a very powerful tool that can shed some light on the hidden ordering patterns is the spin structure factor, i.e. the Fourier transform of the spatial spin-spin correlations. Although I will not present this approach in the following as I will focus on how the ordering patters can be identified in direct space through a geometrical construction, a spin structure factor computation code has been nevertheless implemented. However, the results have not yet been fully analyzed and thus they are not included in this thesis. Nevertheless, the preliminary structure factor data indicates an agreement with the results that have been independently obtained through the arrow picture.

[39] Sometimes, there is a time-reversal symmetry involved as well, besides the rotational symmetry

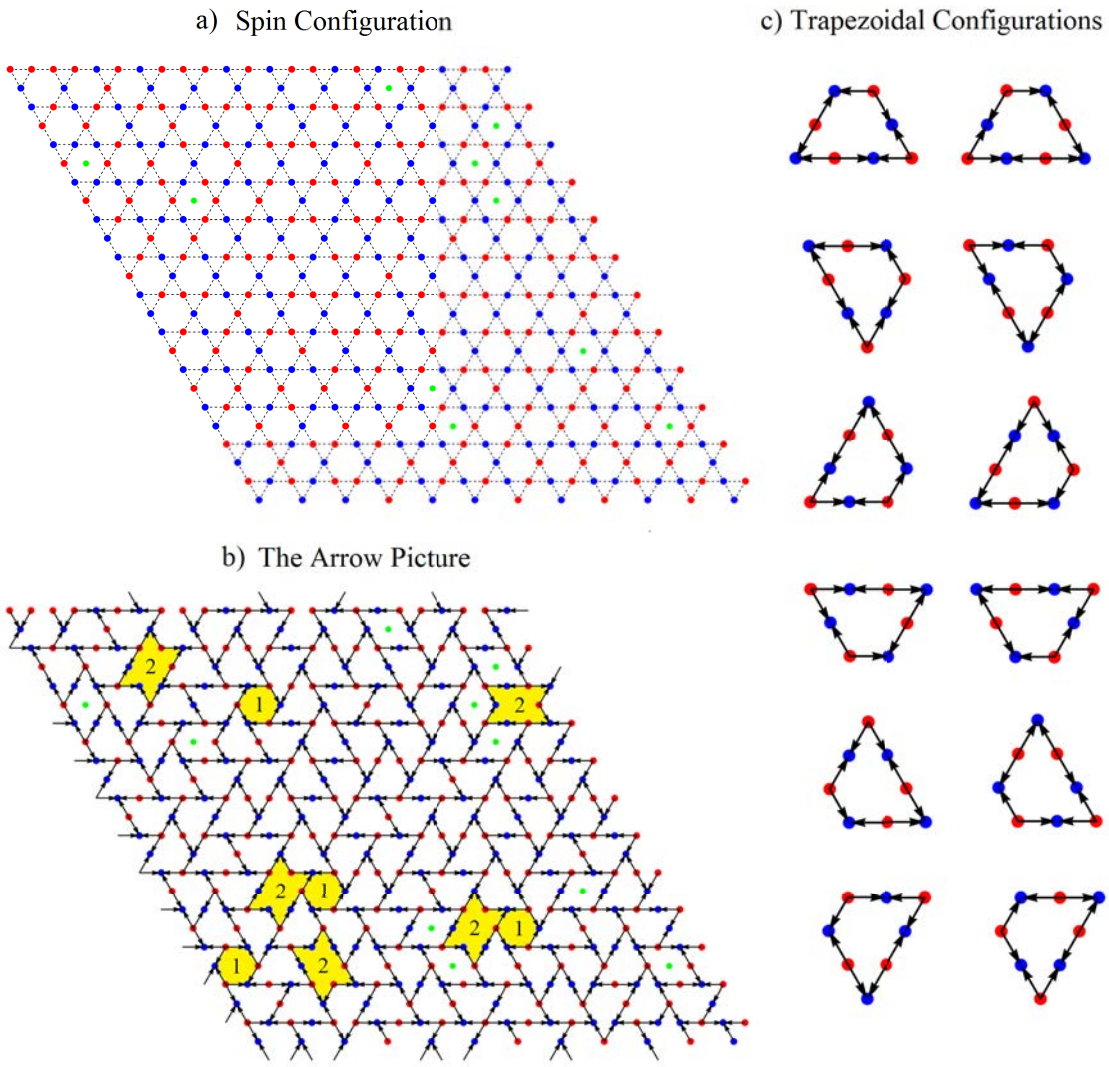

Figure 3.24 - (a) A spin configuration sampled for the lowest temperature simulated so far. The red and black circles correspond to *up* and *down* spin states, respectively. The green circles mark hexagons with non-zero hexagonal charge. (b) The arrow picture of the same configuration revealing how trapezoidal shapes tend to pave the entire network's space. In the end, this low temperature regime appears to be a puzzle of such trapezoidal formations, struggling to arrange in an energetically favorable manner. There are, of course, a few defects left, such as hexagons with non-vanishing hexagonal charge (marked by a green dot), and hexagons that have a zero hexagonal charge, but do not form trapezoidal shapes (highlighted in yellow) (c) The 12 possible trapezoidal configurations. They are all related by $n \cdot \pi/3$-rotation symmetry operation, where n is an integer number, and by time-reversal symmetry.

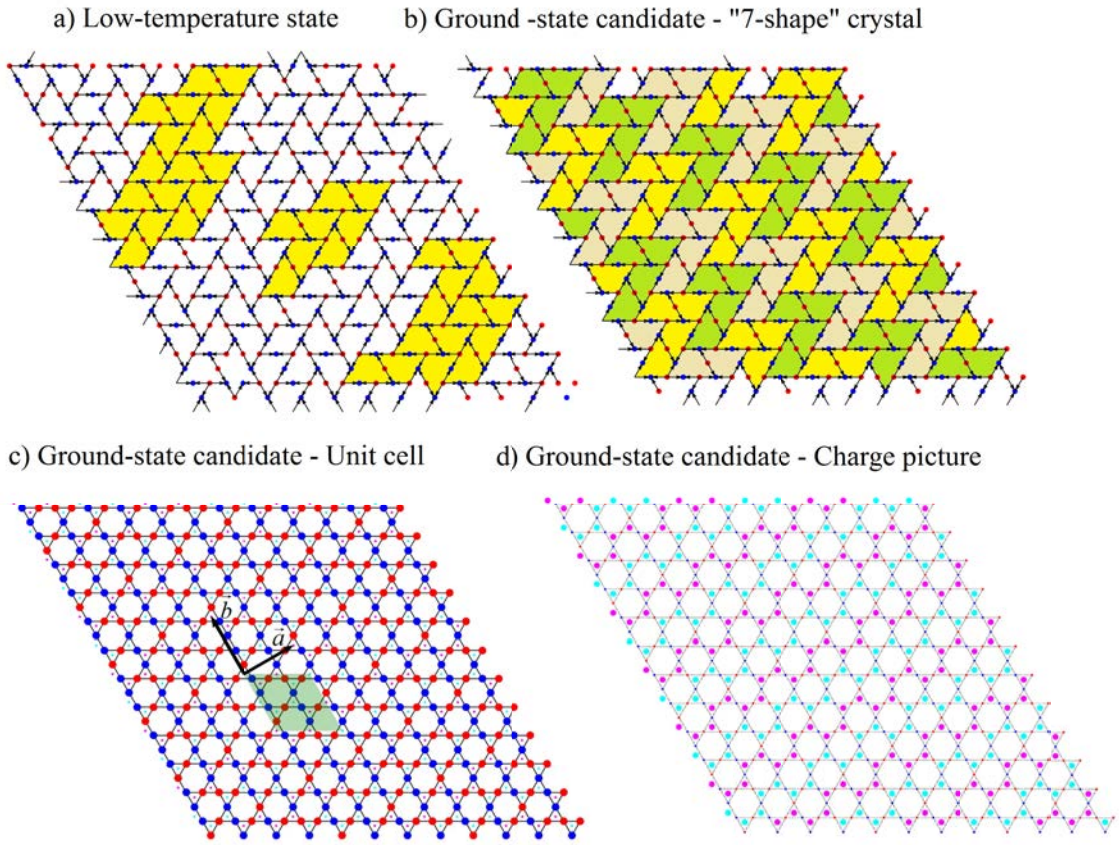

Figure 3.25 - (a) "7-like" shapes found in a low-temperature snapshot. As the system slowly explores its energetic landscape, these regions tend to remain frozen, but their associated clusters may expand. This suggests that they may very well be clusters of the ground state configuration. (b) Paving the entire network's space with such configurations yields a possible candidate for the ground state of dipolar kagome Ising. (b-c) The unit cell of this spin texture contains 12 spins and is charge neutral. The base vectors ($\vec{a}$,$\vec{b}$) form a rectangular network. (d) The charges in this spin configuration are arranged in stripes that wrap all around the torus on which the network is placed.

The next step that can be done is to observe the at-equilibrium evolution of the system in this low-temperature regime starting from such a state. The stored Monte Carlo snapshots sampled during the measurement stage of the lowest temperatures proved to be useful here and by sequentially looking at them there is one interesting feature that can be observed: certain areas present a "7-like" shape formation, made out of 4 trapezoids (see Figure 3.25.a). Furthermore, these areas tend to remain unchanged while the system further struggles to accommodate long-range spin couplings, and even tend to grow in size, covering increasingly larger areas of the network. This suggests that they are, very likely, favorable configurations and may even be patches of the ground state. Therefore, one may try to build an entire kagome network by translating such a "7-shape". This procedure can be done in accordance with the network's periodic boundary conditions[40] and ultimately yields a crystal of such shapes (see Figure 3.25.b), with a rectangular vector basis, as shown in Figure 3.25.b. The unit cell contains 12 spins, has no net magnetization and no net magnetic charge. However, is this a good candidate for the dipolar kagome Ising ground state? There are several tests that can be performed immediately which stand as necessary, but not sufficient conditions for confirming this.

Firstly, for this to be a ground state, its energy has to be lower than those of all the other states sampled so far. Indeed, the energy/spin of this configuration is $e/J_{NN} = -0.675484$ and it is lower than any of the others. In addition, its net magnetization/spin is strictly 0. Furthermore, the spin and charge correlations computed from this snapshot should play the role of target values for the temperature evolutions of their corresponding correlation type. Otherwise said, the temperature plots of the Monte Carlo ensemble averages should normally tend towards these values. As can be seen in Figure 3.26.a, all spin correlations present this feature. Also, the charge correlator is $+1/3$, and it is the value that the charge correlation plot was aiming for (see Figure 3.26.b). As mentioned earlier, a $+1/3$ charge correlation value would imply that each charge is surrounded by two charges of the same sign and one of opposite sign. Indeed, this is the case here, as can be seen in Figure 3.25.d. The charges appear to arrange themselves into long snake-like lines, stretching from one edge of the network to the other[41]. The "7-like" shapes can be all together rotated by multiples of $\pi/3$ to find the three possible charge stripe directions, yielding a total of 6 possible ground state configurations. Indeed, a simulation performed on a larger kagome Ising network with

[40] This is possible due to the number of spins/unit cell, which is equal to 12. Since the current networks have a size of (12×12), this operation can be done without having any difficulties in wrapping the network around the embedded torus. This is generally a delicate aspect when searching for low-energy states that present long-range correlations as the size of an unknown unit cell might not be compatible with the size of the simulated network, and the system thus struggles in vain to order itself.

[41] In fact, the charge lines wrap around the torus on which the network sits, given the periodic boundary conditions.

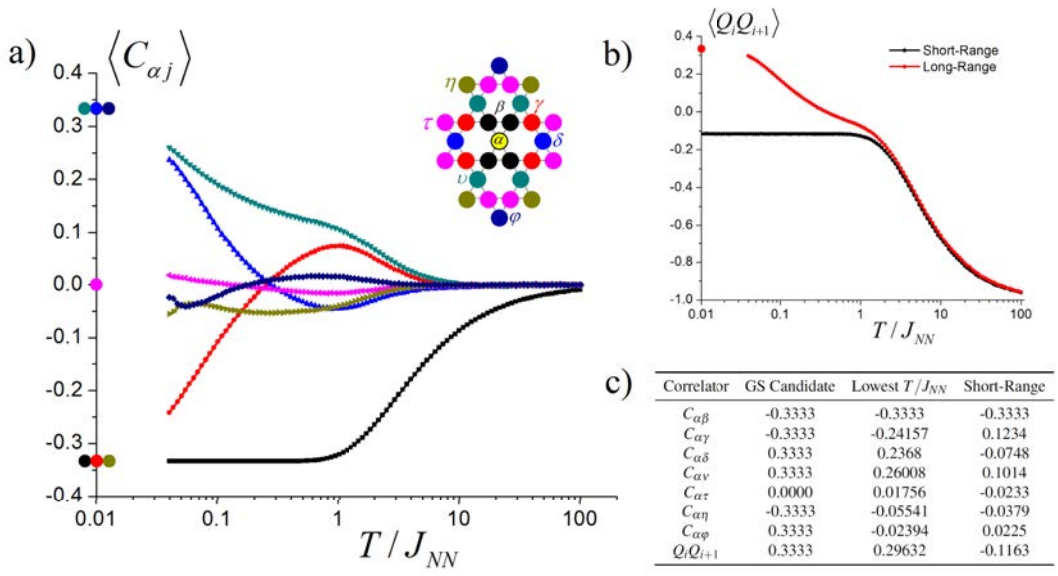

c)

Correlator	GS Candidate	Lowest T/J_{NN}	Short-Range
$C_{\alpha\beta}$	-0.3333	-0.3333	-0.3333
$C_{\alpha\gamma}$	-0.3333	-0.24157	0.1234
$C_{\alpha\delta}$	0.3333	0.2368	-0.0748
$C_{\alpha\upsilon}$	0.3333	0.26008	0.1014
$C_{\alpha\tau}$	0.0000	0.01756	-0.0233
$C_{\alpha\eta}$	-0.3333	-0.05541	-0.0379
$C_{\alpha\varphi}$	0.3333	-0.02394	0.0225
$Q_i Q_{i+1}$	0.3333	0.29632	-0.1163

Figure 3.26 - The spin and charge correlations of this ground state candidtate should act as target values for the Monte Carlo temperature plots. Indeed, this seems to be the case for both the (a) spin correlators and (b) the nearest-neighbor charge correlator. (c) These correlation values along with those of the lowest sampling temperature and the short-range spin ice phase are reported in the table. The inset of Figure (a) is taken from Chioar *et al.*[14].

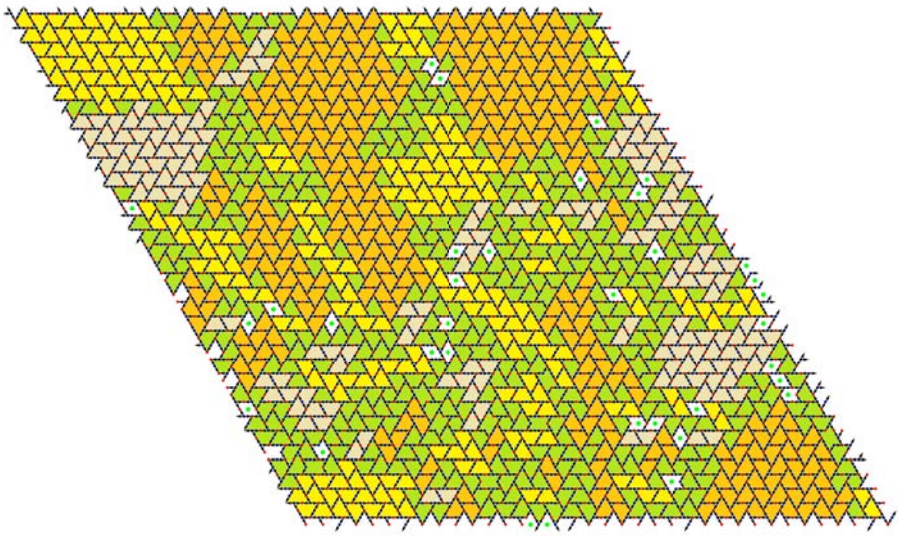

Figure 3.27 - A snapshot of a $36 \times 36 \times 3$ dipolar kagome Ising network with periodic boundary conditions for the lowest temperature achieved so far. The yellow, orange and gray area highlight ground state patches with different charge axis orientations, while the green areas defects that do not fit in either domain. Some domains extend over large network areas, but further expansion is often prevented by neighboring patches. This should eventually lead to a critical slowing down of the driving single spin-flip dynamics.

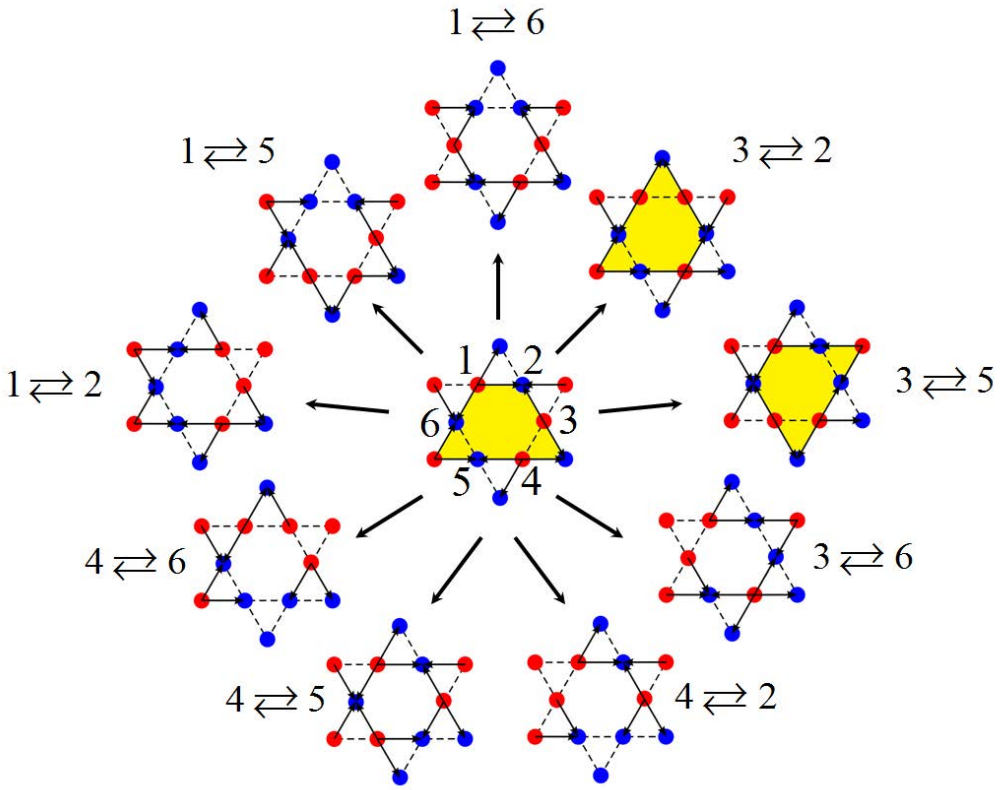

Figure 3.28 - Changing the orientation of a spin trapezoid can be done by flipping a pair of hexagon spins with opposite signs. This can also be seen as interchanging one spin with its pair. The hexagon spins are numbered from 1 to 6 and the 9 possible pair options are indicated by an exchange of spin states. Out of the 9 configurations, only two result in possible favorable states (marked by yellow trapezoids). Depending on the outer spins, forbidden states may be created, which would almost certainly lead to a detailed balance rejection. For the dynamics to be efficient, rejections have to be reduced to a minimum.

$36 \times 36 \times 3 = 3888$ spins and dipolar long-range interactions reveals several clusters of such arrangements (see Figure 3.27). Therefore, the single spin-flip dynamics manages to locally access this ground state candidate, but obtaining a mono-crystal would be very challenging as an entire cluster of "7-like" formations would probably have to be rotated and adjusted with a neighboring one. This is clearly beyond the practical reach of the single spin-flip dynamics in this low-temperature regime and might very well be the root of its critical slowing down effect[42].

Rotating a "7-shape" formation comes down to collectively rotating its composing trapezoids, which in turn requires flipping some spins while still preserving the already imposed

[42]During one single spin-flip simulation run, the system accidentally managed to slip into this candidate state, and then constantly rejected any changes, severely increasing the decorrelation steps. In addition, the transition process hasn't been done smoothly, and a residual entropy was still found.

constrains. This means that at least a pair of oppositely-oriented spins needs to be flipped for each hexagon. There are 9 possible choices here, and 6 result in possible trapezoid configurations, 3 in "onion states" and one in the alternating short-loop state. An example is given in Figure 4.28. Out of the 6 possible trapezoidal states, which seem to be the most favored, some create forbidden states, which would almost certainly be rejected by the detailed balance condition. This depends on the 6 spins surrounding the hexagon. Furthermore, time reversal symmetry should also be considered[43] and the changes would probably have to be performed on the cluster scale to avoid the creation of a defect inside it. This points towards a Wolf cluster-flip approach[131] which might overcome the critical slowing effect of single spin-flips (see Appendix A for more details for general aspects on cluster flips). Some preliminary tests have been performed, but, so far, there are no signs of an efficient dynamics that properly drives the system into a lower energy manifold[44]. Finding the efficient algorithm for exploring the low-temperature regime of dipolar kagome Ising remains a challenge. Nevertheless, these preliminary results appear to be promising and this candidate may yet prove to be the ground state of the kagome Ising network within the dipolar long-range framework.

3.6 Summary

Although the playground of 2D artificial spin ices seems almost limitless, most experimental realizations have focused on in-plane magnetized elements, particularly the square and kagome spin ices. Artificial networks with perpendicularly-magnetized elements have recently come into attention, offering a potential new avenue for exploring frustration effects in two-dimensional systems and the possibility of discovering novel and exotic magnetic textures. However, due to the athermal nature of the constituting elements, demagnetization protocols need to be employed for driving such systems into low energy states. Doing so, Zhang *et al.*[13] found that the remanent states of kagome network with perpendicularly-magnetized nanodots are well described by models involving only nearest-neighbor couplings. Furthemore, within a short-range framework, an antiferromagnetic out-of-plane-magnetized kagome lattice has an equivalent thermodynamic behavior to a ferromagnetic in-plane kagome multiaxial network. Therefore, a certain university in pairwise spin correlation development

[43]Figure 3.27 presents two clusters of the same type (same color), but related through a time reversal symmetry. Connecting them with just a rotation operation would not be possible and inversion has to be considered as well.

[44]Dimer flips have been implemented. In this case, a dimer is a pair of neighboring *up* and *down* spins. Although some improvement is seen, the evolutions of several thermodynamic quantities are abrupt and the system shows signs of a continuous struggle to thermalize even during the measurement stage. Therefore, dimer-flips are not a good option for exploring the energetic landscape of low-temperature kagome Ising.

has been reported, transcending the particular orientation of the magnetic moment axes[13], which would ultimately render the study of such out-of-plane magnetized arrays rather redundant.

In this chapter we have seen that demagnetized kagome networks of perpendicularly magnetized TbCo nanodots present signatures of long-range order, reflecting the magnetostatic nature of the inter-island coupling. Since the long-range part of the dipolar Hamiltonian differs with respect to kagome spin ice, this new kagome Ising system should present a different low temperature behavior, and this was indeed confirmed by Monte Carlo simulations. An interesting feature that distinguishes the two kagome lattices resides in the behavior of the effective magnetic charge, which can be defined for kagome Ising using the same convention as the one that was established for kagome spin ice. Contrary to the in-plane multiaxial case, it has been shown that these kagome Ising charges present an effective ferromagnetic coupling and that, due to the topology of the underlying kagome spin lattice and the kagome spin ice rules, a ferromagnetic charge crystal cannot be constructed.

The nearest-neighbor charge correlator has proven to be useful yet again when the experimental frozen snapshots have been confronted with Monte Carlo predictions for different interaction models. This requires a certain fitting procedure and a correlation scattering analysis was proposed that involves minimizing the overall deviations of the spin and charge correlators with respect to their Monte Carlo ensemble averages. While this procedure yields an effective temperature, it is important to emphasize that this quantity is not a real temperature that characterizes the equilibrium properties of the kagome spin network, but rather plays the role of an energetic label, quantifying the efficiency of the demagnetization process. While some of the current experimental data agrees with the universality reported by Zhang *et al.*[13], an overall better fit with the dipolar long-range model has been found and several spin and charge correlators present severe deviations from their corresponding short-range spin ice plateaus. Interestingly, the experimental correlators seem to follow the Monte Carlo plots, particularly for the charge correlator, thus raising questions about the existence of an effective thermodynamics related to the demagnetization protocol. The results clearly show that long-range interactions need to be taken into account when the remanent demagnetized states of kagome Ising networks are described and limits the reported universality to an effective high-temperature paramagnetic regime.

These results imply that new and possibly exotic spin textures can be found in the low-temperature regime of the kagome Ising network. However, a standard Metropolis Monte Carlo simulation is unable to access its ground state manifold, suffering from a critical slowing down effect in the proximity of an apparent phase transition. By looking at the Monte Carlo snapshots from the lowest sampling temperature, a preference for hexagons with

zero net magnetization is observed. A geometrical construction that relies on reproducing the stray field lines of the network's magnetic moments reveals an ordering pattern in the low-temperature regime: the spins tend to form trapezoidal shapes that pave the entire 2D plane. A certain preferred arrangement of these trapezoids is also observed and by extrapolating it to the network scale a ground state candidate is found, which successfully passes all preliminary tests. The symmetries of its unit cell reveal why the single spin-flip dynamics has difficulties in accessing lower energy manifolds and a cluster-flip dynamics is very likely required. Although challenging, this is probably the first step to be taken for confirming if this is the true ground state of the dipolar kagome Ising array.

Chapter 4

Summary, Conclusions and Perspectives

4.1 Summary and Conclusions

Since their introduction as potential toy-spin models in 2006[1], lithographically-patterned arrays of magnetic nano-islands have proven to be an exciting avenue of research for the investigation of complex phenomena emerging in frustrated magnetic systems[95]. With almost limitless opportunities for design, these artificial spin ices facilitate the real-space observation of the magnetic degrees of freedom, which generally present themselves as classical Ising spins that interact with each-other in a magnetostatic framework. With the help of either a field-driven protocol or the more recently-introduced thermal annealing techniques, the phase spaces of these artificial spin models can be visualized and explored in the ongoing quest for novel and exotic spin textures, particularly found in frustrated geometries.

The current thesis has focused on the study of correlation development in artificial kagome spin networks along with the exploration of the thermodynamic behavior of their corresponding spin models. Two types of artificial kagome arrays have been fabricated and studied: the kagome spin ice and the novel kagome Ising system. The former has been a central point of interest for the community particularly due to exotic spin phases it presents, while the latter is a rather novel artificial realization of a spin model, with promising features for new magnetic spin textures.

The kagome spin ice system presents remarkable thermodynamic properties[65]. If driven solely by nearest-neighbor ferromagnetic interactions, it displays a cross over from a high-temperature paramagnetic regime to a ground-state spin ice manifold in which all vertices respect the so-called kagome ice rule (one in-two out/two out-one in). This manifold is macroscopically degenerated and is characterized by a residual entropy/spin of $0.50183k_B$[67], the highest value reported for a two-dimensional classical Ising spin model.

However, in a dipolar framework, this degeneracy is gradually lifted as the network undergoes two phase transitions towards long-range dipolar order, passing through an exotic spin ice 2 state in which the spin network is partially-disordered and fluctuates, but it is at the same time constrained by the emergence of a crystalline phase associated to the classical magnetic charge.

The first works on artificial realizations of this geometry have signaled a match with the predictions of the short-range spin ice model[46, 72], in spite of the long-range nature of the dipolar coupling between the magnetic elements. This has excited the community at the prospect of realizing an artificial example of a spin model that can exhibit massive degeneracy. However, by performing a careful analysis of the spin correlation development obtained after demagnetizing these athermal artificial spin ices, the signatures of a dipolar long-range interactions have been found[73]. The dipolar interaction model thus manages to account better for the observed spin arrangements yielded by ac demagnetization protocols. The quest has effectively turned towards accessing the exotic spin ice 2 regime, but this has not been managed so far via ac demagnetization which generally blocks the system at the onset of the spin ice phase. However, using thermally-active artificial kagome spin ices, the local crystallization of the magnetic charge embedded in the spin lattice has been achieved[6, 12, 14].

In this context, the present thesis has addressed the formation of such charge crystallites through an annealing above the Curie point of a GdCo-based artificial kagome spin ice network. The magnetic configurations of the networks were imaged by XMCD-PEEM after the samples were cooled back to room temperature. These snapshots reveal the formation of large antiferromagnetically-ordered charge domains, similarly to those reported previously by Zhang *et al.*[6]. However, by computing the pairwise spin and charge correlators at the network scale, a contradiction is found when comparing this data with at-equilibrium Monte Carlo simulations based on the dipolar spin ice model. While the spin correlator would indicate that the network is found in a deep spin ice regime, prior to the transition towards the spin ice 2 phase, the charge correlator is specific to a high-temperature spin ice regime, barely out of the cross over temperature window. We firstly interpret these results as signatures of an out-of-equilibrium dynamics that very likely occurs during the crossing of the Curie point upon cooling. Interestingly, the spin correlators computed within the charge domains are in good agreement with typical values found at the onset of the spin ice 2 phase, thus giving additional proof for the local access of this exotic phase. To address the apparent paradox between the correlation values computed at the network scale, a kinetic algorithm has been proposed that sequentially remagnetizes the network by tracking the maximum local field value given by already-magnetized spins and then magnetizes a spin

accordig to a Boltzmann-like probability. Simulating this kinetic algorithm for different temperatures, we found a good match between the simulated snapshots and those found experimentally, and the two correlator types agree upon the same effective temperature. We thus associate the efficiency of this thermal annealing approach for creating large charge crystallites to the kinetic pathways that the system undertakes upon cooling through the Curie point. Interestingly, this procedure appears to perform well in reaching this exotic spin state possibly due to the initial absence of dipolar pairwise couplings between the spins. In fact, the dipolar couplings develop and are accomodated gradually as the spins are "switched-on", thus avoiding the challenging search for energy minimization in the complex energetic landscape created by dipolar interactions on a kagome spin ice network. In light of these result, another important conclusion that can be drawn is that, although these artificial spin ices are thermally-active, this does not necessarily mean that they are well thermalized, reaching thermal equilibrium conditions.

The artificial kagome Ising system remains rather unexplored to date. In a short-range interaction picture, the associated kagome Ising spin model displays identical thermodynamic behavior as its in-plane counterpart, the kagome spin ice. This is rather an expected feature, as the short-range Hamiltonian can be tailored in the latter case to reveal an effective antiferromagnetic coupling between scalar spin values. When dipolar long-range interactions are brought in the game, the two systems continue to present similar behavior down to the onset of the spin ice phase, but then part ways and develop different spin and charge correlators for lower temperatures. This behavior has been captured in this work by employing Monte Carlo simulations.

A study on the artificial kagome Ising system that predates this work has concluded that the demagnetized states of artificial kagome Ising systems are well described by models involving only nearest-neighbor interactions. Since the two kagome artificial arrays present similar behavior in this short-range framework, they conclude that there is a universality arising in demagnetized artificial spin networks that transcends the particular geometry of the magnetic components. As reported in reference [14], the current thesis presents experimental results that overall disagree with this conclusion and underlines that there are clear limits to the reported universality. By performing a correlation scattering analysis around the Monte Carlo averages given by both short and dipolar long-range interaction models, an overall better match is found with the dipolar description, which accounts rather well for lower energy configurations where the short-range model starts to increasingly fail in this task. The difference between the short-range and the long-range behavior for both kagome networks is nicely reproduced by the temperature-dependence of the nearest-neighbor charge correlator, a quantity that has helped in identifying the effecting temperature regime and thus

discriminating the two cases. The results thus conclude that dipolar long-range interaction between the magnetic nano-islands of artificial kagome spin networks should not be neglected when describing the output of an ac demagnetization protocol.

In addition, these last results also show that this artificial kagome Ising array is described by a new and different low-energy behavior than kagome spin ice, a phase space that is yet to be explored fully both experimentally and numerically. The exploration of the low-temperature manifold of the kagome Ising spin model has nevertheless been undertaken in the framework of this thesis. The Monte Carlo snapshots show no sign of magnetic charge crystallization and the inability to construct a charge crystal has been proven with the help of a microscopic dipolar Hamiltonian. While the simulations are unable to fully recover the magnetic degrees of freedom due to critical slowing down effects of several spin dynamics that have been tried, the lowest states sampled show signs that the system tends to develop long-range spin order. With the help of an original geometrical construction, the ordering patterns in real space have been revealed, and the low-temperature state appears to be a tessellation of trapezoidal spin chains. Extending this tendencies to the network scale, a ground-state candidate has been proposed that, so far, passes all preliminary tests and is in accord with all correlation developements.

Overall, the dipolar interaction model has been the cornerstone for this work's theoretical and numerical modeling. In fact, this is the main highlight and conclusion of this work: systematically and regardless of the chosen protocol (field or thermal demagnetization) and of the spin orientation (in-plane or out-of-plane), dipolar long-range interactions manifest themselves in such artificial kagome spin networks and drive their effective thermodynamic behavior. By neglecting them, one may actually miss certain aspects of the physics that develops in such structures. Simulations have shown that these long-range higher order dipolar terms gradually lift the degeneracy of certain manifolds and can ultimately yield intriguing and potentially exotic spin textures.

4.2 Future Work

There are many other exciting features that are yet to be explored and tested for artificial kagome arrays, both experimentally and numerically.

The kinetic algorithm proposed displays an exciting feature: for sufficiently low temperatures, the sequential remagnetization of the lattice can access the ground state of dipolar kagome spin ice. This encourages further engineering of artificial kagome spin ice arrays from materials with ideally lower Curie points and higher spontaneous magnetizations. Also, the final results appear to be sensitive to the number of nucleation centers, the spins that

"switch-on" first at the Curie point crossing. The lowest energy states are numerically reached if this number is as low as possible and preferably only one center should first magnetize. This could be done experimentally by introducing on purpose a defect in the lattice so that it magnetized before all the others.

Also, a recent work[9] has proposed a different description of the spin ice 2 phase, which encompasses the one previously employed with a spin disorder existing atop a magnetic charge crystal. The description proposes that the spins effectively fragment into two parts: a static vector field related to the emerging charge magnetic crystal and a highly-fluctuating field which bears the signatures of a Coulomb phase[90]. The study also suggests that such a fragmentation can potentially be observed with the help of artificial spin ices. This work has been undertaken within our research group and we have indeed seen the signatures of this spin fragmentation[50]. Results are currently processed for publication and encourage future works on locally manipulating the individual magnetic degrees of freedom for observing and tailoring such exotic phenomena. Performing this with an artificial kagome array that is subjected to thermal fluctuations would be an ideal setup, since the fluctuation of the Coulomb phase could be seen in real space. However, as presented in this manuscript, superparamagnetic artificial kagome spin ice already has increased difficulties in exploring its phase space as more hexagons are added to the lattice[53].

The prospects for the kagome Ising network are also promising. Probably one of the main numerical tasks that are to be undertaken in the near future is the discovery of a adequate spin dynamics that can overcome the critical slowing down effect the single spin-flip experiences near a presumed critical point. The geometrical construction presented in this work has already unraveled ordering patterns at low temperatures, and the grouping and flipping of spin pairs with opposite orientations manages to rotate the trapezoidal formations and can ultimately group together the different domains that develop near the supposed transition point. Also, it would be interesting to analyze the nature of this transition, determining its universality class.

Another interesting feature can be of particular interest for future work: the demagnetized states of the artificial kagome Ising network can display miraculous resemblance to at-equilibrium behavior simulated via Monte Carlo. The spread-out function analysis introduced in this work shows that minima of the K(T) function are generally of the same order of magnitude for both demagnetized states and at-equilibrium sampled states within a dipolar long-range framework. This signals the possible development of an effective thermodynamics for these athermal systems. Such a description has already been proposed for artificial square spin ices[54, 55, 91], but the kagome network has not been addressed so far. In the context of this work, such a task has been undertaken. Preliminary results show that the disorder

in the island switching fields plays a crucial task in determining the effective temperature of a demagnetized state. In addition, the effective temperature can be tuned by controlling this disorder, thus potentially exploring the phase space. Therefore, a semi-deterministic out-of-equilibrium process can be tuned to yield magnetic configurations that are effectively described, to a certain extent, by at-equilibrium thermodynamic behavior. This is clearly an exciting feature, worthy of more in depth analysis in future works.

Experimentally, the artificial kagome Ising network is yet to join the family of second generation artificial spin ices and become thermally-active. If this can be done in the framework of an annealing procedure, lower energy spin textures can potentially be obtained. The kinetic algorithm described in this text has been applied for the dipolar kagome Ising case as well. While this geometry fails to access the suppose spin ordered ground-state proposed here, it does show small patches of it. Nevertheless, this can prove to be a difficult task as the islands have to retain their Ising nature after the Curie point crossing, a fact which is a priori not easily achieved.

In short, there are many different avenues for further research into artificial spin ices in the years to come on both fundamental aspects, exploiting their toy-spin model character, and possible applications.

Bibliography

[1] R. F. Wang, C. Nisoli, R. S. Freitas, J. Li, W. McConville, B. J. Cooley, M. S. Lund, N. Samarth, C. Leighton, V. H. Crespi, and P. Schiffer, "Artificial 'spin ice' in a geometrically frustrated lattice of nanoscale ferromagnetic islands," Nature, vol. 439, pp. 303–306, Jan. 2006.

[2] M. J. Harris, S. T. Bramwell, D. F. McMorrow, T. Zeiske, and K. W. Godfrey, "Geometrical Frustration in the Ferromagnetic Pyrochlore $Ho_2Ti_2O_7$," Phys. Rev. Lett., vol. 79, pp. 2554–2557, Sept. 1997.

[3] R. F. Wang, J. Li, W. McConville, C. Nisoli, X. Ke, J. W. Freeland, V. Rose, M. Grimsditch, P. Lammert, V. H. Crespi, and P. Schiffer, "Demagnetization protocols for frustrated interacting nanomagnet arrays," Journal of Applied Physics, vol. 101, p. 09J104, May 2007.

[4] J. P. Morgan, A. Stein, S. Langridge, and C. H. Marrows, "Thermal ground-state ordering and elementary excitations in artificial magnetic square ice," Nat Phys, vol. 7, pp. 75–79, Jan. 2011.

[5] A. Farhan, P. M. Derlet, A. Kleibert, A. Balan, R. V. Chopdekar, M. Wyss, L. Anghinolfi, F. Nolting, and L. J. Heyderman, "Exploring hyper-cubic energy landscapes in thermally active finite artificial spin-ice systems," Nat Phys, vol. 9, pp. 375–382, June 2013.

[6] S. Zhang, I. Gilbert, C. Nisoli, G.-W. Chern, M. J. Erickson, L. O'Brien, C. Leighton, P. E. Lammert, V. H. Crespi, and P. Schiffer, "Crystallites of magnetic charges in artificial spin ice," Nature, vol. 500, pp. 553–557, Aug. 2013.

[7] G. Möller and R. Moessner, "Magnetic multipole analysis of kagome and artificial spin-ice dipolar arrays," Phys. Rev. B, vol. 80, p. 140409, Oct. 2009.

[8] G.-W. Chern, P. Mellado, and O. Tchernyshyov, "Two-Stage Ordering of Spins in Dipolar Spin Ice on the Kagome Lattice," Phys. Rev. Lett., vol. 106, p. 207202, May 2011.

[9] M. E. Brooks-Bartlett, S. T. Banks, L. D. C. Jaubert, A. Harman-Clarke, and P. C. W. Holdsworth, "Magnetic-Moment Fragmentation and Monopole Crystallization," Phys. Rev. X, vol. 4, p. 011007, Jan. 2014.

[10] F. Montaigne, D. Lacour, I. A. Chioar, N. Rougemaille, D. Louis, S. M. Murtry, H. Riahi, B. S. Burgos, T. O. Menteş, A. Locatelli, B. Canals, and M. Hehn, "Size

distribution of magnetic charge domains in thermally activated but out-of-equilibrium artificial spin ice," Sci. Rep., vol. 4, July 2014.

[11] I. A. Chioar, B. Canals, D. Lacour, M. Hehn, B. Santos Burgos, T. O. Menteş, A. Locatelli, F. Montaigne, and N. Rougemaille, "Kinetic pathways to the magnetic charge crystal in artificial dipolar spin ice," Phys. Rev. B, vol. 90, p. 220407, Dec. 2014.

[12] J. Drisko, S. Daunheimer, and J. Cumings, "$FePd_3$ as a material for studying thermally active artificial spin ice systems," Phys. Rev. B, vol. 91, p. 224406, June 2015.

[13] S. Zhang, J. Li, I. Gilbert, J. Bartell, M. J. Erickson, Y. Pan, P. E. Lammert, C. Nisoli, K. K. Kohli, R. Misra, V. H. Crespi, N. Samarth, C. Leighton, and P. Schiffer, "Perpendicular Magnetization and Generic Realization of the Ising Model in Artificial Spin Ice," Phys. Rev. Lett., vol. 109, p. 087201, Aug. 2012.

[14] I. A. Chioar, N. Rougemaille, A. Grimm, O. Fruchart, E. Wagner, M. Hehn, D. Lacour, F. Montaigne, and B. Canals, "Nonuniversality of artificial frustrated spin systems," Phys. Rev. B, vol. 90, p. 064411, Aug. 2014.

[15] J. R. Otteson, Adam Smith: Selected Philosophical Writings. Andrews UK Limited, Oct. 2012.

[16] *frustration*, Longman Dictionary of Contemporary English, Pearson Longman, 1 ed., 2014.

[17] Claudine Lacroix, Philippe Mendels and Frédéric Mila (editors), Introduction to Frustrated Magnetism - Materials, Experiments, Theory. No. v, Springer Berlin Heidelberg, 2011.

[18] B. Canals, "Modèles de spins topologiquement frustrés: une introduction," memoire d'habilitation à diriger les recherches, Université Joseph Fourier, Grenoble, Apr. 2010.

[19] E. Ising, "Beitrag zur Theorie des Ferromagnetismus," Z. Physik, vol. 31, pp. 253–258, Feb. 1925.

[20] G. H. Wannier, "Antiferromagnetism. The Triangular Ising Net," Phys. Rev., vol. 79, pp. 357–364, July 1950.

[21] S. Blundell and K. M. Blundell, Concepts in Thermal Physics. OUP Oxford, 2010.

[22] L. Pauling, "The Structure and Entropy of Ice and of Other Crystals with Some Randomness of Atomic Arrangement," J. Am. Chem. Soc., vol. 57, pp. 2680–2684, Dec. 1935.

[23] G. Toulouse, "Theory of the frustration effect in spin glasses," Comm. on Phys., no. 2, p. 115, 1977.

[24] W. F. Giauque and M. F. Ashley, "Molecular Rotation in Ice at 10°K. Free Energy of Formation and Entropy of Water," Phys. Rev., vol. 43, pp. 81–82, Jan. 1933.

[25] W. F. Giauque and J. W. Stout, "The Entropy of Water and the Third Law of Thermodynamics. The Heat Capacity of Ice from 15 to 273°K.," J. Am. Chem. Soc., vol. 58, pp. 1144–1150, July 1936.

[26] J. D. Bernal and R. H. Fowler, "A Theory of Water and Ionic Solution, with Particular Reference to Hydrogen and Hydroxyl Ions," The Journal of Chemical Physics, vol. 1, pp. 515–548, Aug. 1933.

[27] S. T. Bramwell and M. J. Harris, "Frustration in Ising-type spin models on the pyrochlore lattice," J. Phys.: Condens. Matter, vol. 10, p. L215, Apr. 1998.

[28] A. P. Ramirez, A. Hayashi, R. J. Cava, R. Siddharthan, and B. S. Shastry, "Zero-point entropy in 'spin ice'," Nature, vol. 399, pp. 333–335, May 1999.

[29] R. G. Melko, B. C. den Hertog, and M. J. P. Gingras, "Long-Range Order at Low Temperatures in Dipolar Spin Ice," Phys. Rev. Lett., vol. 87, p. 067203, July 2001.

[30] P. W. Anderson, "Ordering and Antiferromagnetism in Ferrites," Phys. Rev., vol. 102, pp. 1008–1013, May 1956.

[31] S. T. Bramwell and M. J. P. Gingras, "Spin Ice State in Frustrated Magnetic Pyrochlore Materials," Science, vol. 294, pp. 1495–1501, Nov. 2001.

[32] B. C. den Hertog and M. J. P. Gingras, "Dipolar Interactions and Origin of Spin Ice in Ising Pyrochlore Magnets," Phys. Rev. Lett., vol. 84, pp. 3430–3433, Apr. 2000.

[33] R. G. Melko and M. J. P. Gingras, "Monte Carlo studies of the dipolar spin ice model," J. Phys.: Condens. Matter, vol. 16, p. R1277, Nov. 2004.

[34] D. Pomaranski, L. R. Yaraskavitch, S. Meng, K. A. Ross, H. M. L. Noad, H. A. Dabkowska, B. D. Gaulin, and J. B. Kycia, "Absence of Pauling/'s residual entropy in thermally equilibrated Dy2ti2o7," Nat Phys, vol. 9, pp. 353–356, June 2013.

[35] C. Castelnovo, R. Moessner, and S. L. Sondhi, "Magnetic monopoles in spin ice," Nature, vol. 451, pp. 42–45, Jan. 2008.

[36] P. a. M. Dirac, "Quantised Singularities in the Electromagnetic Field," Proceedings of the Royal Society of London A: Mathematical, Physical and Engineering Sciences, vol. 133, pp. 60–72, Sept. 1931.

[37] D. Davidović, S. Kumar, D. H. Reich, J. Siegel, S. B. Field, R. C. Tiberio, R. Hey, and K. Ploog, "Correlations and Disorder in Arrays of Magnetically Coupled Superconducting Rings," Phys. Rev. Lett., vol. 76, pp. 815–818, Jan. 1996.

[38] E. Olive and P. Molho, "Thermodynamic study of a lattice of compass needles in dipolar interaction," Phys. Rev. B, vol. 58, pp. 9238–9247, Oct. 1998.

[39] H. Hilgenkamp, Ariando, H.-J. H. Smilde, D. H. A. Blank, G. Rijnders, H. Rogalla, J. R. Kirtley, and C. C. Tsuei, "Ordering and manipulation of the magnetic moments in large-scale superconducting π-loop arrays," Nature, vol. 422, pp. 50–53, Mar. 2003.

[40] Y. Han, Y. Shokef, A. M. Alsayed, P. Yunker, T. C. Lubensky, and A. G. Yodh, "Geometric frustration in buckled colloidal monolayers," Nature, vol. 456, pp. 898–903, Dec. 2008.

[41] A. Libál, C. Reichhardt, and C. J. O. Reichhardt, "Realizing Colloidal Artificial Ice on Arrays of Optical Traps," Phys. Rev. Lett., vol. 97, p. 228302, Nov. 2006.

[42] M. Tanaka, E. Saitoh, H. Miyajima, T. Yamaoka, and Y. Iye, "Domain structures and magnetic ice-order in NiFe nano-network with honeycomb structure," Journal of Applied Physics, vol. 97, p. 10J710, May 2005.

[43] M. Tanaka, E. Saitoh, H. Miyajima, T. Yamaoka, and Y. Iye, "Magnetic interactions in a ferromagnetic honeycomb nanoscale network," Phys. Rev. B, vol. 73, p. 052411, Feb. 2006.

[44] E. Mengotti, L. J. Heyderman, A. Fraile Rodríguez, A. Bisig, L. Le Guyader, F. Nolting, and H. B. Braun, "Building blocks of an artificial kagome spin ice: Photoemission electron microscopy of arrays of ferromagnetic islands," Phys. Rev. B, vol. 78, p. 144402, Oct. 2008.

[45] E. Mengotti, L. J. Heyderman, A. Bisig, A. F. Rodríguez, L. L. Guyader, F. Nolting, and H. B. Braun, "Dipolar energy states in clusters of perpendicular magnetic nanoislands," Journal of Applied Physics, vol. 105, p. 113113, June 2009.

[46] Y. Qi, T. Brintlinger, and J. Cumings, "Direct observation of the ice rule in an artificial kagome spin ice," Phys. Rev. B, vol. 77, p. 094418, Mar. 2008.

[47] S. A. Daunheimer, O. Petrova, O. Tchernyshyov, and J. Cumings, "Reducing Disorder in Artificial Kagome Ice," Phys. Rev. Lett., vol. 107, p. 167201, Oct. 2011.

[48] L. Néel, "Théorie du trainage magnétique des ferromagnétiques au grains fin avec applications aux terres cuites. Ann. Géophys. 5 (1949), pp. 99–136.," Annals de Géophysique, vol. 5, pp. 99–109, 1949.

[49] J. P. Morgan, A. Bellew, A. Stein, S. Langridge, and C. Marrows, "Linear field demagnetization of artificial magnetic square ice," Front. Physics, vol. 1, p. 28, 2013.

[50] B. Canals, I.-A. Chioar, V.-D. Nguyen, M. Hehn, D. Lacour, F. Montaigne, A. Locatelli, T. O. Menteş, B. S. Burgos, and N. Rougemaille, "Fragmented-spin crystallites and emergent Coulomb phase in artificial magnetic ice," to be published, 2015.

[51] U. B. Arnalds, M. Ahlberg, M. S. Brewer, V. Kapaklis, E. T. Papaioannou, M. Karimipour, P. Korelis, A. Stein, S. Ólafsson, T. P. A. Hase, and B. Hjörvarsson, "Thermal transitions in nano-patterned XY-magnets," Applied Physics Letters, vol. 105, p. 042409, July 2014.

[52] A. Farhan, P. M. Derlet, A. Kleibert, A. Balan, R. V. Chopdekar, M. Wyss, J. Perron, A. Scholl, F. Nolting, and L. J. Heyderman, "Direct Observation of Thermal Relaxation in Artificial Spin Ice," Phys. Rev. Lett., vol. 111, p. 057204, Aug. 2013.

[53] A. Farhan, A. Kleibert, P. M. Derlet, L. Anghinolfi, A. Balan, R. V. Chopdekar, M. Wyss, S. Gliga, F. Nolting, and L. J. Heyderman, "Thermally induced magnetic relaxation in building blocks of artificial kagome spin ice," Phys. Rev. B, vol. 89, p. 214405, June 2014.

[54] C. Nisoli, R. Wang, J. Li, W. F. McConville, P. E. Lammert, P. Schiffer, and V. H. Crespi, "Ground State Lost but Degeneracy Found: The Effective Thermodynamics of Artificial Spin Ice," Phys. Rev. Lett., vol. 98, p. 217203, May 2007.

[55] C. Nisoli, J. Li, X. Ke, D. Garand, P. Schiffer, and V. H. Crespi, "Effective Temperature in an Interacting Vertex System: Theory and Experiment on Artificial Spin Ice," Phys. Rev. Lett., vol. 105, p. 047205, July 2010.

[56] A. Libál, C. J. O. Reichhardt, and C. Reichhardt, "Creating Artificial Ice States Using Vortices in Nanostructured Superconductors," Phys. Rev. Lett., vol. 102, p. 237004, June 2009.

[57] S. Ladak, D. E. Read, G. K. Perkins, L. F. Cohen, and W. R. Branford, "Direct observation of magnetic monopole defects in an artificial spin-ice system," Nat Phys, vol. 6, pp. 359–363, May 2010.

[58] S. Ladak, D. E. Read, W. R. Branford, and L. F. Cohen, "Direct observation and control of magnetic monopole defects in an artificial spin-ice material," New J. Phys., vol. 13, p. 063032, June 2011.

[59] E. Mengotti, L. J. Heyderman, A. F. Rodríguez, F. Nolting, R. V. Hügli, and H.-B. Braun, "Real-space observation of emergent magnetic monopoles and associated Dirac strings in artificial kagome spin ice," Nat Phys, vol. 7, pp. 68–74, Jan. 2011.

[60] K. Zeissler, S. K. Walton, S. Ladak, D. E. Read, T. Tyliszczak, L. F. Cohen, and W. R. Branford, "The non-random walk of chiral magnetic charge carriers in artificial spin ice," Sci. Rep., vol. 3, Feb. 2013.

[61] N. Rougemaille, F. Montaigne, B. Canals, M. Hehn, H. Riahi, D. Lacour, and J.-C. Toussaint, "Chiral nature of magnetic monopoles in artificial spin ice," New J. Phys., vol. 15, p. 035026, Mar. 2013.

[62] M. J. P. Gingras, "Spin Ice," arXiv:0903.2772 [cond-mat], Mar. 2009. arXiv: 0903.2772.

[63] L. Onsager, "Crystal Statistics. I. A Two-Dimensional Model with an Order-Disorder Transition," Phys. Rev., vol. 65, pp. 117–149, Feb. 1944.

[64] K. Husimi and I. Syôzi, "The Statistics of Honeycomb and Triangular Lattice. I," Prog. Theor. Phys., vol. 5, pp. 177–186, Mar. 1950.

[65] I. Syôzi, "Statistics of Kagomé Lattice," Prog. Theor. Phys., vol. 6, pp. 306–308, June 1951.

[66] M. Mekata, "Kagome: The story of the basketweave lattice," Physics Today, vol. 56, pp. 12–13, Feb. 2003.

[67] K. Kanô and S. Naya, "Antiferromagnetism. The Kagomé Ising Net," Prog. Theor. Phys., vol. 10, pp. 158–172, Aug. 1953.

[68] P. Azaria, H. T. Diep, and H. Giacomini, "Coexistence of order and disorder and reentrance in an exactly solvable model," Phys. Rev. Lett., vol. 59, pp. 1629–1632, Oct. 1987.

[69] M. Wolf and K. D. Schotte, "Ising model with competing next-nearest-neighbour interactions on the Kagome lattice," J. Phys. A: Math. Gen., vol. 21, p. 2195, May 1988.

[70] T. Takagi and M. Mekata, "Magnetic Ordering of Ising Spins on Kagomé Lattice with the 1st and the 2nd Neighbor Interactions," J. Phys. Soc. Jpn., vol. 62, pp. 3943–3953, Nov. 1993.

[71] A. S. Wills, R. Ballou, and C. Lacroix, "Model of localized highly frustrated ferromagnetism: The kagomé spin ice," Phys. Rev. B, vol. 66, p. 144407, Oct. 2002.

[72] J. Li, X. Ke, S. Zhang, D. Garand, C. Nisoli, P. Lammert, V. H. Crespi, and P. Schiffer, "Comparing artificial frustrated magnets by tuning the symmetry of nanoscale permalloy arrays," Phys. Rev. B, vol. 81, p. 092406, Mar. 2010.

[73] N. Rougemaille, F. Montaigne, B. Canals, A. Duluard, D. Lacour, M. Hehn, R. Belkhou, O. Fruchart, S. El Moussaoui, A. Bendounan, and F. Maccherozzi, "Artificial Kagome Arrays of Nanomagnets: A Frozen Dipolar Spin Ice," Phys. Rev. Lett., vol. 106, p. 057209, Feb. 2011.

[74] E. H. Lieb, "Exact Solution of the Problem of the Entropy of Two-Dimensional Ice," Phys. Rev. Lett., vol. 18, pp. 692–694, Apr. 1967.

[75] E. H. Lieb, "Residual Entropy of Square Ice," Phys. Rev., vol. 162, pp. 162–172, Oct. 1967.

[76] G. Möller, Espaces dynamiques réduits en physique de la matière condensée : Systèmes à effet Hall bicouches, réduction dimensionnelle et systèmes de spins magnétiques. PhD Thesis, Université Paris Sud - Paris XI, Sept. 2006.

[77] E. H. Lieb, "Exact Solution of the F Model of An Antiferroelectric," Phys. Rev. Lett., vol. 18, pp. 1046–1048, June 1967.

[78] G. Möller and R. Moessner, "Artificial Square Ice and Related Dipolar Nanoarrays," Phys. Rev. Lett., vol. 96, p. 237202, June 2006.

[79] A. Grimm, "Artificial Kagome Spin Ices," tech. rep., Université Joseph Fourier, Grenoble, June 2011.

[80] I.-A. Chioar, "Frustration in Artificial Spin Ice Systems," internship report, Université Joseph Fourier, Grenoble, June 2012.

[81] A. J. Macdonald, P. C. W. Holdsworth, and R. G. Melko, "Classical topological order in kagome ice," J. Phys.: Condens. Matter, vol. 23, p. 164208, Apr. 2011.

[82] J. Villain, "Insulating spin glasses," Z Physik B, vol. 33, pp. 31–42, Mar. 1979.

[83] X. Ke, J. Li, C. Nisoli, P. E. Lammert, W. McConville, R. F. Wang, V. H. Crespi, and P. Schiffer, "Energy Minimization and ac Demagnetization in a Nanomagnet Array," Phys. Rev. Lett., vol. 101, p. 037205, July 2008.

[84] K. K. Kohli, A. L. Balk, J. Li, S. Zhang, I. Gilbert, P. E. Lammert, V. H. Crespi, P. Schiffer, and N. Samarth, "Magneto-optical Kerr effect studies of square artificial spin ice," Phys. Rev. B, vol. 84, p. 180412, Nov. 2011.

[85] Z. Budrikis, P. Politi, and R. L. Stamps, "Disorder regimes and equivalence of disorder types in artificial spin ice," Journal of Applied Physics, vol. 111, p. 07E109, Feb. 2012.

[86] Z. Budrikis, J. P. Morgan, J. Akerman, A. Stein, P. Politi, S. Langridge, C. H. Marrows, and R. L. Stamps, "Disorder Strength and Field-Driven Ground State Domain Formation in Artificial Spin Ice: Experiment, Simulation, and Theory," Phys. Rev. Lett., vol. 109, p. 037203, July 2012.

[87] Z. Budrikis, P. Politi, and R. L. Stamps, "A network model for field and quenched disorder effects in artificial spin ice," New J. Phys., vol. 14, p. 045008, Apr. 2012.

[88] D. J. Griffiths, Introduction to Electrodynamics. Addison Wesley, 3 edition ed., Dec. 1998.

[89] P. P. Ewald, "Die Berechnung optischer und elektrostatischer Gitterpotentiale," Ann. Phys., vol. 369, pp. 253–287, Jan. 1921.

[90] C. L. Henley, "The "Coulomb phase" in frustrated systems," arXiv:0912.4531 [cond-mat], Dec. 2009. arXiv: 0912.4531.

[91] J. P. Morgan, J. Akerman, A. Stein, C. Phatak, R. M. L. Evans, S. Langridge, and C. H. Marrows, "Real and effective thermal equilibrium in artificial square spin ices," Phys. Rev. B, vol. 87, p. 024405, Jan. 2013.

[92] Z. Budrikis, P. Politi, and R. L. Stamps, "Diversity Enabling Equilibration: Disorder and the Ground State in Artificial Spin Ice," Phys. Rev. Lett., vol. 107, p. 217204, Nov. 2011.

[93] Z. Budrikis, K. L. Livesey, J. P. Morgan, J. Akerman, A. Stein, S. Langridge, C. H. Marrows, and R. L. Stamps, "Domain dynamics and fluctuations in artificial square ice at finite temperatures," New J. Phys., vol. 14, p. 035014, Mar. 2012.

[94] Y. Qi, Artificial Kagome Spin Ice. PhD thesis, University of Maryland, College Park, 2008.

[95] C. Nisoli, R. Moessner, and P. Schiffer, "Colloquium: Artificial spin ice: Designing and imaging magnetic frustration," Rev. Mod. Phys., vol. 85, pp. 1473–1490, Oct. 2013.

[96] L. J. Heyderman and R. L. Stamps, "Artificial ferroic systems: novel functionality from structure, interactions and dynamics," J. Phys.: Condens. Matter, vol. 25, p. 363201, Sept. 2013.

[97] V. Kapaklis, U. B. Arnalds, A. Harman-Clarke, E. T. Papaioannou, M. Karimipour, P. Korelis, A. Taroni, P. C. W. Holdsworth, S. T. Bramwell, and B. Hjörvarsson, "Melting artificial spin ice," New J. Phys., vol. 14, p. 035009, Mar. 2012.

[98] J. M. Porro, A. Bedoya-Pinto, A. Berger, and P. Vavassori, "Exploring thermally induced states in square artificial spin-ice arrays," New J. Phys., vol. 15, p. 055012, May 2013.

[99] V. Kapaklis, U. B. Arnalds, A. Farhan, R. V. Chopdekar, A. Balan, A. Scholl, L. J. Heyderman, and B. Hjörvarsson, "Thermal fluctuations in artificial spin ice," Nat Nano, vol. 9, pp. 514–519, July 2014.

[100] I. Gilbert, G.-W. Chern, S. Zhang, L. O'Brien, B. Fore, C. Nisoli, and P. Schiffer, "Emergent ice rule and magnetic charge screening from vertex frustration in artificial spin ice," Nat Phys, vol. 10, pp. 670–675, Sept. 2014.

[101] J. Als-Nielsen and D. McMorrow, Elements of Modern X-ray Physics. John Wiley & Sons, Apr. 2011.

[102] S. Zhang, I. Gilbert, C. Nisoli, G.-W. Chern, M. J. Erickson, L. O'Brien, C. Leighton, P. E. Lammert, V. H. Crespi, and P. Schiffer, "Crystallites of magnetic charges in artificial spin ice - Supplementary Information," Nature, vol. 500, pp. 553–557, Aug. 2013.

[103] J. Coey, Magnetism and Magnetic Materials. Cambridge University Press, Apr. 2010.

[104] P. Hansen, C. Clausen, G. Much, M. Rosenkranz and K. Witter, "Magnetic and magneto-optical properties of rare-eart transition-metal alloys containing Gd, Tb, Fe, Co," Journal of Applied Physics, vol. 66, pp. 756–767, July 1989.

[105] F. Montaigne, D. Lacour, I. A. Chioar, N. Rougemaille, D. Louis, S. M. Murtry, H. Riahi, B. S. Burgos, T. O. Menteş, A. Locatelli, B. Canals, and M. Hehn, "Size distribution of magnetic charge domains in thermally activated but out-of-equilibrium artificial spin ice - Supplementary Information," Sci. Rep., vol. 4, p. 5702, July 2014.

[106] R. J.Glauber,"Time-Dependent Statistics of the Ising Model,"Journal of Mathematical Physics, vol. 4,pp. 294-307,Feb.1963.

[107] J. Li, S. Zhang, J. Bartell, C. Nisoli, X. Ke, P. E. Lammert, V. H. Crespi, and P. Schiffer, "Comparing frustrated and unfrustrated clusters of single-domain ferromagnetic islands," Phys. Rev. B, vol. 82, p. 134407, Oct. 2010.

[108] Z. Budrikis, P. Politi, and R. L. Stamps, "Vertex Dynamics in Finite Two-Dimensional Square Spin Ices," Phys. Rev. Lett., vol. 105, p. 017201, June 2010.

[109] J. P. Morgan, A. Stein, S. Langridge, and C. H. Marrows, "Magnetic reversal of an artificial square ice: dipolar correlation and charge ordering," New J. Phys., vol. 13, p. 105002, Oct. 2011.

[110] C. Phatak, A. K. Petford-Long, O. Heinonen, M. Tanase, and M. De Graef, "Nanoscale structure of the magnetic induction at monopole defects in artificial spin-ice lattices," Phys. Rev. B, vol. 83, p. 174431, May 2011.

[111] S. Zhang, J. Li, J. Bartell, X. Ke, C. Nisoli, P. E. Lammert, V. H. Crespi, and P. Schiffer, "Ignoring Your Neighbors: Moment Correlations Dominated by Indirect or Distant Interactions in an Ordered Nanomagnet Array," Phys. Rev. Lett., vol. 107, p. 117204, Sept. 2011.

[112] L. A. S. Mól, A. R. Pereira, and W. A. Moura-Melo, "Extending spin ice concepts to another geometry: The artificial triangular spin ice," Phys. Rev. B, vol. 85, p. 184410, May 2012.

[113] J. H. Rodrigues, L. a. S. Mól, W. A. Moura-Melo, and A. R. Pereira, "Efficient demagnetization protocol for the artificial triangular spin ice," Applied Physics Letters, vol. 103, p. 092403, Aug. 2013.

[114] G.-W. Chern, M. J. Morrison, and C. Nisoli, "Degeneracy and Criticality from Emergent Frustration in Artificial Spin Ice," Phys. Rev. Lett., vol. 111, p. 177201, Oct. 2013.

[115] "Perpendicular Magnetic Recording Technology.", URL: http://www.hgst.com/tech/techlib.nsf/techdocs/f47bf010a4d29dfd8625716c005b7f34/$file/pmr_white_paper_final.pdf, Date Accessed: 13.04.2015.

[116] "Perpendicular Magnetic Recording (PMR) - WD Addresses Hard Drive Capacity Challenge with PMR Technology." URL: https://wdc.com/wdproducts/library/other/2579-701185.pdf, Date Accessed: 13.04.2015.

[117] C. Ross, "Patterned Magnetic Recording Media," Annual Review of Materials Research, vol. 31, no. 1, pp. 203–235, 2001.

[118] B. D. Terris and T. Thomson, "Nanofabricated and self-assembled magnetic structures as data storage media," J. Phys. D: Appl. Phys., vol. 38, p. R199, June 2005.

[119] M. Grobis, O. Hellwig, T. Hauet, E. Dobisz, and T. Albrecht, "High-Density Bit Patterned Media: Magnetic Design and Recording Performance," IEEE Transactions on Magnetics, vol. 47, pp. 6–10, Jan. 2011.

[120] T. Albrecht, D. Bedau, E. Dobisz, H. Gao, M. Grobis, O. Hellwig, D. Kercher, J. Lille, E. Marinero, K. Patel, R. Ruiz, M. Schabes, L. Wan, D. Weller, and T.-W. Wu, "Bit Patterned Media at 1 Tdot/in2 and Beyond," IEEE Transactions on Magnetics, vol. 49, pp. 773–778, Feb. 2013.

[121] S. Alebrand, M. Gottwald, M. Hehn, D. Steil, M. Cinchetti, D. Lacour, E. E. Fullerton, M. Aeschlimann, and S. Mangin, "Light-induced magnetization reversal of high-anisotropy TbCo alloy films," Applied Physics Letters, vol. 101, p. 162408, Oct. 2012.

[122] S. Shiomi, T. Ikeda, M. Koshiro, and M. Masuda, "Effect of Substrate Bias on In-Plane Uniaxial Magnetic Anisotropy in Amorphous TbCo Films Prepared by DC-Sputtering," Jpn. J. Appl. Phys., vol. 30, p. L364, Mar. 1991.

[123] S. Shimanuki, K. Ichihara, N. Yasuda, K. Ito, and K. Kon, "Perpendicular Magnetic Anisotropy in Amorphous TbCo Sputtered Films," IEEE Translation Journal on Magnetics in Japan, vol. 2, pp. 338–339, Apr. 1987.

[124] H. T. Seiji Yoshino, "Perpendicular Magnetic Anisotropy of TbCo Films," Japanese Journal of Applied Physics, vol. 23, pp. 188–191, 1984.

[125] M. Gottwald, M. Hehn, F. Montaigne, D. Lacour, G. Lengaigne, S. Suire, and S. Mangin, "Magnetoresistive effects in perpendicularly magnetized Tb-Co alloy based thin films and spin valves," Journal of Applied Physics, vol. 111, p. 083904, Apr. 2012.

[126] "Gwyddion", URL: http://gwyddion.net/

[127] J. P. Morgan, Ordering and defects in artificial magnetic square ice: thermodynamic and field-driven processes. phd, University of Leeds, Sept. 2011.

[128] "The Object Oriented MicroMagnetic Framework (OOMMF).", URL: http://math.nist.gov/oommf/

[129] S. Zhang, J. Li, I. Gilbert, J. Bartell, M. J. Erickson, Y. Pan, P. E. Lammert, C. Nisoli, K. K. Kohli, R. Misra, V. H. Crespi, N. Samarth, C. Leighton, and P. Schiffer, "Perpendicular Magnetization and Generic Realization of the Ising Model in Artificial Spin Ice," Phys. Rev. Lett., vol. 109, p. 087201, Aug. 2012.

[130] P. E. Lammert, V. H. Crespi, and C. Nisoli, "Gibbsianizing nonequilibrium dynamics of artificial spin ice and other spin systems," New J. Phys., vol. 14, p. 045009, Apr. 2012.

[131] U. Wolff, "Collective Monte Carlo Updating for Spin Systems," Phys. Rev. Lett., vol. 62, pp. 361–364, Jan. 1989.

[132] D. W. H. Kurt Binder, Monte Carlo Simulation in Statistical Physics - An Introduction. Springer Berlin Heidelberg, 2010.

[133] N. Metropolis, A. W. Rosenbluth, M. N. Rosenbluth, A. H. Teller, and E. Teller, "Equation of State Calculations by Fast Computing Machines," The Journal of Chemical Physics, vol. 21, pp. 1087–1092, June 1953.

[134] L.-P. Henry, Glace bidimensionnelle classique et quantique : phases de Coulomb et phases ordonnées. PhD thesis, Ecole normale supérieure de lyon - ENS LYON, Nov. 2013.

[135] B. Bhushan, ed., Springer Handbook of Nanotechnology. Berlin, Heidelberg: Springer Berlin Heidelberg, 2010.

Appendix A

The Monte Carlo Method

A.1 Direct Sampling and Selective Sampling

A few words about the Monte Carlo method should be said, as it is a recurring tool that has been used throughout this work. It is, in fact, a powerful tool for investigating the thermodynamic properties of model systems that cannot be solved analytically or for system sizes that make a partition function calculation practically impossible. It is probably needless to say that the method has grown into a widely-employed technique, transcending the field of statistical physics, but the current appendix only aims to describe what the general idea is in the context of classical Ising-spin models, presenting some of the advantages and challenges associated to it, the algorithms used and also describing how relevant thermodynamical and physical quantities are computed throughout a typical simulation cycle performed for this work.

When interested in the thermodynamic properties of a system, the first reflex is to find the partition function, as this quantity contains all the necessary information for the computation of the thermodynamic state functions[21] (see Figure A.1). This quantity is defined as the sum over all the possible microstates of a thermodynamic system, weighted by the Boltzmann factor:

$$Z = \sum_i exp(-\frac{E_i}{k_B T}) \tag{A.1}$$

where E_i is the energy of the state indexed i and the $k_B T$ is the thermal energy. This is, of course, available for a discrete system, but the sum turns into an integral for continuous ones. However, this approach works well if the function can be determined analytically, such as for an N-level discrete system or for a paramagnetic gas. For more complex interaction

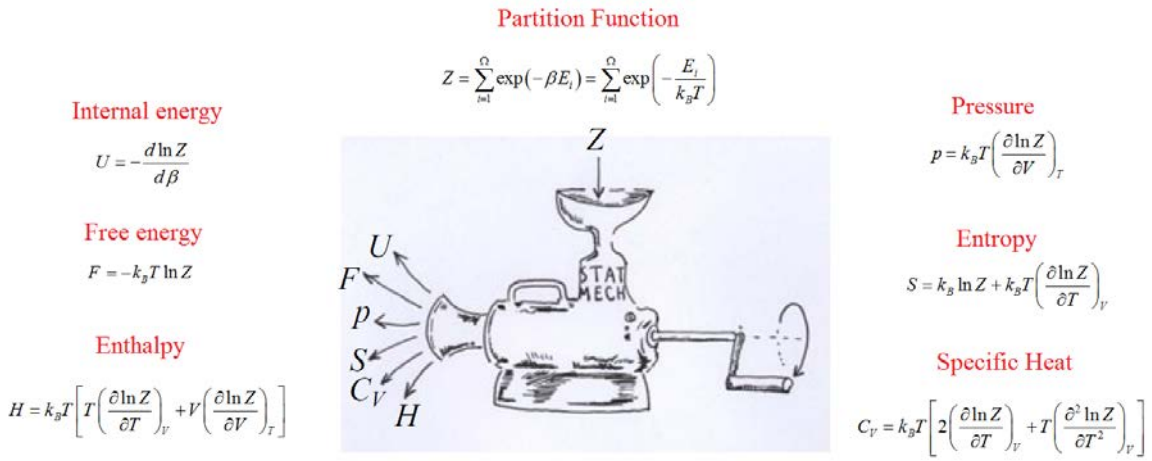

Figure A.1 - If the partition function is known, the other thermodynamic quantities can be computed from it and its derivatives. Steven and Katherine Blundell suggestively describe this procedure as a "thermodynamic sausage machine" that needs only the partition function as an input and can then output the function of states: "it takes only a turn of the handle on our "sausage machine" to produce other functions of state". Image taken from *Concepts in Thermal Physics*[21] by S.J. Blundell and K.M Blundell.

systems, this approach can be quite challenging. Of course, simulations can be made to evaluate all possible microstates and store their respective energy, but this quickly becomes impractical as the size of the system increases. For instance, for an network with N Ising spins, the total number of configurations is 2^N. For $N \lesssim 30$, this can still be done in rather reasonable conditions, but given the exponential increase of the number of states, this will not be practical anymore for larger systems[1]. Furthermore, one is often interested in the behavior at the thermodynamic limit, $N \to \infty$, so finding a way to determine, at least with a certain accuracy, the thermodynamic behavior of larger system is important.

One way to do this is by randomly sampling microstates. In the end, a thermodynamic system explores its phase space over time, and, if the ergodic condition holds (the time-average is equal to the ensemble average), then the thermal average of an observable A can be computed using an ensemble of randomly selected states:

$$< A >_T = \frac{\sum_{i=1}^{N} A_i \cdot exp(-\frac{E_i}{k_B T})}{\sum_{i=1}^{N} exp(-\frac{E_i}{k_B T})} \tag{A.2}$$

[1] Also, the computation effort can significantly increase depending on the webs of interactions. If all components interact with each other, like in the case of a dipolar framework, this costs additional runtime.

where A_i is the value of A sampled at step i of a random sampling sequence of N microstates. In fact, this expression is similar to the estimation of the average value of a function whose argument is a discrete random variable $\mathbf{x}$, with a set of values x_i and their associated probabilities $p(x_i)$:

$$< f(\mathbf{x}) >= \frac{\sum_{i=1}^{N} f(x_i) \cdot p(x_i)}{\sum_{i=1}^{N} p(x_i)} \tag{A.3}$$

Given that we are dealing with a classical system in-equilibrium, the probabilities are given by the Boltzmann factor, $p(E) = \frac{1}{Z} \cdot exp(-\frac{E_i}{k_B T})$. Therefore, this method follows the standard laws of probability distributions, and the more states are sampled, the more the average approaches its expectation value, with the standard deviation of the probability distribution $\rho(A)$ decreasing as $1/\sqrt{N}$.

This method is called the direct sampling Monte Carlo method and is largely used for evaluating estimators of random variables and for simulating self-avoiding random walks[132]. It can also be used for determining thermal averages, as was presented, but for a canonical ensemble picture, this method has certain issues. For instance, it can be shown that the probability distribution of a system's energy, $\rho(E)$, is a Gaussian, provided that critical points are avoided[132][2]. Using direct sampling implies a random selection of configurations X_i, with energies E_i form the Gaussian. In the limit $T \to \infty$, all states are equally probable and if the thermal average of the energy is sought, this method works rather well in this infinite-temperature limit, as a system explores with the same probability all its possible microstates. However, when dealing with finite temperatures in a canonical ensemble, the microstates no longer share the same probability of occurrence, which results in a shifting of the sampled probability distribution towards lower energy values (see Figure A.2. The direct sampling method however continues to randomly select microstates from $\rho(E)$ without any particular filter, and while the thermal average is performed by weighting the contribution of each state X_i by a Boltzmann factor, this results in a very slow and difficult convergence towards the expected value of the energy for the considered temperature. As an example, consider the case of an Ising ferromagnet on a square lattice. For temperatures far below the critical point, the system is ordered and the energy does not change anymore. Direct sampling will randomly explore all the phase space, and it will select microstates that are

[2]This is like the histogram of all the energy values. In addition, for the spin models that are presented in this work, this Gaussian is centered at 0.

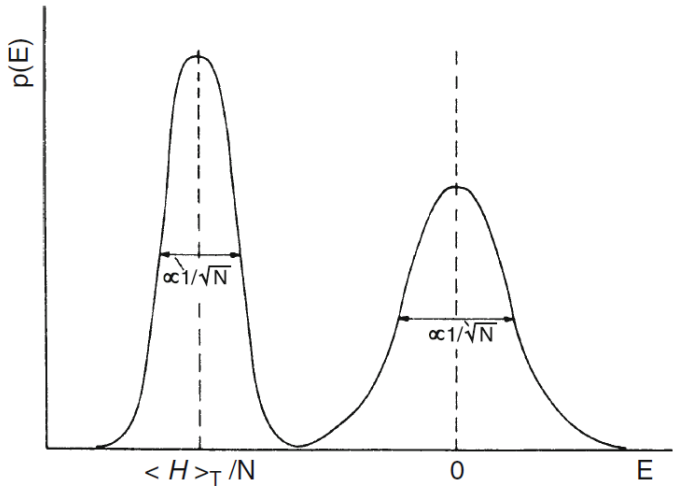

Figure A.2 - Normalized energy distributions $\rho(E)$ for the microstates sampled. Considering a spin model that has the property $< E >_{T\to\infty} = 0$, a direct sampling method with N tryouts would yield the Gaussian on the right. A system found in a heat bath at finite temperature T would have an average energy value lower than 0 and its normalized energy distribution would be shifted from the direct sampling one (Gaussian on the left). Though the direct sampling thermal averages give a small contribution to the average value of the system energy in a finite-temperature canonical picture, the convergence is very slow and subject to deviations for a relatively low number of sampling steps N. This encourages the use of selective sampling to enhance the exploration of the representative manifold rather then wonder around the entire phase space. Image taken from *Monte Calo Simulations in Statistical Physics*[132] by K. Binder and D.W. Heermann.

not completely ordered and have a high chance of appearing in the paramagnetic regime[3]. Indeed, the Boltzmann factor will give these selected states a minimal contribution to the thermal average, but since we want to get as close as possible to the thermodynamic limit, this exploration away from the representative manifolds might be regarded as a waste of computation power and can even result in inaccurate averages. The idea is then to weighted the sampling of the microstates so that the subset of selected states reproduces the features of the entire ensemble of states explored at finite temperatures within a canonical ensemble. Otherwise said, the subset of states must replicate the Boltzmann distribution specific to the whole ensemble of system states in the given heat bath conditions. This is, in fact, the basis of the selective sampling Monte Carlo method.

In a famous paper, Metropolis *et al.*[133] proposed to not to choose the successive states in an independent manner, but to generate the next configuration from the precedent state using an adapted transition probability, thus creating a Markov chain of microstates. As

[3]For finite-size systems, the situation can be different as additional fluctuations can be induced by finite-size effects and the energy can still slightly vary even after the system has shown the signs of a phase transition. Strictly speaking, critical phenomena are described properly at the thermodynamic limit.

mentioned in the previous paragraph, the idea is to have a final subset that respects the Boltzmann distribution, so the transition probability should be chosen accordingly. In fact, this idea mimics the behavior of a system in a heat bath: it "jumps" from one configuration to another, thus exploring its representative manifold, and its exploration results in a distribution of microstates that follow the Boltzmann statistics.

Let's consider again an Ising ferromagnet on a square lattice of N sites and select a configuration **x**, i.e. a point in the phase space. Using only elementary moves like single spin-flips, we can jump from this configuration to another, **x'**, thus creating a Markov chain. There are, of course, N possibilities to do this at each step, where N stands for the number of spins. This can be pictured by a graph representation that connects states which differ from each-other by a single spin-flip. The Boltzmann statistics gives us the probability for each of these states, but it doesn't say anything about the transition probabilities. However, the time-evolution of the probability P(**x**,t) to stumble upon the state **x** at time t is given by the Markovian master equation[132]:

$$\frac{dP(\mathbf{x},t)}{dt} = -\sum_{x'} W(\mathbf{x} \to \mathbf{x'}) \cdot P(\mathbf{x},t) + \sum_{x'} W(\mathbf{x'} \to \mathbf{x}) \cdot P(\mathbf{x'},t) \tag{A.4}$$

where $W(\mathbf{x} \to \mathbf{x'})$ and $W(\mathbf{x'} \to \mathbf{x})$ stand for the transition probabilities from state **x** to **x'** and vice-versa and t is the time of the Markov process, which is measured in terms of sequential steps[4]. The first term corresponds to all the possible transitions towards the state **x**, while the second one represents the outgoing processes. Of course, this has to be filtered by the probability of the states themselves. This way, if P(**x**) has an initial high value, then the Markov process will seek to sample it often in the early stages[5], but its occurrence will be modified according to this equation. Over time, which in this cas translates into the number of "jumps", the system eventually reaches a stationary regime in which these probabilities are not time-dependent anymore, P(**x**,t) = P(**x**). This regime corresponds to thermal equilibrium and the transitory process is called thermalization. Under such conditions, the above equation simplifies to:

$$\sum_{x'} W(\mathbf{x} \to \mathbf{x'}) \cdot P(\mathbf{x}) = \sum_{x'} W(\mathbf{x'} \to \mathbf{x}) \cdot P(\mathbf{x'}) \tag{A.5}$$

[4]Thoughout this appendix I have used the notation employed by K. Binder and D.W.Heermann[132].

[5]The time variable here can be regarded as steps in the Markov sequence.

If we take just one jump $\mathbf{x} \rightarrow \mathbf{x'}$, we have $W(\mathbf{x} \rightarrow \mathbf{x'}) \cdot P(\mathbf{x}) = W(\mathbf{x'} \rightarrow \mathbf{x}) \cdot P(\mathbf{x'})$, and given that $p(E_\mathbf{x}) = \frac{1}{Z} \cdot exp(-\frac{E_\mathbf{x}}{k_B T})$, this can be conveniently rewritten as:

$$\frac{W(\mathbf{x} \rightarrow \mathbf{x'})}{W(\mathbf{x'} \rightarrow \mathbf{x})} = \frac{P(\mathbf{x'})}{P(\mathbf{x})} = exp(-\frac{E_{\mathbf{x}'} - E_\mathbf{x}}{k_B T}) \tag{A.6}$$

Notice that the partition function vanishes at the last step, and its calculation is not required anymore. This is one of the major advantages of selective sampling, given that the evaluation of the partition function is a major inconvenience when dealing with systems with relatively large number of components and complex webs of interaction between the elements. This result also highlights the fact that the transition probabilities, $W(\mathbf{x} \rightarrow \mathbf{x'})$, are not uniquely defined and there is a freedom of choice here, so long as they respect this condition. One of the most common choices is the following:

$$W(\mathbf{x} \rightarrow \mathbf{x'}) = \begin{cases} \frac{1}{\tau_s} \cdot exp(-\Delta E / k_B T), & \text{if } \Delta E > 0 \\ \frac{1}{\tau_s}, & \text{otherwise} \end{cases} \tag{A.7}$$

where $\Delta E = E_{\mathbf{x}'} - E_\mathbf{x}$ and $1/\tau_s$ is a unit of Monte Carlo time for one single transition (this aspect will be discussed shortly). This description is the basis of the so-called Metropolis algorithm for simulating spin models, which is discussed in the following section.

A.2 The Single Spin-Flip Metropolis Algorithm

When simulating the thermodynamic properties of spin models, the Metropolis algorithm[133] is a common option. To exemplify how it is applied, suppose we have an Ising ferromagnet on a square lattice with N spins and plan to simulate its thermodynamic behavior in heat bath conditions at temperature T. Firstly, we need to initialize the lattice (take all spins pointing up for example) and compute its energy and, for example, its magnetization (other thermodynamic quantities can also be computed, depending on the goal). This requires the choice of a certain interaction model. In this case, let's assume a nearest-neighbor coupling of the form $H = -J \cdot \sum_{<i,j>} \vec{S}_i \cdot \vec{S}_j$, where $J > 0$ is the coupling constant. Afterwards, to simulate the exploration of the energetic manifold that the system undertakes, we follow the next steps:

1) choose randomly a spin form the set of N spins and provisionally flip it.

2) Calculate the energy of this new state and compute the transition probability $W(\mathbf{x} \rightarrow \mathbf{x'}) = exp(-\Delta E / k_B T)$.

3) To see if the flip is accepted or rejected, uniformly choose a random number r between 0 and 1.

4) If $W(\mathbf{x} \rightarrow \mathbf{x'}) > r$, accept the flip, otherwise, reject it. This is the so-called *detailed balance condition*.

5) Afterwards, update the values of the thermodynamic quantities, especially the energy, and store the data of interest.

6) Go back to randomly choosing a spin (step 1) and keep repeating steps 1 to 6 until sufficiently relevant statistical samples have been acquired.

As simple as it appears to be, this single spin-flip algorithm has certain delicate aspects. Firstly, the goal here is to perform averages of thermodynamic quantities like the energy and the magnetization in heat bath conditions. If at-equilibrium behavior is sought, then we must first ensure that the system is in thermal equilibrium with its heat-bath. Otherwise said, we have to perform several steps for thermalization as was described in the previous section, without storing any data for statistical evalutation purposes[6]. The obvious question is how many single spin-flip events have to be performed to ensure thermal equilibrium? There is no universal recipe here and one cannot generally guarantee thermal equilibrium, but there are some indicators that can be computed during this thermalization step which can help determine if the system is effectively in-equilibrium. I will discuss this shortly, but for now, the first main message is that a thermalization procedure has to precede any sampling for the determination of at-equilibrium thermodynamic properties.

Secondly, suppose we are now in thermal equilibrium and we seek to sample states for determining the average values of the physical quantities. For the statistical averages performed on the ensemble of sampled states to be relevant, the stored snapshots during the measurement stage should be very different from one-another or, otherwise said, should be decorrelated/statistically-independent. Performing just one spin-flip and then storing the data is therefore not a good idea, as the only difference between these two consecutive states is an elementary spin-flip move. In a general sense, for considering that two states are decorelated, the system has to undergo a number of elementary moves which is at least equal to the number of its components. This is called a unit of Monte Carlo time or a *Monte Carlo step*, whereas a single elementary modification in the system is denoted as a Monte Carlo microstep. Since we are performing flips by randomly selecting the lattice spins, we must perform at least N such steps to ensure that this is true. Even in this situation, some of the selected spins may not have flipped, and this is usually what happens at relatively low temperatures where the system consistently rejects movements that might increase its energy. In this case, the number of steps has to be even greater than the number of components,

[6] In some cases, it is the transitory process that is of interest and data should be stored during this early stage

and a unit of Monte Carlo time becomes equal to $\tau_s N$, where τ_s is the average unit time for a microstep. This latter quantity can be related to the spin-flip acceptance ratio (s), i.e. the number of accepted elementary movements, $MC_{steps}^{accepted}$, within a set of MC_{steps} single spin-flip tryouts ($s = MC_{steps}^{accepted}/MC_{steps}$). For example, if we perform sampling for the Ising ferromagnet on a square lattice for a temperature $T/J \cong 4$, only 2 out of 3 tryouts are accepted on average, and to ensure that a unit of Monte Carlo time passes between two system states that we store, we must perform a minimum of $\tau_s N = 3/2N$ steps. This flip acceptance ratio can actually be computed during the thermalization stage. Presuming that this procedure is sufficiently long so that the fingerprints left by the transitory process on the acceptance ratio can be neglected, the flip acceptance ratio computed during thermalization should be equal to that specific to equilibrium conditions. This is, in fact, a way to quantify the efficiency of the thermalization process and adapt the number of thermalization Monte Carlo steps to ensure proper thermalization as much as possible[7]. Since a Monte Carlo step is usually thought of as a sweep through the lattice, i.e. N tryouts of spin flips, I shall call the $\tau_s N$ steps a *modified Monte Carlo step* throughout this work. In fact, it is this quantity that serves as the unitary increment of Monte Carlo time.

Another important factor that should be mentioned is the influence of the network boundaries on the overall thermodynamic behavior. Obviously, we cannot simulate infinite networks, but the smaller the network is the more significant are the effects of the borders which can lead to deviations from bulk behavior. To circumvent this without needing to simulate very large systems, periodic boundary conditions can be implemented. This implies wrapping the network on the surface of a torus so that one border connects to the opposite one. However, this method should be used cautiously and the size of the lattice should be chosen in accordance with the interaction model as in some cases, the development of long-range order might be prevented by an improper wrapping of the network on the torus, and the system would struggle in vain to order itself. However, if the goal is to simulate the effects given by the anisotropic environment of the borders, then such conditions should not be implemented. The current work presents both cases.

The size of the network also plays a crucial role, even when periodic boundaries are implemented. For instance, an infinite lattice in equilibrium with its heat bath has a well-defined

[7] In the simulations presented throughout this work, sampling was performed for each temperature starting form a high temperature regime. Initially, the temperature is sufficiently high to ensure that flips are almost always accepted. Indeed, at the end of the thermalization cycle, the flip acceptance ratio is close to unity in this case. The number of decorrelation steps is computed as $\tau = 2 \cdot \tau_s$, where τ_s is the inverse of the flip acceptance ratio computed during thermalization[8]. The same quantity is measured during the sampling stage and, if the two inverse acceptance ratios are approximately the same, then thermalization can be deemed as successful. Also, these values can serve as inputs for the thermalization phase of the next simulated temperature, which is determined by gradually stepping down the temperature, $T_{i+1} = T_i/T_s tep$.

value for its energy, but a finite-size lattice will fluctuate around this expected value. To improve the accuracy of the measurements, the number of sampling snapshots, MC_{steps}, should be increased as much as possible. This way, the average value converges to the expected value with a $1/\sqrt{MC_{steps}}$ standard deviation[9]. Nevertheless, the artificial spin ice networks that are studied in this work have finite sizes, so fitting the dimensions of the simulated lattice to them is a requirement for proper comparison. However, a precise determination of the quantities characterizing critical phenomena with Monte Carlo simulations requires the implementation of finite-size scaling[132], a procedure that has not been used in the current work.

Last but not least, it is important to remind that all quantities that are recurrently used during a Monte Carlo simulation should be computed during the initialization stage and stored accordingly. This is a standard optimization procedure and usually implies the storing of the neighboring graphs (which component is neighbor to which), the coupling constants (J_{ij}) and the correlation webs if these quantities are sampled.

A.3 Cluster and Loop Algorithms

Near a critical point, a single spin-flip Metropolis algorithm may experience a *critical slowing down* of the spin dynamics. Otherwise said, the acceptance ratio of the flips drops drastically to zero as the critical point is approached. This is particularly due to the fact that a certain ordering pattern is developing in the system at this stage and continuing to perform individual, local moves like single spin-flips disrupts this tendency, thus making such attempts to be very often rejected. If we go back to the Ising ferromagnet on a square lattice governed by nearest-neighbor interactions only, it presents a phase transition at $T_C \cdot (k_B/J) = \dfrac{2}{ln(1+\sqrt{2})} \cong 2.269$, according to Onsager's condition, $sinh(\dfrac{2J}{k_B T_C}) = 1$[63]. In fact, the ordered state sought is either an all-up or all-down configuration and in the proximity of the critical point a simulated finite-sized system starts to form domains of each type. Flipping a spin that is within a domain is very unlikely, since it results in an increase of the energy, an operation that starts to be severely filtered out by the detailed balance condition, and the disruption of the already-established local order. The Metropolis algorithm

[9] In fact, it can be shown (see reference [132]) that the average statistical error for an observable A, $< (\delta A)^2 >=< 1/MC^2 \sum_{i=1}^{MC} < (A_i - < A >)^2 >$, sampled by a selective sampling Monte Carlo simulation is approximately given by $< (\delta A)^2 >= 2\tau_A/\tau_{obs} \cdot [< A^2 > - < A >^2]$, where τ_A is the so-called relaxation time after which the system is effectively decorrelated from a precedent state and τ_{obs} stands for the total observation time. Since the total observation time in this work's simulations is enhanced so that $\tau_{obs} \cong MC \cdot \tau_A$, the statistical errors follow standard error analysis laws and their values depend on the variance of the variable and the number of modified Monte Carlo steps: $< (\delta A)^2 >= 2/MC \cdot [< A^2 > - < A >^2]$.

described previously might be used for sampling states just above the critical point ($T > T_C$), but this requires a long series of decorrelation steps between successive stored configurations. Even so, this reinforced decorrelation sequence cannot guarantee that the two consecutive snapshots stored are relevant statistical states. In fact, if a spin flip does occur, it is very often the same spin that is later on selected and brought back to its initial state. Looking only at the flip acceptance ratio, one might conclude that the single-spin flip dynamics can still explore the energetic manifold but it "just need more time". However, this turns out to be misleading, as ergodicity is broken and continuing the sampling results in final averages that present significant statistical errors and are not representative to the heat bath conditions in which the system is placed.

In such situations, the single spin-flip dynamics is practically unable to link two statistically-relevant states. To prevent the system from freezing and enable the further exploration of its energetic landscape, non-local moves are required. Suppose we have a small "spin-down" domain in a large "spin-up domain". Flipping some of the spins that are in the center of the smaller domain will still be very likely rejected by the detailed balance condition, but if we try to flip the entire domain or a cluster of spins that correspond to it, then this attempt has a better chance of passing the test since it could significantly expands the nearby larger domain. This non-local move is called a cluster update and is typically used to overcome the critical slowing down phenomena encountered by the single spin-flip dynamics near critical points.

One of the most common examples of cluster updates is the Wolff algorithm[131]. The main idea is to construct a cluster of ordered spins and then flip them either sequentially during the cluster growth or once the cluster is completely defined. One way to do this is by following the sequence of operations listed below[134]:

1) Let K be the growing cluster, and S a list that we use to store the pathways for its expansion.

2) Choose randomly a spin i from the network and add it to K.

3) Determine all nearest neighbors of the selected spin i that are not contained in K and add them to S.

4) If there are no spins to add and S is empty, go to the last step of this sequence. Otherwise, take the first available element j of S.

5) Add j to K with the following probability:

$$p(j) = max(0, 1 - exp(-\frac{2 \cdot J \cdot \vec{S}_i \cdot \vec{S}_j}{K_B T})) \tag{A.8}$$

6) Clear j from the temporary list S.

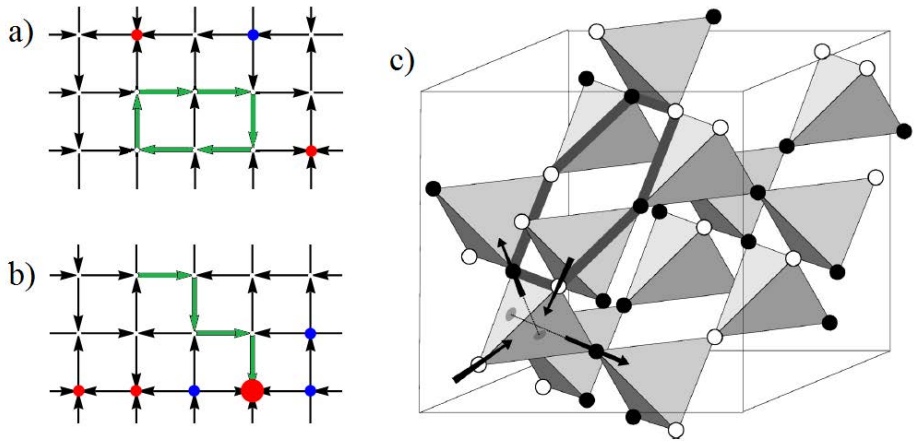

Figure A.3 - For networks that present loop-like configurations, the cluster dynamics is generally replaced with loop flips. For the square ice network, loops made of head-to-tail spins can close in on thermselves. (a) If the loop passes through configurations that respect the ice-rules, flipping it does not result in ice-rule breaking. This makes this dynamics ideal for sampling statistically-relevant states within a spin ice regime. (b) However, if defects are present, one might end up blocked in a type IV vertex. (c) Such loop movements have been used to simulate the thermodynamic behavior of dipolar spin ices and managed to overcome the critical slowing down of the single spin-flip dynamics, ultimately driving the system in an ordered state. A short-loop hexagon is represented in (c) by a grey contour. The white and dark spots correspond to spins pointing "in" and "out" of a "downwards" tetrahedron. Figure (c) taken from Melko *et al.*[29].

7) If j was accepted into K, make j the new point of growth for the cluster and go back to step 3). Otherwise, go back to step 4) and check if there are other spins in S.

8) Flip the spins in cluster K (without any additional conditions).

This algorithm is very useful for overcoming the critical slowing down of the single spin flip dynamics. However the current work has employed a different non-local update algorithm involving the selective flipping of spin loops, a protocol that is nevertheless part of the family of cluster algorithms.

Let's consider that the spins of the Ising ferromagnet now lie in the plane of the network along the links between the sites. This still yields a square lattice that mimics artificial square spin ices[1]. This geometry can form closed loops of spins. To generate one, simply start form a spin randomly selected and move to a neighboring one making sure that the move follows the spin arrow directions. Keep on repeating the process until the loop closes in on itself. If the ice-rules are obeyed unanimously, there is always a way in and a way out of a vertex. An example of a closed loop is given in Figure A.3.a). Interestingly, if this loop is flipped, then the ice rules are not broken, making such non-local updates ideal for sampling the spin ice manifold. Nevertheless, since the generation of a loop is deterministic and does not depend on the interaction model, the stochastic ingredient in a loop-flip algorithm is

assured by the detailed balance condition, very similarly to the single spin-flip Metropolis algorithm described before. This is in contrast with the Wolff algorithm where the stochastic nature lies in the cluster's construction and then the cluster is flipped without any additional conditions. The loop-update algorithm goes as follows:

1) Generate a closed-loop of spins by moving from one spin to its neighbors by following the arrow directions. If multiple choices exist at a certain vertex point, choose between the compatible ones randomly. Halt the operation if there is no continuity.

2) Store the energy of the system in this state, E_i.

3) Flip the loop and calculate the energy in the new state, E_f.

4) Calculate the loop-flip probability, $W = exp(-(E_f - E_i)/k_BT)$.

5) Generate a random number r uniformly between 0 and 1.

6) If $W > r$ accept the flip, otherwise reject it and return to the previous state.

7) Move back to step (1) and continue sampling loop updates for ensuring proper decorrelation and measurements.

Perhaps one of the most common and successful applications of such loop updates can be found in the study of the low-temperature energetic manifolds of dipolar pyrochlore spin ices made by Melko *et al.*[29]. As it was discussed in section 1.2, pyrochlore spin ices show an overall effective short-range behavior in the low-temperature regime, despite the long-range nature of the driving dipolar interactions. The difficulty in developing stronger long-range correlations seems to lie in the freezing of the single spin-flip dynamics, which cannot successfully escape local energy minima within the energetic landscape. However, for an ice-like obeying configuration, the "two-in/two-out" ice rule ensures that, if we are to walk around the lattice by following the spin arrows, there is always a way in and a way out for each tetrahedron, just like in the square spin ice. If a closed spin-loop is found, flipping it cannot break the ice rules, which is a necessary requirement for a non-local cluster dynamics on this system. Furthermore, although the single spin-flip dynamics is practically inefficient, it still has to be preserved for the sake of ergodicity.

In the current work, a combination of single spin-flip and loop-flip tryouts has been employed at each Monte Carlo microstep[10]. Also, the acceptance ratio is updated according to the overall estimated number of single spin-flips. For example, in a square spin ice network, the minimum length of a loop is 4 spins. Taking a worst case scenario in account, the overall acceptance ratio (f) computed during a series of Monte Carlo steps would be a linear combination between the spin acceptance ratio (s) and the loop acceptance ratio (l):

[10]I call this a hybrid flip. It involves one single spin-flip tryout followed by the generation of a loop and, if successful, a conditioned loop-flip.

$f = s + 4 \cdot l$. The number of decorrelation steps necessary for insuring statistical independence is then $\tau_s = 1/f$.

A.4 Computing the Relevant Thermodynamic Quantities

Apart from the average values of the energy and the magnetization, the specific heat (C), the susceptibility (χ) and the entropy (S) are the main thermodynamic quantities that are computed after a sampling cycle at a prefixed Monte Carlo temperature T. Given that the sampling is done at thermodynamic equilibrium, the first two quantities are given by the fluctuation-dissipation theorem[21]:

$$C = \frac{< E^2 > - < E >^2}{T^2} \quad \chi = \frac{< M^2 > - < M >^2}{T} \tag{A.9}$$

Therefore, the energy and the magnetization of each sampled snapshot, along with their square values, are stored during the measurement stage and, at the end of the sequence, their variances are computed to retrieve these functions of state.

The entropy is directly related to the specific heat by the following thermodynamic identity:

$$\frac{dS}{dT} = \frac{C}{T} \tag{A.10}$$

Therefore, the entropy/spin for a given temperature is determined by integration

$$S(T) = S(T \to \infty) + \int_{\infty}^{T} \frac{C}{T} dT. \tag{A.11}$$

and the reference for $S(T \to \infty)$ is taken to be $N \cdot ln(2)$, given the Ising nature of each spin.

The pairwise spin correlators, $C_{\alpha j}$ are a very fine measure of the degree of order that is established in a system at a certain temperature. Therefore, the first seven spin correlators have also been computed during the measurement cycle. Their definition has to be made in accordance with the lattice symmetry and the coupling constant.

For each correlation type, a network average is firstly computed by summing up through all the corresponding pairs. This network average is, in fact, the average of a binomial distribution generated by the +1 and -1 correlation values computed locally, $\sigma_i \cdot \sigma_j = \pm 1$. This distribution also has an intrinsic standard deviation. During a Monte Carlo cycle for a given temperature, a network average for each correlation type is calculated for every

sampling snapshot. Finally, once all measurement steps have been completed, a final average for the given temperature and for each correlation type can be computed. In fact, this is an average that corresponds to another distribution, formed by the all the network averages taken during sampling. To distinguish between the two cases, I shall call the latter the *ensemble average*, $< C_{\alpha j} >$, since it is performed over the set of sampled snapshot averages, and the former will be called a *network average*, $C_{\alpha j} =< \sigma_\alpha \cdot \sigma_j >$. The ensemble average corresponds to a distribution that has a Gaussian form and a standard deviation that is very sensitive to the system size. Therefore, it is imperative that the size of the simulated systems match the size of the experimental artificial spin network if a comparison between correlations is made.

Appendix B

Some Basic Aspects of Magnetic Force Microscopy

Magnetic Force Microscopy (MFM) is a technique that is part of the Atomic Force Microscopy (AFM) family, which in turn is a member of the grand family of Scanning Probe Microscopy techniques (SPM). The latter have become standard characterization tools for nano-materials and nano-scale devices[135].

There are many different operation modes for Atomic Force Microscopy, but the general idea is to employ a sharp tip, located at the edge of a highly-flexible cantilever, for the mapping of surface topography or for measuring a specific type of interaction in the proximity of a sample's surface. The micrometer-sized cantilever is usually put into oscillation at a resonance frequency through the use of piezoelectric elements, thus insuring a fine adjustment of the oscillation frequency and amplitude. The proximity to the sample surface is finely controlled via piezoelectric elements as well (see Figure B.1.a). If the tip is far from the sample surface, the cantilever oscillates at its preset resonant frequency. However, near the sample surface, different types of forces start to develop between the tip and the sample (particularly Van der Waals and capillary forces), and the resonant frequency suffers a shift proportional to the spatial derivative of the interaction, while also being sensitive to its sign. This process can be modeled by a forced harmonic oscillator and the interaction can be translated into a change in the effective spring constant of the cantilever (for more details on the matter, consult reference [80].). The amplitude and phase of the oscillations are therefore modified and by recording these changes one can reconstruct an interaction map of the tip with each region of the scanned surface.

Spatial deviations and changes in the cantilever motion are immediately detected through a laser deflection setup (see Figure B.1.b). This consists in shinning a laser-beam on the apex of the cantilever and detecting the average deviations by using a 4-quadrant photo-detector.

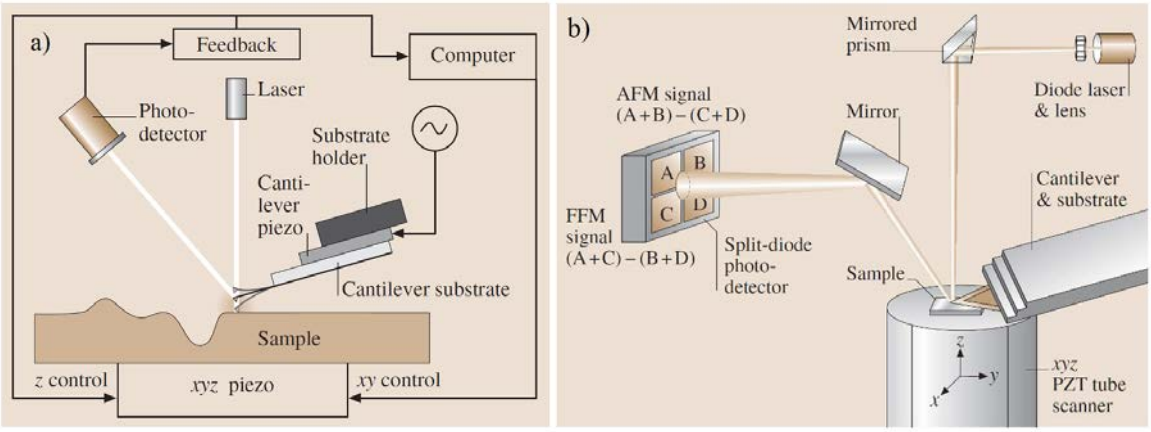

Figure B.1 - (a) The operation mode schematics for an AFM/MFM microscope. A very sensitive cantilever is placed in oscillation in the proximity of the sample surface. The spatial deviations are detected via a laser detection setup and a feedback loop, which ensures a real-time processing of the received signals. (b) The schematics of the laser detection setup. The laser spot is reflected by the oscillating edge of the cantilever and, through a system of mirrors, it hits the center of a photo-detection device which is generally divided into four quadrants. Vertical displacements of the cantilever are detected through a bias in the recorded intensity between the upper and the lower quadrants. Similarly, torsions of the cantilever can also be detected by taking the bias intensity between the left and right quadrants. The latter is called Friction Force Microscopy (FFM). Both images were taken from the *Springer Handbook of Nanotechnology*[135] edited by B. Bhushan.

The laser spot hits the center of the detector by default, resulting in equal intensities registered by each of the quadrants. A spatial deviation of the cantilever triggers a biased output signal from the quadrants, which is then analyzed by the microscope's electronic components to reconstruct the topographic or the interaction map. A feedback loop is also implemented to ensure that the laser spot is brought back to its central position after a deviation was registered. This way, upcoming shifts can be detected in the same conditions.

There are many different operation modes available, the most commonly used being the contact mode, the tapping mode, the constant-height and constant-force modes and the non-contact mode. The contact and tapping modes are very useful for mapping the surface topography, with spatial resolutions that can reach the order of 10nm, making this technique a powerful tool for characterizing nanomaterials. The non-contact modes can be used to evaluate long-range interactions such as magnetic and electric ones. By coating the tip with a thin magnetic layer, the cantilever becomes sensitive to magnetostatic interactions that may develop between the tip and a magnetized surface. However, to properly quantify this interaction, the scan needs to be performed at a certain height from the sample surface, otherwise the magnetic interaction will be overshadowed by contact forces and capillarity effects. This is, in fact, the principle of a Magnetic Force Microscopy scan: for each scanning

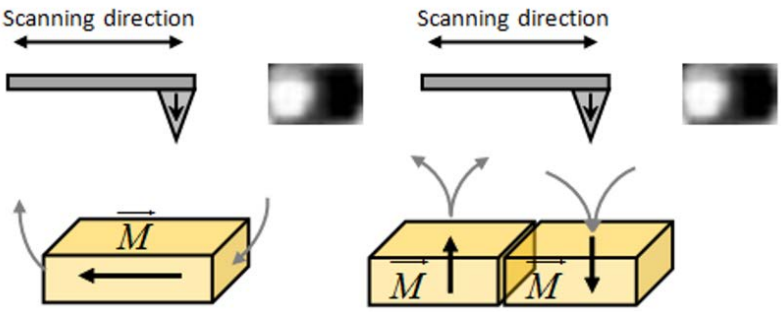

Figure B.2 - The interpretation of MFM magntic contrast can be a delicate task. The example given here shows how two different magnetic configurations can yield the same MFM contrast map through the stray-field lines. However, additional information on the magnetic properties of the sample can help elucidate between the different possibilities. A soft magnetic material would rather have the magnetization lying along the long-axis of a nano-particle, whereas a hard material with a strong uniaxial anisotropy along the vertical axis can present "up" and "down" magnetic domains, which can result in similar stray field lines to the former case. Knowing which type of material the sample is made of can therefore facilitate the interpretation. Figure taken and slightly modified form reference[80].

line of the probing region, the topography of the surface is firstly charted, usually in tapping mode, followed by a lift of the cantilever at a certain height. A second scan is afterwards performed by following the surface profile established during the first scan. By doing so, the magnetic sample-tip interactions are quantified and this ultimately yields both a surface profile and a magnetic map. The latter generally has brighter and darker contrasts that reproduce both qualitatively and quantitatively the attraction and repulsion between the tip's magnetic moment and the magnetized sample.

It should be noted, however, that the interpretation of the magnetic contrast resulting from an MFM scan can be a delicate matter. In fact, many different magnetic configurations can result in the same MFM map, as can be seen in Figure B.2. Knowledge of the magnetic material and the general properties of the sample are useful at this point for better determining the underlying magnetic texture of the scanned surface.

For more details on Magnetic Force Microscopy and related techniques, I encourage the interested reader to consult the Springer Handbook of Nanotechnology[135], which offers a detailed description for the technique and gives additional information one microscope instrumentation.

Appendix C

The Charge Correlator as a Function of Spin Correlations

The nearest-neighbor charge correlator can be written down as a linear combination of the first three spin correlators, $C_{\alpha\beta}$, $C_{\alpha\gamma}$ and $C_{\alpha\nu}$, for both the in-plane and out-of-plane kagome networks. Using the spin unit vectors (see Figure 2.4.a), each vertex charge can be expressed as a sum of the local scalar spin values (σ_i):

$$Q_{\Delta} = \sum_{i \in \Delta} \sigma_i. \quad Q_{\nabla} = -\sum_{i \in \nabla} \sigma_i. \tag{C.1}$$

The validity of the above expressions can be easily verified by taking an "all-in/all-out" kagome spin ice configuration ($\sigma_i = 1, \forall i$). They are also the cornerstone for defining the vertex charges for the kagome Ising network.

A charge correlation pair, $Q_i \cdot Q_{i+1}$, is therefore the product between two such sums, which can further expanded to yield a sum of scalar spin correlation pairs. Figure C.1 presents the general case for a charge correlation pair. In this case, the product between the two sums is therefore:

$$Q_{\Delta} \cdot Q_{\nabla} = -\sum_{i \in \Delta} \sigma_i \cdot \sum_{j \in \nabla} \sigma_j = -(\sigma_1 + \sigma_3 + \sigma_4)(\sigma_0 + \sigma_1 + \sigma_2). \tag{C.2}$$

and by performing the above-mentioned expansion and conveniently rearranging the pairs one can find:

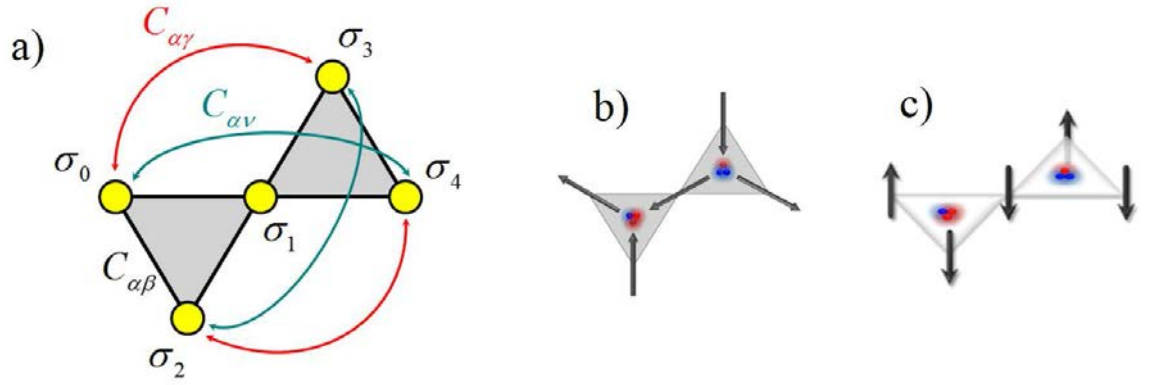

Figure C.1 - (a) Every spin is the connection point between two vertex charges and contributes with a +1 magnetic charge in one triangle and -1 in the other. In the general case, the vertex charges can be found by summing up the spin scalar values per triangle (σ_i). The constituting spins of a charge correlation pair form $\alpha\beta$, $\alpha\gamma$ and $\alpha\nu$ pairs. A (σ_0,σ_1,σ_2,σ_3,σ_4) = $(1,-1,-1,1,-1)$ configuration for the (b) kagome spin ice and the (c) kagome Ising networks.

$$Q_\Delta \cdot Q_\nabla = -(\sigma_1\sigma_1 + \sigma_1\sigma_0 + \sigma_1\sigma_2 + \sigma_1\sigma_3 + \sigma_1\sigma_4 + \sigma_0\sigma_3 + \sigma_2\sigma_4 + \sigma_0\sigma_4 + \sigma_2\sigma_3). \tag{C.3}$$

The first term of the sum is always equal to 1. The following four terms consist of nearest-neighboring $\alpha\beta$ correlations, the sixth and the seventh terms are $\alpha\gamma$ pairs, while the last two terms represent $\alpha\nu$ correlations. We therefore find that the correspondence between a local charge correlation and the correlations between the constituting spin pairs is:

$$(Q_i \cdot Q_{i+1}) = -(1 + 4 \cdot C^l_{\alpha\beta} + 2 \cdot C^l_{\alpha\gamma} + 2 \cdot C^l_{\alpha\nu}). \tag{C.4}$$

The next step is summing up through all charge correlation pairs to retrieve the network averages. Assuming periodic boundary condition, the number of charge pairs, N_{QQ}, is equal to the number of network spins, N_{spins}. Furthermore, the total number of $\alpha\beta$, $\alpha\gamma$ and $\alpha\nu$ pairs is $N_{\alpha\beta} = N_{\alpha\gamma} = N_{\alpha\nu} = 2 \cdot N_{spins}$. During the summation of the charge pairs, every $\alpha\beta$ pair is counted twice, while the $\alpha\gamma$ and $\alpha\nu$ pairs are counted just once. This will yield:

$$\sum_{i=1}^{N_{QQ}} Q_i \cdot Q_{i+1} = -(N_{QQ} + 2 \cdot \sum_{b=1}^{N_{\alpha\beta}} \sigma_b \cdot \sigma_{b+1} + \sum_{g=1}^{N_{\alpha\gamma}} \sigma_g \cdot \sigma_{g+1} + \sum_{n=1}^{N_{\alpha\nu}} \sigma_n \cdot \sigma_{n+1}). \tag{C.5}$$

The network averages of the charge and spin correlators are defined as[1]:

$$Q_iQ_{i+1} = \frac{1}{N_{QQ}} \sum_{i=1}^{N_{QQ}} Q_i \cdot Q_{i+1} = \qquad C_{\alpha\lambda} = \frac{1}{N_{\alpha\lambda}} \sum_{i=1}^{N_{\alpha\lambda}} \sigma_i \cdot \sigma_{i+1} \tag{C.6}$$

By inserting C.6 in C.5 we find:

$$N_{QQ} \cdot Q_iQ_{i+1} = -(N_{QQ} + 2 \cdot N_{\alpha\beta}C_{\alpha\beta} + N_{\alpha\gamma}C_{\alpha\gamma} + N_{\alpha\nu}C_{\alpha\nu}) \tag{C.7}$$

and by dividing the expression with N_{spins} we finally obtain:

$$Q_iQ_{i+1} = -(1 + 4 \cdot C_{\alpha\beta} + 2 \cdot C_{\alpha\gamma} + 2 \cdot C_{\alpha\nu}) \tag{C.8}$$

Note that this expression does not take into account the geometrical factors that arise due to the relative orientation of the spin unit vectors. The kagome Ising system presents only one anisotropy axis, hence all geometrical factors are equal to 1 and the above expression holds. However, the $\alpha\beta$ and $\alpha\gamma$ correlations of the kagome spin ice network present a $-1/2$ geometrical factor. Taking these into account, the expressions for each network type are:

$$(Q_iQ_{i+1})_{ksi} = -1 + 8 \cdot C_{\alpha\beta} + 4 \cdot C_{\alpha\gamma} - 2 \cdot C_{\alpha\nu} \tag{C.9}$$

$$(Q_iQ_{i+1})_{kI} = -1 - 4 \cdot C_{\alpha\beta} - 2 \cdot C_{\alpha\gamma} - 2 \cdot C_{\alpha\nu} \tag{C.10}$$

[1]Note that the summation is performed over all correlation pairs and counts a pair only once. Therefore, the $1/2$ factor is not required as in the spin-index counting case.

Appendix D

The Microscopic Kagome Spin Ice Dipolar Hamiltonian

The general form of the dipolar spin ice Hamiltonian is:

$$H_{DSI} = -\frac{J_1}{2}\sum_{<i,j>}\vec{S}_i\cdot\vec{S}_j + \frac{D}{2}\cdot\sum_{(i\neq j)}[\frac{\vec{S}_i\cdot\vec{S}_j}{r_{ij}^3} - \frac{3\cdot(\vec{S}_i\cdot\vec{r}_{ij})\cdot(\vec{S}_j\cdot\vec{r}_{ij})}{r_{ij}^5}]. \tag{D.1}$$

where $\vec{S}_i$ and $\vec{S}_j$ correspond to a spin pair, $\vec{r}_{ij}$ stands for the relative position vector between the two spins, $D = \frac{\mu_0\cdot\mu^2}{4\pi}$ is the dipolar coupling constant, and J_1 is a nearest-neighbor coupling correction accounting for the deviations from the point-dipole approximation. This expression can be further adapted to the kagome spin ice system by using the spin unit vectors ($\vec{e}_i$) and the spin scalars (σ_i):

$$H_{DSI} = \frac{J_1}{4}\sum_{<i,j>}(\sigma_i\cdot\sigma_j) + \frac{1}{2}\cdot\frac{D}{r_{nn}^3}\cdot\sum_{(i\neq j)}\frac{r_{nn}^3}{r_{ij}^3}\cdot[1-3\cdot\frac{(\vec{e}_i\cdot\vec{e}_r)\cdot(\vec{e}_j\cdot\vec{e}_r)}{(\vec{e}_i\cdot\vec{e}_j)}]\cdot(\vec{e}_i\cdot\vec{e}_j)\cdot(\sigma_i\cdot\sigma_j). \tag{D.2}$$

with r_{nn} being the distance between nearest-neighbors and $\vec{e}_r = \vec{r}_{ij}/r_{ij}$.

The Hamiltonian can also be written down as a linear combination of the spin-spin correlations. This is a rather intuitive way for looking at the overall energetic contribution of each correlation type. Generally speaking, one can write:

$$H_{DSI} = \sum_{\lambda} J_{\alpha\lambda} \cdot N_{\alpha\lambda} \cdot C_{\alpha\lambda}. \tag{D.3}$$

where $J_{\alpha\lambda}$ is the coupling constant between any λ-order pair, $N_{\alpha\lambda}$ is the total number of λ-type pairs and $C_{\alpha\lambda}$ is the network average correlator defined as:

$$C_{\alpha\lambda} = \frac{1}{2N_{\alpha\lambda}} \sum_{(i,j)|\lambda} \vec{S}_i \cdot \vec{S}_j. \tag{D.4}$$

With the exception of the nearest-neighboring case, all coupling constants $J_{\alpha\lambda}$ are defined by the point-dipole approximation. For the sake of clarity and simplicity, I shall avoid carrying along the J_1 sum throughout this deduction and I shall split the dipolar spin ice Hamiltonian in two parts: $H_{DSI} = H^{\mu}_{DSI} + H^{dip}_{DSI}$, where $H^{\mu}_{DSI} = \frac{J_1}{4} \sum_{<i,j>} (\sigma_i \cdot \sigma_j)$ is the micromagnetic correction and H^{dip}_{DSI} is the point-dipole approximation Hamiltonian for all spin pairs. For all pairs beyond nearest-neighbors we have $J_{\alpha\lambda} = J^{dip}_{\alpha\lambda}$, while for the particular case of $C_{\alpha\beta}$ we have $J_{\alpha\beta} = -J_1 + J^{dip}_{\alpha\beta}$.

By identifying D.3 with the second sum of D.2, we can determine the expressions of the dipolar coupling constants:

$$J^{dip}_{\alpha\lambda} = D_{eff} \cdot R_{\alpha\lambda} \cdot G_{\alpha\lambda}. \tag{D.5}$$

where $D_{eff} = D/r^3_{nn}$. The other two constants are specific to each correlation type. $R_{\alpha\lambda}$ is a relative distance ratio, while $G_{\alpha\lambda}$ is a network geometrical factor associated to the relative position between the spin vectors of a considered correlation pair. Although the latter might seem to depend on the chosen pair, it proves to be a universal constant within a correlation class. The definitions of these two quantities are:

$$R_{\alpha\lambda} = \frac{r^3_{nn}}{r^3_{\alpha\lambda}} \quad G_{\alpha\lambda} = [1 - 3 \cdot \frac{(\vec{e_\alpha} \cdot \vec{e}_r) \cdot (\vec{e_\lambda} \cdot \vec{e}_r)}{(\vec{e_\alpha} \cdot \vec{e_\lambda})}]. \tag{D.6}$$

and their values for the first seven spin correlators of the kagome spin ice network are given in Table D.1, along with the relative strengths of each coupling constant with respect to the nearest-neighboring dipolar one.

Table D.1 - Spin correlation coupling strengths and related constants for dipolar kagome spin ice

Correlation	$r_{\alpha\lambda}$	$R_{\alpha\lambda}$	$G_{\alpha\lambda}$	$g_{\alpha\lambda}$	$J^{dip}_{\alpha\lambda}/J^{dip}_{\alpha\beta}$
$C_{\alpha\beta}$	$1/2\cdot l$	1	$-7/2$	$-1/2$	1
$C_{\alpha\gamma}$	$\sqrt{3}/2\cdot l$	$1/(3\sqrt{3})$	$5/2$	$-1/2$	$-10/(21\sqrt{3})$
$C_{\alpha\nu}$	l	$1/8$	$-5/4$	1	$5/112$
$C_{\alpha\delta}$	l	$1/8$	1	1	$-1/28$
$C_{\alpha\tau}$	$\sqrt{7}/2\cdot l$	$1/(7\sqrt{7})$	$-13/14$	$-1/2$	$13/(343\sqrt{7})$
$C_{\alpha\eta}$	$3/2\cdot l$	$1/27$	$-7/2$	$-1/2$	$1/27$
$C_{\alpha\varphi}$	$\sqrt{3}\cdot l$	$1/(24\sqrt{3})$	-2	1	$1/(42\sqrt{3})$

As expected, the relative coupling strength ratio ($J^{dip}_{\alpha\lambda}/J^{dip}_{\alpha\beta}$) decreases rapidly as the correlation order increases and it thus contributes less and less to the system energy. Figure D.1 gives the energy sampled throughout a Monte Carlo simulation[1] along with the energy computed using (D.3) and the temperature-evolution of the spin correlations from $C_{\alpha\beta}$ to $C_{\alpha\varphi}$. The two plots match very well, but the importance of higher order correlations in selecting certain configurations from others should not be underestimated, especially at low temperatures.

The exotic spin ice II phase of kagome spin ice motivates a description of the energy behavior by making the magnetic charges directly appear in the dipolar spin ice Hamiltonian. This can be done by using the dumbbell picture proposed by Castelnovo *et al.* for Ising pyrochlore spin ices, but it will limit the evolution to the spin ice II manifold, leaving the ground-state order inaccessible. However, given the relation between the nearest-neighbor charge correlator (Q_iQ_{i+1}) and the first three spin correlations, $C_{\alpha\beta}$, $C_{\alpha\gamma}$ and $C_{\alpha\nu}$, a nearest-neighboring charge coupling term can be made to appear in the Hamiltonian, accounting for the system's desire for charge order. I shall present this procedure in detail in the following paragraphs.

The nearest-neighbor charge correlator can be written as:

$$Q_iQ_{i+1} = -1 + 8\cdot C_{\alpha\beta} + 4\cdot C_{\alpha\gamma} - 2\cdot C_{\alpha\nu}. \tag{D.7}$$

all variables corresponding to network averages. This can be more conveniently reshaped into a more compact form by using the correlator defined by scalar spin values and dropping

[1] All data plotted here correspond to simulations performed on a (12×12) kagome lattice with periodic boundary conditions using single spin-flip and loop-flip dynamics and a cut-off radius of 5.0 lattice parameters.

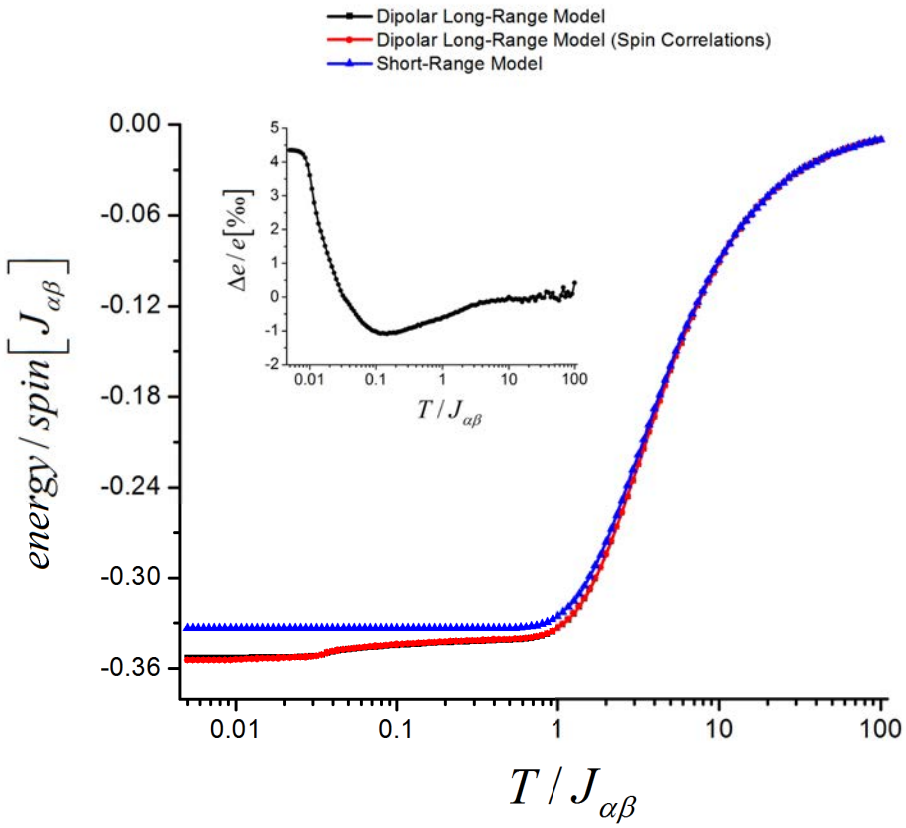

Figure D.1 - The energy of the kagome spin ice network can also be estimated by using the spin correlators and the relative coupling strengths. Using the Monte Carlo data for $C_{\alpha\beta}$ and up to $C_{\alpha\varphi}$ a very good agreement between the correlation computed energy (red line) and the directly sampled one (black line) can be found. The inset gives the relative error for this approach. While it is always less than 0.5% in absolute value, it increases as the temperature drops, signaling the importance of even higher order contributions. The short-range energy is also given for comparison(blue line).

the geometrical factors $g_{\alpha\lambda} = (\vec{e}_i \cdot \vec{e}_j)$. Hence, we have:

$$Q_i Q_{i+1} = -(1 + 4 \cdot \widetilde{C_{\alpha\beta}} + 2 \cdot \widetilde{C_{\alpha\gamma}} + 2 \cdot \widetilde{C_{\alpha\nu}}). \tag{D.8}$$

where

$$\widetilde{C_{\alpha\lambda}} = \frac{1}{2N_{\alpha\lambda}} \sum_{(i,j)|\lambda} \sigma_i \cdot \sigma_j = g_{\alpha\lambda} \cdot C_{\alpha\lambda}. \tag{D.9}$$

Using the spin scalar correlations, the Hamiltonian of D.3 becomes:

$$H_{DSI} = \sum_{\lambda} \widetilde{J_{\alpha\lambda}} \cdot N_{\alpha\lambda} \cdot \widetilde{C_{\alpha\lambda}}. \tag{D.10}$$

where $\widetilde{J_{\alpha\lambda}} = J_{\alpha\lambda} \cdot g_{\alpha\lambda}$, absorbing the geometrical factors. Expanding the expression up to $C_{\alpha\nu}$ we get:

$$H_{DSI} = \widetilde{J_{\alpha\beta}} \cdot N_{\alpha\beta} \cdot \widetilde{C_{\alpha\beta}} + \widetilde{J_{\alpha\gamma}} \cdot N_{\alpha\gamma} \cdot \widetilde{C_{\alpha\gamma}} + \widetilde{J_{\alpha\nu}} \cdot N_{\alpha\nu} \cdot \widetilde{C_{\alpha\nu}} + O(1/r^3)_{r \geq 2r_{nn}}. \tag{D.11}$$

and we can further bring it to an dimensionless form by dividing with the nearest-neighbor dipolar coupling constant ($\widetilde{J_{\alpha\beta}}$):

$$H_{DSI}/\widetilde{J^{dip}_{\alpha\beta}} = (1 + f_\mu) \cdot N_{\alpha\beta} \cdot \widetilde{C_{\alpha\beta}} + f_\gamma \cdot N_{\alpha\gamma} \cdot \widetilde{C_{\alpha\gamma}} + f_\nu \cdot N_{\alpha\nu} \cdot \widetilde{C_{\alpha\nu}} + O(1/r^3)_{r \geq 2r_{nn}}. \tag{D.12}$$

with $f_{\alpha\lambda} = \widetilde{J^{dip}_{\alpha\lambda}}/\widetilde{J^{dip}_{\alpha\beta}}$ as the relative ratio between the scalar-spin coupling constants and $f_\mu = -\widetilde{J_1}/\widetilde{J^{dip}_{\alpha\beta}}$. To further simplify the expression, we consider the case of a periodic lattice in which every spin has the same number of correlation pairs. Since there are 4 pairs/spin for $\alpha\beta$, $\alpha\gamma$ and $\alpha\nu$, we have:

$$N_{\alpha\beta} = N_{\alpha\gamma} = N_{\alpha\nu} = 4 \cdot N_{spins}/2 = 2 \cdot N_{spins}. \tag{D.13}$$

where the $1/2$ factor is taken to avoid counting the same pair twice. Since we are finally interested in introducing the nearest-neighbor charge correlator within, the number of charge correlation pairs has to be determined too. There are $N_\nabla = N_\Delta = N_{spins}/3$ ∇-type and Δ-type triangles in the lattice and each one carries a network charge. Therefore, $N_{charges} = 2 \cdot N_{spins}/3$

and since each charge has three nearest-neighbors, we find that:

$$N_{QQ} = 3 \cdot N_{charges}/2 = 3/2 \cdot 2/3 \cdot N_{spins} = N_{spins}. \tag{D.14}$$

Coming back to expression D.12 we have:

$$H_{DSI}/\widetilde{J^{dip}_{\alpha\beta}} = N_{spins}[(1+f_\mu)\cdot 2\cdot \widetilde{C_{\alpha\beta}} + 2\cdot f_\gamma \cdot \widetilde{C_{\alpha\gamma}} + 2\cdot f_\nu \cdot \widetilde{C_{\alpha\nu}}] + O(1/r^3)_{r\geq 2r_{nn}}. \tag{D.15}$$

and we can introduce and extract some terms to make expression D.8 appear. The idea is to leave to the pending term only pairs which are separated by a distance of $2r_n n$ or higher. Therefore, we shall artificially introduce f_γ in every term to keep the first and second order contributions. We therefore have:

$$H_{DSI}/\widetilde{J^{dip}_{\alpha\beta}} = N_{spins}[f_\gamma - f_\gamma + (1+f_\mu+2f_\gamma-2f_\gamma)\cdot 2\widetilde{C_{\alpha\beta}} + 2f_\gamma\widetilde{C_{\alpha\gamma}} + f_\nu(1+f_\gamma/f_\nu - f_\gamma/f_\nu)\cdot 2\widetilde{C_{\alpha\nu}}] + O(1/r \tag{D.16}$$

Rearranging the terms and using the fact that $N_{QQ} = N_{spins}$ we get:

$$H_{DSI}/\widetilde{J^{dip}_{\alpha\beta}} = N_{\alpha\beta}\cdot(1+f_\mu-2f_\gamma)\cdot\widetilde{C_{\alpha\beta}} - N_{QQ}\cdot f_\gamma\cdot[-1-4\widetilde{C_{\alpha\beta}} - 2\widetilde{C_{\alpha\gamma}} - 2\widetilde{C_{\alpha\nu}}] + O(1/r^3)_{r\geq 2r_{nn}}. \tag{D.17}$$

where $O(1/r^3)_{r\geq 2r_{nn}}$ has absorbed the remaining contributions of $C_{\alpha\nu}$ and the constant term $-f_\gamma$. Using D.8 we find:

$$H_{DSI}/\widetilde{J^{dip}_{\alpha\beta}} = N_{\alpha\beta}\cdot(1+f_\mu-2f_\gamma)\cdot\widetilde{C_{\alpha\beta}} - N_{QQ}\cdot f_\gamma\cdot Q_i Q_{i+1} + O(1/r^3)_{r\geq 2r_{nn}}. \tag{D.18}$$

or, writing it down with sums over spin pairs and charge pairs:

$$H_{DSI}/\widetilde{J^{dip}_{\alpha\beta}} = \frac{1+f_\mu-2f_\gamma}{2}\sum_{<i,j>}\sigma_i\cdot\sigma_j - \frac{f_\gamma}{2}\sum_{<u,v>}Q_u\cdot Q_v + O(1/r^3)_{r\geq 2r_{nn}}. \tag{D.19}$$

where $f_\gamma = (J^{dip}_{\alpha\gamma}\cdot g_{\alpha\gamma})/(J^{dip}_{\alpha\beta}\cdot g_{\alpha\beta}) = -10/(21\sqrt{3})$ and $\widetilde{J^{dip}_{\alpha\beta}} = (7/4)D_{eff}$. This will finally yield:

$$H_{DSI} = \frac{\overline{J_{\alpha\beta}}}{2}\sum_{<i,j>}\sigma_i\cdot\sigma_j + \frac{\overline{J_{QQ}}}{2}\sum_{<u,v>}Q_u\cdot Q_v + O(1/r^3)_{r\geq 2r_{nn}}. \tag{D.20}$$

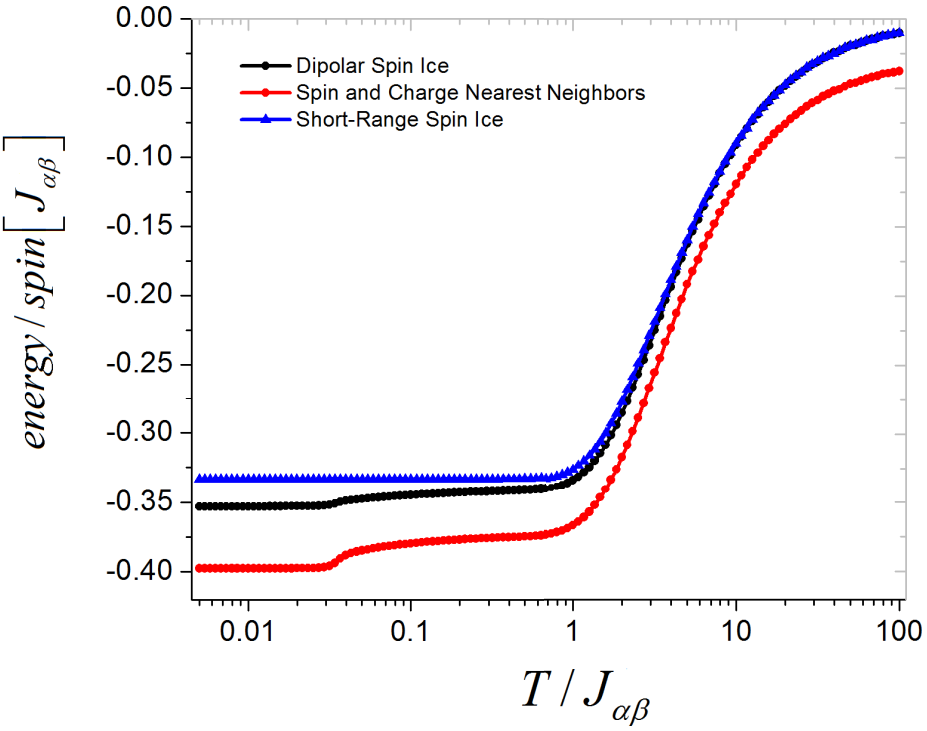

Figure D.2 - The dipolar spin ice energy (black) along with the energy given by taking only the first two terms of D.20 and leaving aside the high order contributions. The red line has two clear drops, the first one leading the spin ice manifold, and the second one to the quasi-spin ice II manifold. As expected, the remaining terms become more and more important as the temperature is decreased and they smoothly lead the system into its final ordered state. The short-range model energy is also given for comparison (blue line).

with $\overline{J_{\alpha\beta}} = -J_1/2 + D_{eff} \cdot (7/4 + 5\sqrt{3}/9)$ and $\overline{J_{QQ}} = 5\sqrt{3}/18 \cdot D_{eff}$. Since the two coupling constants are positive they signal a ferromagnetic coupling between the nearest neighboring spins (recall that there is a geometrical factor of $-1/2$ for $\alpha\beta$ pairs) and an antiferromagnetic coupling between the nearest neighboring vertex charges.

This Hamiltonian composed of both spins and charges captures the essence of kagome spin ice behavior in the dipolar spin ice model. Since $\overline{J_{\alpha\beta}} > \overline{J_{QQ}}$, the minimization of the scalar spin sum is the system's first priority and yields the spin ice manifold. Moving on to the charge pair sum, its minimization requires the creation of a charge crystal, apparently leading to the spin ice II state. The remaining contributions come form all spin pairs separated by a distance of $r_{ij} \geq 2 \cdot r_{nn}$[2] and are of great importance for energetically filtering charge ordered states (see Figure D.2) and eventually select the ground state configuration.

[2]It is important to remind that the $C_{\alpha v}$ contribution is only partially included here.

Notice that a charge crystal can be easily obtained by saturating the network, but this does not correspond to a true spin ice II state with preferential spin-loop configurations. At low temperatures, such a configuration is ruled out by these remaining terms. Cutting them off will eventually lead to a charge crystal phase, but this manifold will include more states than the true spin ice II one and is expected to have a slightly higher entropy/spin.

Appendix E

Experimental Images for Demagnetized Artificial Kagome Ising Networks

The set of 10 MFM images from which the correlation data was extracted after demagnetizing the artificial kagome Ising networks are reported in this appendix. Each dot corresponds to a nanomagnet with an average diameter of 300nm and each image is reproduced with its corresponding index number. The associated correlation data is reported in Table 3.3. There are a few remarks that need to made.

The first four images are given in grayscale. The reason behind this is purely technical and the editing was done to help the MATHEMATICA recognition program better identify the "up" and "down" states of each element. However, we noticed this is not required as it manages equally well with the default gold-color palette of the MFM software.

Some of the images can contain large areas for which the spin states cannot be identified due to contamination and, in some cases, there are areas for which the spins are actually missing, possibly detached from the network during fabrication. Nevertheless, large uncontaminated areas are still accessible and the reconstruction code manages to capture the spin arrangements quite well, yielding a good statistical ensemble for the evaluation of the spin correlators.

In some cases the images are, in fact, reconstructions from even smaller images that were afterwards grouped together. Although scanning smaller areas increases the total probing time, it can yield a better spatial resolution and the quality of the magnetic contrast is also improved. However, gluing them together can prove to be a rather challenging task, and the borders are not always straight since editing the figures requires shearing and rescaling to ensure the continuity of the network, thus resulting in irregular border shapes.

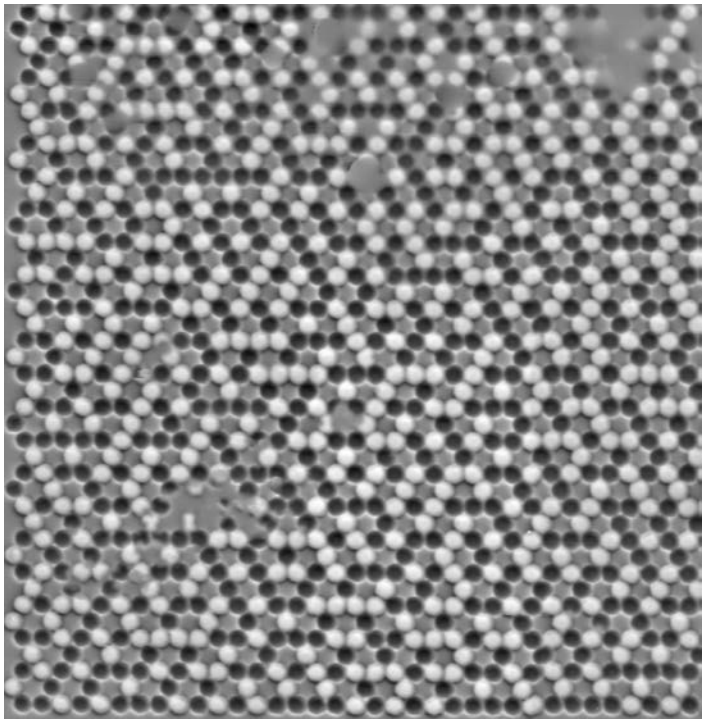

Figure E.1 Artificial Kagome Ising - MFM Image 1

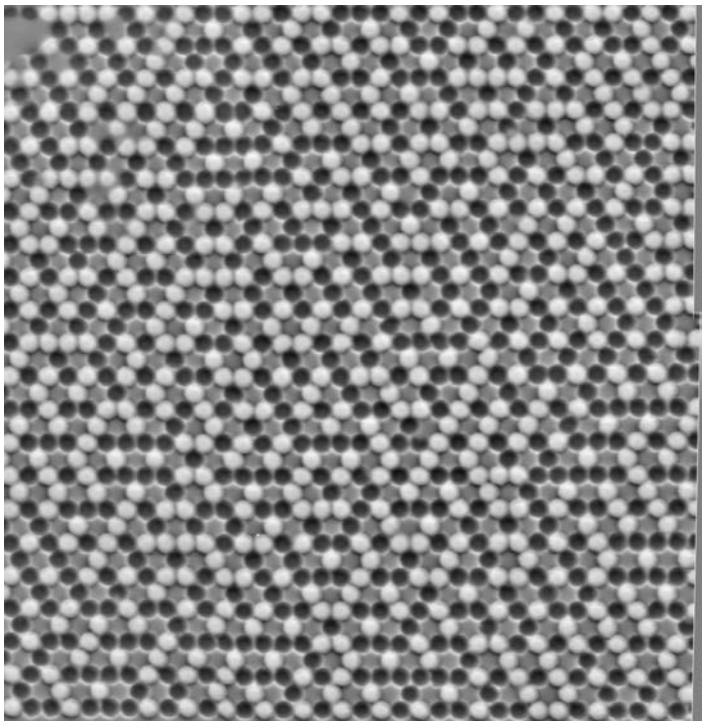

Figure E.2 Artificial Kagome Ising - MFM Image 2

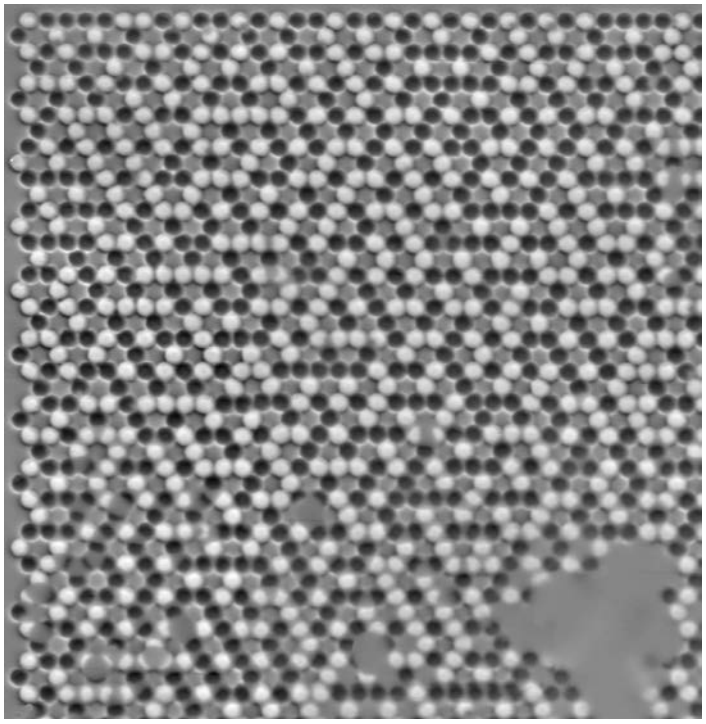

Figure E.3 Artificial Kagome Ising - MFM Image 3

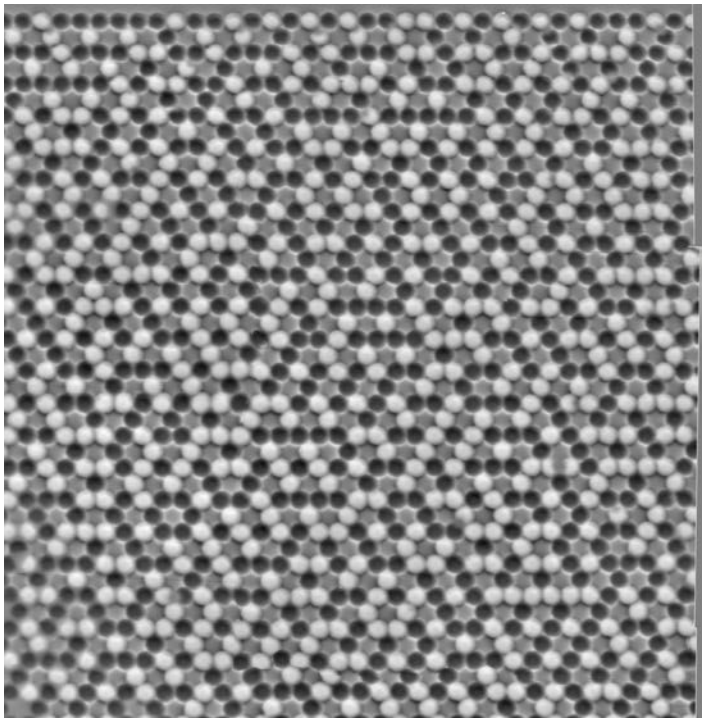

Figure E.4 Artificial Kagome Ising - MFM Image 4

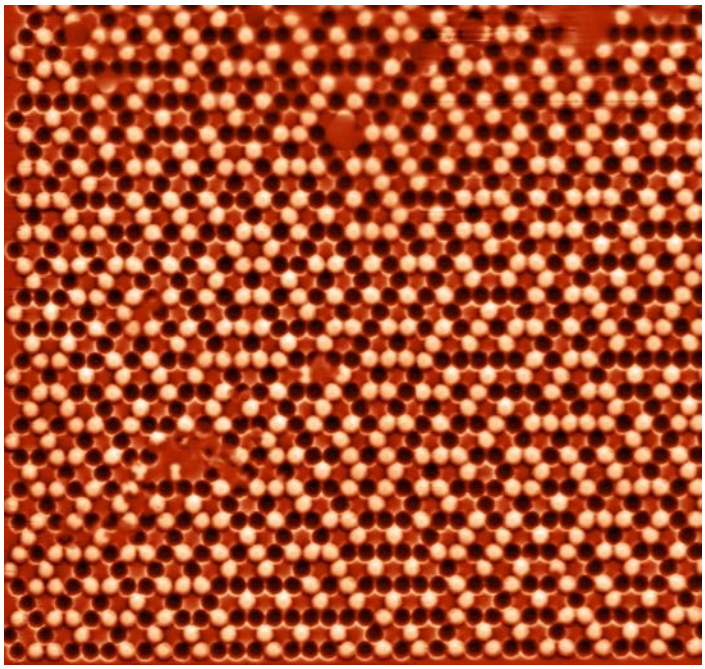

Figure E.5 Artificial Kagome Ising - MFM Image 5

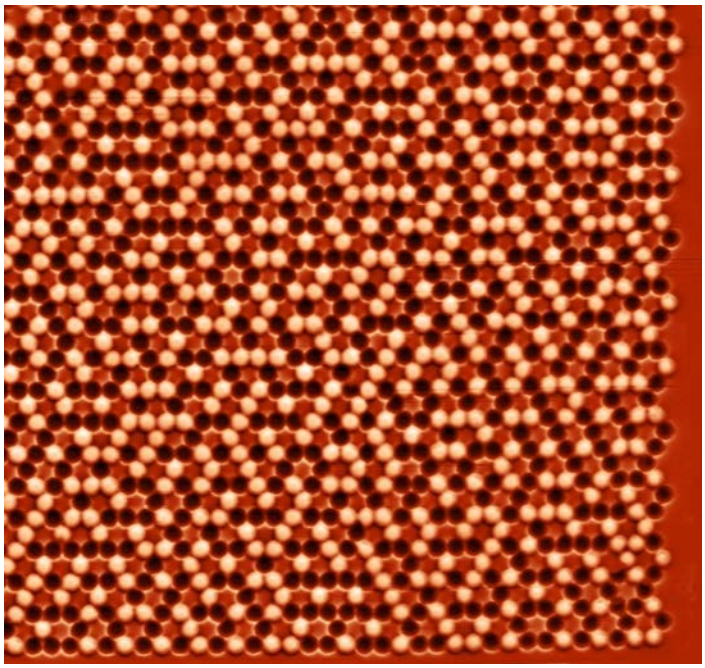

Figure E.6 Artificial Kagome Ising - MFM Image 6

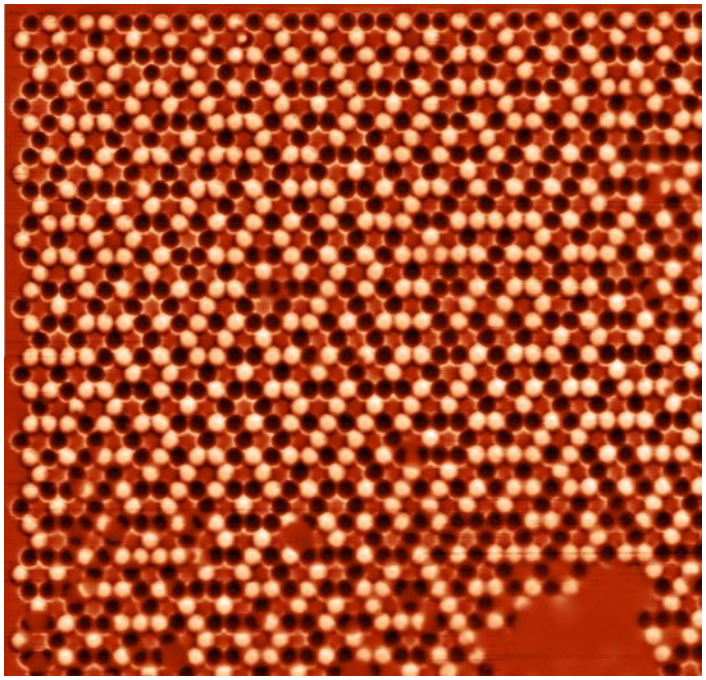

Figure E.7 Artificial Kagome Ising - MFM Image 7

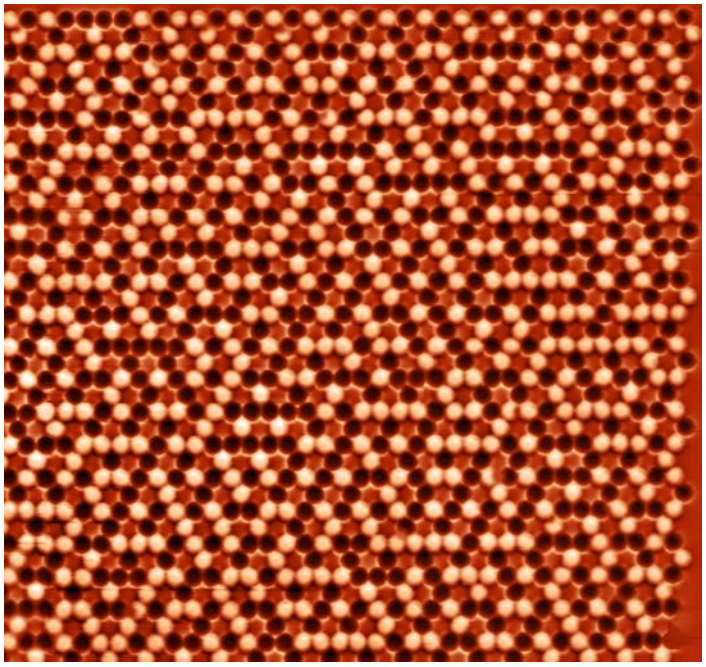

Figure E.8 Artificial Kagome Ising - MFM Image 8

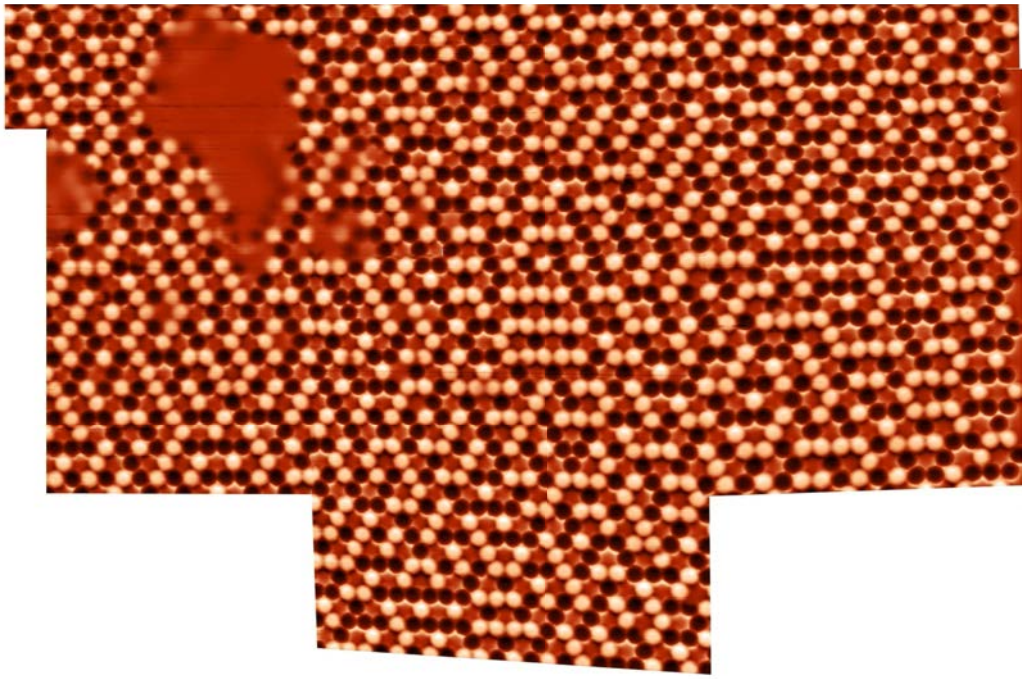

Figure E.9 Artificial Kagome Ising - MFM Image 9

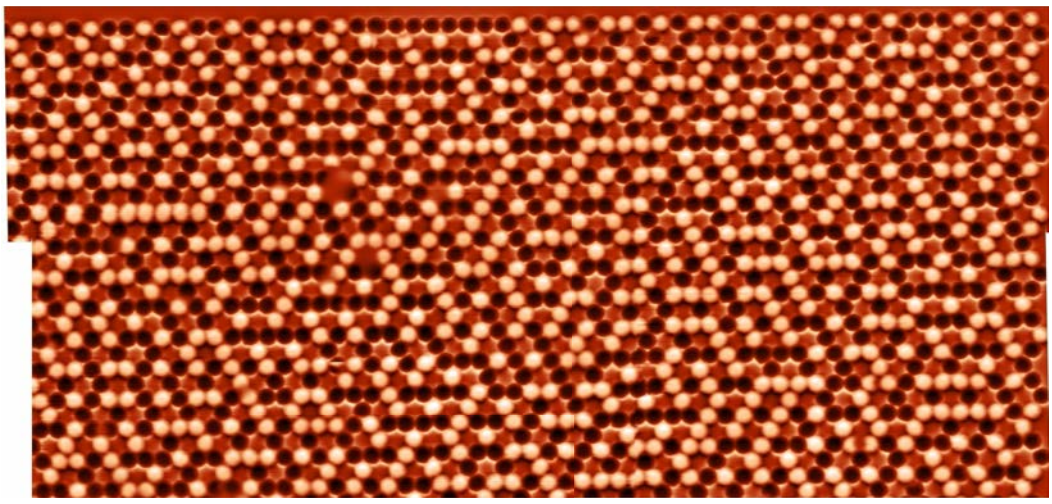

Figure E.10 Artificial Kagome Ising - MFM Image 10

Appendix F

Switching Field Distribution for the Artificial Kagome Ising Arrays

To obtain information about the saturation field and the distribution of the island switching fields, a series of MFM scans were performed with the help of a retrofitted MFM setup that can support measurements under applied magnetic field. In short, an electromagnetic coil that generates the field is situated underneath a adapted MFM specimen stage and it can provide vertical applied fields up to 1.2 T.

The experimental protocol involves saturating the networks along the vertical axis, bringing the field back to zero, and then gradually increasing the field in the opposite direction by a preset step. After each step, a scan is performed, but this needs to be done is zero field to avoid triggering island reversals by the passing of the tip. Otherwise said, if imaging is performed while the field is still applied, some islands may find themselves very close to their intrinsic switching point, and it takes only a small perturbation to cause their magnetization reversal. This perturbation is given by the stray field of the magnetic moment of the tip, and it can trigger several reversals that significantly alter the magnetic configuration of the network, thus compromising the field swipe data. Since islands cannot be switched in the original saturation direction by bringing the field back to zero, the solution is to do this return-to-zero-field after each step and then do the probing.

A region of the sample containing about 236 nanomagnets of 300nm diameter each has been scanned for different field values. The coil was calibrated during the same measurement session. The first image gives the magnetic configuration as it was prior to starting the sweep in the field's positive direction. This state was obtained by saturating the network in a field of $B \cong -800mT$. The next image corresponds to an applied field of $34mT$ and would indicate that all islands have flipped while the field was increased between $0mT$ and $34mT$. However, this is not the case, as it is the magnetic moment of the tip that has reversed and not the

islands. The sign of the interaction between the tip and the sample has therefore changed, thus yielding the opposite magnetic contrast. Further increasing the field would result in islands reversing to align with the external field. As discussed in section 3.2.2, this reversal is conditioned by the intrinsic switching field, the applied field and the local field created by neighboring islands:

$$-\sigma_i \cdot (H_0 + H^i_{local}) \geqslant H^i_{SF} \tag{F.1}$$

where σ_i is the spin scalar value, while H^i_0 and H^i_{local} are the projection of the applied and local effective fields along the vertical axis.

It is also important to mention that some additional scans were performed during a second field sweep to better sample the region where the hysteresis loop has the largest slope. This corresponds to images indexed by 5, 7, 9 and 11. All images are reproduced along with the applied field value.

The images display the first reversed islands for an applied field of $B = 66mT$, which means that these islands have flipped for an applied field value between 34mT and 66mT. However, recall that, for a reversal to be triggered, the local effective field has to match the intrinsic switching field. In this case, all islands are pointing in the same direction, and the local field created by the dipolar coupling between the elements is at maximum. As presented in section 3.2.1, this value is about $23mT$, which needs to be added to the value of the applied field to get an estimate for the lowest values of the switching field distribution. The same procedure can be applied for the last flipped islands, but in this case the value has to be extracted from the applied field. The region is fully saturated for an applied field value of $B \cong 301mT$. This means that the highest values of the switching field distribution are roughly $\mu_0 H_{SF} \cong 278mT$.

Figure F.16.a gives the histogram of the applied field distributions for which a the islands have switched along with a Gaussian fit. Interestingly, the distribution appears to present two peaks, a fact that might be due to some local defects. Performing scans on larger areas might overcome this effect while it can also improve the statistical accuracy of the experimental data[1]. The distribution of the switching fields appears to be quite broad, signaling the presence

[1]The reason why such a relatively small area was scanned is mainly due to contamination issues or to the randomness in island heights. MFM measurements are very delicate and an abrupt change in the height of the sample surface can destroy the tip, particularly if the scanning frequency is relatively high. Ideally, a larger sample area should be scanned as the tip moves slowly over the surface, but this would increase the measurement time significantly. Since the initial goal of these experiments was to determine roughly the minimum and the maximum value of the external field for which the first and last islands switch, thus giving us an idea about the switching field distribution, a small area has been chosen where there are no contaminating

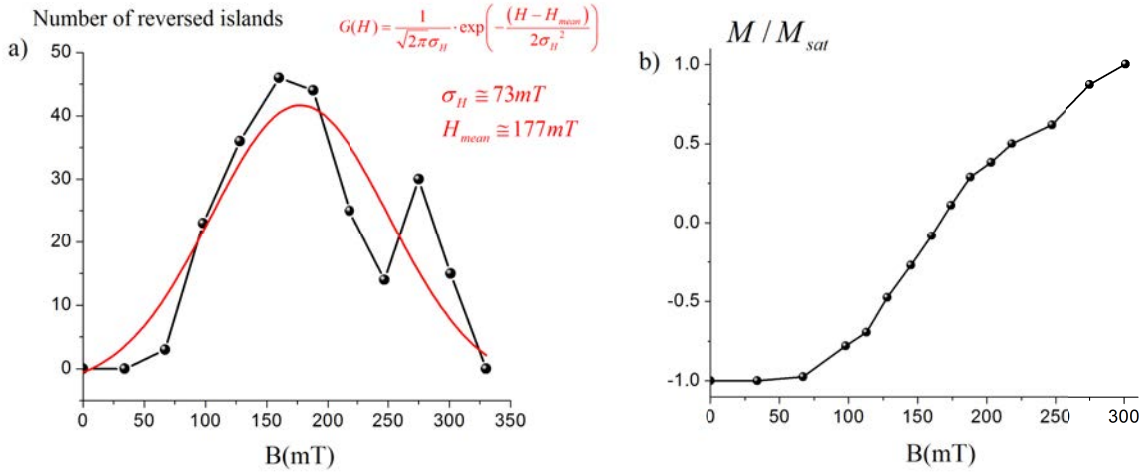

Figure F.1 - The applied field distribution for the switching field window extracted from a region of the artificial kagome Ising sample used. The distribution follows quite roughly a Gaussian, but presents two peaks, probably due to some local defects and the relatively poor statistical accuracy. Nevertheless, a Gaussian fit yields a network coercive field of about $B_C^G \cong 177mT$ and a standard deviation of the distribution $\sigma_{SF}^G \cong 73mT$. Indeed, the reconstruction of this hysteresis loop branch reveals that the coercive field is about $B_C \cong 167mT$, which is roughly in accord with the Gaussian estimation. The broad dispersion of the switching field values might very well be the reason why these artificial dipolar kagome Ising networks have difficulty in developing further long-range order correlations and prevents them from accessing lower energy manifolds.

of a strong disorder. This may very well be the reason why demagnetization does not manage to access lower effective temperatures, as disorder-induced-switching dominates over the reversals triggered solely by the inter-island magnetostatic couplings. Figure F.16.b gives a branch of the hysteresis loop for this scanned area. The region has an average magnetization of 0 for an applied field of $B_c \cong 167mT$, which thus plays the role of a coercive field. The data is yet to be further analyzed and compared to simulated hysteresis loops of a dipolar kagome Ising network with different degrees of switching field disorder.

agents and no abrupt changes in height. This has also encouraged the sampling of several applied field values. These results appear to be quite encouraging, and similar measurements on a larger area might be undertaken in the future.

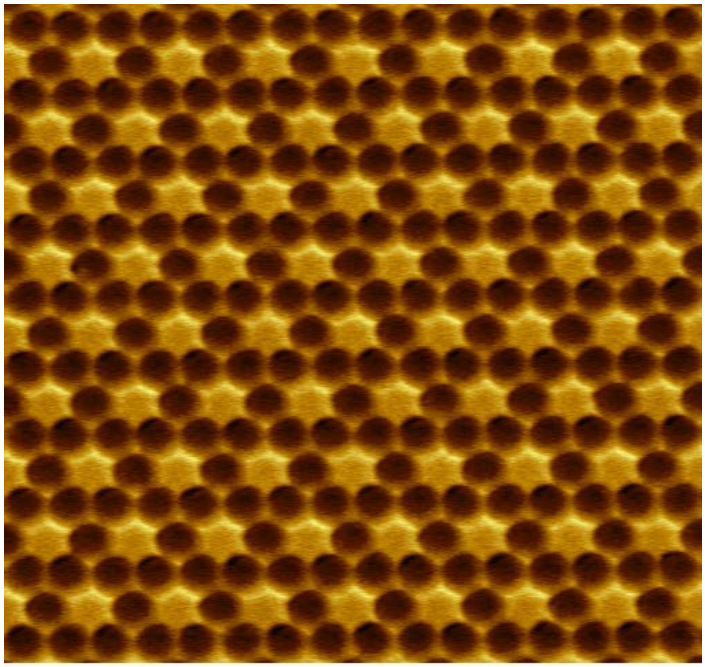

B = 0mT

Figure F.2 Artificial Kagome Ising under applied field - Image 1 - Network saturated in the opposite direction.

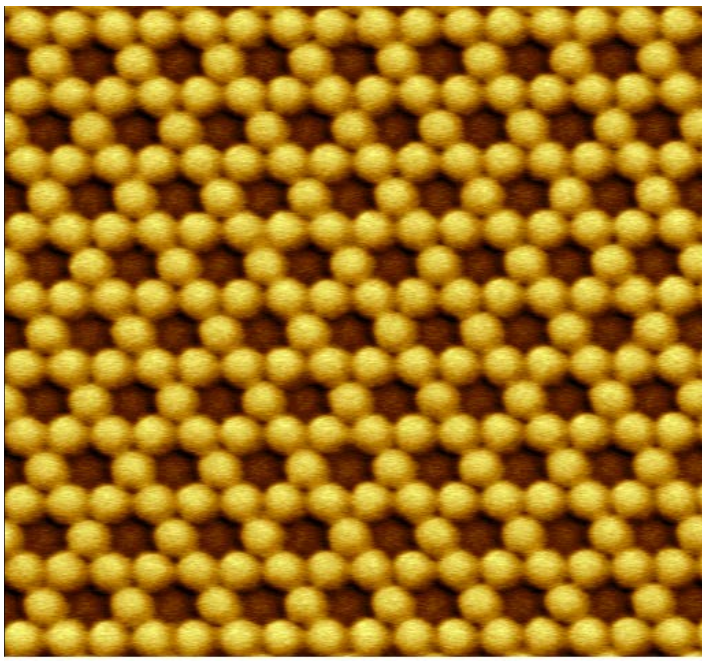

B = 34mT

Figure F.3 Artificial Kagome Ising under applied field - Image 2 - The magnetic moment of the tip has switched!

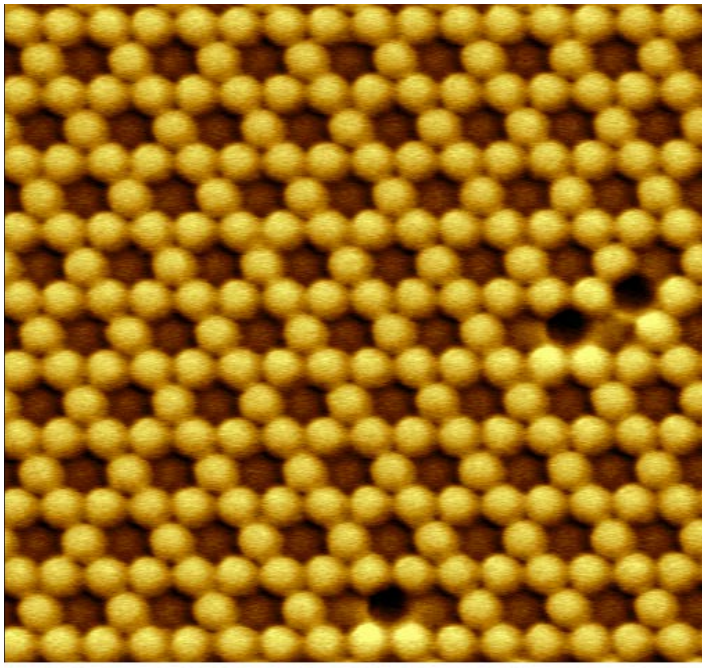

Figure F.4 Artificial Kagome Ising under applied field - Image 3

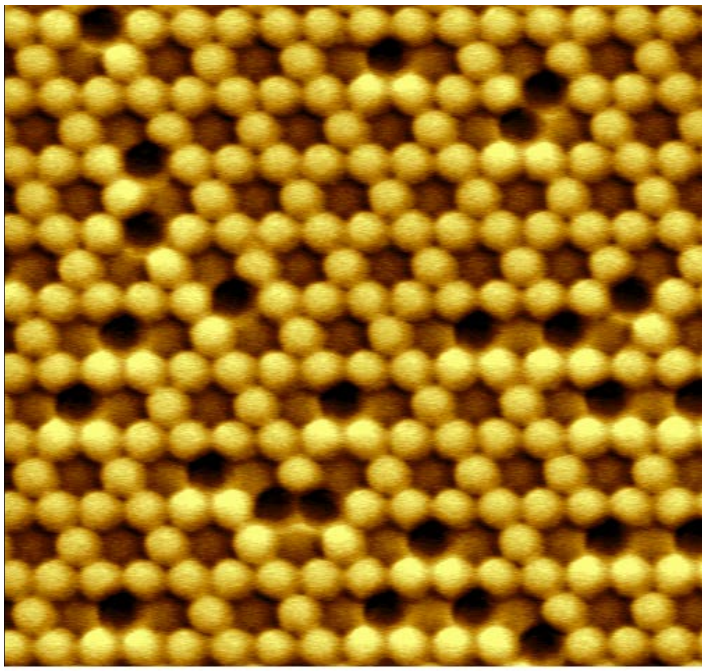

Figure F.5 Artificial Kagome Ising under applied field - Image 4

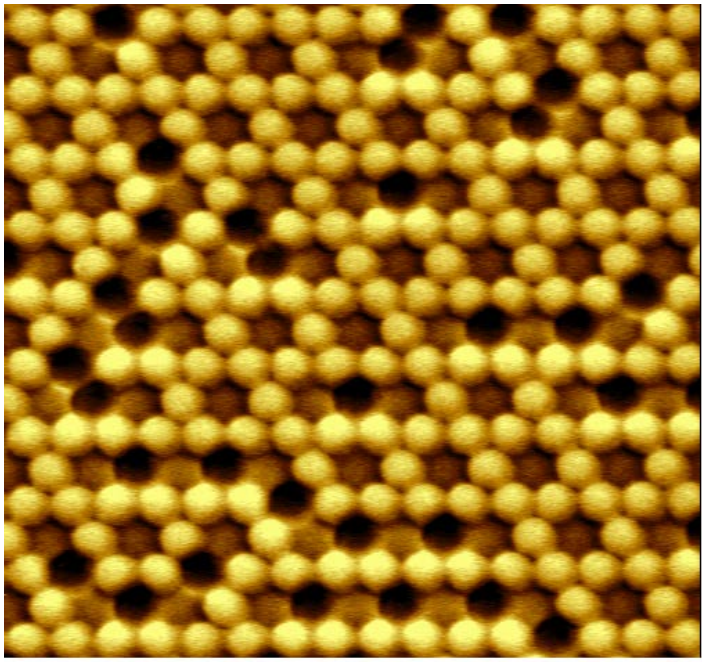

Figure F.6 Artificial Kagome Ising under applied field - Image 5

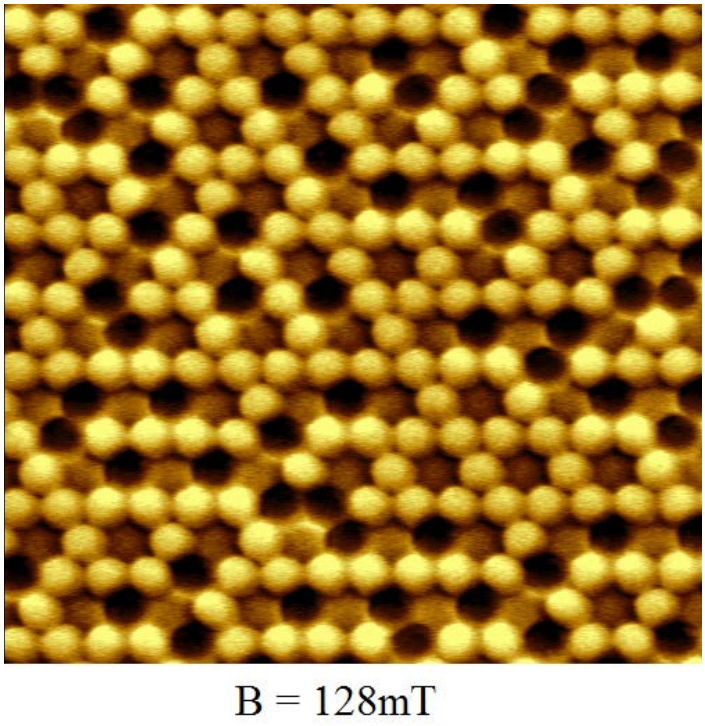

Figure F.7 Artificial Kagome Ising under applied field - Image 6

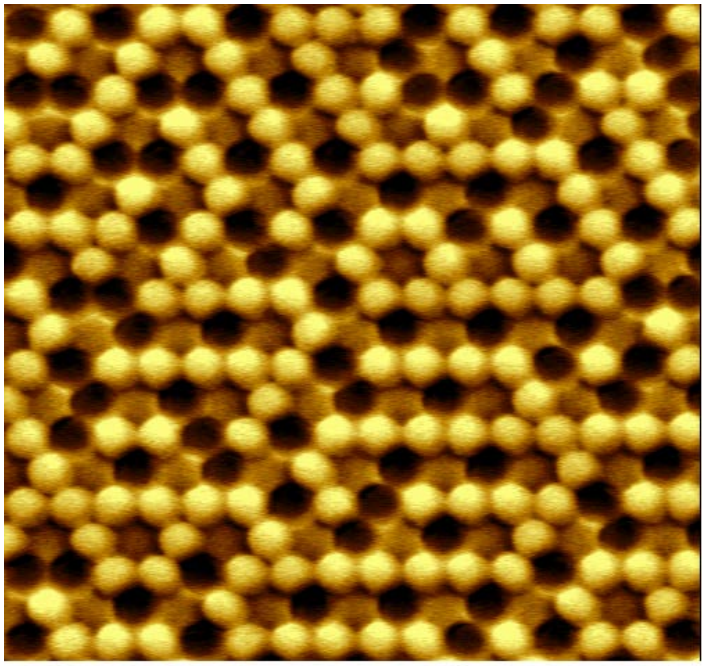

B = 145mT

Figure F.8 Artificial Kagome Ising under applied field - Image 7

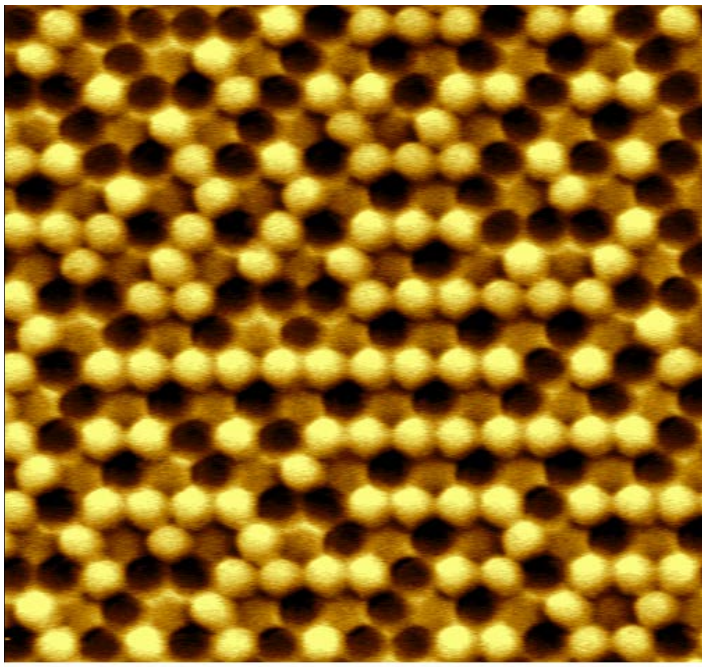

B = 160mT

Figure F.9 Artificial Kagome Ising under applied field - Image 8

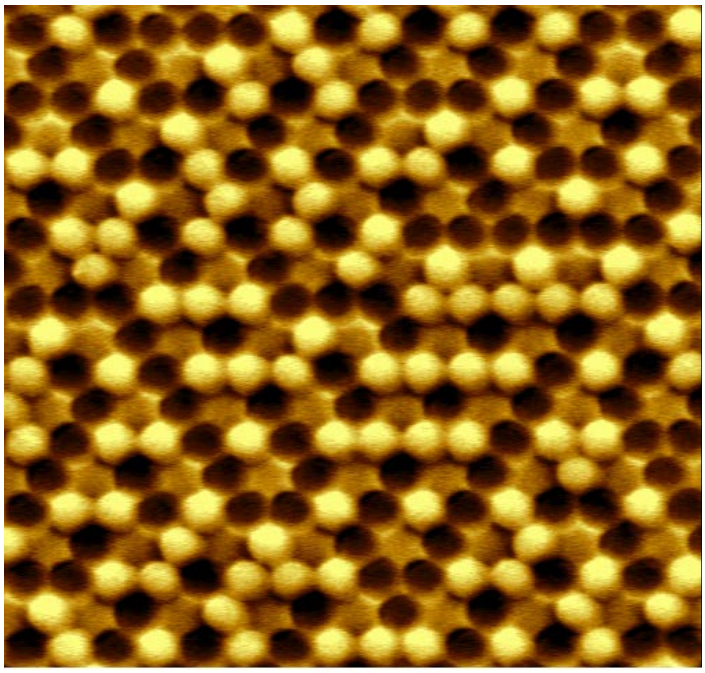

Figure F.10 Artificial Kagome Ising under applied field - Image 9

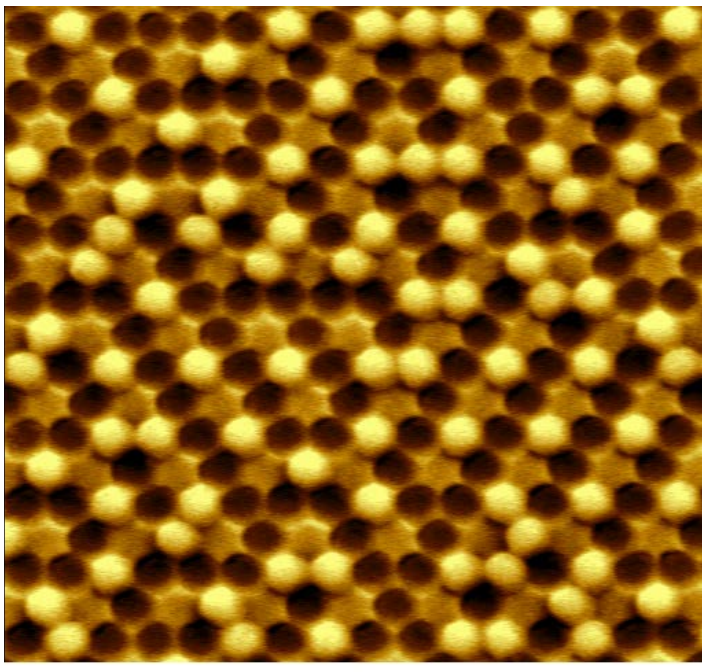

Figure F.11 Artificial Kagome Ising under applied field - Image 10

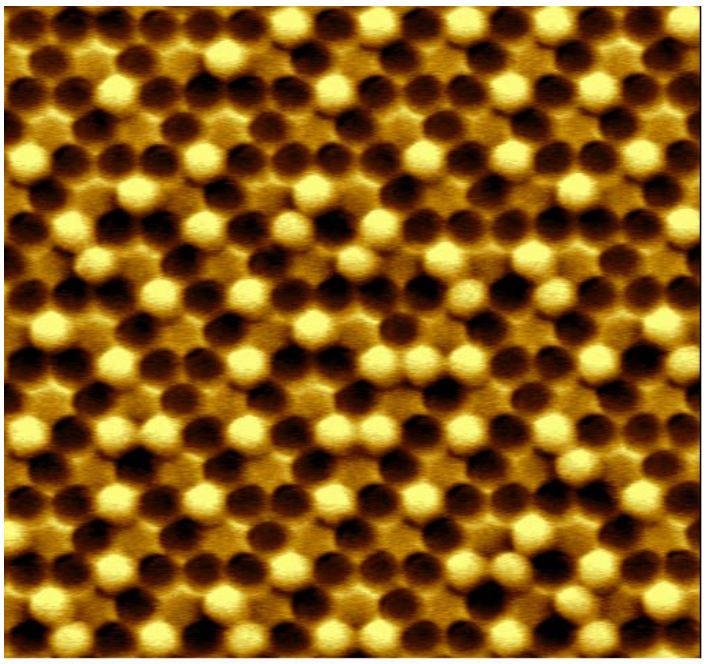

B = 203mT

Figure F.12 Artificial Kagome Ising under applied field - Image 11

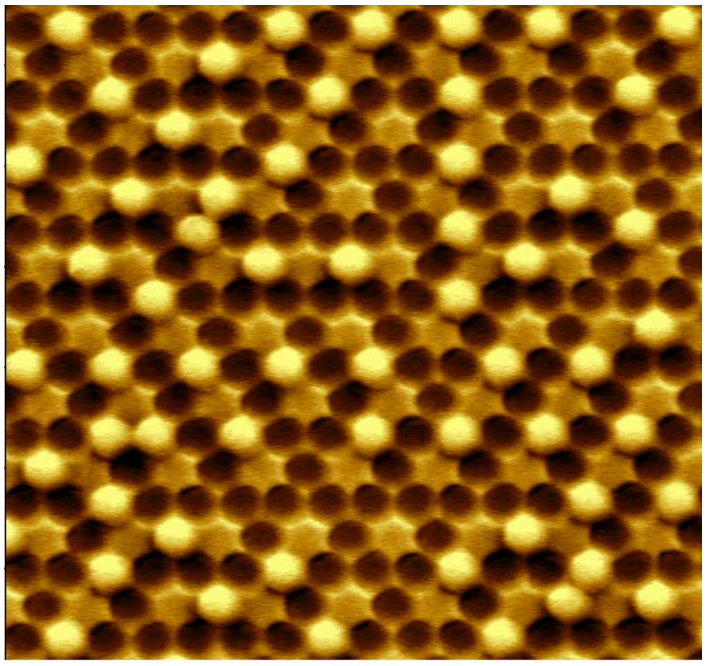

B = 218mT

Figure F.13 Artificial Kagome Ising under applied field - Image 12

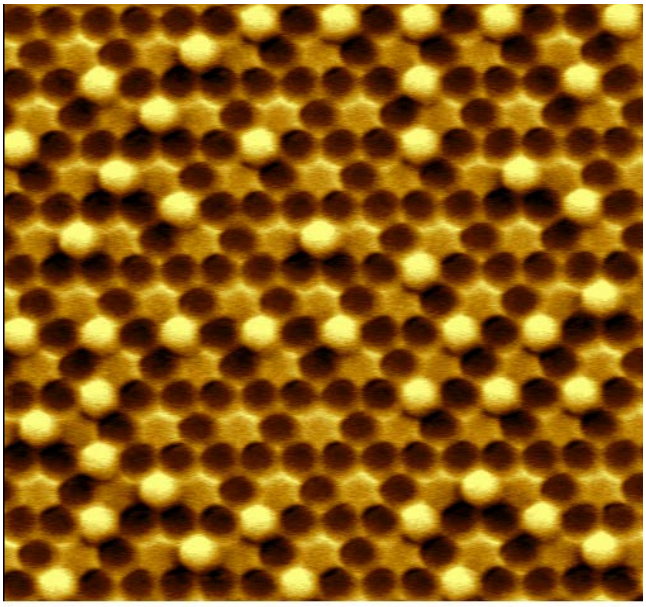

B = 247mT

Figure F.14 Artificial Kagome Ising under applied field - Image 13

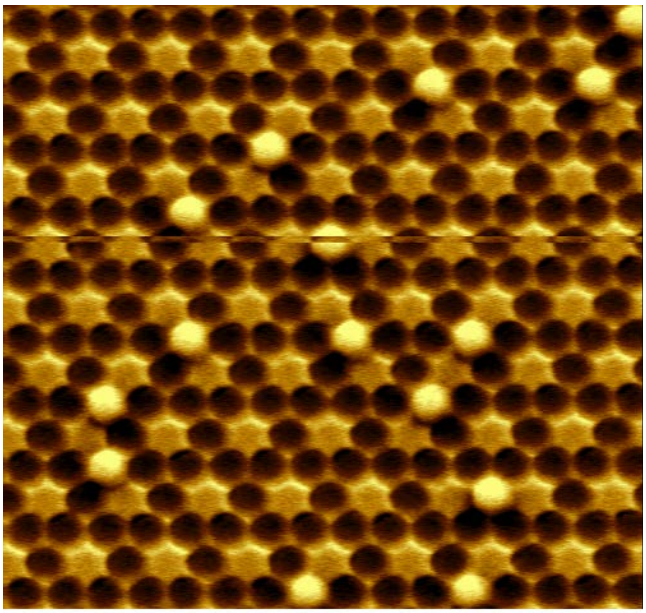

B = 275mT

Figure F.15 Artificial Kagome Ising under applied field - Image 14 - During the second pass of the MFM scan, the tip has hit the surface, causing a temporary loss of magnetic contrast. Nevertheless, the magnetic configuration can still be fully reproduced.

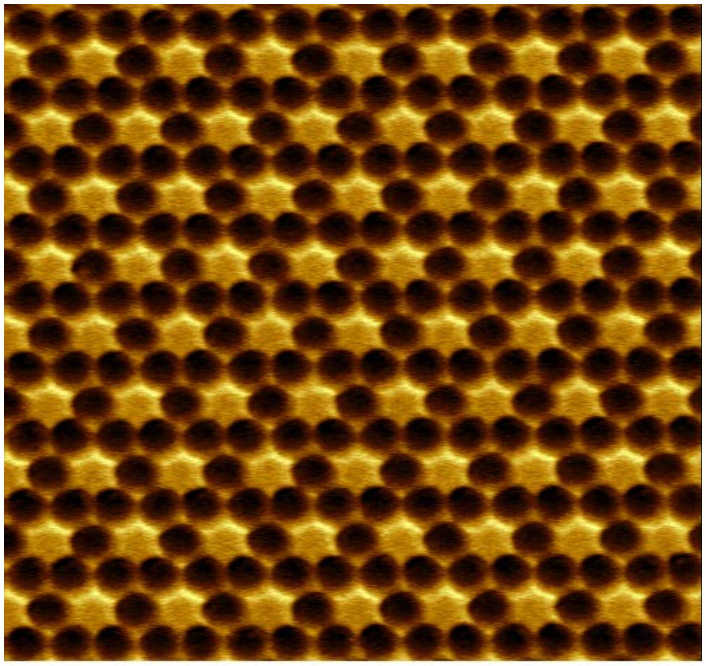

Figure F.16 Artificial Kagome Ising under applied field - Image 15